Grain Size Effects in Polycrystalline Exchange Biased Systems

by

Gonzalo Vallejo Fernández

Submitted for the Degree of Doctor of Philosophy

University of York
Department of Physics

December 2006

Abstract

The capability of a novel sputtering technology known as HiTUS to produce thin films with controlled grain size and distribution has been evaluated. This has been achieved for different materials chosen due to their importance in industrial applications. The grain size of the deposited films was measured from TEM images in bright field mode. All the distributions were lognormal and over five hundred particles were measured to recompose each lognormal function. For a range of materials close control of grain size between 4nm and 30nm was achieved.

The grain size was controlled through the deposition rate. This has allowed the investigation of the effect of the antiferromagnetic grain size on exchange bias without the use of underlayers, additives or substrate heating. It was found that the magnitude of the loop shift strongly correlated to the distribution of grain volumes in the antiferromagnetic layer. Using detailed measurements of the grain size distribution the features of exchange bias in these systems can be explained on the basis of a grain volume model with coherent rotation.

For example using measurement protocols that ensure reproducibility of data has allowed the development of a new measurement technique for the anisotropy constant of metallic antiferromagnets. This is a key result since the anisotropy is used in all theoretical models of exchange bias as a fitting parameter. The anisotropy was determined only from experimental features and only its temperature dependence had to be assumed to be of the form $K(0K)(1-T/T_N)^3$ in order to calculate the values. For IrMn $K(293K) = 4.14 \times 10^6$erg/cc and for FeMn $K(293K) = 1.36 \times 10^6$erg/cc.

Table of Contents

List of Figures

List of Tables

Acknowledgements

I would like to thank the European Union Training Network NEXBIAS for funding this research for the past three years.

I would like firstly to thank Prof. Kevin O'Grady, my supervisor, for his generosity, guidance and care throughout the course of this PhD. It has been a pleasure to work with him over the past three years, and I look forward to working under his supervision in the future.

Dr. Marian Vopsaroiu has been a huge support, particularly during the first two years of my PhD. He showed me how to use essential equipment and had it not been for his help, this thesis could not have been completed. I would also like to thank Dr. Sadia Manzoor for her help and fruitful discussions during the year she spent in York as a visiting research fellow. I would like to thank the technical staff in the Physics department at the University of York – specifically David Coulthard and Richard Armitage for their help.

My period as a visiting researcher at SIEMENS in Erlangen was valuable, both personally and professionally. I would particularly like to thank Dr. Joachim Wecker and Dr. Manfred Ruehrig for inviting me to their lab. Also, I want to acknowledge my officemates at SIEMENS. In particular, Dr. Theo Dimopoulos for making my stay more pleasant.

I wish to thank my officemates for making my life in York so enjoyable, especially during the last year of my PhD: Anne, Nick, Tom and Jenny. Also, I would like to thank Dr. Luis Eugenio Fernández Outón for his support and friendship during this time.

Finalmente quisiera agradecer a mi familia el apoyo que me han mostrado durante todo este tiempo, especialmente 'a los de casa' por su cariño, ayuda y comprensión. Finally, I would like to thank Vanny for her love, support and endless patience during all this time. She has been the best support I could have asked for.

Declaration

I declare that the work presented in this thesis is based purely on my own research unless otherwise stated, and has not been submitted for a degree in either this or any other university.

Signed

Gonzalo Vallejo Fernández

Chapter 1 Introduction

Exchange bias (EB) was discovered fifty years ago by William H. Meiklejohn and Charles P. Bean when studying the coercivity of Co fine particles prepared by the electro-deposition of cobalt into mercury. These cobalt particles were removed from the mercury by oxidising their surface. When the samples were field cooled to 77K to measure their magnetic properties a shift in the hysteresis loop along the field axis by an amount H_{ex} (Figure 1) and a sinΘ torque curve were observed. Another important feature was the increase of the coercivity H_c, defined as the half width of the loop, when compared to the samples that did not undergo the oxidation treatment. The crystal structure of the samples was studied by X-ray diffraction showing that the oxide was CoO. CoO is antiferromagnetic below room temperature and, therefore, exchange bias was attributed to an exchange coupling between the ferromagnetic (*F*) layer Co and the antiferromagnetic (*AF*) layer CoO. Hence, this phenomenon received the name of '*exchange anisotropy*' (Meiklejohn and Bean, 1956).

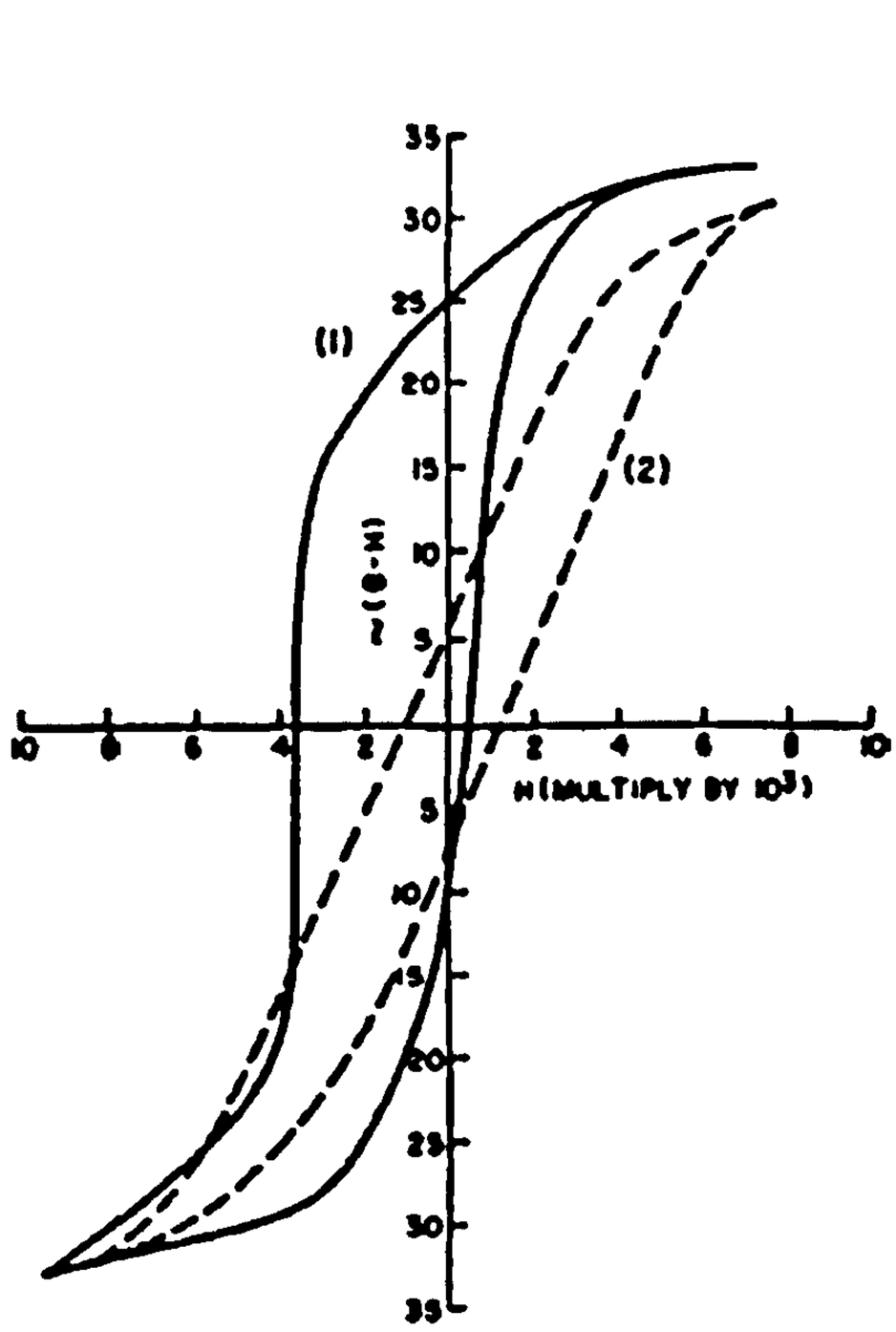

Figure 1. Hysteresis loop of the Co particles embedded in their natural oxide measured at 77K after field cooling in a 10kOe magnetic field (solid line) (Meiklejohn and Bean, 1956).

Materials exhibiting exchange anisotropy were originally proposed for application as permanent magnets. However the only industrial applications of exchange bias are in the form of thin films. In particular, all computers use exchange bias in the form of a thin film sensor that 'reads' the information stored in the magnetic bits. Exchange bias has been a key parameter in achieving the actual performance levels of conventional computers over the past few decades. Nowadays exchange bias is also used in the soft underlayer in perpendicular media to maintain a single domain state in the underlayer and avoid domain wall noise, increasing the recording performance (Jung and Doyle, 2003).

Even though thousands of papers have been published on exchange bias since 1956 a theory that can account for all the experimental features that have been reported is still missing. This in part due to the different nature of the systems studied and, in particular, of the *AF* layer. Nowadays it seems unlikely that a unique theory can be used to explain the features of systems containing a metallic/non-metallic single-crystal/polycrystalline *AF*. For all applications *AF*s are sputtered polycrystalline metallic films with grain size in the range ≈20nm. In this work only exchange biased samples containing a polycrystalline metallic *AF* have been studied and, therefore, the results and their interpretation are only valid for this particular system.

Another important problem when modelling exchange bias is that most of the reports in the literature are not specific with respect to the experimental conditions used to acquire the data. A clear example is the conventional measurement of the blocking temperature i.e. the temperature at which the exchange bias goes to zero. In most of the studies a sample is heated to a given temperature and the hysteresis loop is measured. This procedure is repeated until H_{ex}=0. However, it is known that *AF*s are thermally unstable and are subject to thermal activation during the time of measurement at a logarithmic rate (O'Grady *et al.*, 2002). Therefore, the state of order in the *AF* layer prior to measurement is unknown and this makes the interpretation of the data difficult. Fernandez-Outon *et al.* (2004) developed a measurement procedure by which the state of order in the *AF* was reset between measurements by heating to a given temperature for 90 minutes in the presence of a saturating field. Following that measurement procedure thermal effects were reproducible making the interpretation of the data easier.

Most of the models proposed to explain exchange bias are based on the formation of domains either parallel (e.g. Mauri *et al.*, 1987a) or perpendicular (e.g. Malozemoff, 1987) to the *F/AF* interface. All these models succeed to some extent to explain some experimental results as discussed in several reviews of exchange bias [e.g. Nogues and Schuller (1999), Stamps (2000), Kiwi (2001)]. However, these models can only be applied to single crystal systems. Since all the samples studied in this work are granular, a model that treats the *F* and the *AF* as an assembly of grains (e.g. Fulcomer and Charap, 1972a) seems more appropriate.

As the thickness of the films is reduced towards the nanometre scale the microstructure of the films becomes dominant in defining their physical properties. The most important of these micro structural properties are grain size, grain size distribution, crystallographic texture and interface/surface roughness. One of the topics that still remains unclear about exchange bias is the role of the *AF* grain size and conflicting reports can be found in the literature regarding this issue. While exchange anisotropy has been found to decrease with increasing *AF* grain size (e.g. Takano *et al.*, 1997) the opposite trend can also be found in the literature (e.g. Tsunoda *et al.*, 1997). Conventional techniques to control the grain size in thin films are based on the use of additives (e.g. Ajan and Okamoto, 2002), seed layers (e.g. Lee *et al.*, 1994) or annealing (e.g. Kale and Lokhande, 2004). In this work, a novel sputtering technology known as HiTUS (Thwaites, 2002) has been used to control directly the grain size and its distribution of the sputtered samples via close control of the growth-rate. It is the aim of this work to evaluate the capability of the HiTUS system to produce thin films with controlled grain size and grain size distribution and to characterise the effect of the *AF* grain size on exchange bias samples containing a metallic *AF* layer.

Since the Gaussian c.g.s units system is widely used by the magnetic recording industry and the applied magnetism community, this system has been used in all the equations in this work. Information about other units system can be found in e.g. Cullity (1972) or O'Handley (2000).

Chapter 2 Magnetism of thin films

2.1. Introduction

In this chapter the basic concepts of magnetism as they apply to exchange bias systems will be introduced. These ideas are necessary for the understanding of the experimental results obtained in this work. Magnetic anisotropy and, in particular, magnetocrystalline anisotropy, are fundamental in the design of most magnetic materials for commercial applications. Anisotropy is found in both the ferromagnetic *F* and antiferromagnetic *AF* layers of exchange couples. Magnetic domains are a key parameter in the understanding of the mechanism of magnetic hysteresis. In particular the alloy $Co_{60}Fe_{40}$ has been studied in this work and exhibits complex grain size effects. Exchange bias is an exchange anisotropy and therefore an understanding of the different exchange mechanisms responsible for the types of magnetic response is necessary. Exchange coupling controls the *F* and *AF* layers and importantly interfacial spin strucutures affect H_{ex}. Hence, a brief introduction of antiferromagnetism is required to describe the effects.

2.2. Magnetic anisotropies

Magnetic anisotropy refers to the fact that the magnetic properties of a given material are dependent upon the measurement direction. Among all the magnetic anisotropies only the magnetocrystalline anisotropy is intrinsic to the material. This refers to the fact that a material with a certain crystalline structure will magnetise more easily when the field is applied along certain crystallographic directions. In the case of the alloy $Co_{60}Fe_{40}$, studied in this work, the crystalline structure is bcc where <100> are *easy directions* and <111> are *hard directions*. Magnetocrysalline anisotropy plays a key role in the modelling of exchange bias as it controls the possible energy states of the magnetic moments in the *AF*. Important extrinsic anisotropies are exchange anisotropy, shape anisotropy and stress anisotropy although the last two will be treated very briefly as they are not relevant for this work.

2.2.1. Magnetocrystalline anisotropy

The saturation magnetisation M_s of a specimen can be easily achieved when an external field is applied along certain directions which are accordingly called *easy directions* of magnetisation. The magnetocrystalline anisotropy is the energy necessary to rotate a magnetic moment from an easy to a hard direction. Therefore, a quantitative measure of the strength of the magnetocrystalline anisotropy is given by the field necessary to saturate a crystal along one of its hard directions. When the field is removed after reaching saturation, a greater proportion of the magnetisation will remain in the direction in which the field was applied if it is in an easy as opposed to a hard direction.

Magnetocrystalline anisotropy arises due to spin-orbit coupling between the spins and the lattice of the material. The spin part of the magnetic moment interacts with the electron orbits. These orbits are linked to the crystallographic structure and therefore the spins prefer to align along the easy crystallographic axis. In 1929 Akulov showed that the magnetocrystalline anisotropy energy E_a could be expressed as a series expansion of the direction cosines of M_s relative to the crystal axes (Cullity, 1972). In a cubic crystal, letting α_1, α_2, and α_3 be the cosines of these angles, then

$$E_a = K_0 + K_1\left(\alpha_1^2\alpha_2^2 + \alpha_2^2\alpha_3^2 + \alpha_3^2\alpha_1^2\right) + K_2\left(\alpha_1^2\alpha_2^2\alpha_3^2\right) + \ldots \qquad \text{Eq. 2.1}$$

where K_0, K_1 and K_2... are the anisotropy constants for a given material. Sometimes K_2 is so small that it can be neglected and also higher power terms. The first term, K_0, is usually ignored as it is angle independent. A crystal with a single easy axis is referred to as a uniaxial crystal. In such a case, and neglecting K_0 and K_2 the crystal anisotropy energy can be rewritten as $E_a = K_1 \sin^2\theta$ where θ is the angle between the easy axis of the crystal and the moment direction. However, the value of anisotropy constants for certain cubic materials have been calculated using large ab-initio computer models (e.g. Ostanin *et al.*, (2003), Staunton *et al.*, (2004)). Magnetocrystalline anisotropy plays a key role in exchange bias as the energy barrier to reversal of an *AF* grain is given by $K_{AF}V_{AF}$ where V_{AF} is the volume of the *AF* grain (Fulcomer and Charap, 1972a,b). This is true for uniaxial *AF*s. In the case of cubic *AF*s the energy barrier is given by $K_{AF}V_{AF}/4$ due to the crystal symmetry (Joffe and Heuberger, 1974).

Hoffmann (2004) showed that cubic *AF*s such as IrMn and FeMn relax into a uniaxial configuration once the *F* is reversed for the first time after the system is set. Carey *et al.* (2001) reported a value of 1.8×10^6 erg/cc for the uniaxial anisotropy constant of IrMn when studying the thermally assisted decay of pinning in polycrystalline exchange biased systems. Steenbeck *et al.* (2004) studied the *AF* energy loss and exchange coupling of IrMn/CoFe bilayers. They supposed a three-axial in-plane anisotropy for their (111) textured IrMn films and calculated a value for the anisotropy of 1.4×10^6 erg/cc at 10K. In the case of FeMn, Mauri *et al.* (1987a) showed that the magnetic anisotropy could be estimated from the critical thickness of the *AF* layer above which there was a sharp onset of the exchange bias in FeMn/NiFe bilayers resulting in a value of $\approx 1.35 \times 10^5$ erg/cc.

2.2.2. Shape anisotropy

In 1947 L. Néel explained this type of anisotropy as being due to the formation of free poles at the ends of single domain particles. If a specimen is not spherical, e.g. an elongated particle, it is easier to magnetise along a long axis as the demagnetising field is stronger along a short axis. In order to achieve the same field inside the specimen, the field applied along the short axis is required to be much stronger than the field applied along a long axis. Therefore, shape alone can be a source of anisotropy. The shape anisotropy constant for such a system is given by

$$K_s = \frac{1}{2}(N_a - N_c)M_s^2 \qquad \text{Eq. 2.2}$$

where N_a and N_c are the demagnetising factors along the semi axes of the particle and M_s is the saturation magnetisation. The strength of the shape anisotropy depends both on the axial ratio c/a of the specimen and on the square of the saturation magnetisation. All the *F* layers in the samples studied in this work are polycrystalline and even if the grains are not equiaxed they are very strongly exchange coupled and the films are almost 100% dense preventing the formation of free poles and therefore shape anisotropy does not apply.

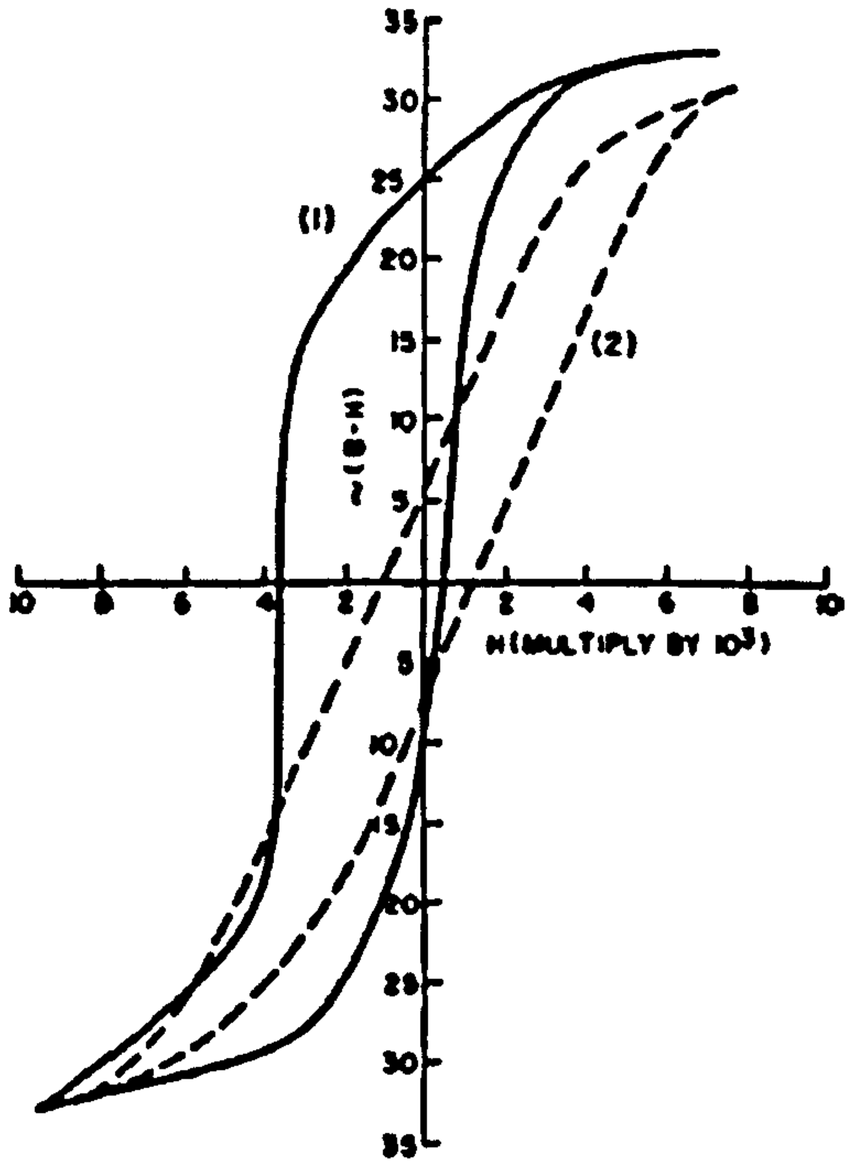

Figure 2. Hysteresis loops at 77K after cooling in a 10kOe magnetic field (solid line) and after zero field cooling (dashed line) (Meiklejohn and Bean, 1956).

2.2.3. Exchange anisotropy

Exchange anisotropy arises when a ferromagnetic *F* material is in direct contact with an antiferromagnetic *AF* material. The *AF* pins the magnetisation of the *F* and as a consequence the loop is displaced by an amount H_{ex} along the field axis and the coercivity, defined as the half width of the loop, is enhanced. This loop displacement is known as the exchange field. Exchange anisotropy was discovered by Meiklejohn and Bean (1956) when trying to demonstrate the predicted coercive force of aligned elongated, single domain cobalt particles. The Co particles were prepared by electro-deposition of Co into Hg. The surface of the particles was oxidized to separate them from the Hg. Magnetic measurements at 77 K after field cooling the sample in a 10kOe magnetic field showed a displaced hysteresis loop and a sinΘ torque curve. However when the sample was cooled in zero magnetic field the loop was symmetric. Hence, the loop displacement was attributed to an exchange coupling between the Co particles and the CoO layer. Figure 2 shows the hysteresis loops for the Co particles at 77K. This is a unidirectional anisotropy as found from the torque curve and is the subject of this thesis. Exchange anisotropy is nowadays used in all modern computers in the magnetic sensor that reads the information stored in the bits of the magnetic hard disk. Since its

discovery, exchange bias has been reported for many different systems (for a review see Nogués and Schuller, 1999). A detailed introduction to exchange anisotropy will be given in Chapter 3.

2.2.4. Other anisotropies

The direction of the magnetisation of a specimen can be controlled by the application of a stress due to orbital reorientation of the magnetic atoms in the direction of the applied field. Accordingly this type of anisotropy receives the name of stress anisotropy. Although it is not relevant for this work there are reports on the literature regarding the effect of stress on exchange bias (Binek *et al.*, 2005).

Another type of uniaxial anisotropy can be induced simply by plastic deformation. This directional order is created by slip. In alloys, slip by a unit distance can create like-atom pairs where none existed before along a certain direction. This direction then becomes a local easy axis. Rolling has been widely used as a deformation method (e.g. Si-Fe, Kim *et al.*, 1998). Finally, the irradiation of a specimen with high energy particles in a magnetic field is known as magnetic irradiation. As a consequence, an anisotropy arises due to a series of atomic rearrangements. This technique has been used to tune the exchange bias field and the coercivity in exchange coupled systems (Juraszek *et al.*, 2002).

2.2.5. CoFe nanoparticulate films

High moment films are essential for applications such as the soft underlayer in perpendicular media. The highest known magnetisation values occur in the bcc $Fe_{100-x}Co_x$ alloy systems in the range $30 \leq x \leq 50$ (Bozorth, 1993). The samples studied in this work contained a $Co_{60}Fe_{40}$ layer. However, soft magnetic properties are required and CoFe alloys do not naturally exhibit soft properties. Thomson *et al.* (1998) reported values of the coercivity in CoFe films grown on Au/MgO seed layers as low as 16 Oe. Similar results were reported by Platt *et al.* (2000) when $Co_{50}Fe_{50}$ was grown on top of a CoO layer. The coercivity dropped from 140 Oe to 12 Oe. The CoO underlayer promoted the growth of a soft polycrystalline CoFe film composed of single crystal columnar grains that extended through the entire thickness of the film (Figure 3). It was

concluded that the reduction in H_c was due to a reduction in the grain size from 20-35 nm to 5-15 nm.

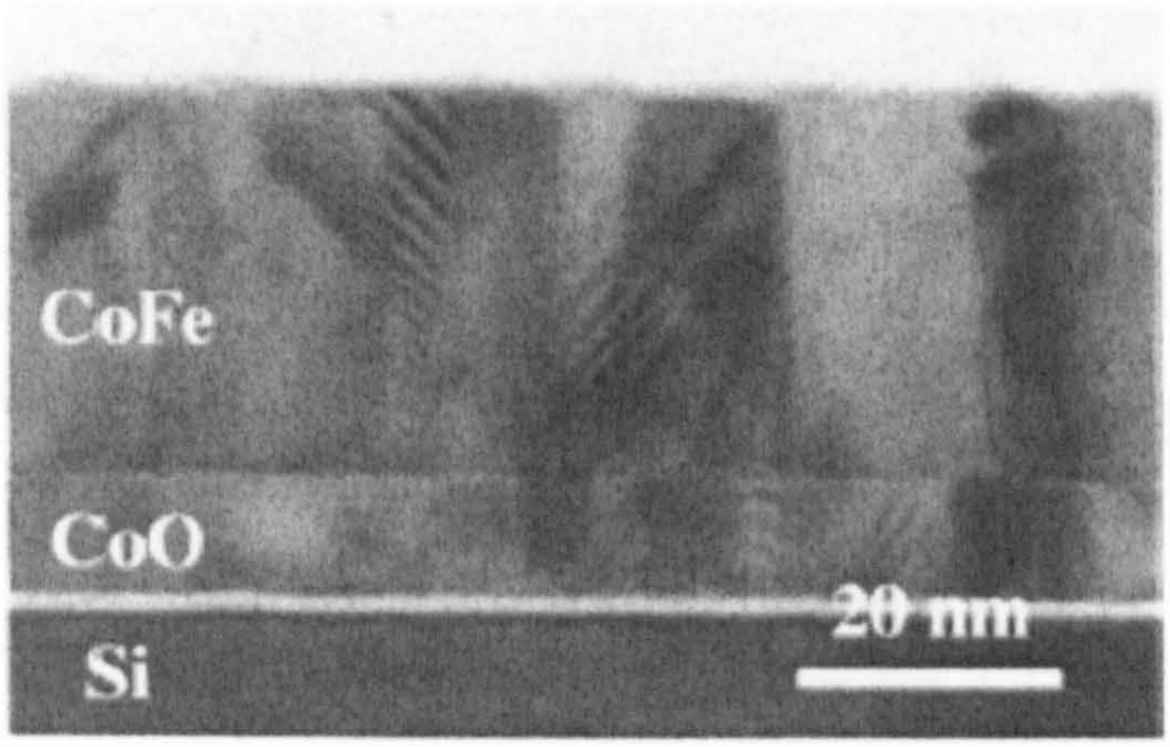

Figure 3. Cross section TEM image of a si/CoO(10nm)/CoFe(30nm) grown at 100°C (Platt *et al.*, 2000)

It is clear that the use of underlayers has a strong effect on the magnetic properties of CoFe. Jung *et al.* (2003) studied the effect of different underlayers on $Co_{35}Fe_{65}$ in order to understand the origin of the soft properties in this alloy. They showed that a Cu seed layer as thin as 2.5 nm could reduce the coercivity of 50 nm thick CoFe films from 120 Oe in the case of samples with no seed layer down to 12 Oe. They demonstrated that the primary effect of the Cu, NiFe and Ru underlayers was to reduce the grain size in CoFe which caused a reduction in the coercivity. Their results were explained in the basis of Hoffmann's ripple theory (1973).

Additives have also been used to reduce the coercivity to less than 20 Oe in CoFe films (e.g. N, Wang *et al.*, (2000)). Vopsaroiu *et al.* (2005a) reported on the preparation of soft 20 nm thick $Co_{60}Fe_{40}$ films without the use of seed layers or additives. The samples were prepared using a HiTUS (Thwaites, 2002) sputtering system which allows close control of the grain size in polycrystalline thin films (Vopsaroiu *et al.*, 2004). Samples with a mean grain diameter below 15 nm showed soft magnetic properties with coercivities less than 25 Oe and a minimum of 12 Oe. The results were explained in terms of the random anisotropy model (Herzer, 1990). More recently, Craig *et al.* (2006) showed that the inclusion of 1.5 nm thick Al_2O_3 non-magnetic spacers between $Co_{35}Fe_{65}$ layers reduced the mean crystallite size leading to lower values of the

coercivity when compared to values of a single magnetic layer. Figure 4 shows a cross section transmission electron microscope TEM image of the laminated structures.

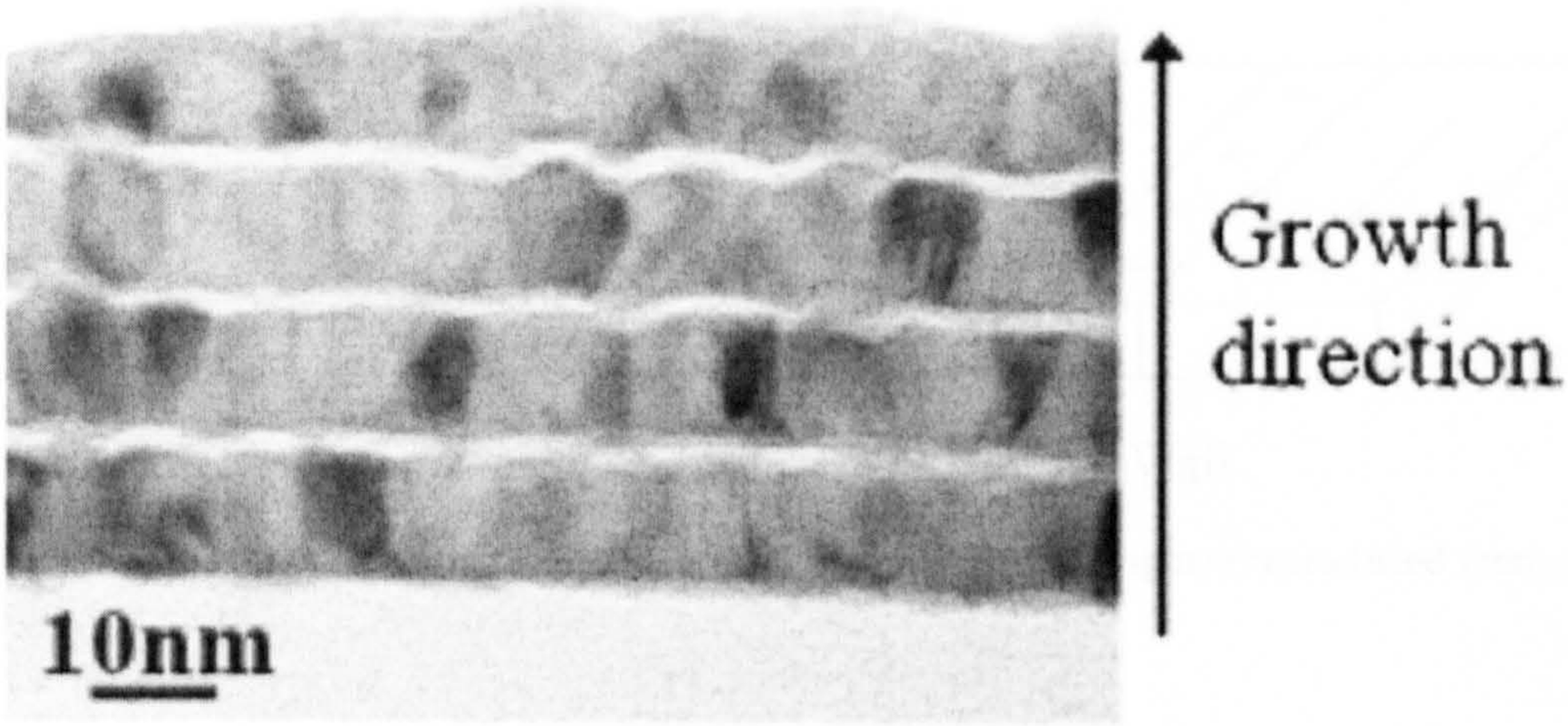

Figure 4. Cross section TEM image of NiFe/CoFe/(Al_2O_3/NiFe/CoFe)x3 (Craig *et al.*, 2006).

2.3. Magnetic domains and domain walls

Magnetic domains are regions where the spontaneous magnetisation has different directions. The boundary between those regions is known as domain wall and within the wall the magnetisation must change direction. The idea of domain structures was first introduced by Weiss in 1906 when trying to explain why a piece of ferromagnetic material could be in a demagnetised state.

2.3.1. Néel walls

If we assume an abrupt change of magnetisation the exchange energy associated with it would be very large. This energy can be reduced if we allow the 180° change in spin direction to take place over a certain amount of atoms N. The angle ϕ between adjacent spins would be π/N reducing the exchange energy. However, the anisotropy energy within the wall is high as there are spins pointing in non-easy directions. Therefore, there is a competition between exchange energy, trying to make the wall as thick as possible, and anisotropy energy trying to reduce the number of spins pointing in non-easy directions. As a consequence, the domain wall has a certain width δ and structure.

The first theoretical examination of a domain wall was made by Bloch in 1932 and they are often called Bloch walls (Cullity, 1972). This is valid for bulk specimens where the magnetisation within the wall lies normal to the plane of the material.

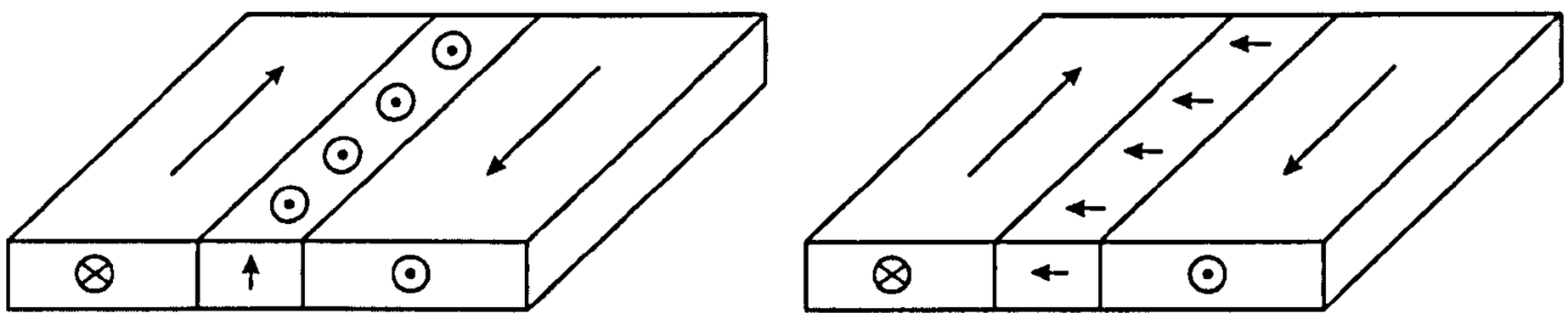

Bloch Wall Néel Wall

Figure 5. Schematic diagram of a Bloch wall (left) and Néel wall (right) (reproduced from Cullity, 1972).

As the thickness of the specimen is reduced, the magnetostatic energy of the wall increases as a consequence of the free poles at the top and bottom of the wall. Therefore, the spins within the wall must change direction in such a way that the magnetostatic energy is reduced. Hence, the rotation of the spins lies in plane. This special form of domain wall is known as Néel wall (Figure 5). Only thin film samples have been studied in this work and therefore only Néel walls are relevant.

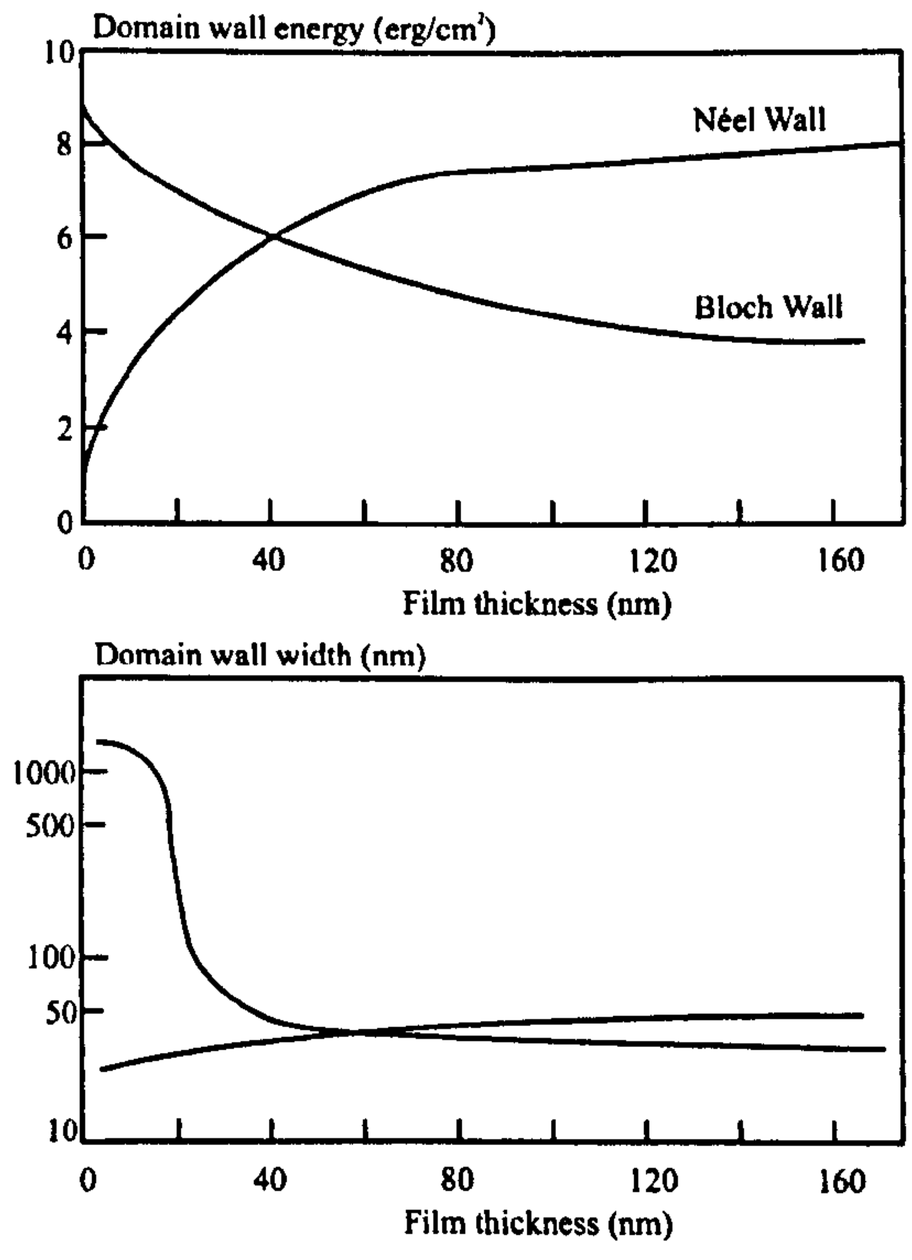

Figure 6. Energy per unit area (top) and thickness (bottom) of a Bloch and a Néel wall as a function of the film thickness (reproduced from O'Handley, 2000).

Figure 6 shows the film thickness dependence of both the domain wall energy and the domain wall width for both Bloch and Néel walls. Néel walls are observed to be stable in many different types of magnetic films for thicknesses up to 50-60 nm (O'Handley, 2000). In the case of 30 nm thick $Co_{50}Fe_{50}$ samples Platt *et al.* (2000) reported domain wall widths of 8 and 40 nm for low angle and 180° walls respectively. For 20 nm thick $Co_{60}Fe_{40}$ samples Vopsaroiu *et al.* (2005) estimated a value of 41 nm for the domain wall width. The transition between Bloch and Néel walls is gradual leading to the formation of more complex structures such as cross-tie walls in films with thickness in the region 40-50 nm (Figure 6).

2.3.2. Domain formation in CoFe

NiFe and CoFe alloys are widely used in technological applications based on the exchange bias effect. The latter is characterised by a high magnetocrystalline anisotropy and therefore domain nucleation and growth characterises the magnetisation reversal of such systems.

Domains form due to the minimisation of the magnetostatic energy. Magnetic poles will be produced at the surface of a magnetised specimen. This surface charge distribution is the source of a magnetic field that opposes the state of magnetisation of the sample. Accordingly it is called the demagnetising field H_D and is given by

$$H_D = -N_D M_s \qquad \text{Eq. 2.3}$$

where N_D is the demagnetising factor and M_s the saturation magnetisation of the material. The value of the demagnetising factor is dependent upon the shape of the sample varying between 0 and 4π in cgs units (O'Handley, 2000). In the case of thin films, such as the samples studied in this work, N_D equals 0 in the plane and 4π in the perpendicular direction. Therefore, the magnetisation of such systems tends to lie in plane.

Exchange bias measurements of *F/AF* bilayers are usually performed with the magnetisation of the *F* layer parallel to the *AF* interface (N_D=0). However, in some

cases the magnetisation of the *F* layer is promoted to lie perpendicular to the plane (N_D=4π). This can be achieved by using *F*/Pt multilayers as the pinned layer (e.g. Maat *et al.*, 2001). CoFe/IrMn polycrystalline exchange couples are the main system studied in this work. Hence, the formation of domains and domain walls in CoFe thin films has a great importance in the understanding of the magnetisation reversal processes in CoFe/IrMn bilayers.

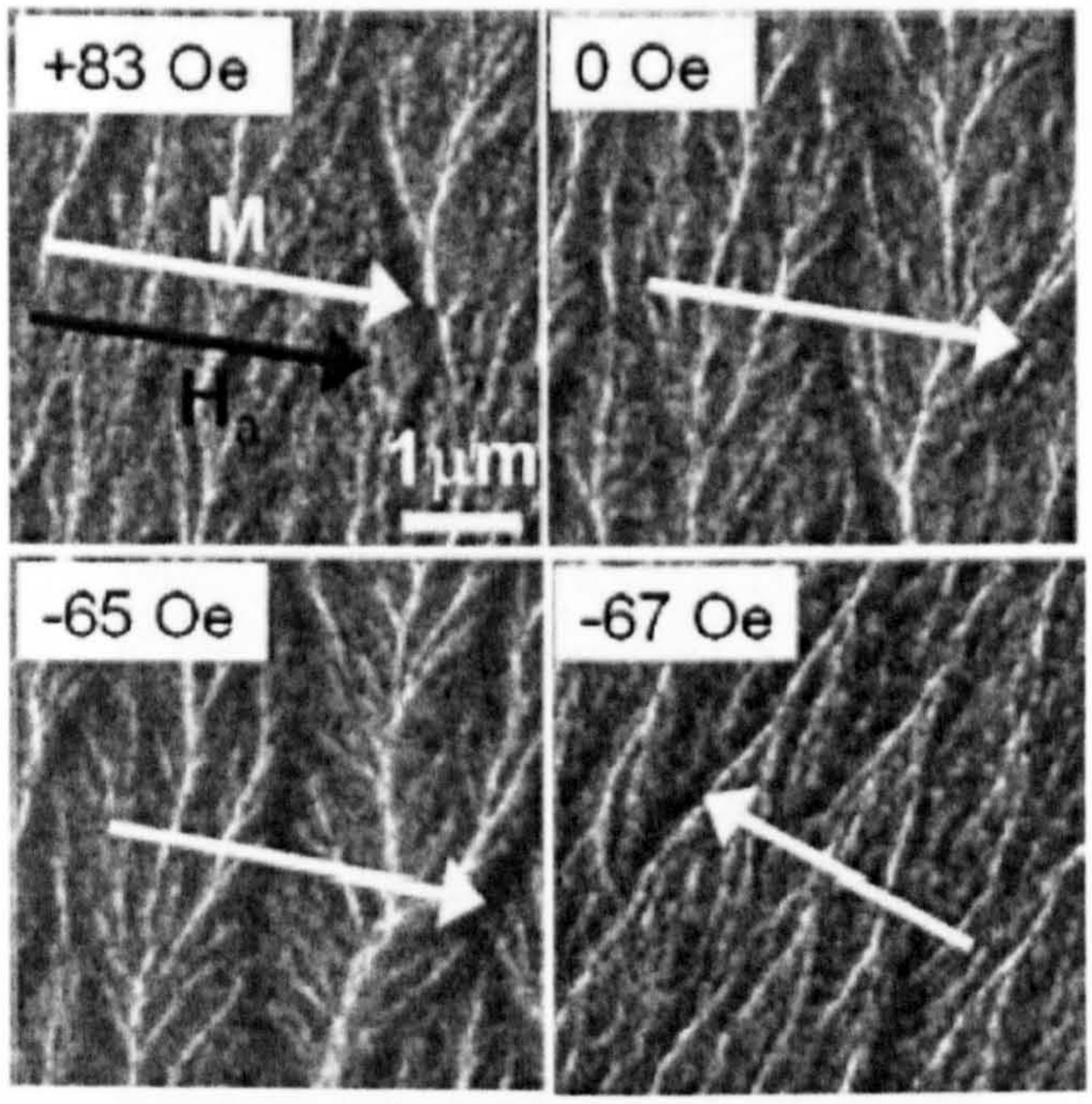

Figure 7. TEM images of the easy axis hysteresis loop of a 50 nm thick CoFe film. Black and white arrows indicate the applied field and the magnetisation directions, respectively (Craig *et al.*, 2006).

A transmission electron microscope TEM can be used for the observation of domain and domain walls with specimens thin enough so they are electron transparent (<100 nm or less). Electrons passing through the specimen will be deviated. The direction and amount of this deviation will be determined by the magnitude and direction of the local M_s vector. In a domain wall this vector changes within the wall and the result is that the wall shows up as a line, either black or white, on the image of the specimen. The microscope must be slightly under- or over focused to make the wall visible. This technique received the name Lorentz microscopy. Craig *et al.* (2006) used this technique to study the magnetisation reversal of 50 nm thick CoFe films with high saturation magnetisation. Although all the samples had the same total thickness the difference between them was the inclusion of a seed layer or the introduction of non-

magnetic spacers to form laminated films. Figure 7 shows TEM observation of the magnetisation reversal of the CoFe single layer. Magnetisation ripple is apparent in all images and the ripple contrast intensified as the field was changed from positive to negative values. Thereafter, a domain wall not captured with the CCD camera of the microscope swept through and affected the magnetisation reversal.

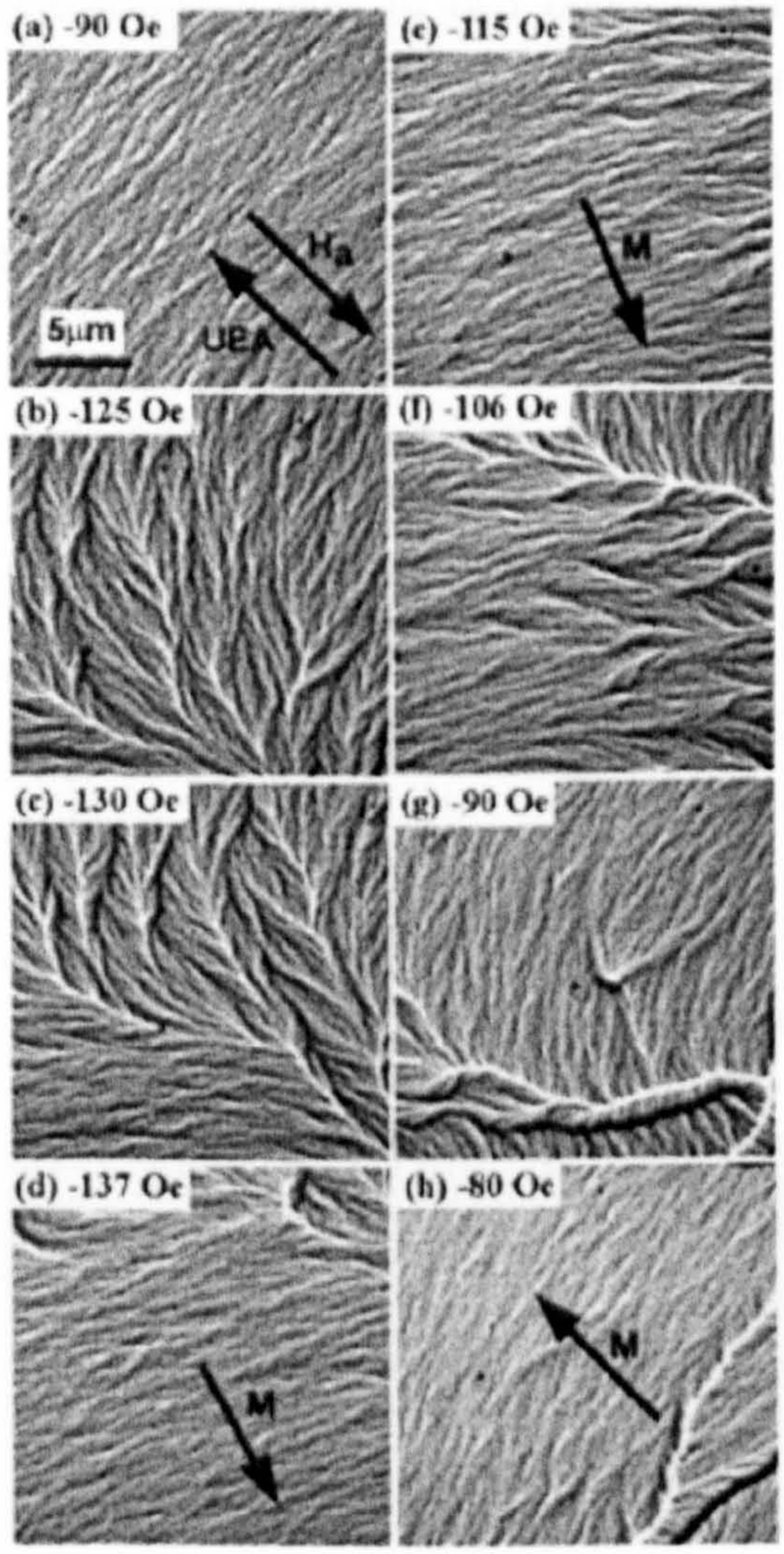

Figure 8. Fresnel images of the magnetisation reversal of a IrMn(10nm)/CoFe(10nm) bilayer. (a)-(d) show the forward reversal and (e)-(h) the recoil reversal. H_a is the applied field and UEA the unidirectional exchange anisotropy (Wang and Petford-Long, 2002).

This technique has also been used to study the reversal mechanism for easy and hard axis in IrMn/CoFe exchange biased systems. Wang and Petford-Long (2002) studied the magnetisation reversal of such a system as a function of the *AF* thickness. Figure 8 shows *in situ* magnetisation reversal images of an IrMn(10nm)/CoFe(10nm) bilayer with a sweep-rate of 0.5 Oe/s. Along the descending branch of the loop the CoFe

remained saturated in the positive direction due to the *F*/*AF* coupling until a field of –91 Oe was applied. In Figure 8(a) magnetisation ripple is visible perpendicular to the magnetisation direction and Figure 8(b)-(d) show images of the film during the reversal. The ripple contrast increases as the applied field decreases indicating some local rotation of the moments away from the positive field direction. The CoFe layer then reverses slowly via coherent moment rotation (Wang and Petford-Long, 2002). Following this the magnetisation rotates in two opposite directions and low-angle domain walls form. This is followed by nucleation and growth of domains with near 90° walls changing to near 180° walls normal to the magnetisation reversal before disappearing (Wang and Petford-Long, 2002).

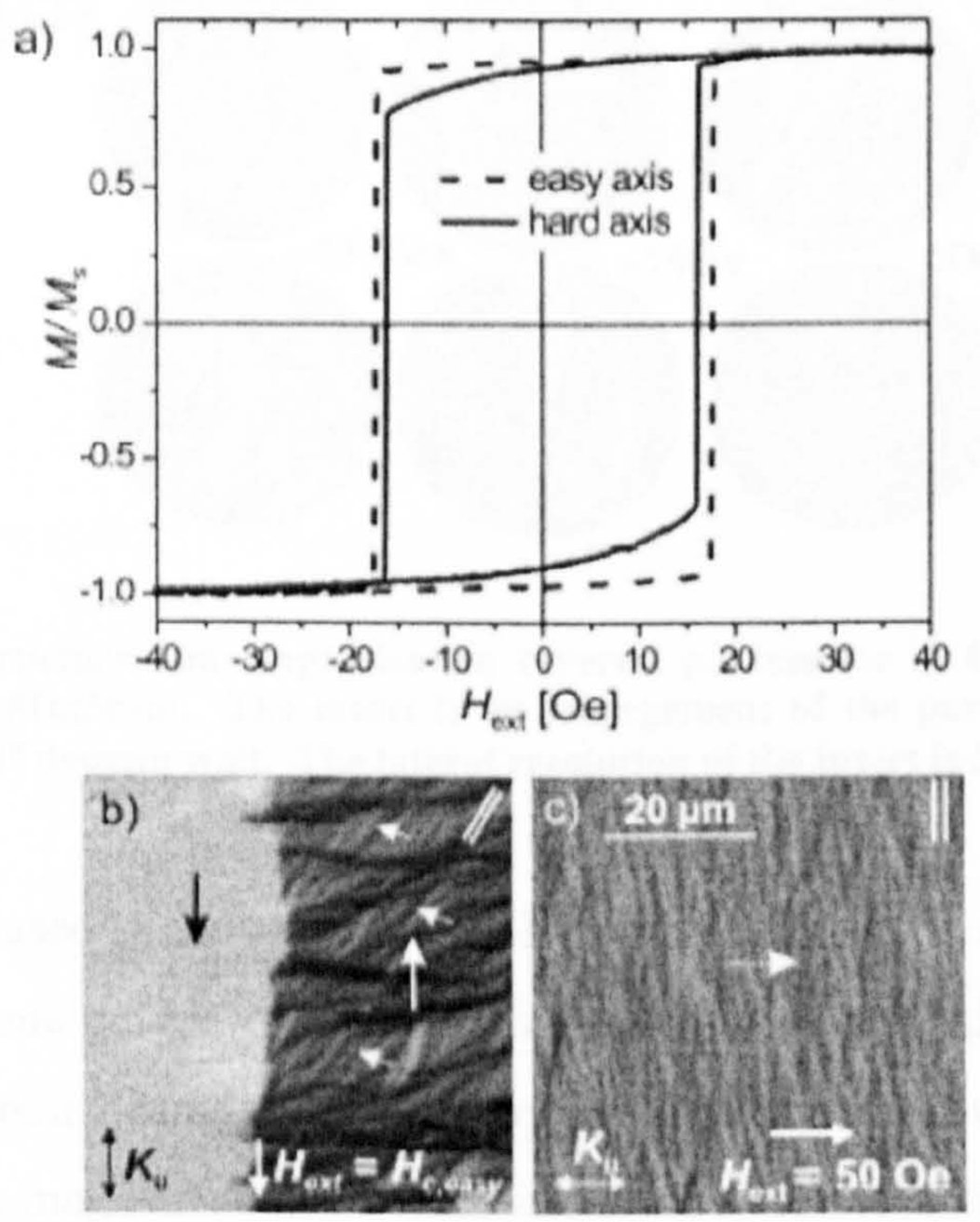

Figure 9. a) Easy and hard axis hystersis loops for a single CoFe film b) Domain state around the coercivity during an easy axis loop c) Domain structure with an external field equal to the field applied during the deposition of the exchange couples (McCord *et al.*, 2003).

The Bitter method consists in the application of magnetite nanoparticles (Fe_3O_4) to the polished surface of a specimen. The fine particles are attracted to the region of the domain wall due to the field created on the surface by the spins within the wall depositing along the domain wall. If the surface is examined with a reflecting microscope in bright field mode illumination the domain walls will appear as a dark line

on a light background. If dark field mode is used, the domain wall appears as a light line in a dark background.

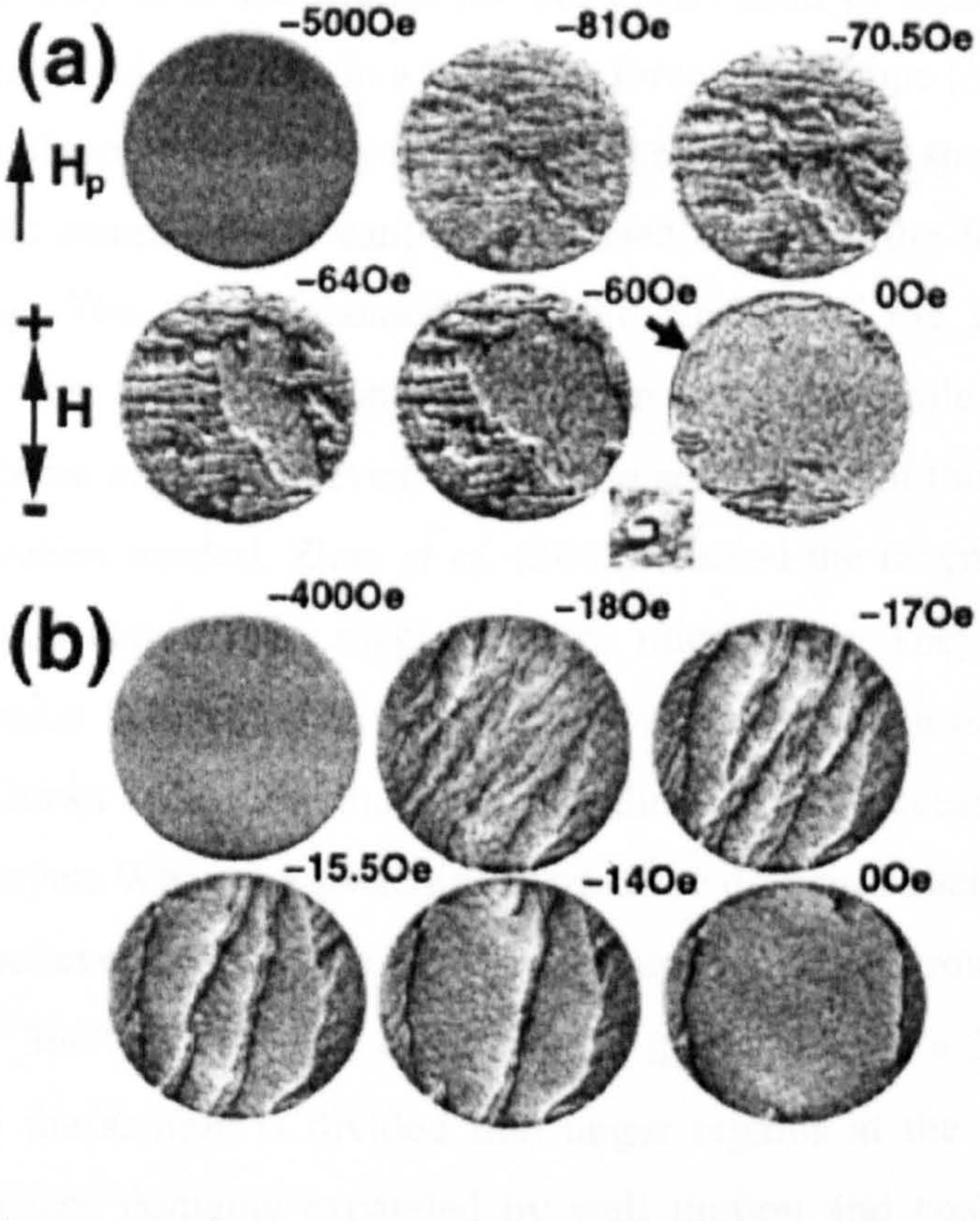

Figure 10. Domain structure and magnetisation reversal process for a) CoFe(10nm)/IrMn(5nm) and b) CoFe(20nm)/IrMn(5nm). The insert is an enlargement of the part pointed by the arrow corresponding to a 360° domain wall. The lateral resolution of the insert is 5m (Zhao *et al.*, 2002).

The Kerr effect is based in the change of polarisation of the light as it is reflected by a specimen. When plane polarised light hits the specimen, supposed to contain only two domains, two different beams will rotate by different amounts when they encounter domains of opposite magnetisation. An analyser is then rotated until one of the beams is extinguished. The other domain appears black while the extinguished domain appears white. McCord *et al.* (2003) studied asymmetric magnetisation reversal processes in $Co_{90}Fe_{10}$(20nm)/$Ir_{23}Mn_{77}$(10nm) bilayers by high resolution Kerr microscopy. They also studied the reversal mechanism of a single $Co_{90}Fe_{10}$ layer. Easy and hard hysteresis loops are shown in Figure 9a. Figure 9b shows the domain structure around the coercive field during an easy axis loop. When an external field of 50 Oe is applied as in Figure 9c magnetisation ripple can be identified. The same field was used for the deposition of

the exchange couples and therefore these small angle domains were expected to get transferred to the *AF* layer when depositing the IrMn layer on top of the CoFe layer.

One of the most widely used techniques for the observation of domains and domain walls is magnetic force microscopy. In a magnetic force microscope (MFM) a magnetic tip is used to probe the magnetic stray field above the surface of a specimen. The tip is brought close to the sample and a cantilever is used to detect the force between the sample and the tip. The tip is scanned over the surface of the sample to obtain information about the magnetic domain structure of the sample. Typical lateral resolution below 50 nm can be achieved. One of the advantages of this technique is the little sample preparation needed. Zhao *et al.* (2002) studied the magnetisation reversal of IrMn/CoFe circular elements by magnetic force microscopy. They observed drastic changes in the domain structure and the reversal process with the thickness of the *F* layer. Figure 10a shows the MFM images during the reversal process in the case of a 10nm thick CoFe layer. When the switching started the domain structure looked like a ripple structure. The reversal seemed to proceed through incoherent rotation as indicated by the presence of 360° walls (Zhao *et al.*, 2002). In the case of a 20nm thick CoFe layer (Figure 10b) the sample is divided into larger regions at the beginning of the reversal process. These domains expanded by wall motion and coalesced with each other.

2.4. Antiferromagnetism

Antiferromagnets are substances with a small positive susceptibility χ at all temperatures. Antiferromagnets exist with two sublattices of opposite magnetisation. If the cancellation of the magnetisation was perfect $\chi(0K)=0$. However, it is clear from Figure 11 that that is not the case. The variation of their susceptibility with temperature is not simple. The theory of antiferromagnetism was firstly developed by Néel in the second quarter of the twentieth century. He applied the Weiss molecular field theory to the problem.

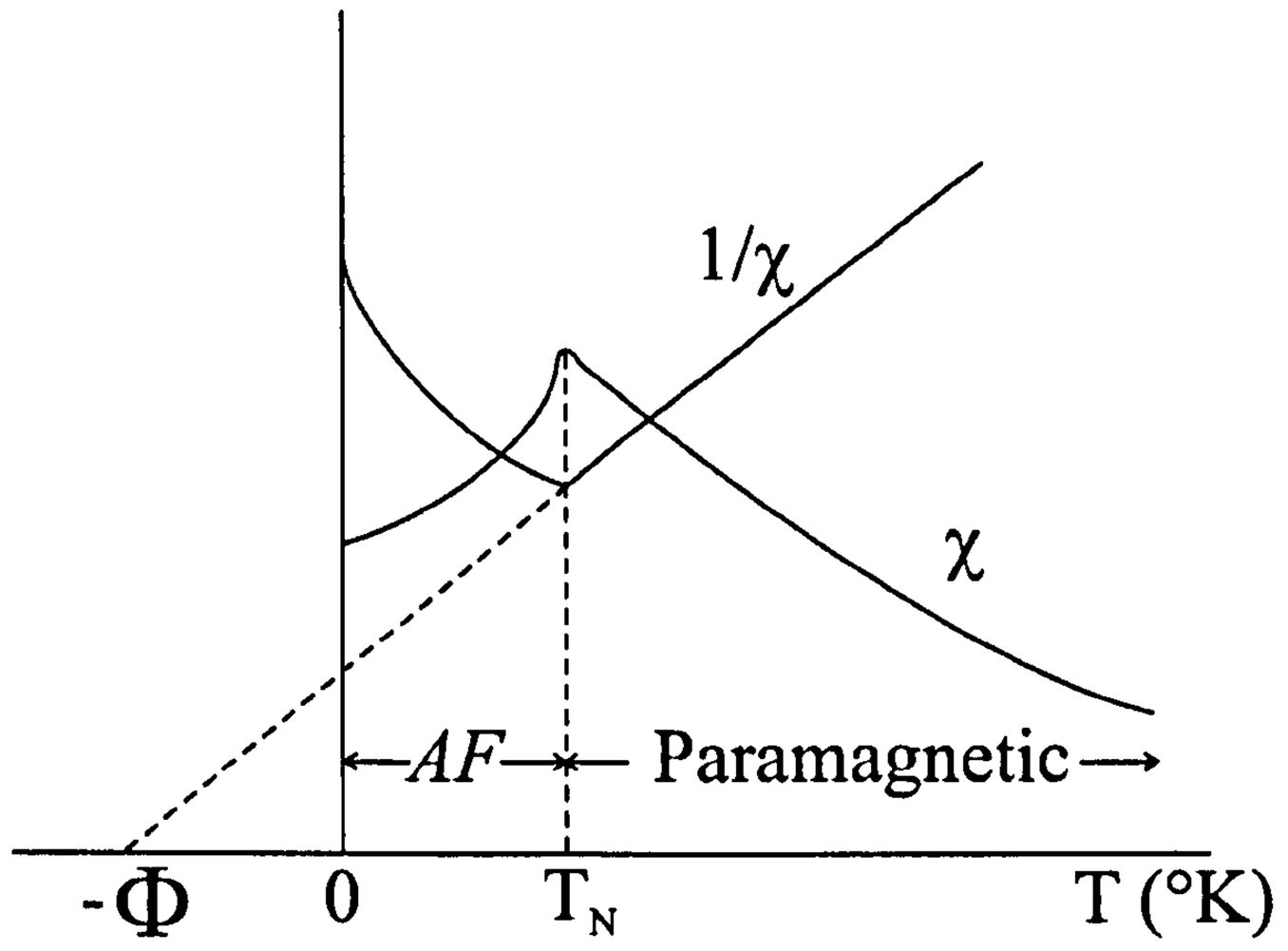

Figure 11. Temperature variation of the *AF* susceptibility.

The variation of the susceptibility of an antiferromagnetic *AF* material is shown in Figure 11. The susceptibility χ increases as the temperature T is reduced and goes through a maximum at a critical temperature called the Néel temperature T_N. The substance is *AF* below T_N and paramagnetic above T_N. Most of the *AF* materials are ionic compounds. The variation of $1/\chi$ with T is also shown in Figure 11. It can be seen that it is a straight line above T_N and this line can be extrapolated to a negative value $-\Phi$ at $1/\chi=0$. The equation of the line can be written as

$$\frac{1}{\chi} = \frac{T+\Phi}{C} \qquad \text{Eq. 2.4}$$

where C is the Curie constant. The material follows a Curie-Weiss law but with a negative value of Φ.

$$\chi = \frac{C}{T+\Phi} = \frac{C}{T-(-\Phi)} \qquad \text{Eq. 2.5}$$

In the paramagnetic region the molecular field H_m is opposed to the applied field. Whereas the applied field tries to align the spins, the molecular field tends to misalign them. Therefore, if an ionic moment tends to point in one direction the moment on an adjacent ion tends to point in the opposite direction due to the molecular field. Below T_N

this tendency of antiparallel alignment is strong enough even in the absence of an applied field. At $T = 0$°K the antiparallel alignment is perfect. An antiferromagnet has no net spontaneous moment and a moment can be acquired only when a large field is applied.

Until the application of antiferromagnetic materials in magnetoresistive spin-valve sensors the interest in *AF* materials was merely academic. The understanding of the *AF* order was a key factor in the understanding of other ordered materials such as ferrimagnets.

2.4.1. Structure of antiferromagnets

Most antiferromagnets exist with two sublattices of opposite magnetisation as depicted in Figure 12. The magnetisation within each sublattice almost cancels. The cancellation is not complete until $T = 0$°K due to defects, thermal effects and spin canting in DC fields. Most antiferromagnetic materials are insulators and therefore they contain no free electrons. Therefore the electrons responsible for their magnetic properties are localized to certain ions. Hence, the behaviour of each sublattice is explained quite well by the molecular field theory.

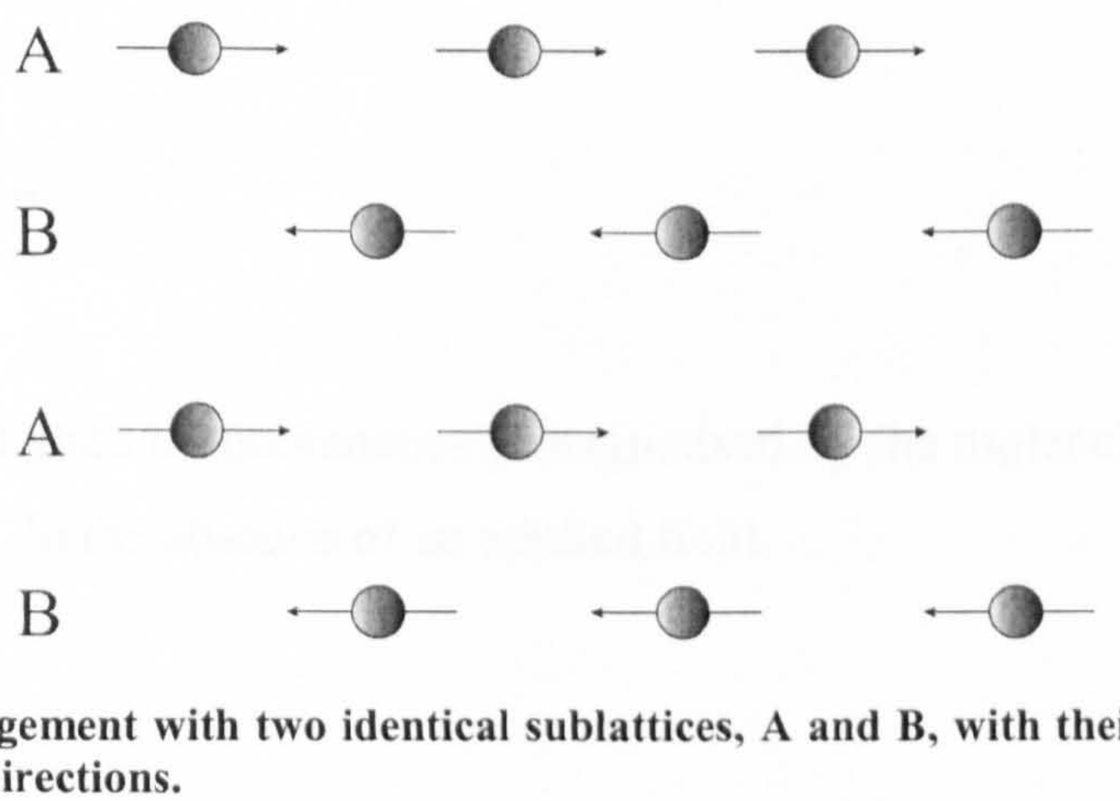

Figure 12. *AF* arrangement with two identical sublattices, A and B, with their magnetic moments pointing in opposite directions.

If the simplest case the molecular field theory is applied to two identical sublattices, A and B, where any A ion has only B ions as nearest neighbours. Second nearest neighbours interactions, AA and BB, are neglected. Two molecular fields have to be

considered: the molecular field H_{ma} acting on the A ions and the molecular field H_{mb} acting on the B ions.

$$H_{ma} = -\gamma H_{mb} \qquad \text{Eq. 2.6}$$

where γ is the molecular field constant. If standard Curie-Law behaviour is assumed above T_N

$$MT = \rho C H_{tot} \qquad \text{Eq. 2.7}$$

where H_{tot} is the total field, both applied and molecular, and ρ is the density. If Eq. 2.7 is written for each sublattice

$$M_A T = \rho C'(H - \gamma M_B) \qquad \text{Eq. 2.8}$$

$$M_B T = \rho C'(H - \gamma M_A) \qquad \text{Eq. 2.9}$$

where C' is the Curie constant of each sublattice and H the applied field. If these two equations are added the susceptibility can be calculated

$$\chi = \frac{M}{\rho H} = \frac{2C'}{T + \rho C' \gamma} \qquad \text{Eq. 2.10}$$

Below T_N each sublattice is spontaneously magnetised by the molecular field created by the other sublattice. In the absence of an applied field

$$M_A = -M_B \qquad \text{Eq. 2.11}$$

The magnetisation of each sublattice will be given by the normal Brillouin function. This is best solved graphically and the solution is shown in Figure 13 where $\sigma_{A\text{-}B}/\sigma_{0A\text{-}B}$ is the fractional spontaneous magnetisation of each sublattice. Even though the spontaneous magnetisation is zero, a small magnetisation can be produced if a magnetic field is applied. The resulting susceptibility is strongly dependent upon the angle that

the external field makes with the axis along which the *AF* spins lie. Values of T/T_N as high as 5 and 6 have been reported. This does not mean that the molecular field theory cannot be applied but that the assumptions made are not totally correct. Therefore, the possibility of AA and BB interactions should not be neglected.

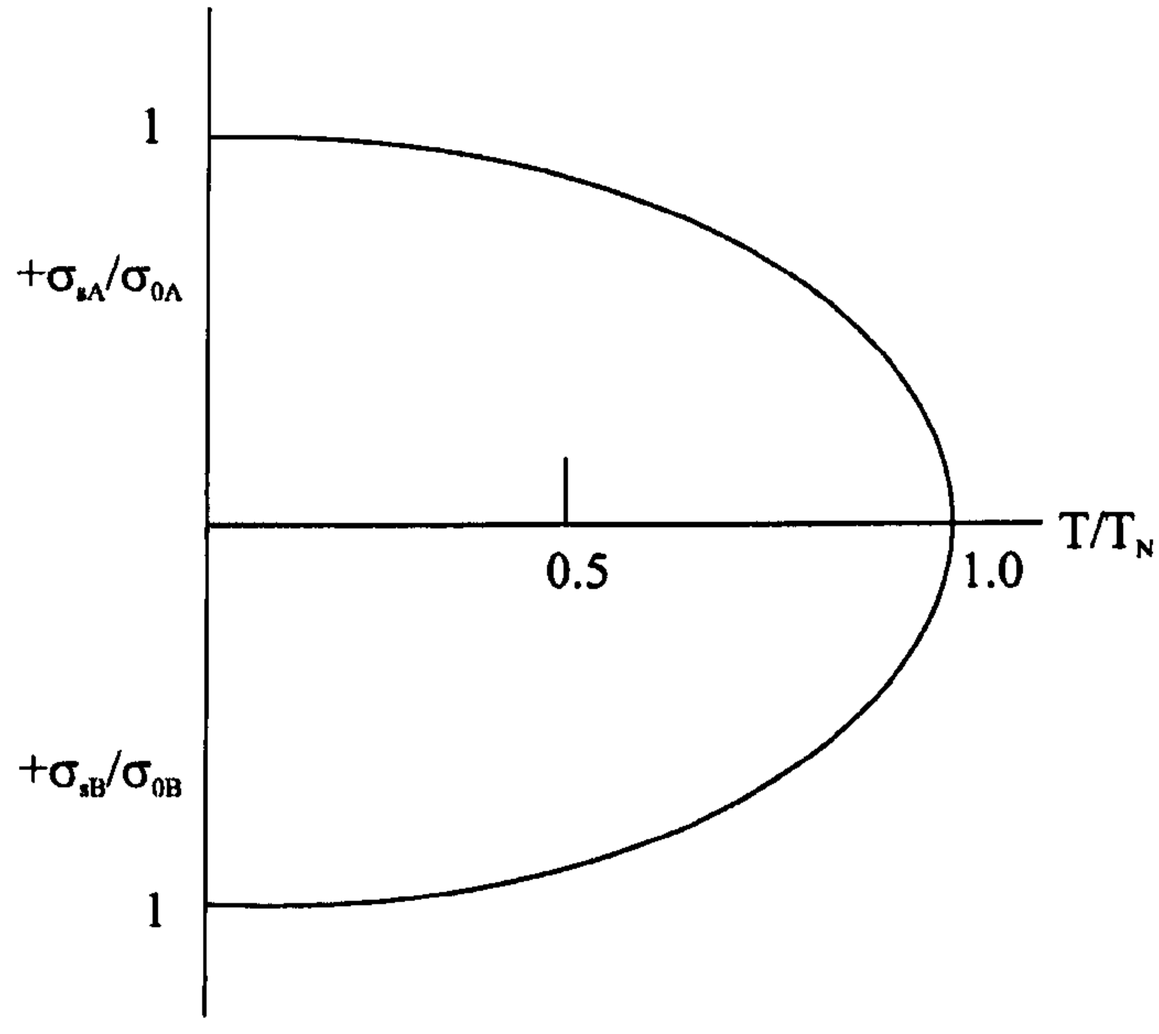

Figure 13. Spontaneous magnetisation of the two *AF* sublattices below the Néel temperature.

2.4.2. Spin structure of antiferromagnets

Until 1949 all the evidence about the spin arrangement in antiferromagnets was due to susceptibility measurements. However, in 1949 C. Shull and Smart demonstrated experimentally that the spin structure in MnO was divided into two groups, one antiparallel to the other. These results had been obtained using neutron diffraction and since then this technique has been widely used to study other systems, not only antiferromagnets but also ferromagnets and ferrimagnets (e.g. Carling *et al.*, 2002).

When the antiferromagnet is in its paramagnetic state there is a random distribution of spin directions. Some of the scattered neutrons will be in phase and some of them out of phase but with the same intensity. As a consequence there will be no reflection in a particular direction. When the *AF* is cooled below its Néel temperature there will be perfect order. Now the neutrons that are scattered in and out of phase will have different intensity and therefore a reflection will be observed. Other reflections planes can be examined and more lines will be present in the diffraction pattern of ordered materials

than in the pattern corresponding to the paramagnetic state. These lines are known as superlattice lines. A superlattice reflection will be observed if the axis of the spins make an angle different than 90° with the reflection plane.

2.4.3. Antiferromagnetic systems

All antiferromagnetic materials can be divided into three groups (Berkowitz, 2005): antiferromagnetic oxides, metallic antiferromagnets and antiferromagnetic fluorides. Only metallic antiferromagnets have been studied in this work. This is important as different mechanisms may apply to different systems.

AF oxides have been studied since the discovery of exchange bias in 1956. Indeed, Co particles embedded in their natural oxide CoO, which is antiferromagnet, were the first system for which exchange anisotropy was reported. Since then a lot of the work reported on exchange bias has included not only CoO but also NiO and $Co_xNi_{1-x}O$. Takano *et al.* (1997) reported on the correlation between interfacial uncompensated spins and H_{ex} when studying NiFe/CoO bilayers. A decrease of H_{ex} with the CoO grain size was reported. These results show an opposite trend to the data presented in this work. However, in CoO it is possible to have intergranular exchange coupling from the superexchange interaction via the p orbitals in the oxygen atoms. This would allow for the formation of domains within the CoO layer. However there is no known mechanism that can give rise to intergranular exchange coupling in metallic *AF*s. Moreover, Takano *et al.* (1997) did not take into account the width of the distribution of grain sizes which is as important as the mean diameter. The interpretation of the results presented in this work is only valid for polycrystalline metallic *AF*s containing small grains (<20nm).

Metallic antiferromagnets usually have Néel temperatures and anisotropies higher than those of *AF* oxides. Therefore, they have been used for most technological applications. The most popular metallic *AF*s are FeMn, IrMn and PtMn. FeMn in its chemically disordered γ-phase is fcc at room temperature in the range 30-55 at% Mn (Umebayashi *et al.*, 1966). In this range T_N was reported to increase from 425 to 525 K (Umebayashi *et al.*, 1966). IrMn is a disordered fcc *AF* in the range 14 to 31 at% Ir. It has a higher T_N than FeMn, 750K for 31 at% Ir (Yamaoka, 1974). Ordered Mn_3Ir has been reported by Imakita *et al.* (2004) after following a detailed deposition procedure. PtMn must be in

its ordered fct structure to observe exchange bias (e.g. Pokhil *et al.*, 2001). A magnetic annealing treatment is usually required although ordered PtMn has been reported in the as deposited state (Choi *et al.*, 2005). Experimental findings on metallic *AF*s will be treated in detail in Chapter 4.

AF fluorides have also been subject of study. Nogués *et al.* (1996) reported positive exchange bias when FeF_2 bilayers were field cooled in a large positive field. They suggested that *AF* spins were polarised in the cooling field direction and that *AF* coupling between *AF* interfacial and *F* spins produced a positive shift of the hysteresis loop.

2.4.4. Polycrystalline vs. single crystal antiferromagnets

In a single crystal the crystal lattice of the entire sample is continuous and unbroken to the edges of the sample, i.e. there are no grain boundaries. Single crystals are mostly grown by Molecular Beam Epitaxy (MBE). This thin film deposition technique is based on the evaporation of atoms from the material to be deposited when the target is heated close to its melting point. The most important features of MBE is the low deposition rate in a UHV system. These are key parameters to achieve epitaxial growth. However, this requires a cleaner atmosphere and therefore, a better vacuum in order to achieve the same level of impurity as other deposition techniques such as sputtering. Another advantage of sputtering over MBE is the deposition speed. As a consequence sputtered samples are polycrystalline, i.e. made of a number of small crystallites. The samples studied in this work have been prepared using sputtering.

All the models that have been proposed to explain exchange bias in the last 30 years can be divided into two groups: domain and granular models. The former are based on the formation of domains in the *AF* layer either parallel (e.g. Mauri *et al.*, 1987a) or perpendicular (e.g. Malozemoff, 1987) to the *AF/F* interface. In the case of polycrystalline metallic antiferromagnets the formation of domains perpendicular to the interface is very unlikely as there is not known mechanism that can account for intergranular exchange coupling in *AF* films. This is a consequence of the required atomic ordering in a crystallographic lattice. Therefore, a granular approach seems to be more reasonable in polycrystalline exchange biased systems. This is in agreement with

the results presented in Chapter 6. However, in single crystal systems the anisotropy directions along the film are very well defined and the interactions between spins are stronger (e.g. Li *et al.*, 2001). Different mechanisms may apply for different systems and the formulation of a universal model for exchange bias does not seem possible.

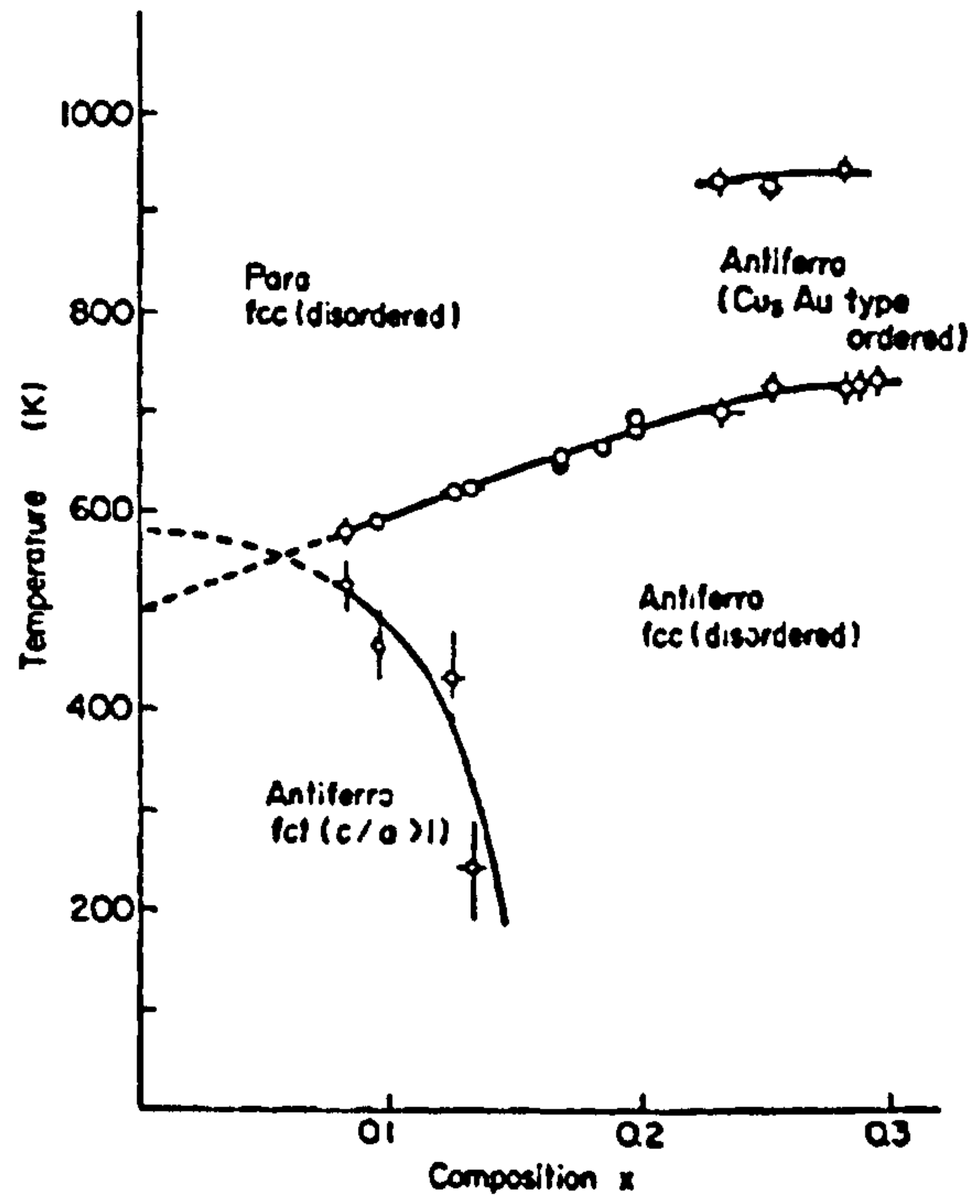

Figure 14. Magnetic phase digram of γ-phase IrMn alloys (Yamaoka, 1974).

2.5. Anisotropy in antiferromagnets: IrMn

Great attention has been focused on exchange anisotropy in the last 20 years due to its important application in giant magneto-resistive sensors (e.g. Childress *et al.*, 2001). Among all the *AF* materials, IrMn is usually chosen due to the fabrication requirements: the temperature at which the exchange bias goes to zero has to be at least 200°C, the exchange field must be at least 500-1000 Oe at an operating temperature of 125°C and the *AF* thickness must be thin enough to allow the spin-valve to fit in the narrow read gaps required for high density environments (Carey *et al.*, 2001). Most of the exchange bias samples studied in this work contain $Ir_{23}Mn_{77}$. The magnetic anisotropy of the *AF* layer and its role in on the magnetisation process of the *F* layer is still an important issue (Takahashi and Tsunoda, 2002).

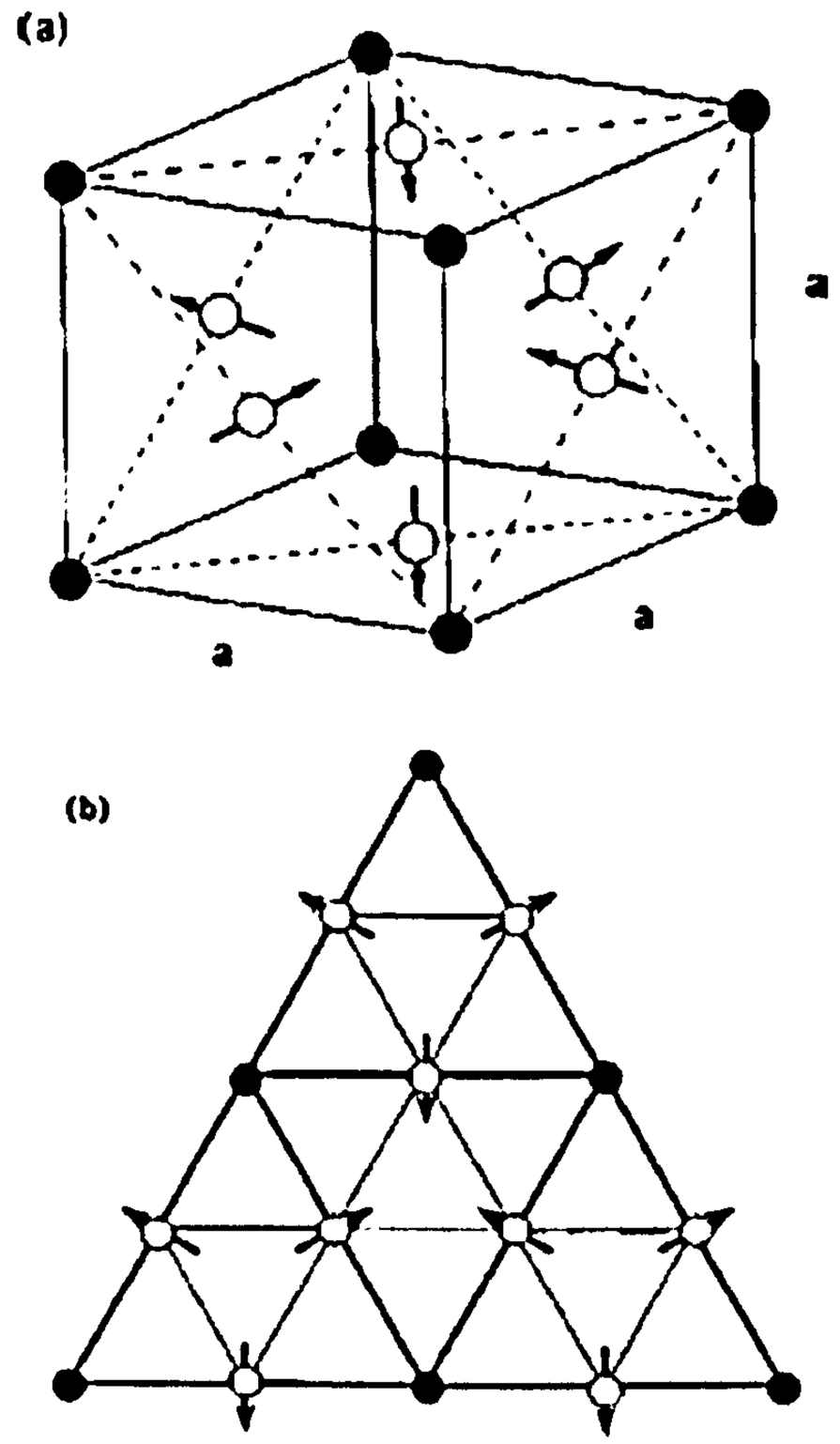

Figure 15. a) Antiferromagnetic structure and b) corresponding <111> spin structure of IrMn3. Open and solid circles represent Mn and Ir atoms, respectively (Tomeno *et al.*, 1999).

Takahashi and Tsunoda (2002) suggested that the magnetocrystalline anisotropy of the *AF* is responsible for its magnetic anisotropy. This was based on magnetic-torque analysis of a polycrystalline NiFe/IrMn and a pseudo-single crystalline NiFe/NiMn bilayer. They introduced a model for polycrystalline bilayers taking into account the two-dimensional random distribution of the magnetic-anisotropy axes of the *AF*. The anisotropy energy was determined from the saturation amplitude of the magnetic torque curve (Takahashi and Tsunoda, 2002).

Figure 14 shows the magnetic phase diagram of the γ-phase Ir_xMn_{1-x} alloy obtained by magnetic susceptibility measurements (Yamaoka, 1974). According to these results the $Ir_{23}Mn_{77}$ target used in this work is nominally in the disordered fcc (γ) phase. The Néel temperature in disordered γ-phase Ir_xMn_{1-x} alloys increases with increasing Ir content from 570K for x=0.08 to 730K for x=0.25. The ordered Cu_3Au-type-$IrMn_3$ is achieved

after annealing at ≈1000K (Yamaoka, 1974). Ordered $IrMn_3$ within the disordered phase has been reported by Imakita *et al.* (2004) after following a detailed deposition procedure. The same group reported the formation of the $L1_2$-phase in $IrMn_3$/CoFe bilayers (Tsunoda *et al.*, 2006). They investigated the degree of order of the IrMn layer as a function of the chemical composition of the *AF* layer, the type of underlayer material and the underlayer thickness. $L1_2$-phase $IrMn_3$ was obtained in the compositional range 22-32 at% Ir. Giant exchange anisotropy exceeding 1 erg/cm^2 (H_{ex}≈2kOe) was obtained in that range (Tsunoda *et al.*, 2006).

The magnetic structure in a disordered $Ir_{25}Mn_{75}$ alloy has been studied using neutron-diffraction experiments (Yamaoka *et al.*, 1974). One possibility is alternating planes of up and down spins along the <001> axis. The alternative is that each spin on the four sublattices is directed along the <111> axis. Tomeno *et al.* (1999) studied the magnetic structure of ordered $IrMn_3$. This is depicted in Figure 15. They found that this alloy maintains an *AF* triangular spin structure up to the Néel temperature.

2.6. Interactions in thin films

The magnetic behaviour of thin films such as those studied in this work can be poorly understood without an introduction to the mechanisms that lead to the different types of ordered magnetism. Hence, in this section, the main interaction mechanisms relevant to thin films will be discussed, i.e. direct exchange interaction, RKKY interaction and super exchange. In general, the exchange interaction is responsible for both ferromagnetism and antiferromagnetism. However, this interaction is really weak and insignificant for some materials such as rare earths metals. Indirect exchange via the conduction electrons is the exchange mechanism for those systems. Finally, in ionic solids the positive metallic ions that carry the magnetic moment are too far apart and therefore the exchange force cannot be the coupling mechanism. However, they interact indirectly through the neighbouring negative ions receiving the name of super exchange interaction.

2.6.1. Direct exchange interaction

Weiss (1906) assumed that the molecular field H_m was proportional to the magnetisation implying that the mechanism involved was a cooperative one. This field cannot be entirely magnetic and its origin was not understood until 1928 when Heisenberg showed that it was due to quantum mechanical inter-atomic exchange forces. If two atoms *i* and *j* have spin angular momentum $S_i h/2\pi$ and $S_j h/2\pi$ then the exchange energy between them is given by

$$E_{ex} = -2J_{ij}\underline{S}_i\underline{S}_j = -2J_{ij}S_iS_j\cos\phi \qquad \text{Eq. 2.12}$$

where J_{ij} is called the exchange integral and ϕ is the angle between the spins. This exchange interaction is responsible for ferromagnetism and antiferromagnetism. When $J_{ij}>0$, E_{ex} is a minimum when $\cos\phi=1$ resulting in ferromagnetic coupling of the spins. However, when $J_{ij}<0$, E_{ex} goes through a minimum when $\cos\phi=-1$ resulting in antiferromagnetic coupling.

Eq. 2.12 is valid for the case of two electrons. However, when a solid is considered it is necessary to sum the exchange over all the electrons of the system so the Hamiltonian is given by

$$\langle H\rangle = -2\sum\sum J_{ij}\underline{S}_i\underline{S}_j \qquad \text{Eq. 2.13}$$

Exchange forces decrease rapidly with distance and therefore only nearest-neighbour interactions are considered and the Heisenberg Hamiltonian is considerably simplified where it is assumed that $J_{ij}=J_{ex}$ is the same for all nearest neighbours. Larson *et al.* (1988) derived an isotropic spatial dependence of $J_{ex}(r)$ in the Gaussian form $\exp(-\eta r^2/a^2)$ where $\eta=4.89$ and 'a' is the fcc lattice constant when studying an antiferromagnetic nearest neighbour Mn-Mn exchange interaction in $Cd_{1-x}Mn_xTe$ semiconductors. A longer-range interaction of the form $J_{ex}(r)\sim (r/a)^{-n}$, with $n\approx5$-7, has been proposed by Twardowski *et al.* (1987) based on low temperature susceptibility data together with the assumption that the Mn ions are distributed randomly in $Zn_{1-x}Mn_xSe$ magnetic semiconductors.

$$\langle H \rangle = -2J_{ex} \sum_{\substack{nearest \\ neighbours}} \underline{S}_i \underline{S}_j \qquad \text{Eq. 2.14}$$

Knowledge that exchange forces are responsible for ferromagnetism has allowed the prediction of the appearance of ferromagnetism in some metals. For instance, the magnetic behaviour of chromium, manganese, iron, cobalt and nickel, all of them 3d elements, was of interest in the early work of the quantum theory of magnetism (Jiles, 1998). Values of the interatomic distances r_{ab} and the radii of the incompletely filled d subshell r_d of some transition elements were reported by Slater (1930a, 1930b). It was found that the sign of the exchange interaction correlated with the values of r_{ab}/r_d. For large values of r_{ab}/r_d the exchange was positive and for small values it was negative.

Bethe made some calculations to obtain the value of the exchange integral J_{ex} as a function of interatomic spacing and radius of d orbitals. The results published by Slater (1930a, 1930b) were used and the exchange integral could be plotted against the ratio r_{ab}/r_d where r_d is the radius of the 3d orbital. This gives the Bethe-Slater curve shown in Figure 16 which can separate the ferromagnetic 3d elements from the antiferromagnetic 3d elements.

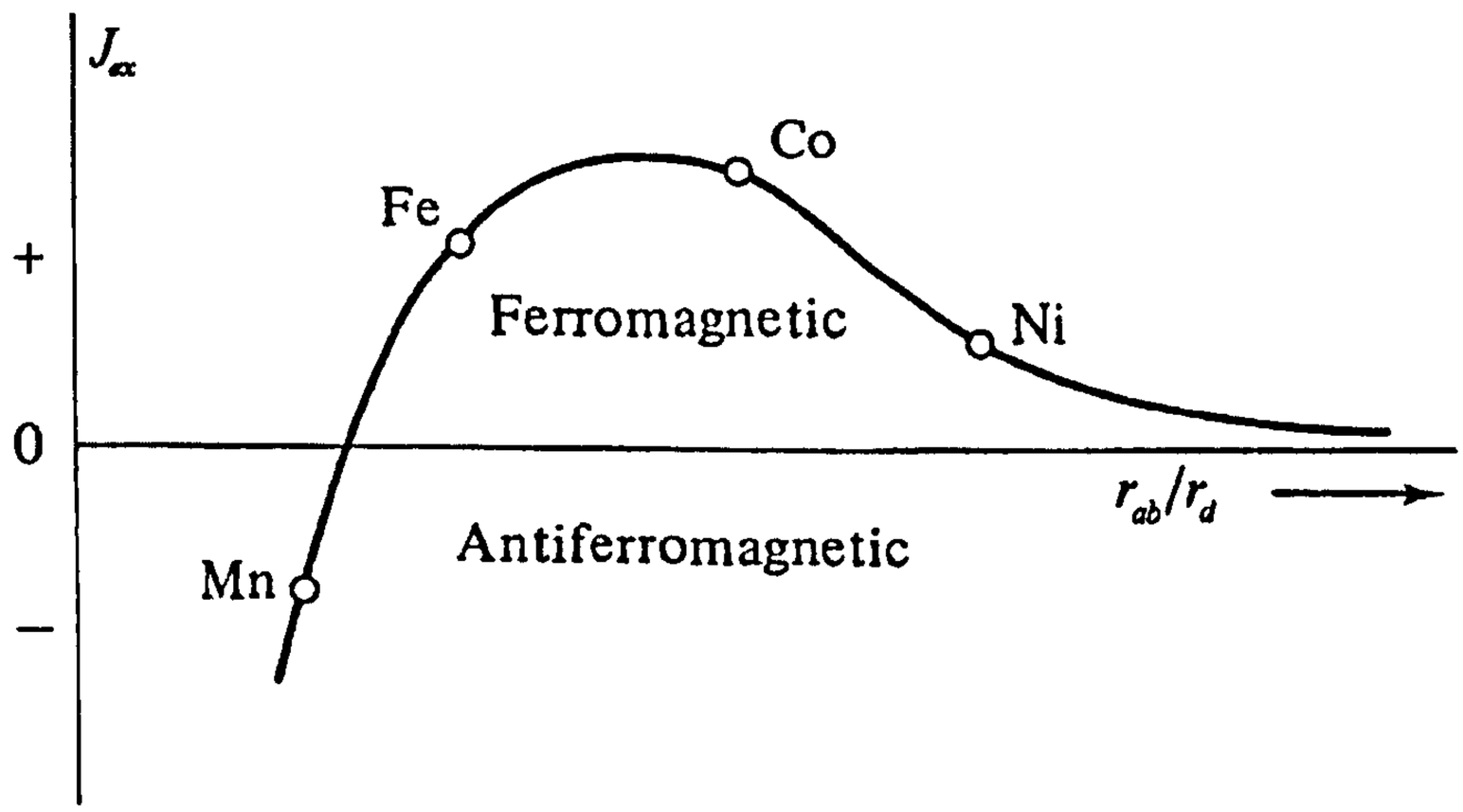

Figure 16. The Bethe-Slater curve (reproduced from Cullity, 1972).

When r_{ab}/r_d is large J_{ex} is small and positive. As the ratio is decreased J_{ex} increases and then goes through a maximum. If the ratio is further reduced J_{ex} continues decreasing and finally becomes negative indicating antiferromagnetic order at small values of r_{ab}.

Even though this approximation provides a useful approach for discussing magnetic interactions of electrons, it has been shown (e.g. Slater, 1936) that some difficulties arise when trying to determine the sign and magnitude of J_{ex}.

2.6.2. Indirect exchange

In the lanthanides metals the 4f magnetic electrons are highly localised and, therefore, it is not easy to imagine how the exchange interaction is propagated. The idea of indirect exchange was firstly introduced by Vonsovski and Zener when studying the 3d elements. They introduced the idea of an indirect exchange between the unpaired magnetic electrons localised in neighbouring atoms via the conduction electrons. This could allow ordering of the electron spins on neighbouring atoms. This type of interaction can lead to different arrangements of the localised magnetic moments: ferromagnetic, antiferromagnetic, sinusoidal and helical. This idea was subsequently studied by Ruderman and Kittel, Kasuya and Yosida when trying to explain the exchange coupling in the rare earth metals. This later theory of indirect exchange receives the name of RKKY interaction and it is the dominant exchange interaction in metals where there is no overlap between neighbouring electrons. The interaction is dominated by a coupling coefficient that can have both positive and negative values depending on the separation between the ions leading to a ferromagnetic or antiferromagnetic peak. This dependence is shown in Figure 17.

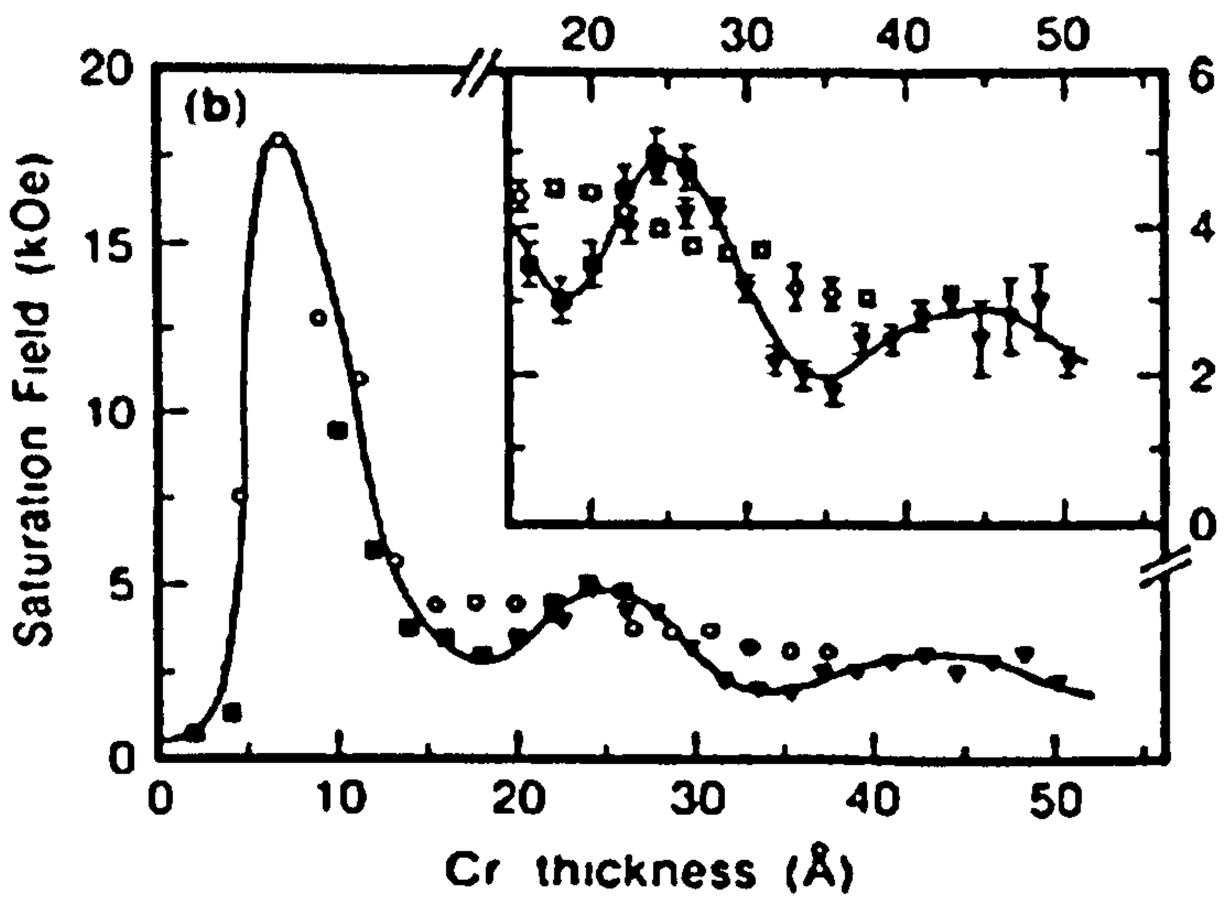

Figure 17. Saturation field at 4.5K versus Cr layer thickness for Si(111)/10nmCr/ [2nmFe/t_{Cr}Cr]N/5nmCr (Parkin *et al.*, 1990).

2.6.3. Intergranular exchange coupling

In thin films, the interactions between different grains are so important that the reversal mechanism of individual grains can be modified (Zhu and Bertram, 1989). Until 1989 the theoretical approaches to CoCr perpendicular film media consisted mainly of two kinds: particulate or continuous. Andra *et al.* (1984) proposed a row-reversal mechanism assuming Stoner-Wohlfarth uniform reversal for the individual grains in the film. However, the long jumps in the hysteresis loops predicted by this model are not observed not even for very small samples (Web and Schultz, 1988). Some other models based on mean field theory calculations fail to predict the correct coercivity (e.g. Wuory and Judy, 1984). In order to describe the possible exchange coupling between nearest neighbouring grains in CoCr perpendicular films Zhu and Bertram (1989) introduced an intergranular exchange coupling in a form analogous to the spin exchange energy

$$E_{exc}(r_i) \propto -\frac{1}{q^2}\underline{M}_i \sum_{\substack{nearest \\ neighbours}} \underline{M}_j, i = 1,2,\ldots,n \qquad \text{Eq. 2.15}$$

where q is the centre-to-centre distance between adjacent grains and $\underline{M}_{i,j}$ is the magnetisation vector of each individual grain.

According to Eq. 2.15 the intergranular exchange coupling is proportional to the magnetisation of the grains. In the case of an *AF* film, the magnetisation of each grain might not be completely zero due to the presence of uncompensated spins at the grain boundaries but it would be very small compared to a *F* where all the spins are aligned in the same direction. Therefore, this coupling will be small if not zero suggesting that it is not a mechanism that can lead to the formation of domain walls within an *AF* film. This implies that a granular process rather than a domain one might be involved in exchange bias. Note that these domains refer to domains perpendicular to the *F*/*AF* interface.

In 2003 R. C. Shull *et al.* observed that domains in the *AF* layer of a $Fe_{76}Mn_6C_{18}$/FeMn bilayer were stationary during magnetisation reversal of the *F* layer. The sample was deposited in the presence of a 4 Oe magnetic field resulting in a non exchange biased hysteresis loop. At H=0, magneto-optic indicator film technique (MOIF) measurements

showed domains in the *F* layer separated by 180° domain walls. When a large field was applied, saturation of the *F* was achieved by the nucleation and growth of domains. When the field was removed, the domain structure was the same as in the original ground state (Shull *et al.*, 2003). The sample was deposited in the presence of a small magnetic field and therefore the *F* would be in a multi-domain state. When the *AF* was deposited on top of the *F*, the spin alignment of the *AF* would differ from one *F* domain to another due to the exchange coupling across the interface. They did not observe a domain structure within the *AF* layer but a print-through of the magnetisation state of the *F*.

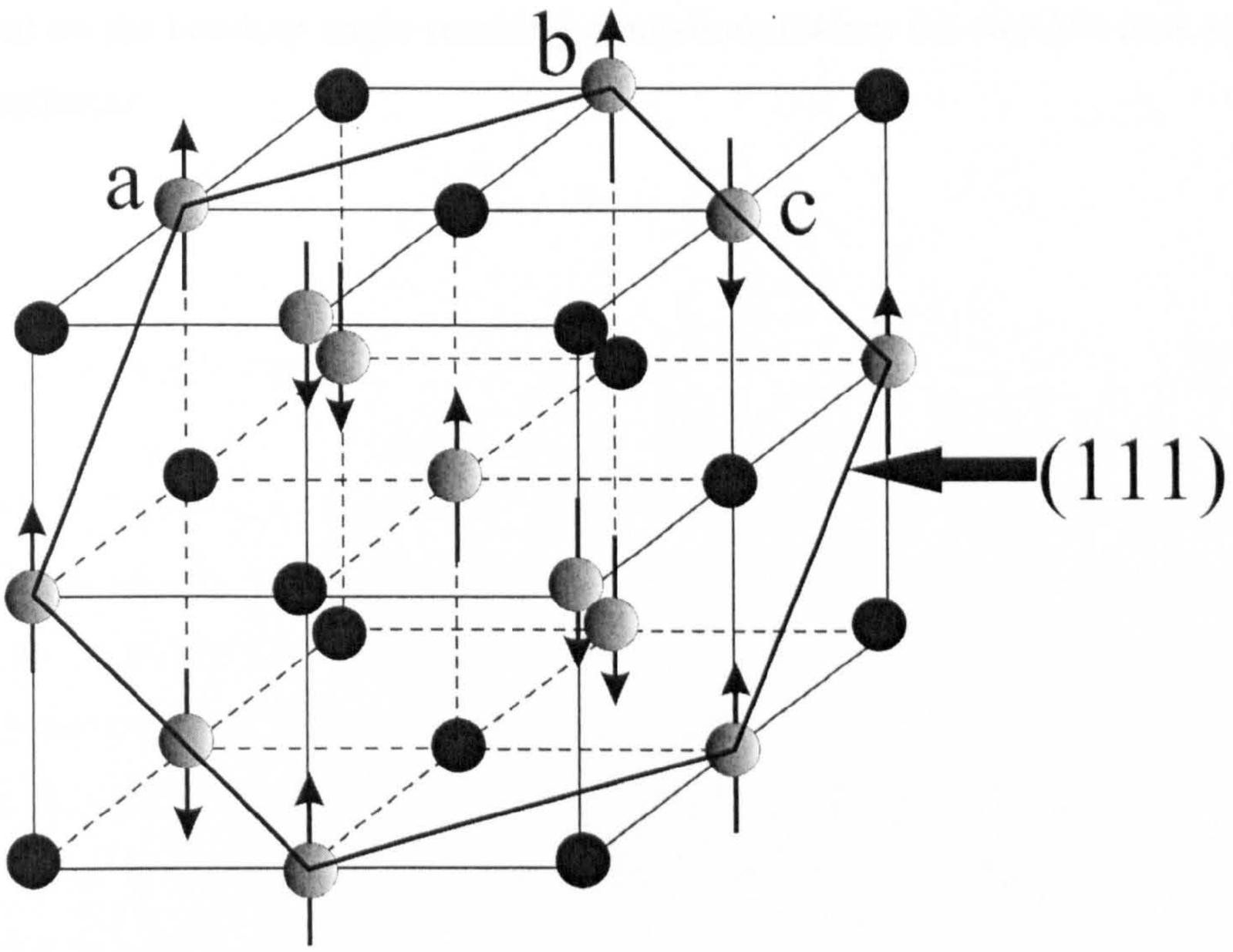

Figure 18. Schematic diagram of the rocksalt structure.

2.6.4. Super exchange

Most natural antiferromagnets, other than metallic alloys, are oxides such as CoO or NiO. Many of these have the rocksalt structure depicted in Figure 18. This is just two interweaved fcc structures. In Figure 18 the moments shown correspond to the M^{++} ions (e.g. Ni, Co, etc...). Some of the nearest neighbours are parallel e.g. a) and b) but others are antiparallel e.g. b) and c). All the spins in any (111) are parallel. So are the spins in each neighbouring plane although they are antiparallel to the original plane. This is classical *AF* behaviour. The planes are too far apart for direct Heisenberg exchange and

therefore some type of indirect coupling must be involved. That indirect coupling is mediated by the oxygen anions.

If two Mn ions are brought up to an oxygen ion from a large distance, the moments of these two ions will not be related. The oxygen ion has no net moment but the outer electrons can be seen as two superimposed orbits, one with spin up and the other one with spin down. When a Mn with an up spin is brought close to the O, the down spin of the oxygen will get closer to the Mn atom as parallel spins repel each other. When a second Mn ion is brought close to the oxygen ion it is forced to have a spin down leading to an antiferromagnetic configuration. The strength of this coupling is strongly dependent on the bonding angle reaching a maximum when the two Mn ions and the O ion are collinear.

Chapter 3 Theory of Exchange Bias

3.1. Introduction

In this chapter a brief introduction to exchange bias (EB) will be given including a summary of some of the most relevant theoretical models that have been proposed since 1956. Interest in exchange bias was merely academic until the Giant Magneto-Resistive (GMR) effect was discovered in 1988 (Baibich *et al.*). All those models rely on different assumptions such as the interface spin configuration, namely whether it is uncompensated or compensated i.e., interfaces having a net surface moment and zero surface moment, respectively.

3.2. Intuitive picture

An exchange bias system consists of a ferromagnetic *F* layer in direct contact with an antiferromagnetic *AF* layer. The main experimental feature of this phenomenon is a shift of the hysteresis loop along the field axis. Exchange bias was discovered 50 years ago by Meiklejohn and Bean (1956) when studying Co fine particles partially surface oxidized. A shift in the hysteresis loop was observed only when the samples were field cooled below the ordering temperature of the oxide layer. They also found that exchange bias was a unidirectional anisotropy as the torque curve was proportional to $\sin\Theta$ and not to $\sin^2\Theta$ as in materials with uniaxial anisotropy such as Co, where Θ was the angle formed between the applied field and the cooling field direction. Even though a lot of research has been carried out since then, a first principle theory which accounts for all the experimental features of exchange bias has not yet been proposed. This might be due in part to the fact that a lot of different systems are subject of study and different mechanisms may apply.

Exchange bias can be qualitatively understood by assuming an exchange interaction at the *AF*/*F* interface. When a field is applied at a temperature above the Néel temperature of the *AF* but below the Curie temperature T_C of the *F* the spins in the *F* align with the

field while the *AF* spins remain randomly oriented (Figure 19a). When the temperature is reduced to $T<T_N$, still in the presence of the field, the *AF* spins next to the *F* align ferromagnetically to those of the *F* as depicted in Figure 19b (assuming ferromagnetic coupling at the interface). Once the field is reversed, the *F* spins in the bulk start to rotate while those in the *AF* do not change. These *AF* spins exert a microscopic torque on the *F* spins trying to keep the *F* spins in their original configuration. Therefore the field needed to reverse the *F* is larger because an extra field is needed to overcome this torque. When the *F* is saturated in negative bias the *AF* stays antiferromagnetically coupled to the *F* (Figure 19c). When the field is set back to its original direction the *F* spins will start rotating for a smaller field as now the *AF* exerts the torque in the same direction as the field.

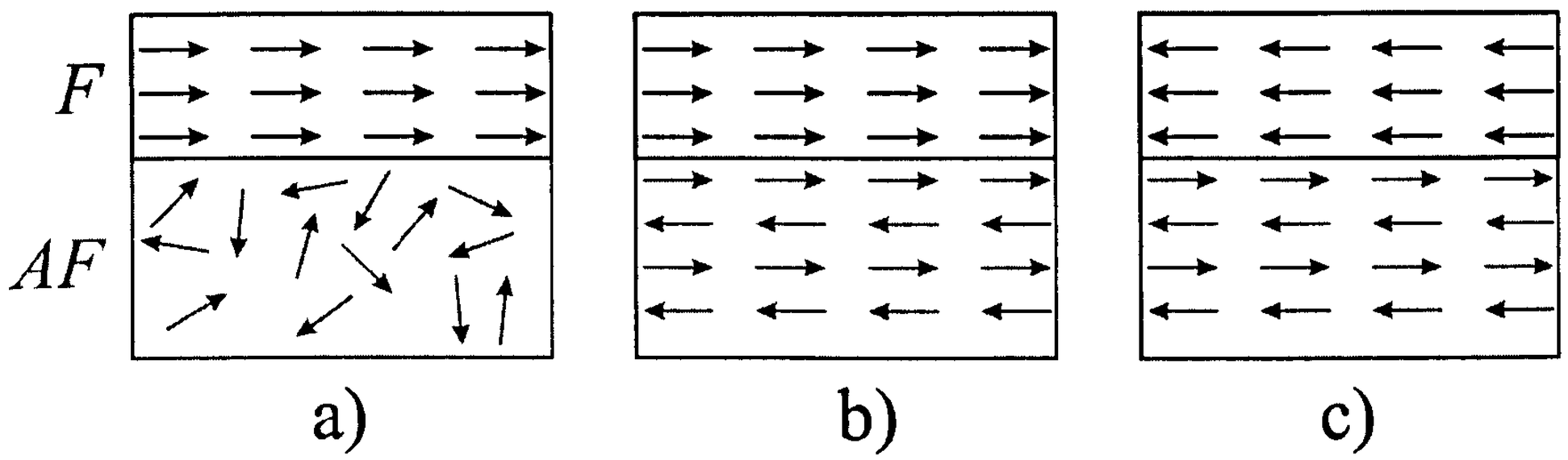

Figure 19. Schematic diagram of the spin configuration of an exchange biased bilayer at different stages: a) when a field is applied above T_N, b) after cooling below T_N still in the presence of the field and c) when the *F* is saturated in negative bias.

3.3. Reversal of exchange biased systems: 7 point model

Goodman *et al.* (2001) proposed a qualitative description of exchange bias based upon the formation of domains within the *AF* whose growth was driven by thermal activation processes. A typical exchange biased hysteresis loop is shown in Figure 20. They proposed seven distinct features that had to be explained by any theoretical model that intends to successfully explain exchange bias.

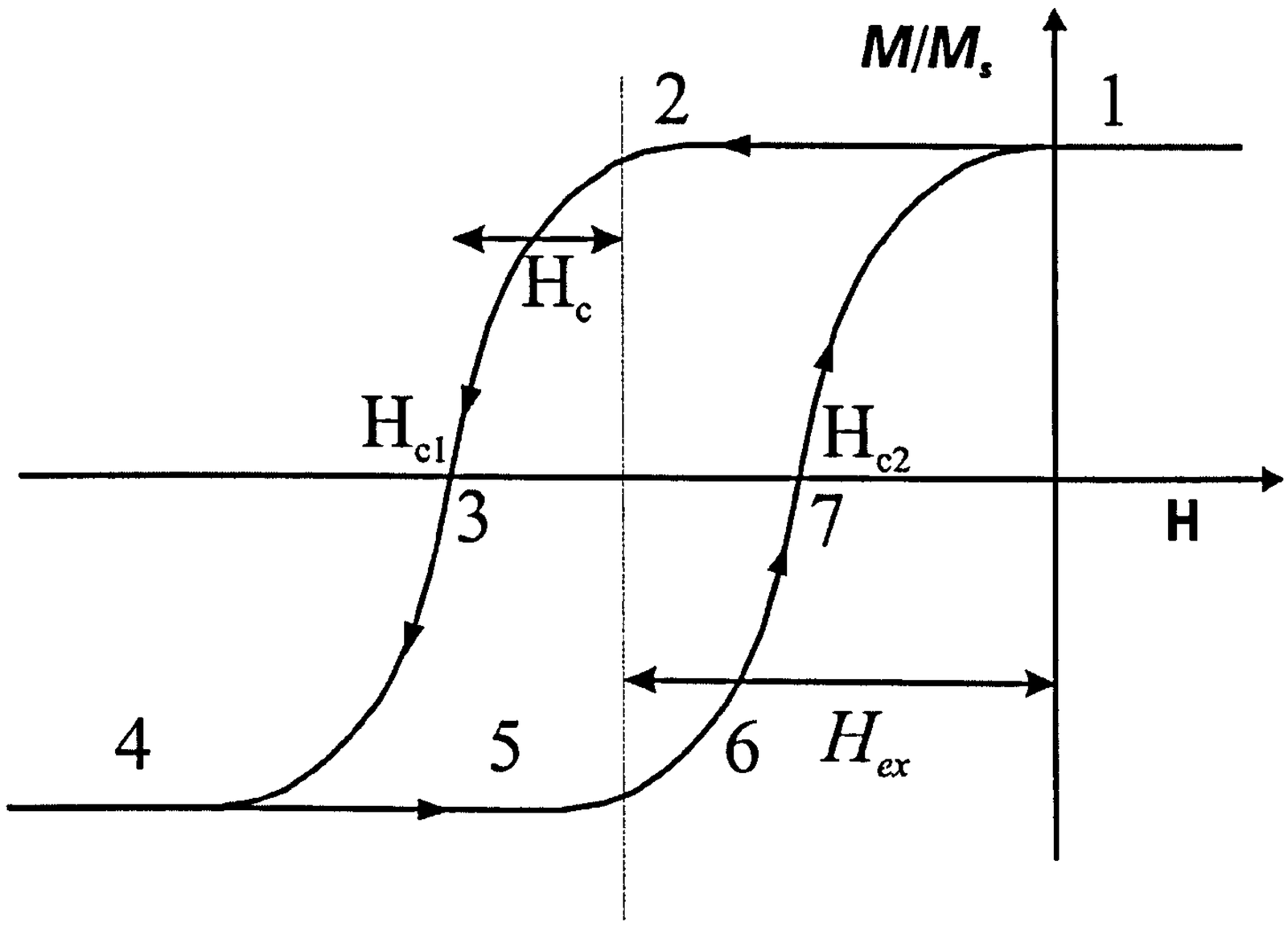

Figure 20. Schematic diagram of the magnetization reversal of an exchange biased system.

1) At point 1 in the hysteresis loop the *F* is fully saturated and contains a single domain.
2) At point 2 the reversal of the pinned layer is initiated. At this stage in the hysteresis curve the nucleation of reverse domains in the ferromagnet is indicated by the degree of saturation at point 1.
3) At point 3 the domains nucleated at point 2 are growing. This growth is promoted by the applied field, the coupling field within the layer and a characteristic thermal activation process. Similar thermal activation processes had been observed for different materials such us NdFeB permanent magnets (Folks *et al.*, 1994) and magnetooptic films with perpendicular anisotropy (Rose *et al.*, 1998). The coercivity at point 3 exhibits normal magnetic viscosity.
4) At point 4 the ferromagnet is now saturated in negative bias and thermal activation processes in the *AF* are driven by the exchange field from the *F* layer. Goodman *et al.* (2001) proposed that at this point there is a growth of domains within the *AF*.
5) At point 5 it would be expected that the *F* layer would reverse. However, that is not the case and to explain this, additional energy barriers have to be introduced in the system. Goodman *et al.* (2001) proposed that those energy barriers arose from the pinning of domain walls in the *AF*. This results in the introduction of

an additional effective anisotropy in the *F* via the exchange interaction between the two layers.

6) At point 6 the reversal of the *F* layer starts. There is a clear difference between the nature of the reversal at points 2 and 6. Goodman *et al.* (2001) proposed some initial domain nucleation between points 5 and 6. These domains could develop either via domain wall movement over pinning sites or domain rotation. The viscosity effects at point 4 suggest that pinning had to be significant.

7) At point 7 anomalous behaviour of the second coercivity H_{c2} was observed. Goodman *et al.* (2001) concluded that H_{c2} was indeterminate and critically dependant on the amount of time spent at negative bias. Similar results had been previously reported by Van der Heijden *et al.* (1998).

3.4. Early models

The first attempts to describe exchange bias had in common the assumption of collinear spin configuration of the *AF* and the *F* at both sides of the interface. However, this is a poor description as the spin configuration at the interface is much more complex due to defects, lattice parameter mismatches, etc... (Kiwi, 2001). In this section the early research by Meiklejohn and Bean and Néel will be presented. The latter implemented the continuum approximation and his results have been taken for granted by other authors.

3.4.1. Rigid model

The first attempt to explain exchange bias was given by Meiklejohn (1962). In this model, where a singe domain *F* was supposed to rotate coherently, the total energy per unit area was written as

$$E = -HM_s t_F \cos(\theta - \beta) + K_F t_F \sin^2 \beta + K_{AF} t_{AF} \sin^2 \alpha - J_{INT} \cos(\beta - \alpha) \qquad \text{Eq. 3.1}$$

where H is the applied field, M_s is the saturation magnetisation of the *F*, t_{AF} is the thickness of the *AF* layer, t_F is the thickness of the *F* layer, K_{AF} is the anisotropy of the *AF* and J_{INT} the interface coupling constant. The angles are defined as follows: β is the

angle between the magnetisation and the F anisotropy axis, α is the angle between the AF sublattice magnetisation (m_{AF}) and the AF anisotropy axis and θ is the angle between the applied field and the F anisotropy axis. The AF and F anisotropy axes are assumed parallel. The interface is supposed to be perfectly uncompensated. The AF was supposed to be in a single domain state. For a schematic diagram of the angles see Figure 21.

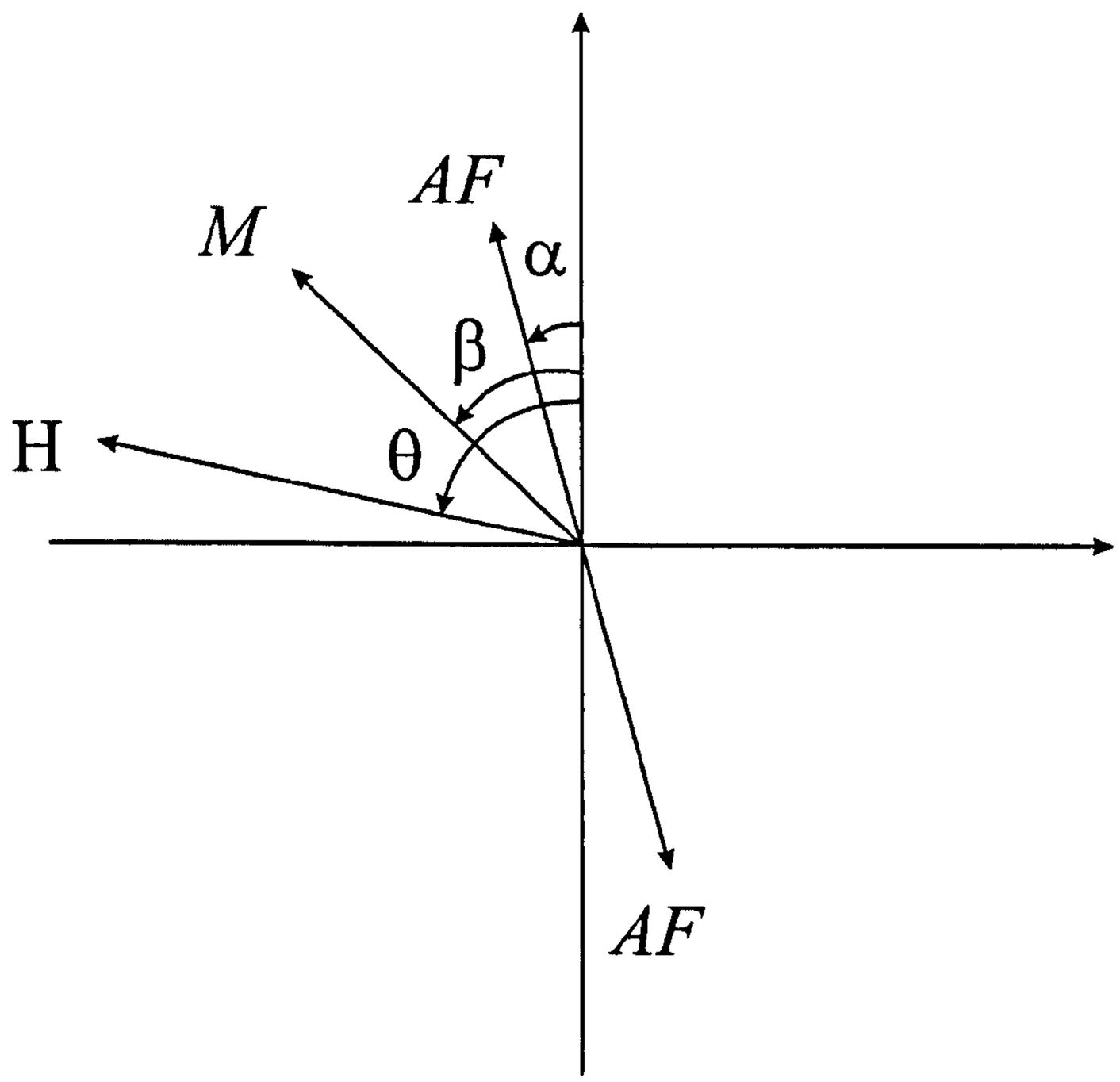

Figure 21. Angles involved in an exchange bias system in the model of Meiklejohn and Bean.

Assuming $K_F \approx 0$, the energy can be rewritten as follows

$$E = -HM_s t_F \cos(\theta - \beta) + K_{AF} t_{AF} \sin^2 \alpha - J_{INT} \cos(\beta - \alpha) \qquad \text{Eq. 3.2}$$

Minimising the energy with respect to α and β the loop shift is given by

$$H_{ex} = \frac{J_{INT}}{M_s t_F} \qquad \text{Eq. 3.3}$$

Another important conclusion from this minimisation is that $K_{AF}t_{AF} \geq J_{INT}$ is required in order to generate an EB. If this is not satisfied, the *AF* rotates with the *F* and no shift is observed, just an increase in H_c.

The values of EB predicted by this model are far too high, typically two orders of magnitude larger than the experimental result (Jungblut *et al.*, 1994). In order to account for these discrepancies, several corrections of the energy equation have been proposed. In the following sections some of those models will be discussed.

3.4.2. Uncompensated interfaces (Néel)

Ten years after exchange bias was discovered Néel (1967) proposed a theory that applied to a weakly uniaxial anisotropic *AF* layer exchange coupled to a *F* layer. Ferromagnetic coupling was assumed at the interface and the magnetisation of both the *F* and the *AF* were assumed to be uniform and parallel to the interface. A discrete Hamiltonian was given for the magnetisation of each *AF* sublattice and by applying the continuum approximation the magnetisation profile was derived. The continuum approximation lead to the formation of domains in both the *F* and the *AF*. Special attention was given to the behaviour of *F*/*AF* bilayers under subsequent field cycling.

The model failed to predict the right magnitude for the exchange field. Moreover, a minimum thickness for the *F* and the *AF* layer are required with this continuum approximation. For example, a *F* layer as thick as 100 nm was required to obtain exchange bias. Therefore this model cannot be used to explain the behaviour of exchange bias systems such as those used in the sensor that reads the information from the stored bits in the hard disk drive in a conventional computer.

3.5. Domain models

The early models of exchange bias described above had been shown to predict values of the exchange field several orders of magnitude larger than the experimental results. Different approximations to Eq. 3.2 had been given since then in order to account for those discrepancies. Many of these new approximations include the formation of

domains in the *AF* [e.g. Mauri *et al.* (1987a), Nowak *et al.*, (2002)]. These models have obtained a better agreement with experimental results although the individual approximations that apply for a specific system are not suitable for other systems. This can be due to rough approximations such as perfectly flat interfaces assumed in some of these models. In the case of polycrystalline sputtered films such as those studied in this work, the interface has associated with it a certain roughness due to the distribution of grain sizes within the sample. This section contains some of the domain models that have made a significant contribution to the understanding of exchange bias.

3.5.1. The model of Mauri

Mauri *et al.* (1987a) suggested that a domain wall (DW) can be present in the *AF* reversing the spins at the interface. The energy per unit area associated with this DW is given by $2\sqrt{A_{AF}K_{AF}}$ where A_{AF} is the *AF* exchange stiffness and K_{AF} the crystalline anisotropy. This way, when the coupling at the interface is strong, Eq. 3.3 can be rewritten as follows:

$$H_{ex}t_F M_s = 2\sqrt{A_{AF}K_{AF}} \qquad \text{Eq. 3.4}$$

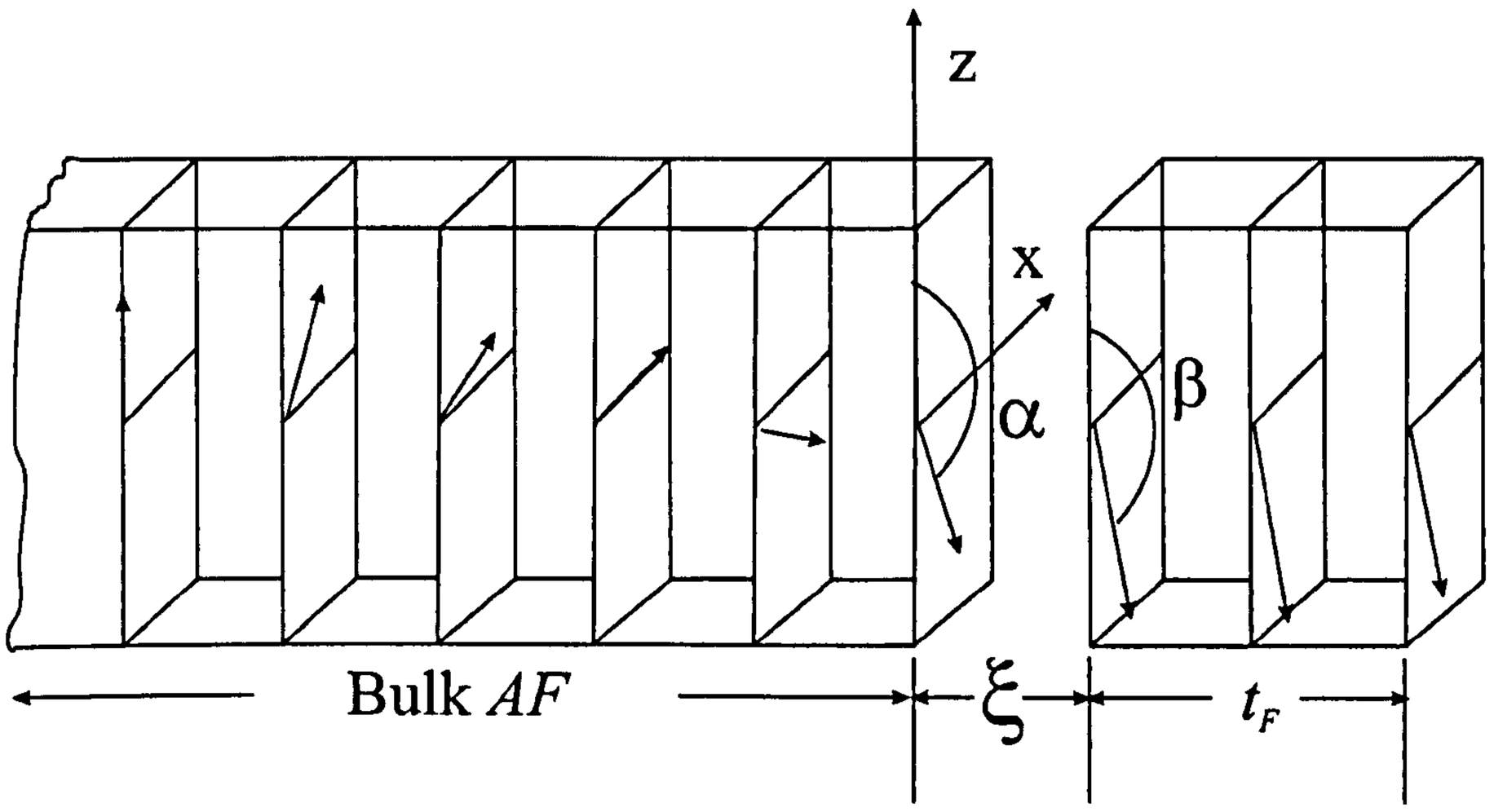

Figure 22. Schematic diagram of a domain wall propagating along the bulk of the *AF* when an external magnetic field is applied along the z direction.

Figure 22 shows a schematic diagram of this model. The thick *AF* layer is supposed to have uniaxial anisotropy along the *z* direction. The *F* and the *AF* layers are supposed to be separated by a distance ξ at the interface. Also, the thickness of the *F* layer t_F is much smaller than the thickness of a DW in the *F*. Therefore, all the *F* spins are aligned along the *z* direction at an angle β. The angle between the interfacial *AF* spins and the *z* direction is defined as α. If $\alpha \neq 0$, a domain wall extends into the *AF*. The total magnetic energy at the interface is written as

$$\delta^* = 2\sqrt{A_{AF}K_{AF}}(1-\cos\alpha)+\frac{A_{F-AF}}{\xi}[1-\cos(\alpha-\beta)]+K_F t_F \cos^2\beta + \\ + HM_s t_F(1-\cos\beta) \qquad \text{Eq. 3.5}$$

The first term is related to the tail of a DW extending into the *AF* according to (Ziljstra, 1979), the second term accounts for the exchange energy where $A_{F\text{-}AF}$ is the exchange stiffness at the interface, the third term is the anisotropy energy of the *F* and the last term refers to the magnetostatic energy. The energy per unit area of a 90° DW in the *AF* is

$$\sigma_{DW} = (1-\cos\alpha)+\psi[1-\cos(\alpha-\beta)]+\varsigma\cos^2\beta+\kappa(1-\cos\beta) \qquad \text{Eq. 3.6}$$

The interface exchange (Mauri *et al.*, 1987a) $\psi = A_{F-AF}/\xi 2\sqrt{A_{AF}K_{AF}}$ can be >0 or <0 depending on whether parallel or antiparallel alignment of the spins is favoured. This is achieved by tuning the value of $A_{F\text{-}AF}$ as it is a fitting parameter. The anisotropy $\varsigma = K_F t_F / 2\sqrt{A_{AF}K_{AF}}$ can also be either >0 or <0 depending on the direction of the easy axis of the *F*. Finally $\kappa = HM_s t_F / 2\sqrt{A_{AF}K_{AF}}$ is the Zeeman energy of the *F* in a field H normalised to the wall energy. Hysteresis loops were calculated from Eq. 3.6 by finding the angles α_0 and β_0 for which σ_{DW} reaches a minimum. Although this model reproduces several features of exchange bias, it does not account for the widening of the coercivity of the *F* layer typical of exchange biased systems.

The first experimental evidence of these spiral structures propagating along the bulk of the *AF* was given by (Yang *et al.*, 2000). Samples with composition

NiFe(20nm)/FeMn(tAF)/Co(10nm) were grown using sputtering. The thickness of the *AF* layer was varied between 5.3nm and 30nm. In the as-deposited state the NiFe layer showed a narrow loop while the Co layer showed a wide loop. Therefore there existed a plateau region where the magnetisation of both layers were opposite. The samples were field cooled at the plateau field. They determined the turn angle of the magnetisation axes of the Co and NiFe layers by measuring a series of hysteresis loops at various angles with respect to the field cooling direction. It was concluded that for t_{AF}<9nm the turn angle varied linearly with t_{AF} as (17.6°/nm)t_{AF}. For t_{AF}>9nm the magnetisation axes of the NiFe and the Co layer were always antiparallel. It is important to note that in the case of a 6nm thick *AF* layer (≈15 atomic layers) the turn angle would be ≈106°. In this and later studies, the results were attributed to the field cooling procedure and not to an intrinsic property of the systems studied.

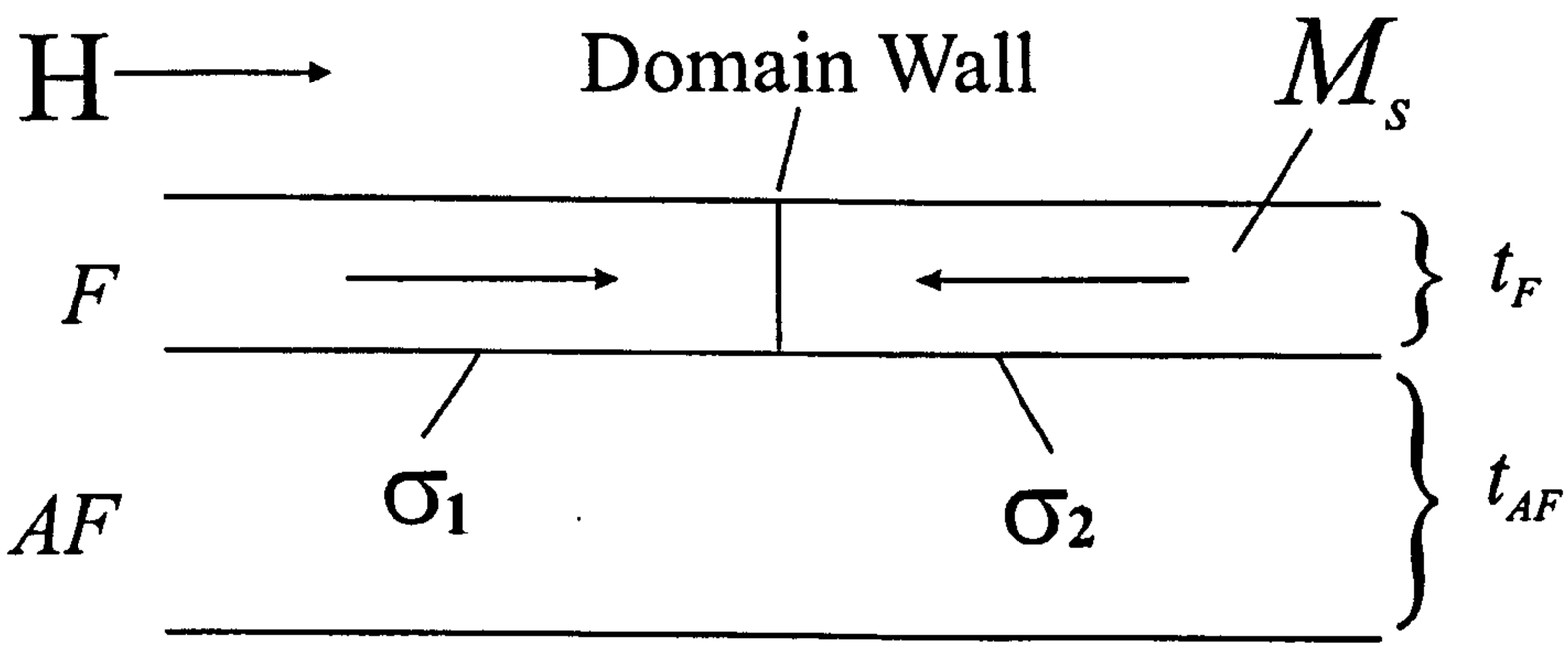

Figure 23. Side view of a *F* layer exchange coupled to an *AF* layer.

3.5.2. Antiferromagnetic domains due to interface roughness

Malozemoff (1987) proposed a model where exchange bias was due to the presence of interface roughness that gave rise to a random field acting on the interface spins. This random field lead to the formation of the so-called "Imry-Ma domains" (Imry and Ma, 1975). The model, sketched in Figure 23, supposed a uniaxial single crystal *F* in contact with an *AF* where a domain wall within the *F* was driven by an applied in-plane field *H*. Supposing that the interfacial energy differed for the two domains the exchange field H_{ex} was determined from the balance of the applied field pressure $2HM_st_F$ and the effective pressure from the interfacial energy difference $\Delta\sigma$:

$$H_{ex} = \frac{\Delta\sigma}{2M_s t_F} \qquad \text{Eq. 3.7}$$

An initial breaking of time-reversal symmetry was required to obtain exchange anisotropy. This was obtained by cooling the *AF* through its Néel temperature while the *F* remained in a single domain state due to the applied field. Furthermore, once the domain wall was formed the *AF* structure, at least away from the interface, remained unchanged. Non-colinearity or an anisotropy that holds the *AF* moments in plane was also required to observe a loop displacement.

With all these assumptions and given a region with a single domain *F*, it was energetically favourable for the *AF* to break up into domains (Imry and Ma, 1975). The size of these domains is given by

$$L \approx \pi\sqrt{\frac{A_{AF}}{K_{AF}}} \qquad \text{Eq. 3.8}$$

where A_{AF} is the *AF* exchange stiffness and K_{AF} the *AF* uniaxial anisotropy constant. The final expression for the exchange field is given by

$$H_{ex} = \frac{2z\sqrt{AK}}{\pi^2 M_s t_F} \qquad \text{Eq. 3.9}$$

In Eq. 3.9 the *z* parameter is of the order of 1 (Imry and Ma, 1975). It is introduced as a consequence of interface irregularities whose average local magnitude is $2zJ_{INT}$ where J_{INT} is the interface exchange constant supposed to be the same at both sides of the interface. Eq. 3.9 is similar to that proposed by Mauri *et al.* (1987a) although the latter suggested a perfectly flat uncompensated interface. The reduction of the coercivity upon field cycling was attributed to slight movement of the *AF* domain walls in the same way as proposed by Néel (1967).

The Malozemoff model (1987) proposed the formation of domains perpendicular to the interface. In polycrystalline *AF*s such domains can only form if there is strong

intergranular exchange coupling. There are no reports in the literature of such coupling and possible mechanisms e.g. RKKY coupling, require highly textured systems. Hence, it is very unlikely that this model could apply to sputtered polycrystalline systems. Malozemoff extended his model to cubic *AF*s (1988a). The temperature dependence of the domain size was determined suggesting that the domain size in cubic systems increased with temperature T. Also, the variation of the loop displacement with T was calculated suggesting different behaviour for uniaxial and cubic *AF*s. He also predicted the existence of a critical thickness t_{crit} below which the exchange bias vanished (Malozemoff, 1988b). Above t_{crit}, H_{ex} decreased with increasing t_{AF} until a second critical thickness at which the exchange field saturated. This behaviour is not followed by the samples studied in this work where there is a sharp increase of the exchange field with the *AF* thickness up to a critical thickness above which the exchange field remains almost constant. These results will be discussed in Chapter 6.

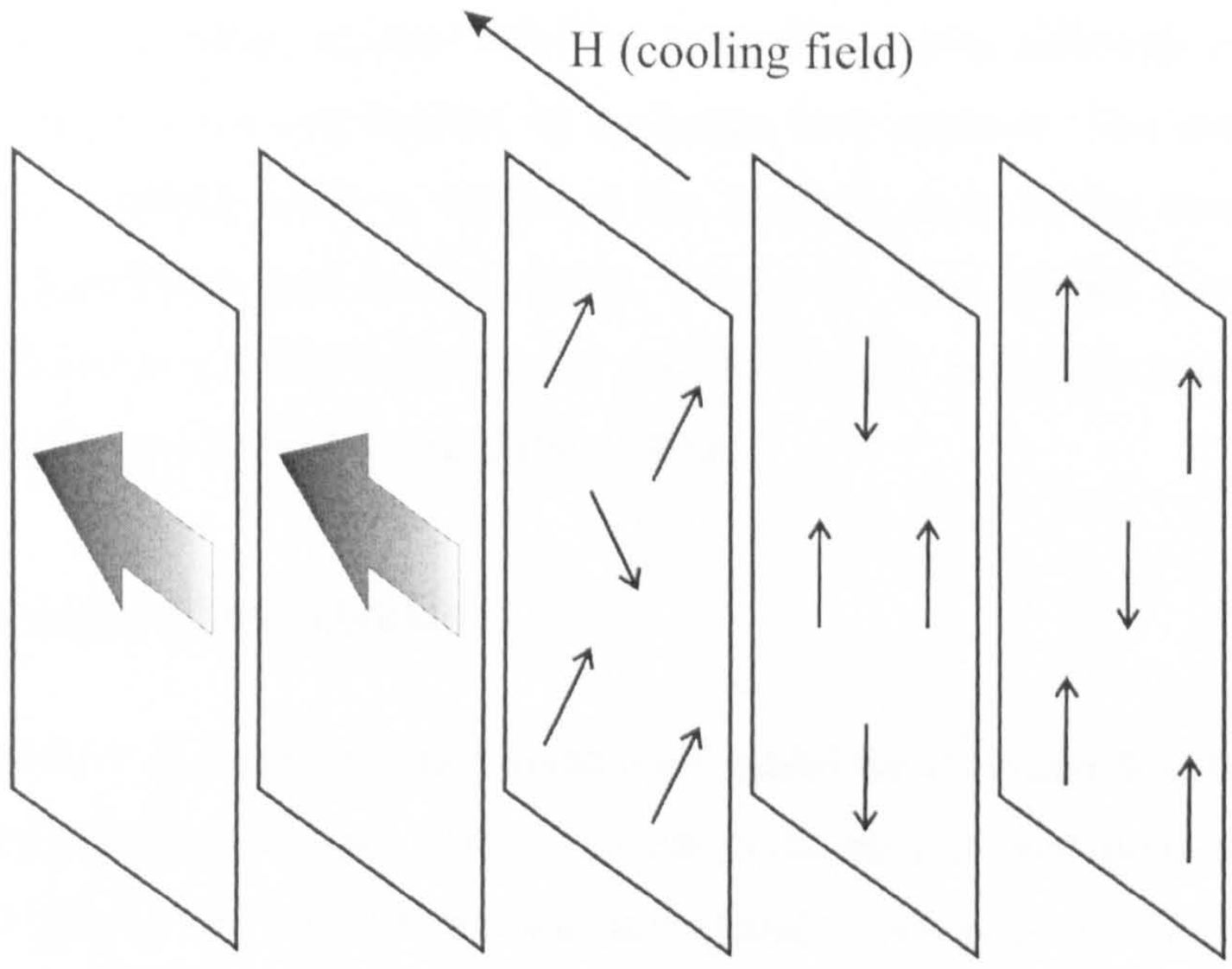

Figure 24. Perpendicular *F*/*AF* coupling with spin canting in the first *AF* layer (reproduced from Kiwi, 2001).

3.5.3. Perpendicular coupling at the interface

40 years after exchange bias was discovered, Koon proposed a microscopic explanation of exchange bias for compensated *F*/*AF* interfaces (Koon, 1997). This work was motivated by the experimental results of Jungblut *et al.* (1994) and Nogues *et al.* (1996)

among others. They found that the *F* magnetisation tended to orient perpendicular to the *AF* easy axis and that compensated/uncompensated interfaces lead to similar values of H_{ex}. These results could not be explained by the theories of Mauri (1987a) and Malozemoff (1987). The main result of the model proposed by Koon was the prediction of a ground state configuration where the bulk *F* moments oriented perpendicular relative to the *AF* easy axes as depicted in Figure 24. This configuration is known as spin-flop coupling. Exchange bias was due to the formation of a domain wall in the *AF* parallel to the interface when the *F* rotates away from the field cooling direction as the applied field is reversed. Furthermore, Koon (1997) also showed that the spins in the *AF* exhibit canting. This canting angle decays rapidly as a function of distance from the interface, becoming zero at 5-6 monolayers.

Schultness and Butler (1998) solved the Landau-Lifshitz-Gilbert equation in order to study the exchange coupling at *F*/*AF* interfaces. They showed that for perfectly flat interfaces spin-flop coupling does not lead to exchange bias although it leads to an increase in the *F* coercivity typical of exchange bias systems. The introduction of defects at the interface leads to values of the exchange field of the correct order of magnitude (Schulthess and Butler, 1998). However, their model only applies to idealised situations in which both the *AF* and the *F* films are single crystals and in a single domain state (Schulthess and Butler, 1999).

3.5.4. Domain state model

In 2002 Nowak *et al.* proposed the domain state model for exchange bias based on their previous work (Miltényi *et al.*, 2000). For their calculations they supposed a *F* layer coupled to a diluted *AF*. The dilution was introduced in the system in the form of non-magnetic atoms. In this model EB arises due to a domain state in the *AF* which develops during field cooling carrying an irreversible magnetisation. During the field cooling process, the *AF* is in contact with a saturated *F* and exposed to a magnetic field *H*. The dilutions introduced in the system favour the formation of this state since domain walls preferentially pass through the non-magnetic sites and, therefore, reduce the energy necessary to create a domain wall (Nowak *et al.*, 2002). The domain state is a metastable state which develops and becomes frozen during cooling. This way no further assumptions about the size or structure of these domains are required. Note that

in the original model $K_{AF} = \infty$ and hence the width of these domain walls is assumed to be zero. More recently lower values of K_{AF} of ~10^7erg/cc have been used but these are up to an order of magnitude greater than experimental values. Several features of exchange bias have been successfully reproduced by this model. For example, strong dependence of the exchange field on dilution, positive exchange bias, temperature dependence of the exchange field, time dependence and t_{AF} dependence of the exchange field etc.... Montecarlo simulations were performed on a model consisting of a *F* monolayer exchange coupled to a diluted *AF*, usually consisting of 9 monolayers. Figure 25 shows a sketch of the model.

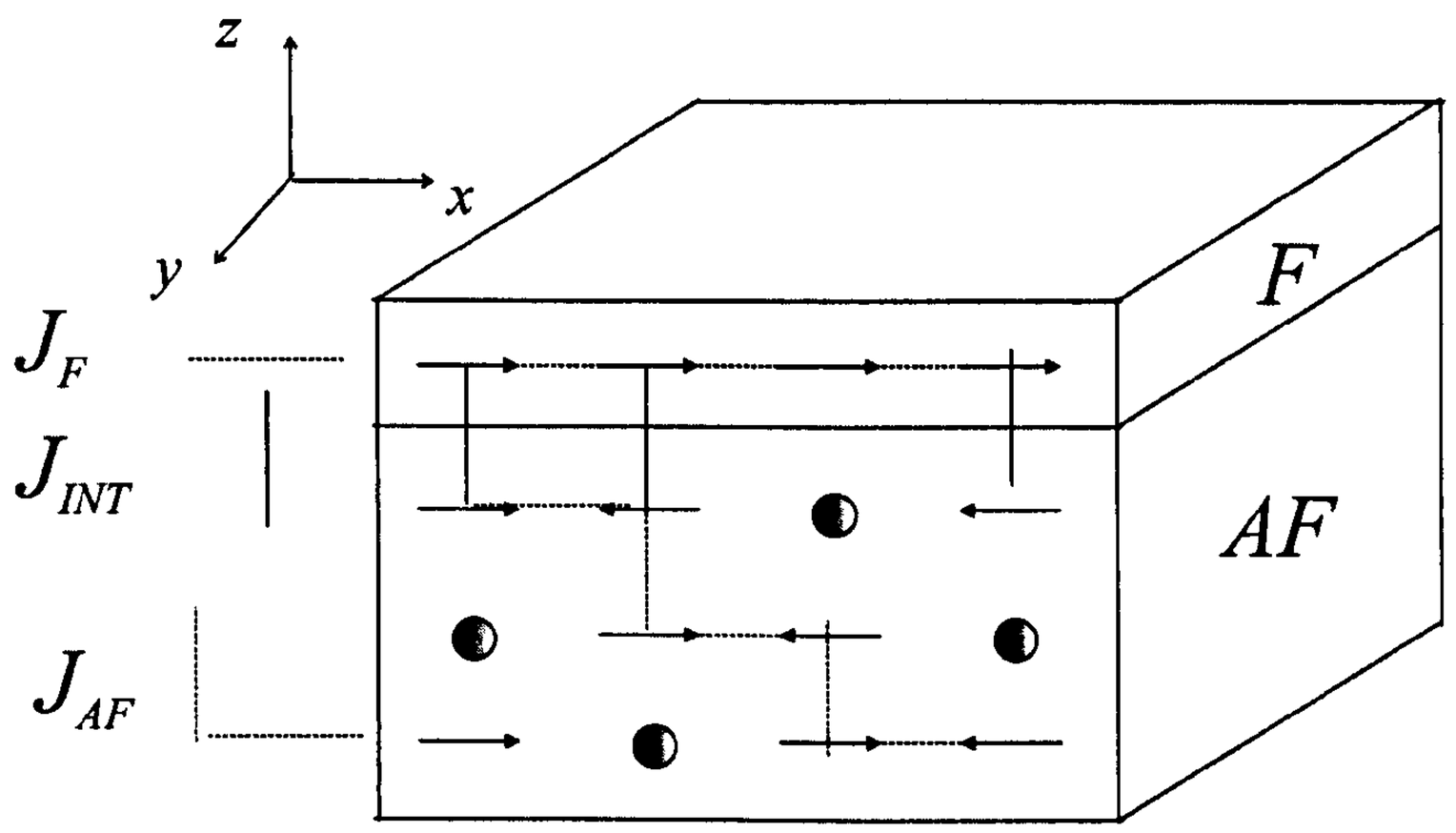

Figure 25. Schematic diagram of the domain state model where the dots refer to defects (reproduced from Nowak *et al.*, 2002).

The behaviour of the *F* was described by a classical Heisenberg model with nearest-neighbour exchange constant J_F while the *AF* was modelled as a magnetically dilute Ising system with an easy axis parallel to that of the *F*. At the interface it was assumed that the Ising spins of the top *AF* layer interact with the *z* component of the *F* Heisenberg spins. J_{AF} was set to J_{AF}=-J_F/2 and for simplicity it was assumed that J_{INT} = $\pm J_{AF}$. Finally the dilution at the interface monolayer of the *AF* was set to 50%, changing only the dilution in the volume of the *AF*.

In order to 'test' the domain state model the same authors studied experimentally the dependence of the exchange field on dilution for both Co/CoO/MgO and Co/CoO epitaxially grown bilayers (Keller *et al.*, 2002). They predicted the correct *AF* thickness dependence, a training effect and the temperature dependence of the bias field amongst

other properties. This model has also been successful in explaining results from other authors such as the size dependence of H_{ex} in NiO/Ni nanostructures (Fraune *et al.*, 2000). However, this model does not seem suitable to explain the results presented in this work due to the high anisotropy (typically 10^7ergs/cc) required for the formation of these domains.

3.5.5. Partial domain walls in the antiferromagnet

Stamps (2000) suggested the existence of two different types of exchange bias, one due to the reversible formation of domain walls and one due to irreversible processes leading to asymmetric hysteresis loops. Shifted asymmetric loops could occur without complete loss of partial wall reversible bias if the interfaces are mixed. The concept of a 'natural angle' was introduced to characterise exchange bias at mixed and geometrically rough interfaces. An equation for the interface energy was proposed suggesting the existence of high order coupling terms when more than one *AF* sublattice is present at the interface. Mean field theory was used to study the temperature behaviour of the exchange and coercive fields. Both fields decreased with increasing temperature. A thermal activation theory over energy barriers was used to describe the rate at which equilibrium was approached. These energy barriers are considered to be of two types, those involved with in-plane rotation of the *F* and those related to out-of-plane rotation. Exchange bias could arise without the need of anisotropy in the *F* layer in contrast to rigid models (Stamps, 2000).

3.6. Granular models

Néel (1949) showed that the relaxation time of a system of ferromagnetic particles with their easy axis parallel to the direction of the applied field follows the Arrhenius-Néel law characterised by an energy barrier to reversal ΔE. In a system where there is a distribution of particles sizes this would lead to a distribution of energy barriers. In the case of sputtered polycrystalline exchange biased samples, like those studied in this work, it would be expected that magnetisation switching would follow a similar law. Fulcomer and Charap (1972a) firstly applied this idea to exchange bias systems.

3.6.1. Thermal fluctuation after-effect model

The first model to describe the temperature and frequency dependence of the exchange field H_{ex} and the coercivity H_c in exchange biased films was proposed by Fulcomer and Charap (1972a). The aim of the model was to reproduce the experimental features observed in a NiFe film 100nm thick (Fulcomer and Charap, 1972b). The sample was oxidised at different temperatures for different periods of time leading to the formation of a discontinuous *AF* layer of NiO islands lying on top of the NiFe layer. Between each oxidation process the sample was treated in a dry hydrogen atmosphere for 3 hours at 250 °C to reduce surface oxides ensuring that the specimen was returning to the same initial state. Another NiFe sample with no oxide layer on top was grown to determine whether the results were characteristic of the *F* film. Finally, another sample was exposed to a heavy oxidising process so the effects of the oxide layer could be emphasized. The samples were measured using the magneto-optic Kerr effect in the range 5-300K at three different frequencies, 100, 20 and 0.05 Hz.

In this model that was compared to the experiments, the *AF* was described as an assembly of *AF* particles which lie on top of an *F* film. No interaction between *AF* particles was assumed but an *AF*/*F* coupling term was introduced. Uniaxial magnetocrystalline anisotropy was assumed for both the *AF* particles and the *F* with aligned easy axis. Each *AF* particle was susceptible to thermal fluctuations in the orientation of its 'moments' above its 'blocking' temperature. These thermal fluctuation effects were based on the theory proposed by Néel and Brown in the mid 50s. In the case of a particle with uniaxial anisotropy with the field applied along the easy axis, an asymptotic expression for the relaxation time of the particle was found (Brown, 1959). The temperature at which the loop displacement vanished was the same as the blocking temperature for the largest of the *AF* particles and it was dependent upon the thickness of the oxide layer.

One important characteristic of this model is that a wide range of particle sizes and shapes was considered within the *AF*. This way the anisotropy and coupling energies were varied widely. The particle size distribution was assumed to be such that all areas are equally probable up to some maximum and that there were no larger particles. They

found that it was important to consider a distribution of particle size although the exact form of that distribution was not critical.

They observed that the sample with no oxide layer on top showed no loop displacement of the easy axis loop. No magnetic aftereffects such as training were observed either, leading to the conclusion that the particular results obtained for the oxidized samples were not a characteristic of the NiFe but rather an interaction with the oxide layer. In the case of the oxidised samples they observed exchange anisotropy effects. Shifted hysteresis loops appeared below a transition temperature ranging from 30 to 90K as the film became more oxidised. The exchange field was observed to increase with decreasing temperature and vanished at a temperature dependent on the amount of oxidation. H_c was found to increase at high frequencies and showed a peak close to the temperature at which the loop displacement vanished.

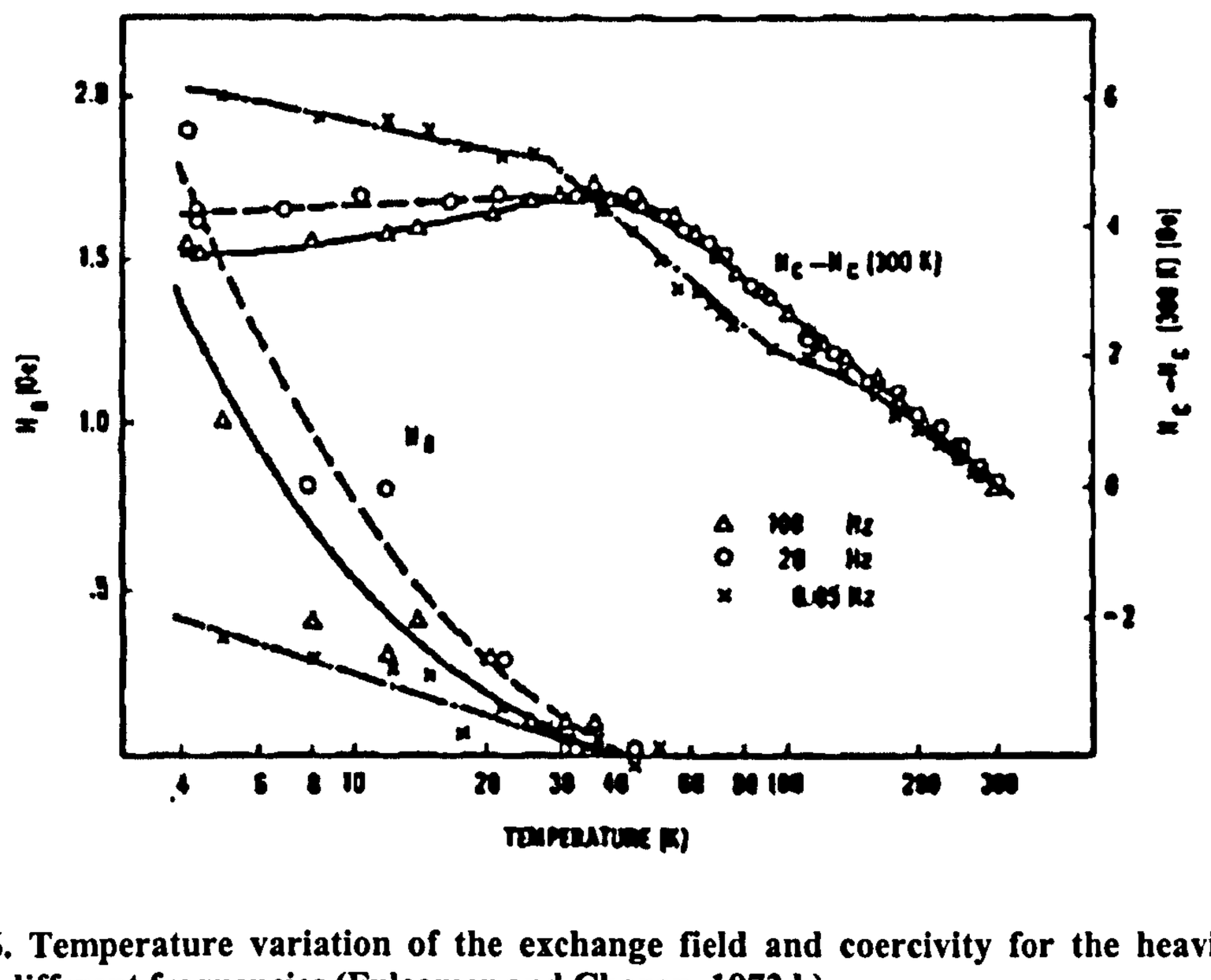

Figure 26. Temperature variation of the exchange field and coercivity for the heavily oxidized sample at different frequencies (Fulcomer and Charap, 1972 b)

Figure 26 shows the variation of H_{ex} and H_c with temperature and frequency measured for the heavily oxidized sample. While the loop displacement was found to increase with increasing frequency an unusual behaviour of decreasing with increasing frequency was reported for the coercivity. This is in contrast to normal *F* behaviour where H_c

increases with the frequency (e.g. De Witte *et al.*, 1993). All these results were explained in terms of their thermal fluctuation model (Fulcomer and Charap, 1972a).

This model has been the base of other granular models based on thermal fluctuation effects. Nishioka *et al.* (1996) investigated the exchange coupling in NiFe/FeMn bilayers taking into account a distribution of grain sizes within the *AF* layer. They analysed the data using the temperature dependence of the coupling proposed by Fulcomer and Charap. The shift in the hysteresis loop was calculated from the probabilities of the *AF* grains being aligned parallel or antiparallel to the applied field. A similar model was used to investigate the temperature dependence of the coupling in Co/CrMnPt (Nishioka *et al.*, 1998). The same author (Nishioka, 1999) also studied the thermal decay of such a system. The same thermal fluctuation model gave the correct activation energy distributions for reversal of the *AF* grains below 130°C. The model assumed coherent rotation although incoherent rotation was suggested for *AF* grains above 150°C to explain the narrow distribution obtained from the model.

3.6.2. Stiles and McMichael

Stiles and McMichael (1999a) proposed a model to describe the behaviour of polycrystalline *F-AF* bilayers. No intergranular coupling between *AF* grains was assumed but *AF* grains were coupled to a *F* layer both by direct coupling to the net moments at the interfaces of the grains and by spin-flop coupling. The coupling is frustrated due to disorder at the interface. Both the shift in the hysteresis loop and hysteresis effects typical of experiments done in high magnetic fields such as high field rotational torque and ferromagnetic resonance (FMR) were explained.

The *F* was assumed to be in a uniform saturated state. The *AF* grains were assumed to be in a single state except for any partial domain walls parallel to the interface created due to the coupling to the *F*. Uniaxial anisotropy was assumed for the *AF* grains each with randomly distributed easy axis. In order to account for high field rotational hysteresis and the loop shift some of the *AF* grains were assumed to make irreversible transitions. These transitions were included in the model in the form of a critical angle α_{crit}. When the partial domain wall within an *AF* grain is wound up to an angle greater than α_{crit} the *AF* becomes unstable and undergoes a transition to another state. As the *F*

is rotated the partial domain wall is wound up to the critical angle and a transition takes place.

The temperature dependence of exchange bias was assumed to arise from thermal instabilities in the state of the *AF* grains (Stiles and McMichael, 1999b). At low temperatures, the *AF* grains are in a stable configuration as the ferromagnet magnetisation is rotated. At high temperatures the *AF* grains remain stable on short time scales becoming unstable on long time scales due to thermal excitations over energy barriers. The spin flop coupling term was not included in the calculations.

A system in which the Curie temperature of the *F* is much greater than the Néel temperature of the *AF* was considered. Hence, the properties of the *F* were assumed to be temperature independent. They also assumed that the interface coupling was temperature independent. Two contributions to the temperature dependence were included. The first source of temperature dependence was included in the domain wall energy in the *AF*, σ_{DW}, assumed to be

$$\sigma_{DW} = \sigma_0 \left[1 - \frac{T}{T_N} \right]^{5/6} \qquad \text{Eq. 3.10}$$

where σ_0 is the domain wall energy at 0K. This formula was based on the fact that $\sigma_{DW} \propto \sqrt{A_{AF} K_{AF}}$ and the approximations $m_{AF} \propto (T - T_N)^{1/3}$, $K_{AF} \propto m_{AF}^3$ for uniaxial anisotropy and $A_{AF} \propto m_{AF}^2$ as indicated approximately by analogy to spin-wave dispersion in some ferromagnets (Stiles and McMichael, 1999b) giving an exponent of 5/6. The second source of temperature dependence was analogous to superparamagnetism (Bean and Livingston, 1959) in small ferromagnetic particles. At certain temperatures the *AF* state in the grains could be switched due to thermal fluctuations. For big grains the mechanisms to switch the *AF* state were assumed to be domain wall nucleation and motion while for grains smaller than a certain size a coherent rotation model could be used (Fulcomer and Charap, 1972a). The reversal of the *AF* state occurred over an energy barrier ΔE given by the reversed state plus a domain wall far from the interface. At a temperature *T*, the probability of remaining in an initial state for a period of time t is given by

$$P(t) = exp\left[-f_0 t\, exp\left(-\frac{\Delta E}{k_B T}\right)\right] \qquad \text{Eq. 3.11}$$

where f_0 is the attempt frequency to reversal and k_B is Boltzmann's constant. Stiles and McMichael observed that this probability is close to one for a range of angles and then makes a rapid transition to close to zero for other angles (Stiles and McMichael, 1999b). These rapid transitions suggested the probability can be chosen to be either 0 or 1 with the borders between the two regimes for a transition time of 0.5s given by

$$\Delta E / k_B T \approx 20 \qquad \text{Eq. 3.12}$$

Hence, if $\Delta E > 20 k_B T$ the grain is considered to be stable and if $\Delta E < 20 k_B T$ it is unstable. The grains were classified as stable, partially stable or unstable as a function of temperature and applied field direction. The behaviour of each grain determines its contribution to the unidirectional anisotropy. This thermally activated switching causes there to be a blocking temperature T_B well below the Néel temperature of the *AF*.

The saturation of the unidirectional anisotropy at low temperatures is determined by the ratio of the average interfacial coupling energy to the zero temperature domain wall energy. The unidirectional anisotropy is determined by the domain wall energy if it is the smaller of the two. However, if the interfacial coupling is the smaller of the two it determines the unidirectional anisotropy which saturates at low temperatures due to the assumed temperature independence of the interface coupling.

The same authors explained the behaviour of the coercivity in exchange bias bilayers (Stiles and McMichael, 2001). Two contributions to the enhanced coercivity were found: one was due to inhomogeneous reversal and the other to irreversible transitions in the *AF* grains. At low temperatures H_c is dominated by inhomogeneities which arise from the random orientation of the easy axis of the *AF* grains. As the field is reduced from a large value the *F* relaxes from its saturated state and parts of the magnetisation are twisted one way and parts the other. When the *F* finally reverses much larger areas will rotate in the same direction and there will be a large number of local energy barriers. As these barriers are overcome the hysteresis loop becomes rounded. This

reversal mechanism is dependent on the ratio of the coupling between the *F* and the *AF* grains to the intergranular exchange coupling in the *F* (Stiles and McMichael, 2001). As a consequence the coercivity is predicted to vary as $H_c \propto t_F^{-2}$. At high temperatures H_c is dominated by irreversible transitions in the *AF* grains. As the magnetisation of the *F* is rotated the *AF* grain can become unstable and switch. As a consequence the coercivity is found to decrease as t_F^{-1}. The model accounted for the peak in the coercivity near T_B and was associated with instabilities in the *AF* grains. The position of this peak has been observed to be dependent on the thickness of *AF* layer (Fernandez-Outon *et al.*, 2004).

3.7. Technological applications of exchange bias

Exchange bias is present in all personal computers in the read-head sensor that reads the information stored in a magnetic hard disk drive (Berkowitz and Kodama, 2005). The sensor consists of a soft *F* layer '*free layer*' separated by a non-magnetic metallic spacer from an exchange bias bilayer '*hard layer*'. This type of structure receives the name of spin-valve. The sensor is mounted on a lever arm suspended 10-20nm above a lubricant layer ~1nm thick that covers the recording layer and shielded from exposure to the flux from bits other than the one being read. The sensing mechanism is the Giant Magnetoresistance (GMR) effect discovered in 1988 (Baibich *et al.*, 1988). A change in the direction of magnetisation of the free layer is produced by the flux from a bit leading to a change in the resistance of the spin-valve. This resistance change is the read signal. A cross-section TEM picture of a real read-head sensor is shown in Figure 27.

Another important application of exchange bias is spin polarised magnetic tunnel junctions (Berkowitz and Kodama, 2005). The basic structure is similar to that of a spin-valve but in the case of the tunnel junction the spacer is an insulator. Electron transport can be achieved when a bias voltage is applied to the *F* layers. The conductance depends upon the relative orientation of the *F* electrodes (Moodera and Mathon, 1999). Since a large tunnel magnetoresistance TMR was demonstrated (Moodera *et al.*, 1995) there has been a special effort to develop magnetic-tunnel-junction based non-volatile magnetic random access memory (MRAM) to replace the conventional semiconductor-based memories. Tunnel magnetoresistance ratios well

above 100% at room temperature (e.g. 410% Yuasa *et al.*, 2006) are necessary for the commercial application of MRAM which has not yet been achieved.

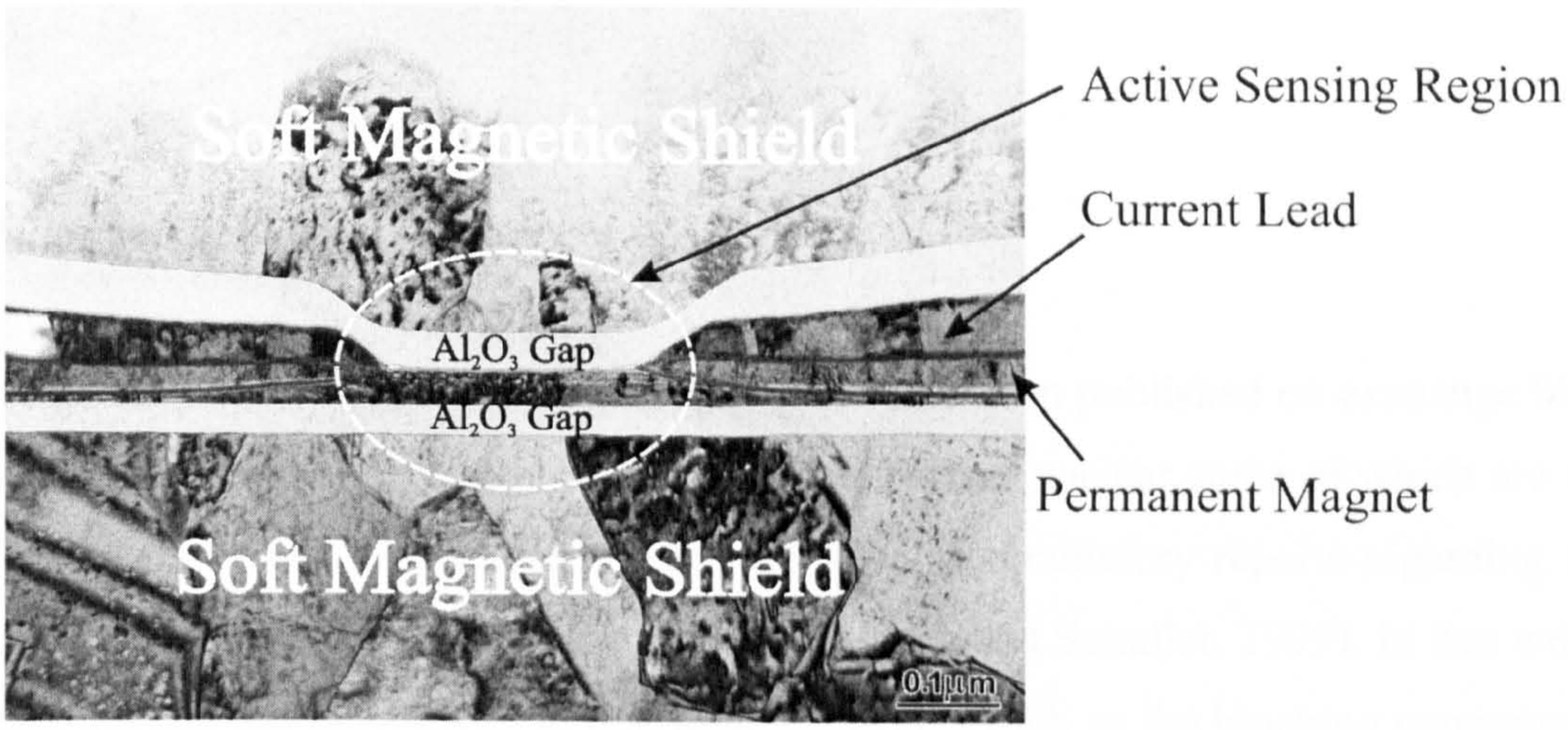

Figure 27. Structure of a spin-valve head (Zhu, 2006).

There is active research seeking new applications of exchange bias. For example, Tondra *et al.* (1998) have reported a picotesla field sensor based on a magnetic tunnel junction. It is very likely that exchange biased spin-valves and magnetic tunnel junctions will find a large number of applications in the future due to their attractive and economical field sensing capabilities (Berkowitz and Takano, 2005).

Chapter 4 Experimental Studies in Exchange Bias

4.1. Introduction

Since its discovery in 1956 thousands of papers have been published on exchange bias. However, there are still experimental issues that remain unclear some of which are the subject of this work. In particular, there are many contradictory reports regarding the effect of the *AF* grain size on exchange bias (Nogues and Schuller, 1999). In this work, special interest has been given to this topic. Concepts such as the blocking temperature as it is usually defined are difficult to interpret. In this chapter some of the most relevant findings in exchange bias will be presented. Special interest will be focused in results achieved for polycrystalline samples as only these systems have been studied in this work.

4.2. Effect of annealing and/or deposition in a field

Exchange anisotropy can be achieved by depositing a sample in the presence of a magnetic field or by heating the sample above the Néel temperature T_N of the *AF* (Jungblut *et al.*, 1994). Exchange bias has also been found in systems that were deposited in the absence of a magnetic field. In 2003 Ng *et al.* reported comparable values of H_{ex} for $Fe_{50}Mn_{50}$(20nm)/$Ni_{80}Fe_{20}$(t_F) bilayers deposited in the presence and in the absence of a dc field. The samples deposited in the absence of the field were predominantly isotropic in nature and had weak unidirectional anisotropy. The presence of the magnetic field during the deposition of the *F* layer induces a uniaxial magnetic anisotropy in the *F* reducing its anisotropy dispersion.

When a field is applied during deposition the order in which the layers are grown plays an important role. Spin valves with a CoFe/IrMn top layer usually exhibit good magnetotransport properties in the as-deposited state while samples with an IrMn/CoFe bottom layer normally require post-deposition magnetic annealing to establish a large

exchange bias (Kerr *et al.*, 2005). However, the opposite behaviour is observed once the samples are annealed (e.g. Kerr *et al.*, 2005). Another important factor is the system studied. Exchange bias can be obtained in the as-deposited state for many kinds of *AF/F* systems (e.g. Xi *et al.*, 2000). However, for systems such as NiFe/NiMn (e.g. Lin *et al.*, 1994) and NiFe/PtMn (e.g. Saito *et al.*, 1997) a post-deposition magnetic annealing is required. In the case of PtMn the annealing is required as PtMn only exhibits antiferromagnetism after phase transformation from the fcc to the fct structure (Sato *et al.*, 2002).

When the *F* is grown first in the presence of a dc field a uniaxial magnetic anisotropy is induced in the *AF* due to the exchange interaction across the interface. All the samples studied in this work were grown in the presence of a ≈300 Oe magnetic field. However when the *F* is deposited in zero-field the *AF* will have no unidirectional anisotropy as the *F* spins have no preferential orientation. In this case, a post-deposition magnetic annealing is required. This is done by heating the specimen above or close to the Néel temperature of the *AF* in a magnetic field. Usually, the system is then field cooled to room temperature (e.g. Li *et al.*, 2001). In systems where T_N is well above room temperature this heating process can result in the deterioration of the microstructure of the sample and therefore lower temperatures are used (e.g. Yoon *et al.*, 2005). The exchange couple can be set at $T<T_N$ because the *AF* is subject to thermal activation which affects barriers around a critical value ΔE_c. This critical value depends on temperature and the potential gradient. In this case the potential gradient is the exchange interaction from the *F*.

Annealing has been subject of many studies in exchange bias as a mean to improve the thermal stability of the exchange field and the GMR properties of spin valve sensors (e.g. Kim *et al.*, 2002). There are three parameters involved in the annealing process: annealing field, annealing temperature and annealing time. Kerr *et al.* (2005) showed that magnetic annealing in large fields enhances the exchange bias and MR of IrMn bottom-pinned spin valves. For annealing fields <5kOe the exchange field increases rapidly. Above 5kOe the increase was more gradual. Magnetic annealing can also promote structural changes in the sample through the annealing temperature (e.g. Jimbo *et al.*, 1997) or the annealing time (e.g. Sato *et al.*, 2002). Rickart *et al.* (2005) reported

that one minute was sufficient to induce the structural phase transition to obtain antiferromagnetic behaviour in PtMn without cooling down in a magnetic field. Higher rapid thermal annealing temperatures reduced the moment of the pinned layer due to the diffusion of Mn atoms (Rickart *et al.*, 2005).

In 2005 Imakita *et al.* developed an in situ thermal annealing procedure where both the underlayer and the *AF* layer were field annealed after being deposited at room temperature. By following this procedure they improved the thermal stability of IrMn/CoFe bilayers through the change of the lateral grain size distribution of the IrMn layer (Imakita *et al.*, 2005). Although the change in grain size between the samples deposited at room temperature and the samples annealed in-situ at 250°C was only ≈2nm, this corresponds to a 52% increase in volume.

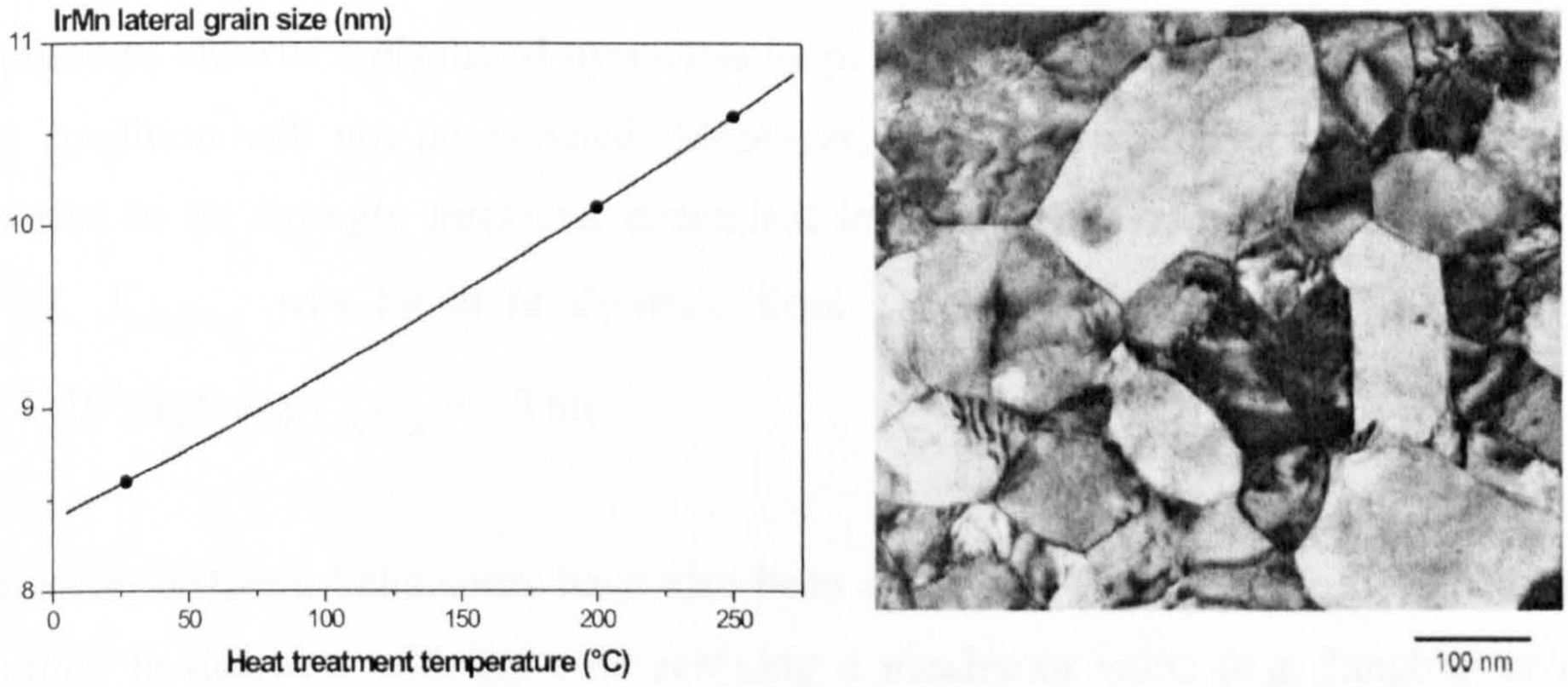

Figure 28. Changes in the lateral grain size of the IrMn films as a function of the in situ annealing temperature and TEM image of a Cu 50 nm underlayer heat-treated at 250°C in ultra-high vacuum (Imakita *et al.*, 2005)

In this work the thermal stability of IrMn/CoFeB bilayers has been studied as a function of the post-deposition magnetic annealing temperature. These results will be presented in Chapter 6.

4.3. Antiferromagnetic thickness dependence

Intuitively the exchange field would increase with the *AF* thickness: the thicker the pinning layer the easier to pin the *F* magnetisation. However, this is more complex as thickness affects grain size and other parameters such as the blocking temperature (e.g. Fernandez-Outon *et al.*, 2004).

It is commonly accepted that the exchange field increases with the *AF* thickness until it saturates above a certain thickness (Nogues and Schuller, 1999). As the *AF* thickness is reduced the exchange field decreases abruptly until it finally vanishes for small *AF* thickness values. The exact thicknesses at which these transitions take place depends on the specific system, its microstructure and the measurement temperature (e.g. Ali *et al.*, 2003). The decrease of the exchange field for small *AF* thicknesses can be related to several factors. As discussed in Chapter 3 the condition $K_{AF}t_{AF} \geq J_{INT}$ is always required to observe a displaced hysteresis loop. Therefore, below a certain value of t_{AF} this condition will not be satisfied. Moreover, the *AF* anisotropy constant has been reported to be strongly thickness dependent in the few nm range (Steenbeck *et al.*, 2004). $K_{Ir_{22}Mn_{78}}$ was found to decrease from $1.4\text{x}10^6$ erg/cc for $t_{Ir_{22}Mn_{78}} \geq 3.5$ nm to $\approx 1.4\text{x}10^5$ erg/cc at $t_{Ir_{22}Mn_{78}} = 1.5$ nm.

However, different behaviours have also been observed. The exchange field has been reported to decrease with t_{AF} after reaching a maximum value (e.g. Jungblut *et al.*, 1994). This effect might be due to microstructural changes in the *AF* layer. In some other cases as the *AF* thickness is decreased from high values a peak in the exchange field before the abrupt reduction has also been observed (e.g. van Driel *et al.*, 2000). This has been attributed to structural changes (van der Zaag *et al.*, 1995) or to changes in the domain structure of the *AF* with decreasing thickness (Malozemoff, 1988b). Ambrose and Chien (1998) found that $H_{ex} \propto 1/t_{AF}$ in CoO/NiFe bilayers. However, Sang *et al.* (1999) found that H_{ex} was proportional to $1/t_{AF}^{0.3}$ when studying the variation of the exchange field with the *AF* thickness in FeMn(t_{AF})/NiFe(30nm) bilayers. Even though the reason for such behaviour was not explained it is clear that different systems behave in different ways.

In this work the dependence of the exchange field on the *AF* thickness in polycrystalline CoFe/IrMn bilayers has been studied. The exchange field increased with t_{AF} for $t_{AF} \leq 8$nm slightly decreasing for higher values. These results and their interpretation will be presented in Chapter 6.

4.4. Ferromagnetic thickness dependence

It has been observed that the exchange field is roughly inversely proportional to the thickness of the *F* layer (Eq. 4.1). This is true for all systems studied (Nogues and Schuller, 1999) although deviations from this behaviour have been observed for certain thickness ranges. Zhou *et al.* (1998) concluded that H_{ex} was small but finite in the limit $1/t_F \rightarrow 0$ from the extrapolation of the plot of H_{ex} against $1/t_F$ in $Fe_{50}Mn_{50}/Ni_{81}Fe_{19}$ bilayers suggesting that the $1/t_F$ dependence of the exchange field is only valid for reasonable small values of the thickness of the *F* layer. When the *F* is too thin Eq. 4.1 is not valid most likely because the *F* layer becomes discontinuous (Parkin and Speriosu, 1990). Moreover, the thickness at which this occurs varies from system to system and depends on both the microstructure and growth of the *F* layer (e.g. Matsumoto *et al.*, 1997 and Chen *et al.*, 1991). Seu *et al.* (2003) studied the Co layer thickness dependence of the exchange field for IrMn/Co and FeMn/Co bilayers. They found that the whole IrMn/Co curve could be fitted assuming a $1/t_F$ dependence of H_{ex}. However, for the FeMn/Co samples, this relationship was not valid for $t_F < 3$ nm. The exchange field is affected by the competition between the Zeeman energy and the exchange coupling across the interface leading to a *F* thickness dependence of H_{ex}. The minimisation of the energy of the system leads to

$$H_{ex} \propto \frac{1}{t_F} \qquad \text{Eq. 4.1}$$

Even though the dependence of the exchange field on the ferromagnetic thickness has not been studied in detail in this work all the samples seemed to follow the $1/t_F$ law.

4.5. Film roughness effects

The atomic scale roughness of *F/AF* systems has been shown to be crucial for their magnetic coupling having important consequences for practical magnetic devices (Blamire and Hickey, 2006). The dependence of the exchange field and the coercivity is totally different for samples prepared differently (Liu *et al.*, 2000). Normally, systems with polycrystalline *AF* layers such as those studied in this work are less sensitive to roughness than samples with single crystal *AFs* (Nogues and Schuller, 1999). For polycrystalline Ta/FeMn/NiFe exchange bias bilayers deposited on reactive ion etched Si substrates, H_c and H_{ex} were relatively insensitive to the change of roughness while for polycrystalline samples grown on ultrathin Cu underlayers both the exchange field and the coercivity increased with roughness (Liu *et al.*, 2000). For epitaxially grown films no simple correlation was found between H_{ex} and interface roughness (Liu *et al.*, 2000). However, most of the studies in the literature seem to agree that the exchange field decreases with increasing interface roughness (e.g. Choukh, 1997) independent of the interfacial spin structure, i.e. compensated or uncompensated (Nogues and Schuller, 1999).

Roughness creates areas of different spin orientation and therefore the total number of spins pinning the *F* magnetisation is smaller than for a flat interface leading to a reduction of the exchange field with increasing interface roughness. However, this argument is only valid for uncompensated interfaces. In the case of compensated interfaces, the surface remains compensated independently of roughness. Some models suggest that roughness affects the interface exchange coupling J_{INT} and therefore the exchange field (e.g. Mauri *et al.*, 1987a).

4.6. Film crystallography

The degree of texture of the *AF* layer of an exchange bias system, also known as crystallinity, has been reported to affect H_{ex} (e.g. Figure 29 IrMn Tsunoda *et al.*, 2006). Exchange anisotropy has also been found to be very sensitive to the dispersion of *F* crystal axis (e.g. NiFe Wang *et al.*, 1996). In the case of IrMn, the *AF* studied in this work, Imakita *et al.* (2004) achieved giant exchange anisotropy in

substrate/$Ni_{27}Fe_7Cr_{66}$/Cu(50nm)/$Ir_{27}Mn_{73}$(10nm)/$Co_{70}Fe_{30}$(4nm)/Cu(1nm)/$Ni_{24}Fe_{10}Cr_{66}$(2nm) systems by following a detailed deposition procedure which involved in-situ thermal annealing. The results were attributed to the Mn_3Ir phase that was partially formed in the *AF* layer (Imakita *et al.*, 2004). However, there are reports in the literature where H_{ex} did not depend on the diffraction intensity from IrMn (111) (Yagami *et al.*, 2001). More recent results by the same group showed that the compositional range where $L1_2$-phase Mn_3Ir could be formed is 22-32 at% Ir resulting in giant exchange anisotropy as high as 1.3 erg/cm^2 (Tsunoda *et al.*, 2006). This corresponds to an exchange field of approximately 2 kOe. Another important factor is the order in which the layers are grown. Pakala *et al.* (2000a) reported no correlation between the IrMn (111) peak intensity and H_{ex} in CoFe/IrMn bilayers when the *AF* was grown on top of the *F*. Similar results were achieved by Devashayam *et al.* (1998). However, when the *AF* was deposited prior to the *F* layer H_{ex} was found to decrease with decreasing IrMn (111) preferred orientation as shown in Table 1 (Pakala *et al.*, 2000a).

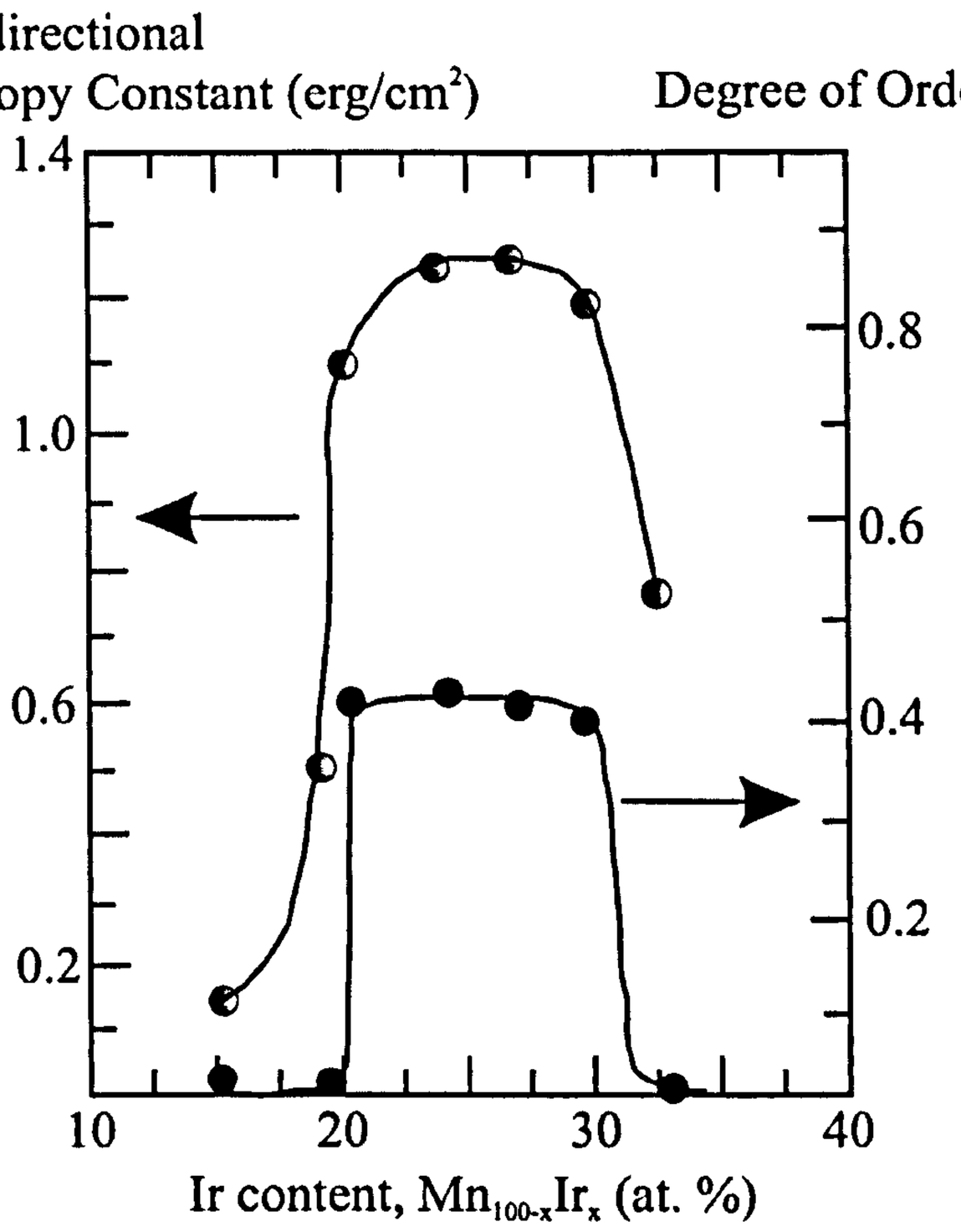

Figure 29. Unidirectional anisotropy constant and degree of order in the *AF* layer as a function of the Ir content in the IrMn layer (reproduced from Tsunoda *et al.*, 2006).

In most of the studies in the literature the samples are annealed to achieve different degrees of texture. In some cases this leads to an increase in grain size in the different layers (e.g. Imakita *et al.*, 2005 and Pakala *et al.*, 2000a). In this work the effect of the *AF* grain size on the exchange field in polycrystalline thin films has been studied. The samples were deposited in the presence of a dc field to avoid a post-deposition magnetic annealing. This way the possibility of grain growth which in turn might modify the crystal structure was avoided. Therefore the changes in the exchange field are mostly if not only due to the different grain sizes of the *AF* layer achieved during the deposition of the samples.

Table 1. Underlayer UL microstructure and H_{ex} for as-deposited and annealed IrMn top and bottom configuration (Pakala *et al.*, 2000a)

t_{UL} (nm)	UL structure and texture	H_{ex} (Oe) as dep.		H_{ex} (Oe) annealed	
		Top	Bottom	Top	Bottom
Ru(5)	hcp-002	238	172	225	295
Ru(15)	hcp-002	295	197	278	336
Ru(40)	hcp-002	295	180	319	377
Ru(100)	hcp-002	270	175	320	320
$[Cu(1)Ru(1)]_3$	hcp-002/fcc-111	151	49	155	74
$[Cu(1)Ru(1)]_7$	hcp-002/fcc-111	239	227	210	510
$[Cu(1)Ru(1)]_{20}$	hcp-002/fcc-111	230	197	270	500
$[Cu(1)Ru(1)]_{50}$	hcp-002/fcc-111	213	190	288	470
Cu(5)	fcc-111	98	49	148	74
Cu(15)	fcc-111	180	210	393	254
Cu(40)	fcc-111	180	197	426	336
Cu(100)	fcc-111	246	197	410	336

4.7. Antiferromagnetic grain size effects

The role of the *AF* grain size on exchange bias still remains unclear. There are reports in the literature that show that H_{ex} decreases with increasing *AF* grain size (e.g. $Ni_{81}Fe_{19}$/CoO Takano *et al.*, 1997). However, the opposite trend has also been observed (e.g. $NiFe_{81}Fe_{19}/Fe_{50}Mn_{50}$ Manzoor *et al.*, 2005) suggesting that different systems might behave in different ways. In this work, only metallic *AF*s have been used as the biasing material. The dependence of H_{ex} on the *AF* grain size has been found to be more complicated. This will be discussed in Chapter 6.

Takano *et al.* (1997) reported a decrease in the exchange field with increasing *AF* grain size in $Ni_{81}Fe_{19}$/CoO bilayers. They showed that the temperature dependence of the thermoremanent magnetisation (TRM) of CoO/MgO multilayers after field cooling from $T>T_N$ was the same as that of $Ni_{81}Fe_{19}$/CoO bilayers also after field cooling. In the case of CoO/MgO it was shown that *AF* uncompensated interfacial spins constituted the TRM and, therefore, they concluded that the uncompensated *AF* spins were responsible for the unidirectional anisotropy. The number of uncompensated spins at the grain boundaries increased with decreasing CoO grain size and, therefore, higher values of the exchange field were due to a reduction in the *AF* grain size (Takano *et al.*, 1997). This can be possible due to the formation of domain walls that would pin at grain boundaries. In their system that is possible due to super exchange through the oxygen atoms. In metallic *AF*s such as IrMn and FeMn this intergranular exchange coupling would be very small if not zero. However, a reduction of the exchange field with the *AF* grain size has been observed for metallic systems such as $Cr_{70}Al_{30}/Ni_{81}Fe_{19}$ (Uyama *et al.*, 1997). The grain size was estimated from X-ray data using Scherrer's equation. The increase in the *AF* grain size was achieved by changing the thickness of a $Ni_{81}Fe_{19}$ underlayer which in turn affected the degree of the [110] orientation. Hence, the behaviour of the exchange field cannot be attributed only to changes in the crystallite size.

The *AF* grain size not only affects the exchange field but also the thermal stability of exchange bias systems (e.g. Imakita *et al.*, 2005). Nishioka *et al.* (1996) reported an increase in the blocking temperature from 300 to 450K with the *AF* grain size in NiFe/FeMn systems. Fernandez-Outon *et al.* (2004) reported an increase in the median blocking temperature from 200K to 310K with increasing IrMn thickness and therefore grain volume. Figure 30 shows a typical measurement of the median blocking temperature (Fernandez-Outon, 2006). Briefly, the *AF* is reset by heating the sample to 373K for 90 minutes in the presence of a positive saturating field. The temperature is then quenched to 77K and the field reversed so the A*F* is in negative bias. The temperature is raised to an activation temperature T_{ACT} where the *F* is held at negative saturation for 30 minutes. The system is then cooled to 77K and the loop measured. The measurement procedure will be described in detail in chapter 5. Almost all the samples studied in this work contained an IrMn layer which has significantly superior temperature stability and exchange biasing properties when compared to FeMn (e.g. Devasahayam *et al.*, 1998).

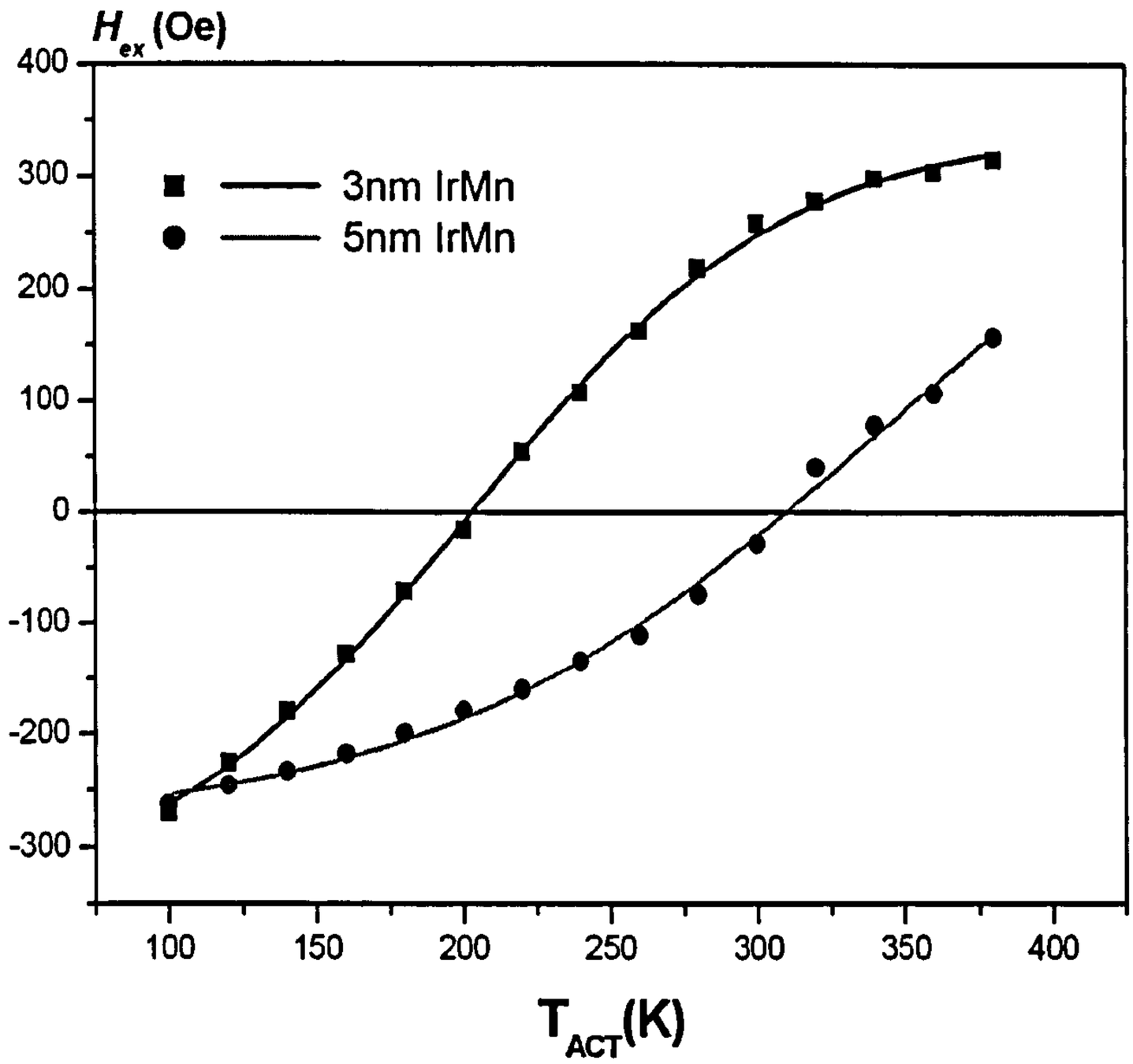

Figure 30. Typical measurement of the median blocking temperature in IrMn/CoFe bilayers (Fernandez-Outon *et al.*, 2004).

4.8. Blocking temperature

The blocking temperature T_B is usually defined as the temperature at which the exchange field goes to zero. The standard method to determine T_B is based on the measurement of the hysteresis loop of an exchange biased system with increasing temperature until the shift in the loop becomes zero (e.g. Imakita *et al.*, 2005). Above T_B the exchange field remains zero. Figure 31 shows a typical measurement of the blocking temperature in $Ir_{27}Mn_{73}/Co_{60}Fe_{20}B_{20}$ bilayers. These measurements were made using a NanoMOKE2™ during an industrial placement at SIEMENS Research Ag. According to Fulcomer and Charap (1972a) T_B will correspond to the blocking temperature of the *AF* grain with the largest anisotropy energy. In polycrystalline samples each grain has its own blocking temperature and therefore the *AF* is characterised by a distribution of blocking temperatures. Xi (2005) proposed a thermal fluctuation model based on Fulcomer and Charap's interpretation of exchange bias where the dependence of T_B on

several parameters such as the *AF* thickness, *AF* grain size, hysteresis loop measurement time among others was calculated.

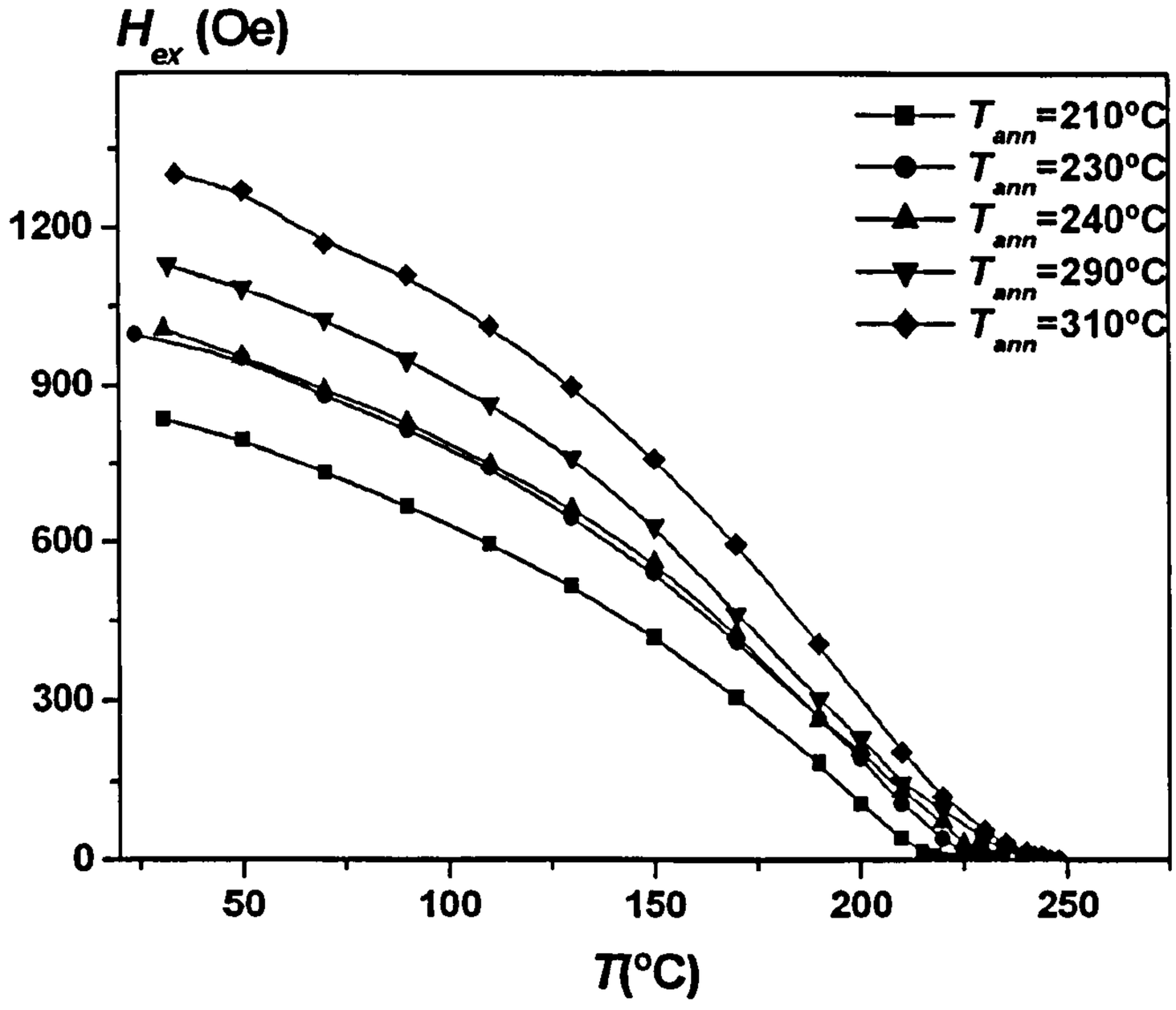

Figure 31. Conventional measurement of the blocking temperature for IrMn/CoFeB bilayers annealed at different temperatures T_{ann}.

When the standard measurement protocol is used, the *AF* is subject to thermal activation during measurement at a logarithmic rate (O'Grady *et al.*, 2002) leading to changes in its state of order from measurement to measurement. Fernandez-Outon *et al.* (2004) showed that the hysteresis loop of an exchange biased system could be shifted in the opposite direction to that in which it was originally set by following a detailed measurement protocol. The measurements were done at a temperature where the *AF* was free of thermal activation and the *AF* was *reset* prior to each measurement to ensure reproducibility of the data (Fernandez-Outon *et al.*, 2004). A standard measurement following this procedure is shown in Figure 32. The way in which this was achieved will be described in Chapter 5. Following this measurement procedure T_B is defined as the temperature at which equal fractions of the *AF* are oriented in opposite directions (Figure 33b) and is a measure of the energy barriers to reversal within the *AF* (O'Grady *et al.*, 2002). Fernandez-Outon *et al.* (2004) showed that the peak in the coercivity could

be seen even though all the measurements were done at the same temperature of 100K and that the peak did not occur at the median blocking temperature of the distribution of energy barriers in the *AF*. Furthermore, for a 5nm thick IrMn layer the peak was below T_B while for a 3nm *AF* layer the peak was well above T_B.

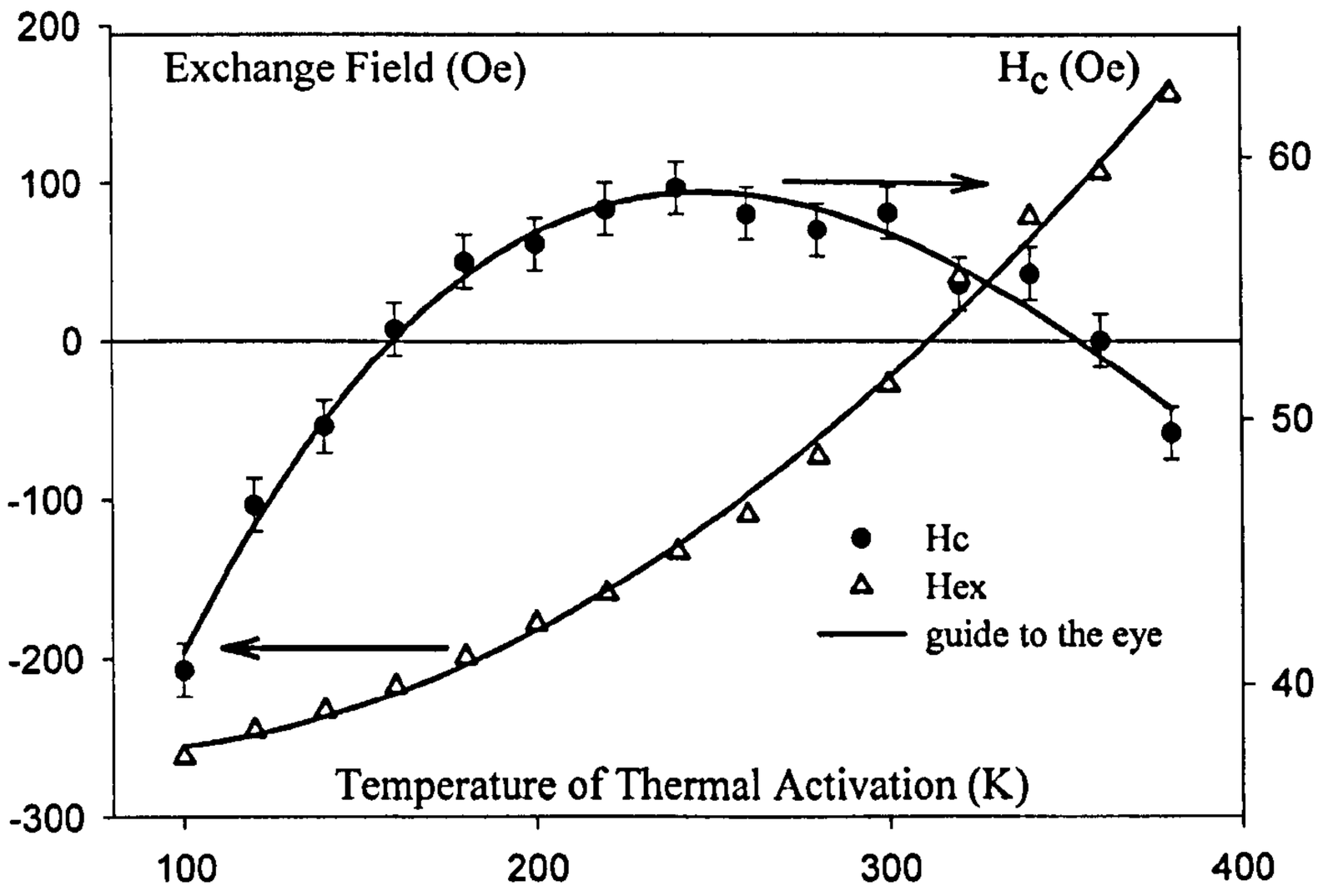

Figure 32. Measurement of the blocking temperature for a CoFe(10nm)/IrMn(5nm) bilayer following the measurement protocol described in Fernandez-Outon *et al.* (2004).

When the conventional measurement procedure is used, at the so called blocking temperature there is a small fraction of the *AF* which is not in a superparamagnetic state as depicted in Figure 33a. Hence the whole *AF* distribution is not thermally activated and therefore this type of measurement has no real physical meaning. When the temperature is raised from room temperature, the amount of *AF* that is being dragged by the *F* increases. Hence, H_{ex} becomes zero and does not acquire positive values.

Most of the studies available in the literature are based on the conventional measurement procedure. Xi *et al.* (2003) studied the dependence of the blocking temperature on composition in $Ni_{81}Fe_{19}/Pt_xMn_{1-x}$ with low Pt content ($0<x<0.2$). The highest T_B was achieved for x = 0.8. Further doping with Pt decreased the blocking temperature. The *AF* grain size and thickness have been reported to have a significant effect on T_B (e.g. Nishioka *et al.*, 1996 and Nishioka *et al.*, 1998). The increase in T_B with the *AF* grain size and thickness has been related is some cases to an increase in the

anisotropy energy of the *AF* grains (e.g. Nishioka *et al.*, 1998) or as a form of finite size effect (e.g. van Driel *et al.*, 2000).

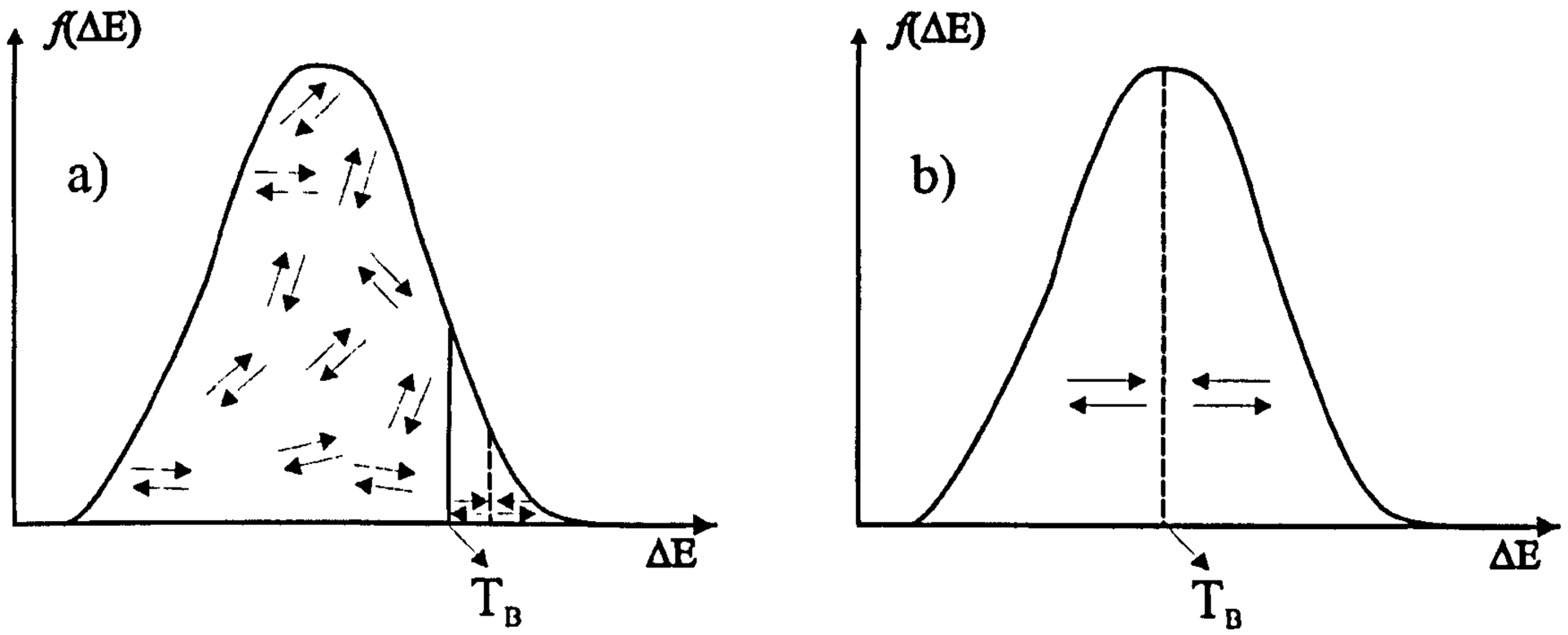

Figure 33. Distribution of energy barriers to reversal within the *AF* layer of an exchange biased system a) following the standard measurement protocol of the blocking temperature and b) following the measurement protocol described by Fernandez-Outon *et al.* (2004)

Nowadays IrMn/CoFe is the most important system from the technological point of view due to the large unidirectional anisotropy achievable with very thin *AF* layers (e.g. Fuke *et al.*, 1999). This is a very important factor as the *AF* thickness is dominant in the total thickness of spin-valves. One of the main limitations is its low blocking temperature when compared to systems containing PtMn, usually used in Hard Disk Drives (HDDs) at the present (Tsunoda *et al.*, 2006). However, the formation of $L1_2$ type Mn_3Ir will give a step to overcome this issue. This has already been achieved by Tsunoda *et al.* (2006) by increasing the substrate temperature during the deposition of the IrMn layer and using a Ru underlayer. A blocking temperature as high as 360°C was reported when the deposition temperature was raised to 170°C (Tsunoda *et al.*, 2006).

4.9. Memory effects

Gökemeijer and Chien (1999) showed that the magnetisation of the *F* is the crucial parameter in the field cooling procedure. A $CoO/Ni_{81}Fe_{19}$ bilayer was measured at 200K after following three different field cooling procedures. The first procedure consisted in cooling down the sample in the presence of a 200 Oe field with $M=M_s$ resulting in a displaced hysteresis loop and an enhanced coercivity as shown in Figure 34a. In the

second procedure the *F* was DC demagnetised and then zero field cooled to 200K resulting in two hysteresis loops shifted to opposite sides as shown in Figure 34b. This was due to the formation of closure domains of opposite magnetisation (Gökemeijer and Chien, 1999). When the sample was field cooled in a 200 Oe oscillating field at 1/4 Hz the measured hysteresis loop had no exchange bias and only an enhanced coercivity as shown in Figure 34c. As the magnetisation of the *F* was changing during field cooling there was no preferential direction to induce an exchange anisotropy across the *F*/*AF* interface (Gökemeijer and Chien, 1999).

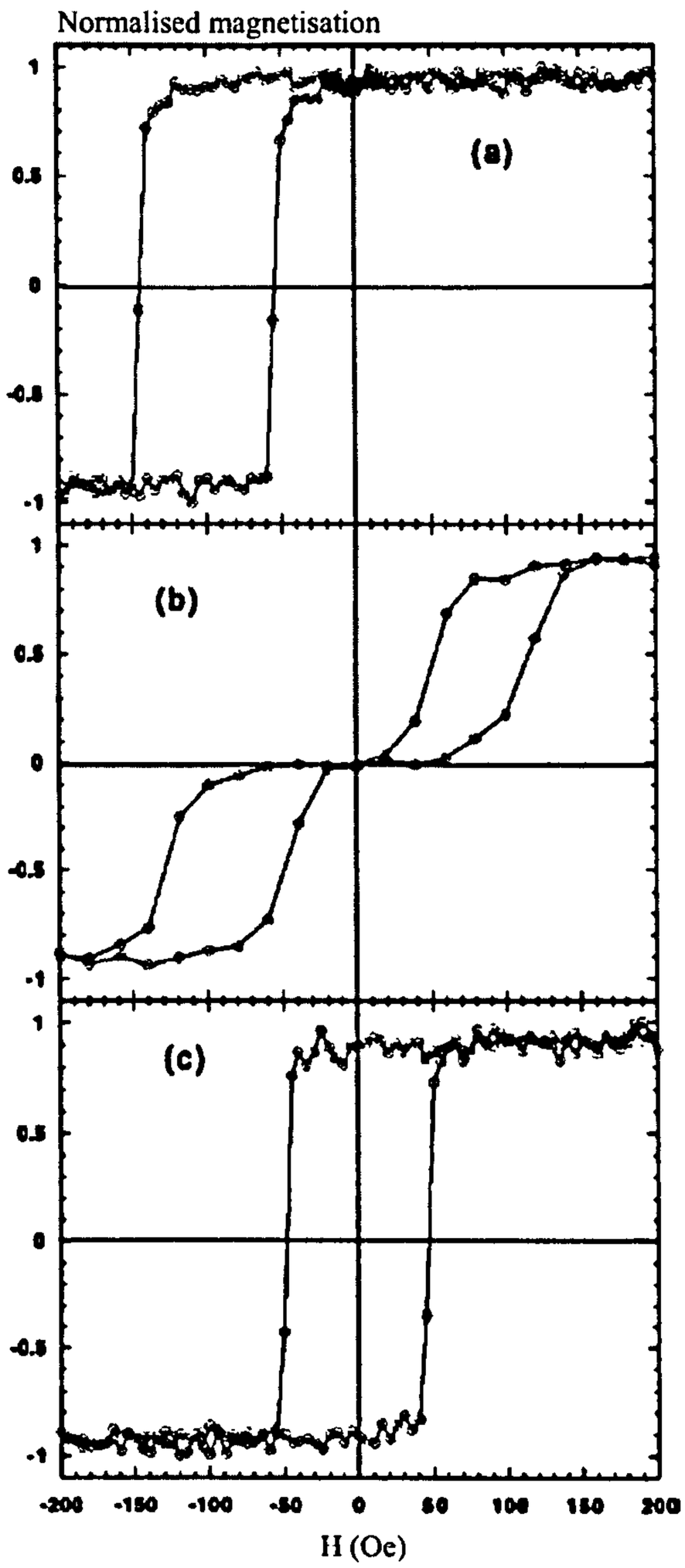

Figure 34. Hysteresis loop of a $CoO/Ni_{81}Fe_{19}$ bilayer at 200 K (a) after field cooling in a +200 Oe field, (b) After demagnetising the sample and zero field cooling and (c) after cooling down in the presence of an alternating field (Gökemeijer and Chien, 1999).

Note that even though the exchange field is strongly dependent on the cooling process the coercivity barely changes for the three different procedures. This is an indication that H_c is dominated by interfacial effects. By following each different procedure the only parameter that changes is the fraction of the *AF* oriented in different directions. The coercivity will be dominated by a fraction of the *AF* that remains in a superparamagnetic state and therefore it does not contribute to the loop displacement. When the sample is field cooled in a DC field the *AF* tends to align parallel to the *F* and the hysteresis loop is displaced along the field axis. However, under demagnetising and zero field cooling the *F* layer is divided in two domains of opposite direction. The state of order of the *AF* would be a print through of the magnetisation state of the *F* and therefore two loops displaced by an equal amount but in opposite direction are observed. Finally, cooling the sample in the presence of an AC field leaves the *AF* oriented in two opposite directions leading to a non-exchange biased loop.

To explore further the establishment of the exchange field the sample was field cooled in two steps. In first place it was cooled in an alternating field at 1Hz to a certain temperature T_s and then cooled to 200 K in the presence of a 200 Oe DC field. The sample only exhibited exchange bias for $T<T_s$. demonstrating that the bilayer has the *memory* of the cooling procedure and the temperature at which the dc field was switched on (Gökemeijer and Chien, 1999).

Gökemeijer and Chien (1999) also studied the effect of reversing the dc field during the cooling process. The sample was cooled in a 200 Oe field to a temperature T_q below which the field was switched to –200 Oe. Measurements were then made at increasing temperature from 200K. This procedure was repeated for different values of T_q in the range 250-270K. As a consequence the values of the exchange field could be changed to a great extent and even change sign demonstrating that the bilayer had the memory effect of a positive field cooling above T_q followed by a negative field cooling to 200 K (Gökemeijer and Chien, 1999). It is important to note that the value of the coercivity was uniquely defined at each temperature. Gökemeijer *et al.* (1999) suggested that this memory effect was due to the formation of a domain wall within the *AF* parallel to the *F*/*AF* interface. These results can be understood in terms of an energy barrier to reversal within the *AF*. When the sample is field cooled above T_q the *AF* tends to align itself in the direction of the *F* due to the exchange coupling across the interface (Figure 35).

However, when the field is reversed below T_q the *AF* is set in the opposite direction. Therefore there are two opposite contributions to the exchange field. Depending on the temperature at which the field is reversed the loop will be shifted to the left or to the right of the magnetisation axis.

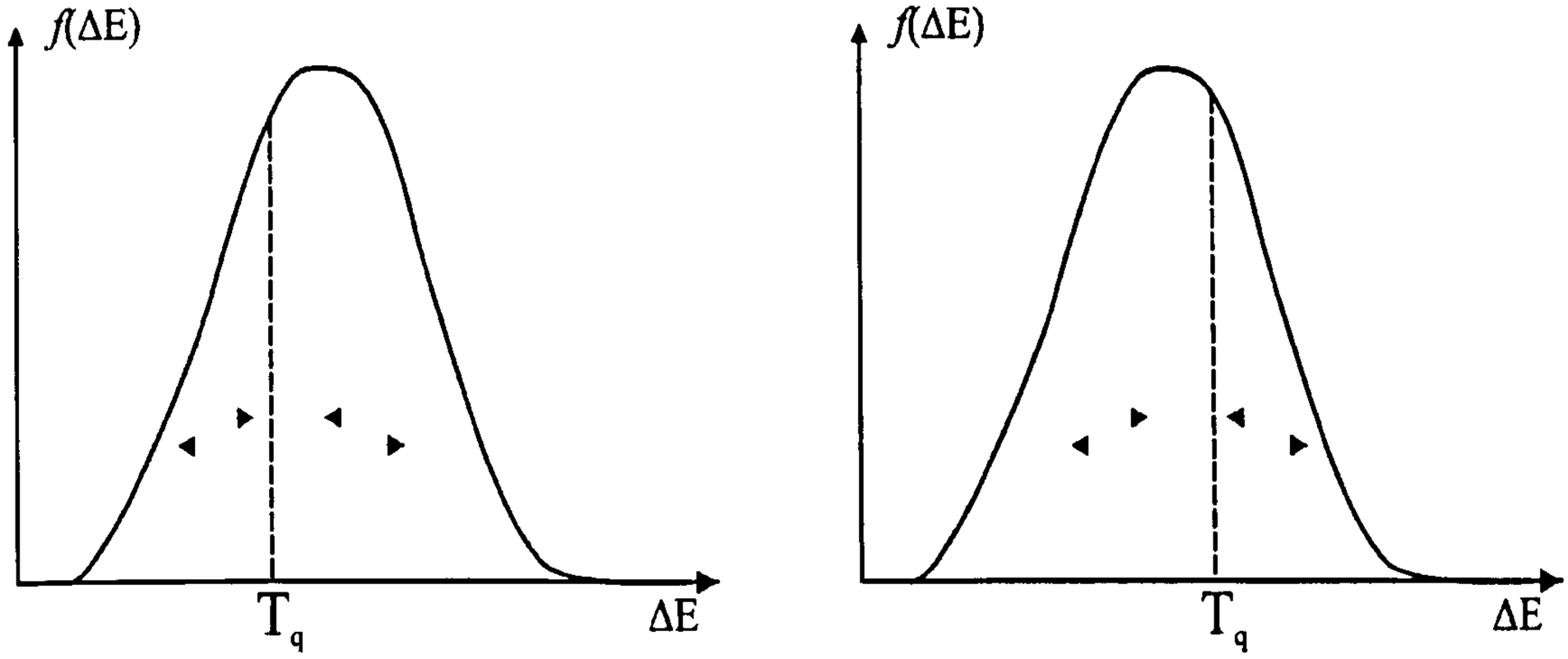

Figure 35. Schematic of the energy barrier distribution within the *AF* when the sample is field cooled in two opposite directions: loop shifted to negative field values (left) and positive field values (right).

4.10. Training effect

In some systems exchange bias has been observed to decrease upon repeated field cycling. This effect is referred to as training and it has been known since 1966 (Paccard *et al.*, 1966). A schematic diagram of the training effect is shown in Figure 36. Training has been observed for both polycrystalline (e.g. Zhang *et al.*, 2002) and single crystal *AF*s (e.g. Wee *et al.*, 2004). In general it is more significant in polycrystalline samples (Nogues and Schuller, 1999) although similar training effects were found for poly- and single-crystal $KCoF_3$ samples (Malkinski *et al.*, 2003). In some cases training has been reported to affect only the descending branch of the hysteresis loop i.e. H_{c1} (e.g. Wee *et al.*, 2004), the ascending branch of the loop i.e. H_{c2} (e.g. Ali *et al.*, 2003) or both i.e. H_{c1} and H_{c2} (e.g. Zhang *et al.*, 2002). All these different types of training are suspected to be due to irreversible changes in the *AF* microstructure during magnetisation reversal.

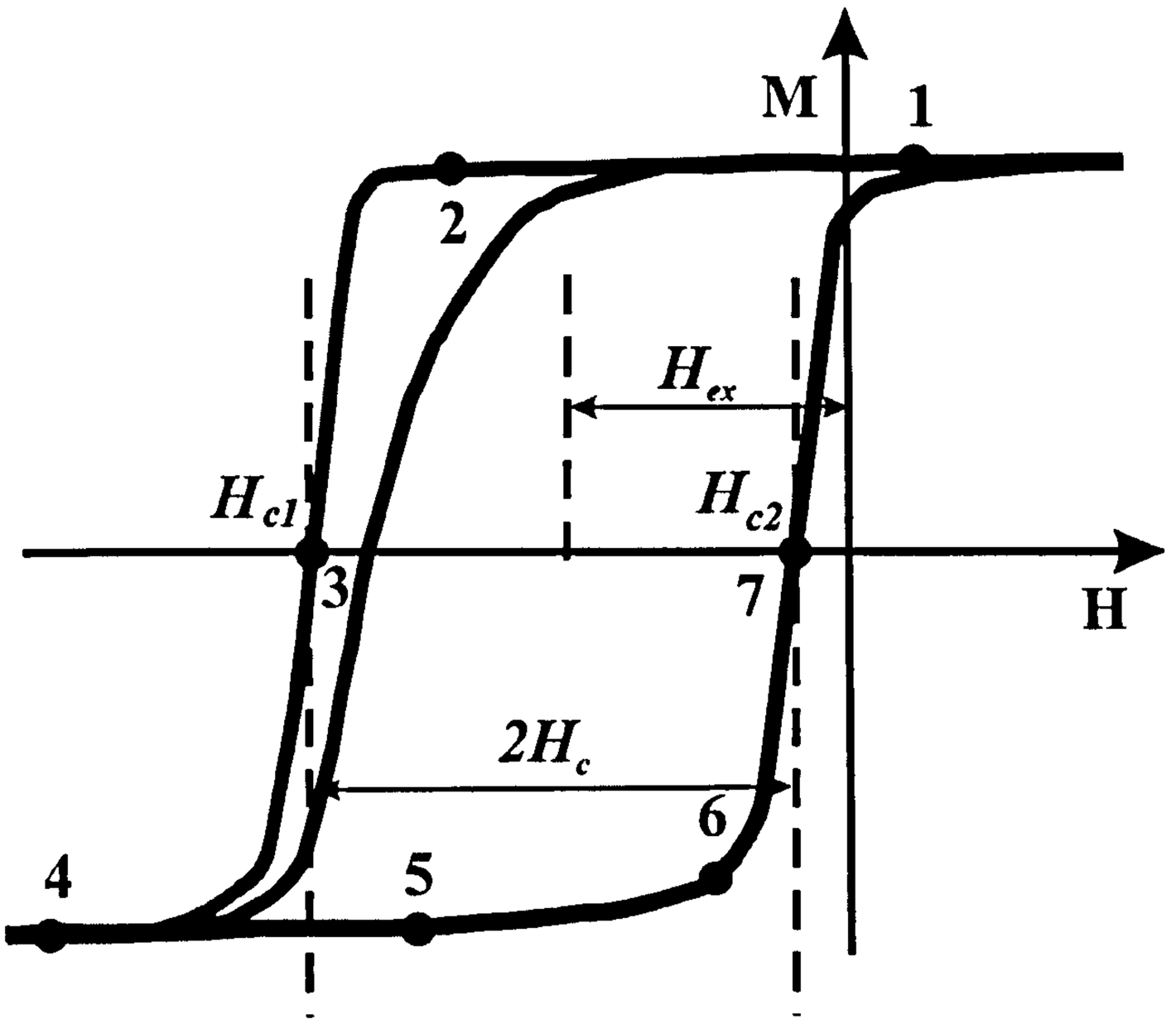

Figure 36. Schematic diagram of the training effect where the exchange field is reduced upon field cycling.

In 2004 Hoffmann proposed a model for training suggesting that the irreversibilities upon field cycling were driven by the symmetry of the anisotropy of the *AF*. The first indication for this was the fact that training has only been observed in systems that contain a high symmetry *AF* with multiple equivalent easy axes (Hoffmann, 2004). Figure 37 shows the orientation of the various magnetisations for the first and second hysteresis loop for the case of a biaxial *AF*. Before the *F* magnetisation is reversed for the first time the *AF* sublattice magnetisations are perpendicular. This is due to some inherent frustration that arises due to the coupling of both *AF* sublattices to the *F* (Hoffmann, 2004). Once the *F* is reversed the *AF* relaxes into a metastable antiparallel configuration where it remains for subsequent hysteresis loops. This spin reorientation effect occurs over an energy barrier distribution (Fernandez-Outon, 2006).

Recently, this big jump in H_{c1} between the first and the second loop has been predicted assuming uniaxial anisotropy in the *AF* (R. W. Chantrell, private communication). This training was due to irreversible changes in the magnetic state of the *AF* during the first loop caused by a rotation of the *F* magnetisation. The key factor in this model was the random distribution of *AF* easy directions in 3D. Also Suess *et al.* (2003) predicted exchange bias and training effect in polycrystalline IrMn/NiFe bilayers with perfectly

compensated interfaces. Training was due to different domain configurations in the *AF* after field cooling and after the first hysteresis loop (Suess *et al.*, 2003).

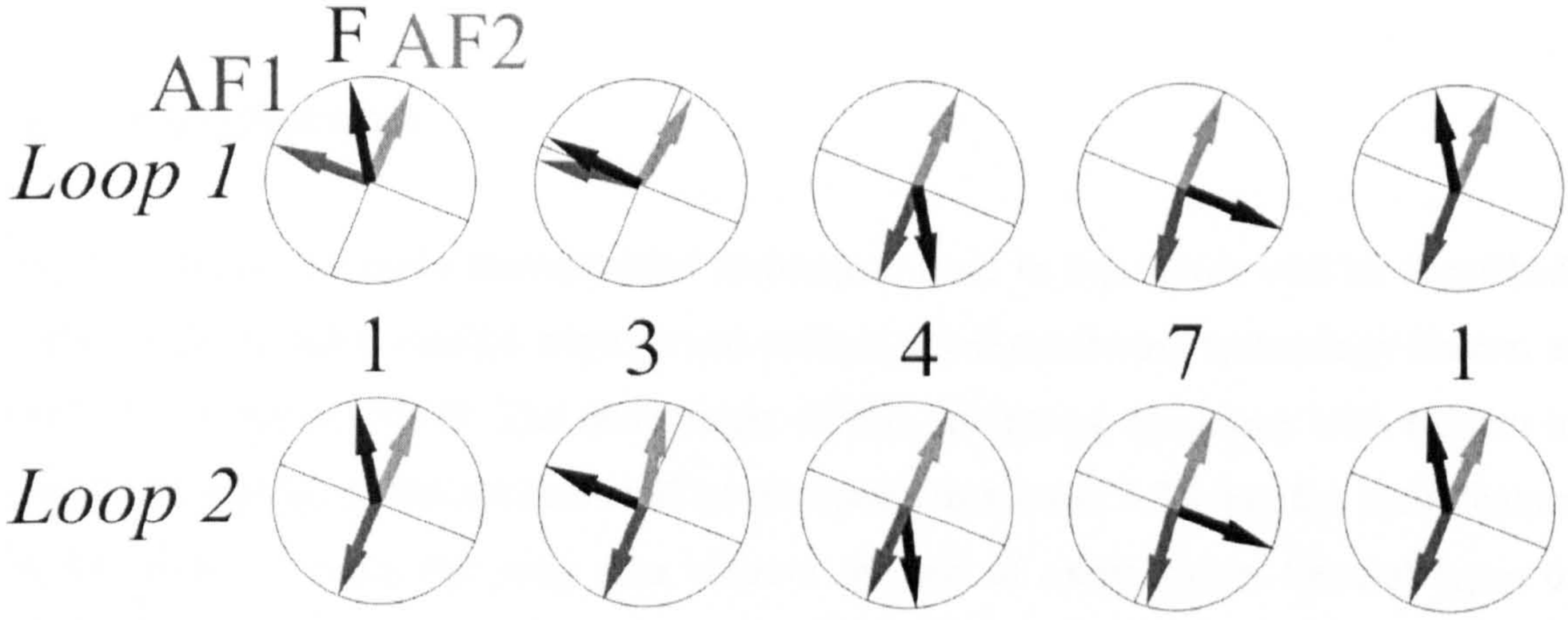

Figure 37. Ferromagnetic and each antiferromagnetic sublattice magnetisation during the first and second hysteresis loops for the case of an *AF* with biaxial anisotropy (reproduced from Hoffmann, 2004).

Thermal effects can also lead to training (e.g. Wee *et al.*, 2004). While the training first described by Hoffmann only affected the descending branch of the loop, thermal training affects both coercive fields. Note that this type of training also occurs over an energy barrier distribution and both distributions, thermal and athermal, overlap. Fernandez-Outon (2006) showed that the jump in H_{c1} was thermally independent in the range 16-325K in CoFe(10nm)/IrMn(5nm) bilayers. Above 325K the jump in the first coercivity was reduced indicating the superposition of both energy barriers. This emphasizes the complexity of this effect.

Clearly a wide range of complex phenomena occur in exchange biased systems. The phenomenon of exchange bias is known to depend on the behaviour of the bulk *AF* and the spin structure at the interface. Unfortunately direct measurements of both these parameters are not possible. Hence, careful measurements procedures that take into account the anticipated behaviour of the *AF* are required. The procedures used in this work are described in Chapter 5.

Chapter 5 Experimental Techniques

5.1. Introduction

In this chapter the main experimental techniques used in this thesis will be described. Most of the samples studied were grown using a novel sputtering technology known as HiTUS (Thwaites, 2002). The advantages of this sputtering technique with respect to conventional magnetron systems will be discussed in section 5.3.1 but the main feature is the ability to vary the grain size without the use of extra layers. Several types of magnetometers were used to characterise the magnetic properties of exchange biased samples: vibrating sample magnetometer (VSM), alternating gradient force magnetometer (AGFM) and magneto-optical kerr effect magnetometer (MOKE). Grain size analysis was determined from TEM pictures in bright field mode using a Zeiss particle size analyser.

5.2. Sample preparation techniques

In this thesis all the samples studied have been prepared using sputtering. This is the most commonly used technique for thin film deposition. It was first reported in 1852 by R. R. Grove when studying electrical conductivity of gases. One of the main advantages of sputtering over other deposition techniques such as molecular beam epitaxy (MBE) is the high growth-rates achievable. This results in lower contamination of the target without the use of UHV. Unlike other deposition techniques there is no melting of the target material.

Sputtering results from the bombardment of a solid target by highly energetic ions. It is driven by momentum transfer between the ions in a plasma and atoms at the target surface. Although the first collision pushes atoms into the core of the target, subsequent collisions between the atoms can result in the ejection of some atoms near the surface. The number of atoms that escape from the surface per incident ion is called the sputter

yield. This sputter yield depends upon the energy of the incident ions, the masses of the ions and target atoms and the binding energy of the target.

It could be thought that sputtering would lead to changes in stoichiometry in the target from the nominal values as the sputter yield depends upon the mass of the atoms. This would have an important effect in alloys where the constituting elements have very different binding energies such as IrMn. However, only surface atoms can be sputtered and if the sputtering rate is much higher for one element than for the others, the surface would become enriched with the other elements. This counteracts the differences in the deposition rates and leads to a need to condition the target before use (Stuart, 1983).

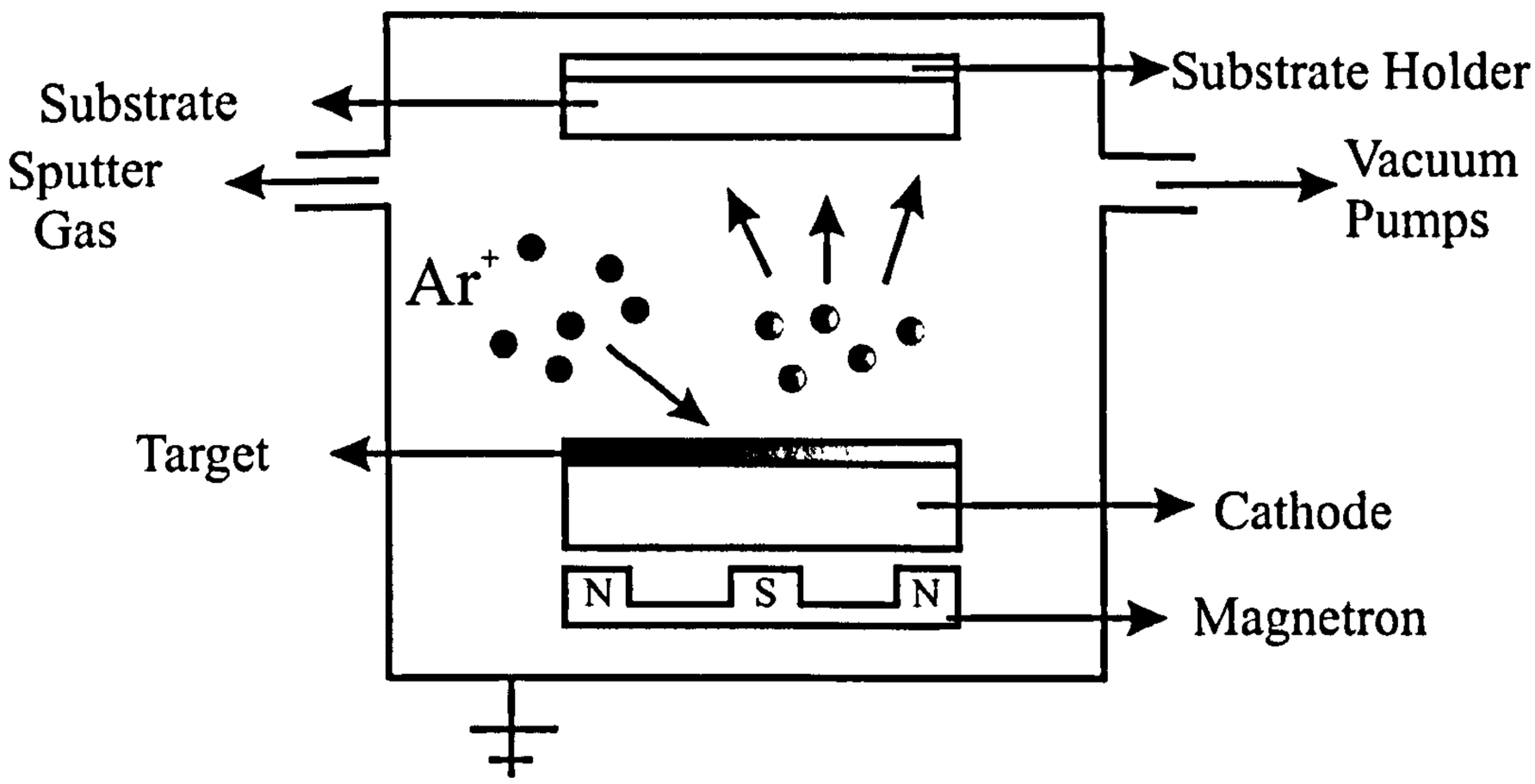

Figure 38. Schematic diagram of a magnetron sputtering system.

The most widely used source of sputtering is a magnetron. However, this type of sputtering system presents some limitations which will be discussed in 5.3.1. In this thesis a HiTUS deposition system has been used. This is a novel sputtering technology which has the key advantage of controlling the grain size of the deposited films without modifying the microstructure of the samples.

5.2.1. Magnetron sputtering (DC and RF)

Figure 38 shows a schematic diagram of a DC magnetron sputtering system. Ar is usually chosen as the sputtering gas. A negative potential up to some hundreds of volts is applied to the target and therefore the Ar^+ ions are accelerated to the target. As a

consequence, some of the surface atoms escape from the target and some secondary electrons are also emitted. The gas is further ionized by these electrons. The gas pressure and the electrode distance set a break-through voltage above which a self-sustained glow discharge takes place.

In magnetron sputtering the ionisation is increased up to one order of magnitude by placing a ring magnet usually underneath the target. This way the problem of having wasted electrons flying around the chamber creating problems is avoided. The electrons are trapped in its field and circulate over the target surface. A higher sputtering rate is achieved below this region and therefore an erosion track appears on the target. These race-tracks are characteristic of magnetron sputtering and limits the lifetime of a target.

DC magnetron sputtering can be used only to sputter metals as a negative voltage is applied to the target. If a conductive plate is placed behind a non-conductive target, as shown in Figure 38, a negative voltage can now be applied to the conductive plate. Ions will be accelerated and they will strike the non-conducting material. This way, sputtering from non-conducting targets is achieved. However, after 10^{-7}s of impinging the target a positive charge will be built on the surface of the insulator. If the connections are now reversed and a positive bias applied to the conductor, electrons will be accelerated towards it striking the insulator and creating a negative surface charge. This process will last 1ns. At this point we can reverse the polarisation again and sputter for another 10^{-7}s. If a sputtering time of 100s is needed, we would have to reverse the connections 10^9 times and therefore it would take almost 200 days to sputter the layer (Stuart, 1983). If we use a radio frequency generator operating at a frequency of at least 1 Megacycle per second, insulators can be sputtered at a practical sputtering rate. DC and RF magnetron sputtering is the most widely used technique for vacuum thin film deposition.

5.3. High Target Utilisation Sputtering (HiTUS)

Almost all the samples used in this thesis were grown using a novel sputtering technology known as HiTUS (Thwaites, 2002). This is an acronym for High Target Utilisation Sputtering. The system was originally developed by a small UK company

called Plasma Quest Ltd but many updates were done to the system during the course of this work. A new target holder was installed allowing us to sputter from up to eight different materials instead of the original single target. Plastic pipes were substituted by metallic ones to avoid impurities in the ionised gas. The installation of a film rate monitor allowed us to control the thickness of the deposited layers. Finally, a substrate heater was installed to study micro-structural effects in magnetic thin films. This system presents several advantages in comparison with other conventional sputtering techniques, in particular the utilisation of almost the whole target area and the ability to control the growth-rate and hence the grain size in the films. In this work several new sputtering procedures were designed.

5.3.1. Limitations of conventional sputtering systems

A very important characteristic of HiTUS is its capability to sputter from ferromagnetic targets without the use of magnetic fields beneath the target. This is very important for my studies as most of the samples described in this work consist of a ferromagnet in direct contact with an antiferromagnet. In conventional magnetron sputtering systems, a magnetic field is required to confine the electrons within the plasma. This leads to a race-track on the target surface limiting its lifetime. Target utilisation as high as 80% is achieved for non-magnetic targets using magnetron sputtering. However, sputtering from ferromagnetic targets is still an important issue. First of all, the thickness of the target is limited in order to achieve a high enough magnetic field at the target surface (225Oe). Secondly, the target utilisation is low compared to non-magnetic materials. This is due to the higher erosion of the target in the centre of the race-track. As there is less ferromagnetic material in that region, a local increase of the magnetic field is observed. These two factors limit the lifetime of the targets and their surface utilisation. A target utilisation as high as 90% is achieved using HiTUS even for ferromagnetic targets. As no magnetic field is applied beneath the target, no race-track is observed. Diode and triode sputtering systems developed in the 1950s have the advantage of more uniform target wear but they are unsuitable for reactive sputtering and cannot achieve high deposition rates due to target poisoning. As the whole target surface is exposed in the HiTUS system, reactive sputtering without poisoning of the targets is achieved.

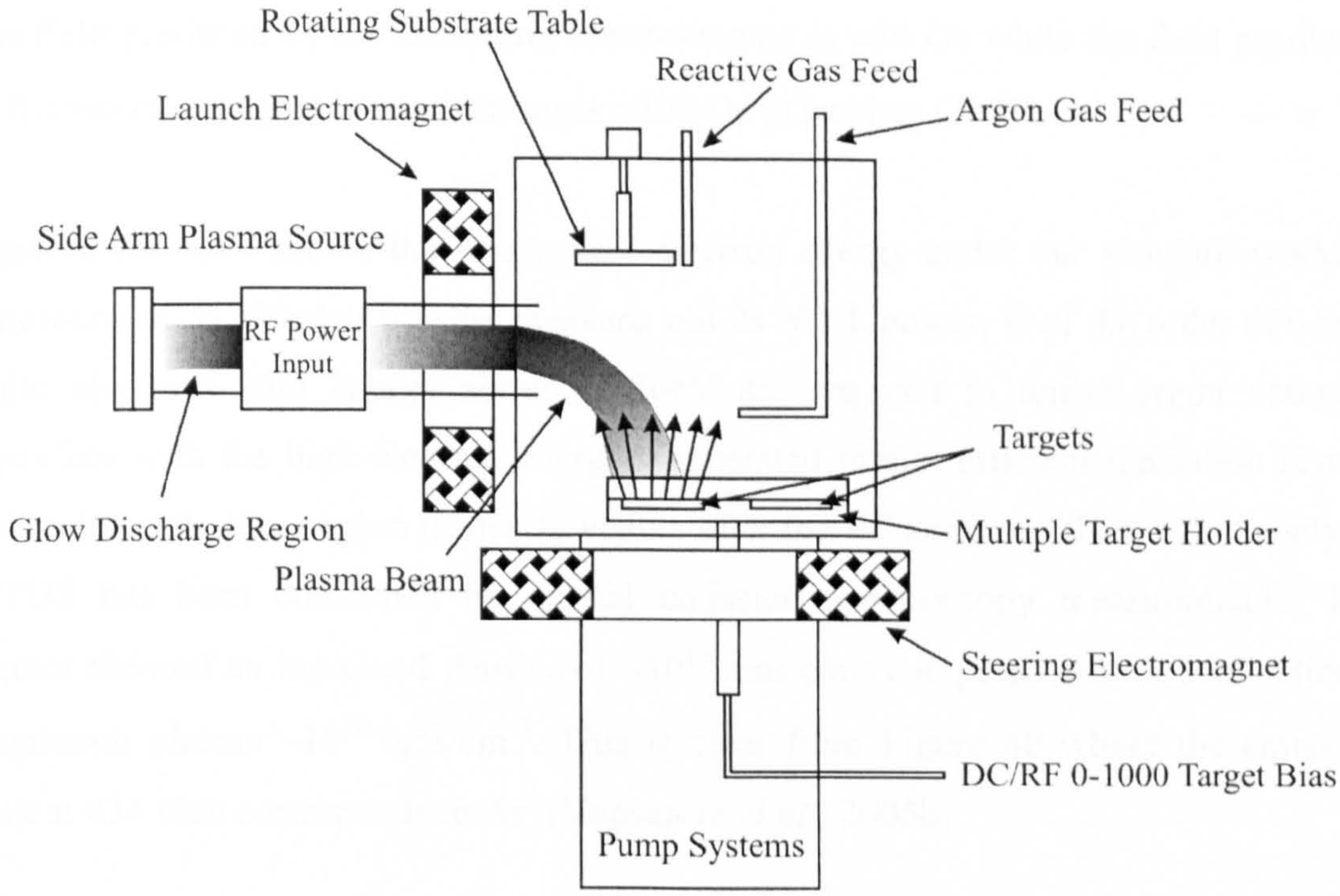

Figure 39. Schematic diagram of a HiTUS system.

Another important characteristic is the capability of HiTUS to control the grain size in sputtered samples by tuning the bias voltage, the sputter gas pressure and the RF power (Vopsaroiu *et al.*, 2004). The importance of grain size and grain size distribution control is well known in the magnetic industry were these two variables have a crucial effect on recording properties. In conventional sputtering systems the control of the grain size is dependent on the use of underlayers, additives or annealing leading to changes in the microstructure of the films. Using HiTUS, a wide control of the crystallite size is achievable without modifying the microstructure of the films.

5.3.2. HiTUS technology

The HiTUS technology is based on a remote high intensity RF plasma system consisting of a side arm as a plasma source linked to the main deposition chamber. The energy is transferred to the electrons in the plasma via the mechanism of Landau damping (Thwaites, 2002). Figure 39 shows a schematic diagram of the unit used in this work. The launching electromagnet accelerates the plasma into the chamber and a second magnet directs it onto the target. The fluxes of the respective magnetic fields are linked to produce a non-axial magnetic field overall relative to the long axis of the antenna.

The field produced by the launching electromagnet is ≈50 Oe while the field produced by the steering magnet is much stronger ≈500 Oe (Thwaites, 2002).

Experiments have shown that the typical electron energy under our standard working conditions of $3x10^{-3}$mbar process pressure and 2kW RF power, is of the order of 65eV, while electrons with energy above 15.76eV are required to ionise argon neutrals. Therefore with the high electron energies generated highly efficient ionisation results and an ion rich, blue region is clearly visible after the RF antennae. The high density in HiTUS has been confirmed by optical emission spectroscopy measurements. The spectra showed an increased density of $\sim10^{13}$ ions·cm^{-3} compared with a conventional magnetron plasma $\sim10^{10}$ ions·cm^{-3}. This is clear from Figure 40 where the emission peak at 434.8nm corresponds to Ar^+ (Vopsaroiu *et al.*, 2005b).

The coupled magnetic flux lines of the launch and steering electromagnet confine the plasma ions. By changing the current applied to the electromagnets and in particular to the steering magnet, the magnetic field strength is altered.

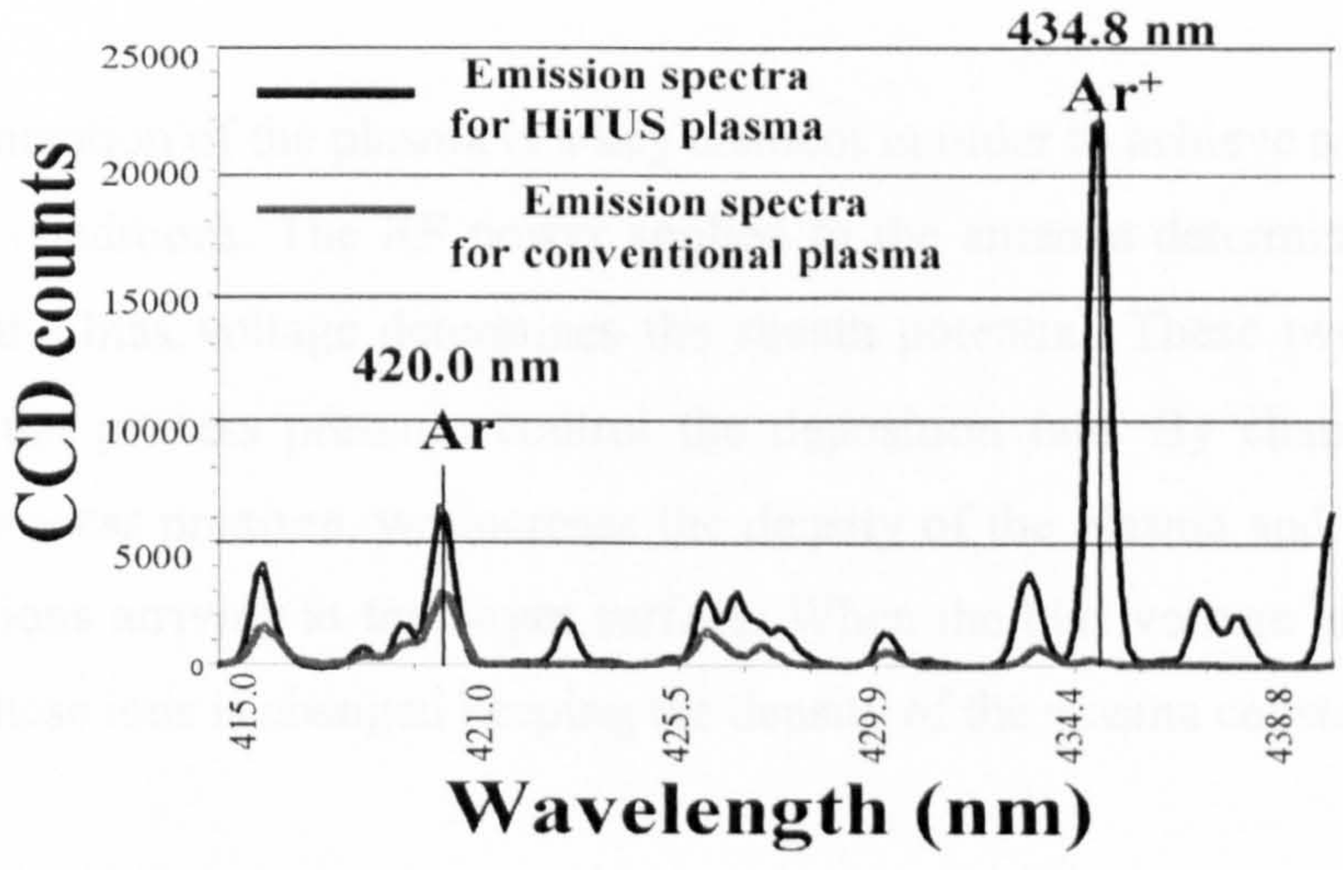

Figure 40. Optical emission of high density plasma and conventional plasma (Vopsaroiu *et al.*, 2005b).

A negative DC bias (-1 to –1000V) can be applied to the target. This bias voltage is not necessary to sustain a plasma glow discharge but without it no sputtering occurs. Above

~–100V the target current saturates and is independent of the voltage as shown in Figure 41. This is a key factor in order to achieve a wide range of sputtering rates whilst maintaining a high-density plasma.

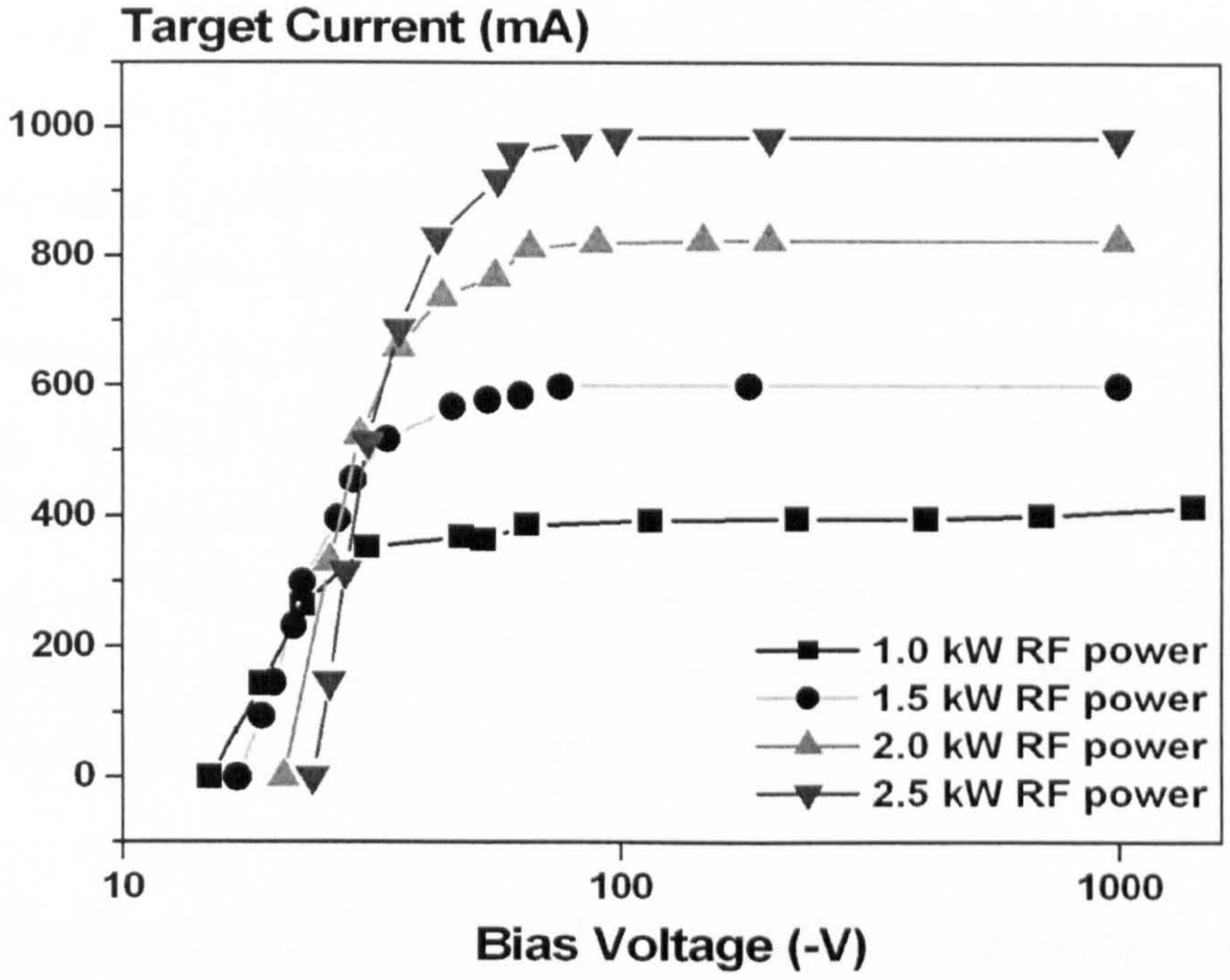

Figure 41. Target current versus bias voltage for different RF powers (Vopsaroiu *et al.*, 2005b).

The remote generation of the plasma is a key element in order to achieve a wide control of the process conditions. The RF power applied to the antenna determines the target current while the bias voltage determines the sheath potential. These two parameters together with the process pressure control the deposition rate. By changing the RF power or the process pressure, we increase the density of the plasma and therefore the number of Ar ions arriving at the target surface. When the bias voltage is the variable the energy of these ions is changed keeping the density of the plasma constant.

5.3.3. Grain size control using HiTUS

The capability of the HiTUS sputtering system to control the grain size of the sputtered films was first described by Vopsaroiu *et al.* (2004). Three sets of Cr thin films were grown changing the bias voltage, the RF power and the process pressure respectively.

The samples were deposited on Carbon coated TEM grids. TEM pictures were taken in bright field mode and over 500 particles were measured. A Zeiss particle size analyzer described in 5.4.5 was used to measure the grain diameters. The thickness of the samples was not determined accurately but it was typically around 50 nm. The mean grain size was determined by using standard statistical averaging. A clear variation of the grain size with the sputtering rate was achieved as shown in Figure 42. The mean grain size could be tuned between 10 and 20 nm. Although the physical mechanism behind the control of the grain size using HiTUS was not fully understood, it was concluded that a faster sputtering rate would generate a bigger mean grain diameter. They explained that the change in grain size for samples prepared using different sputtering conditions could be related to the crystal symmetry. A higher symmetry would mean a higher probability for two neighbouring grains to have closer lattice orientations and, therefore, a higher probability of fussing to form a bigger grain during the growth process. This interpretation was supported by X-ray data where samples with bigger grains showed better crystal orientation.

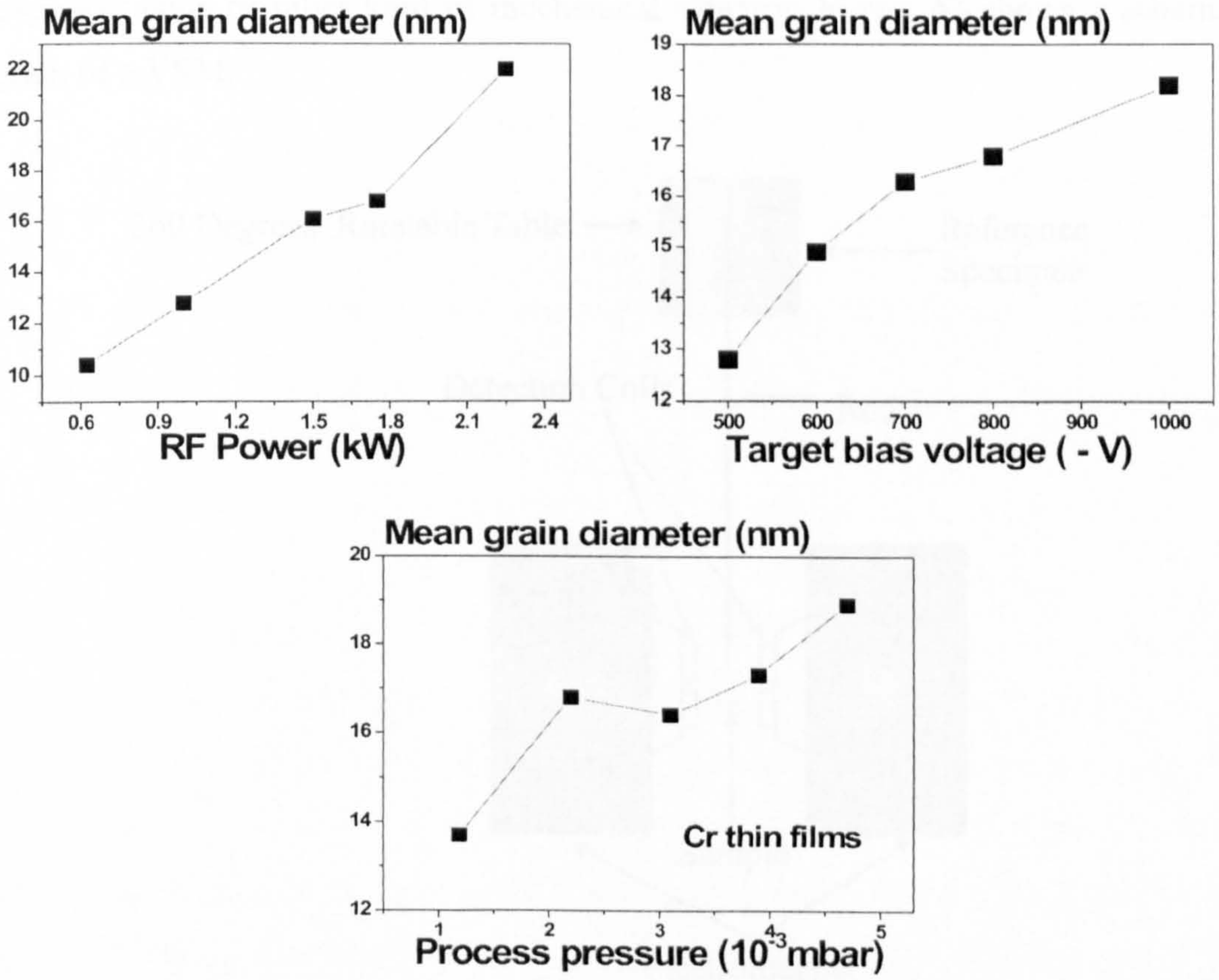

Figure 42. Mean grain diameter as a function of the bias voltage, RF power and process pressure (Vopsaroiu *et al.*, 2004).

Cr is of great importance in the magnetic recording industry where it is commonly used as an underlayer in thin film discs. The crystallographic texture and the grain size of the Cr buffer layer are responsible for the epitaxial growth of the magnetic layer (Park *et al.*, 2003). Therefore, a small and narrow Cr grain size distribution is required to achieve a high recording density in discs.

In this thesis, the control of the grain size distribution in sputtered films using HiTUS has been extended to other materials. This will be discussed in Chapter 6.

5.4. Measurement techniques

5.4.1. Vibrating Sample Magnetometer (VSM)

The first Vibrating Sample Magnetomer was described by Foner (1959). It is based on the variation of the flux in a coil due to the vibration of the sample. The vibration is achieved by placing the sample at the end of a rod that vibrates by the action of a loudspeaker cone or other kind of mechanical vibrator. Figure 43 shows a schematic diagram of a VSM.

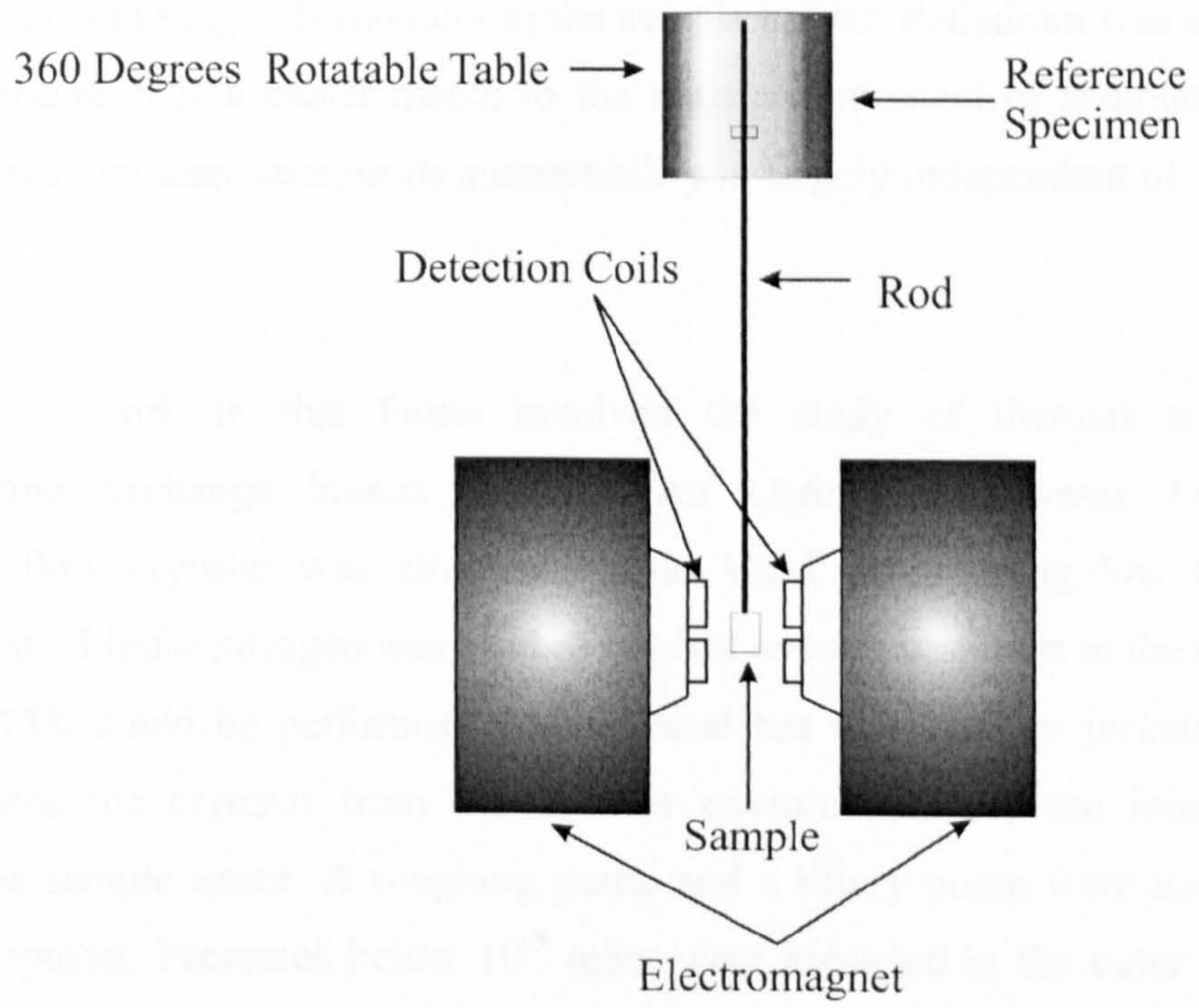

Figure 43. Schematic diagram of a Vibrating Sample Magnetometer (VSM).

The sample is located in a region of uniform DC magnetic field supplied by an electromagnet. The oscillating magnetic field of the sample induces an alternating voltage (EMF) in the detection coils that is measured using a lock-in amplifier. A small electromagnet located near the upper end of the rod works as a reference specimen. The signal that it induces generates an EMF in the detection coils. The induced voltage is proportional to the magnetic moment of the sample. This leads to a measurement independent of the vibration amplitude and frequency. Typical values for these two variables are 0.1-2.0 mm and 81 Hz respectively.

The unit used in this work was a modified EG&G Princeton Applied Research model 4500 VSM. It is controlled with LabView software designed by the Magnetic Materials Research Group at The University of York. Changes in the magnetisation down to $5x10^{-6}$ emu can be detected and fields up to 1 T (10 kOe) can be applied. The field resolution depends on the field range selected being better than 0.1% when the field range is set to 10 kOe.

A calibration is required to determine absolute values of the magnetisation. This was done when studying CoFe samples with controlled grain size and coercivity. This will be explained in detail in 6.2. The calibration is done by placing a reference sample with a known shape and magnetic moment in the sample holder. Palladium was usually used not only because it is a closer match to the magnetic moment of samples of similar shape and size, but also because its susceptibility is largely independent of temperature at 293 K.

Much of the work in this thesis involved the study of thermal activation in polycrystalline exchange biased systems. An *Oxford Instruments Ltd CF1200* continuous flow cryostat was attached to the VSM when doing low temperature measurements. Liquid nitrogen was used as coolant so measurements in the temperature range 77-373K could be performed. The cryostat has two vacuum jackets: the outer jacket isolates the cryostat from the exterior environment and the inner jacket is basically the sample space. A roughing pump and a rotary pump were used to pump down the cryostat. Pressures below 10^{-5} mbar were achieved in the outer jacket. The sample space was usually filled with either nitrogen or helium gas to avoid oxidation of the samples. Temperatures were stable to ±0.2 K/hour during measurement.

5.4.1.1. Measurement protocols

Much of the data in the literature related to exchange bias is not specific in terms of the exact conditions in which the measurements are made. This can lead to misinterpretation of the results as the state of order of the *AF* prior to measurement is unknown (Fernandez-Outon *et al.*, 2004). In 2004 Fernandez-Outon *et al.* described a measurement protocol that ensured reproducibility of the measurements. Following that measurement procedure the magnetic history of the sample is registered allowing simple and fast revision (Fernandez-Outon, 2006).

The first step to achieve reproducibility in the measurements is the reset of the *AF*. This is done by heating the sample to 373K for 90 minutes in the presence of a positive saturating field. This way, the *AF* is always in the same state or order prior to each measurement.

Once the *AF* has been reset it is necessary to establish a temperature T_{NA} at which the hysteresis loops could be measured without thermal activation taking place during measurement. This is done by resetting the *AF* and subsequently cooling down the sample to progressively lower temperatures where the *AF* is held at negative bias i.e. at point 4 of the hysteresis loop in Figure 20. This procedure is repeated until a temperature is found where holding the sample at negative bias for a fixed period of time e.g. 30 minutes, does not result in any change in the hysteresis loop. Above T_{NA} thermal activation produces changes in the *AF* that vary logarithmically with time.

Once T_{NA} is established by experiment the sample can be measured. For that purpose after the sample is reset the temperature is quenched to T_{NA} and the field is reversed so the *F* is saturated in the negative direction. The sample is then heated to an activation temperature T_{ACT} for 30 minutes. After this period the sample is cooled down to T_{NA} and the loop is measured. Note that the samples are always measured at the same temperature T_{NA} and the ascending branch of the loop is measured first. This measurement protocol ensures that thermal effects are reproducible.

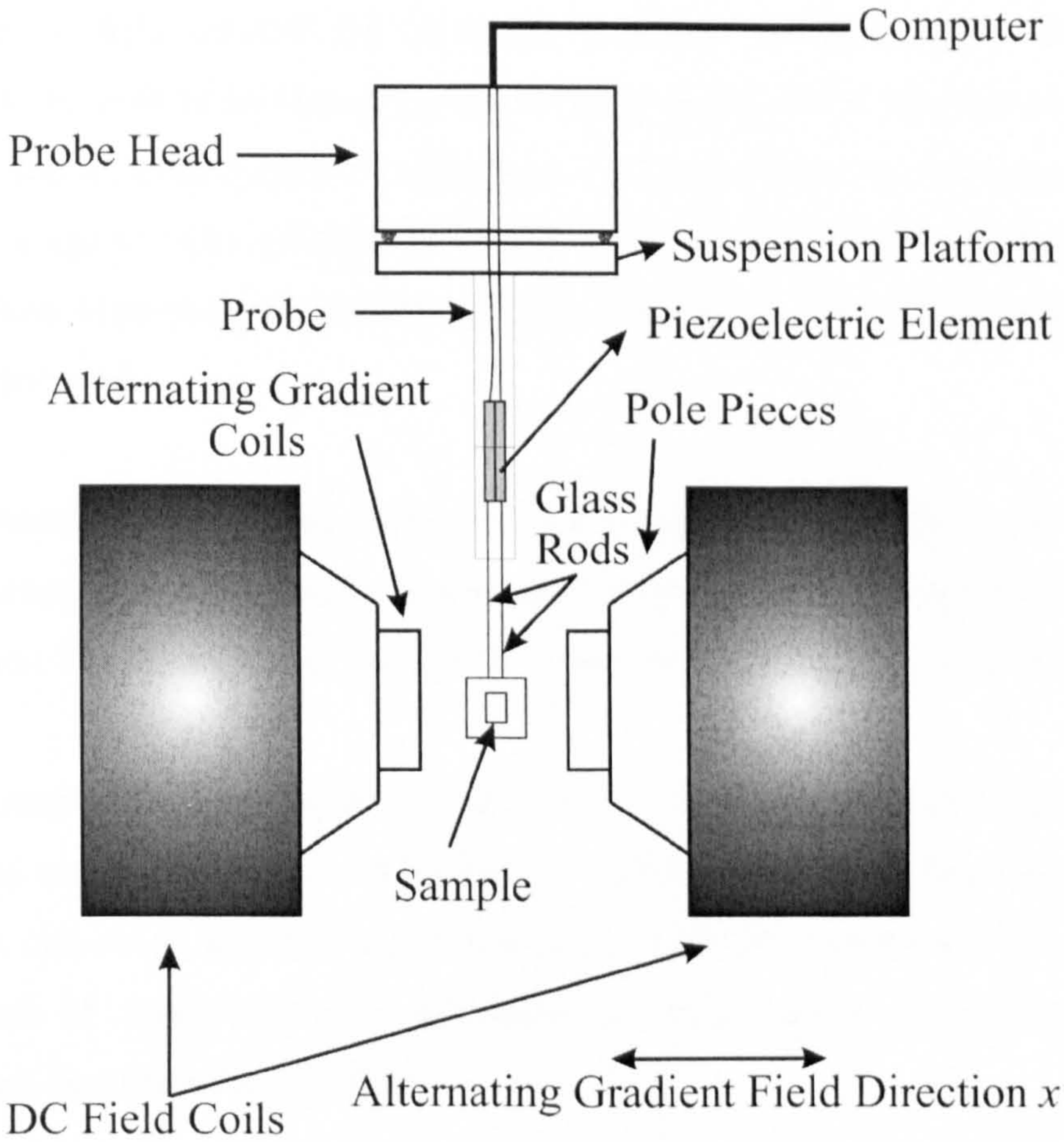

Figure 44. Schematic diagram of an Alternating Gradient Force Magnetometer (AGFM).

5.4.2. Alternating Gradient Force Magnetometer (AGFM)

The first Alternating Gradient Force Magnetometer (AGFM) was developed by Zijlstra (1970). Later improved by Flanders (1988) it has the advantage of being 1000 times more sensitive than the previously described VSM. The acquisition time is also much faster than that of the VSM. The specimen is mounted at the end of a cantilevered rod lying along the z axis as depicted in Figure 44 with a piezoelectric element attached. Using two glass rods instead of one is important when determining the resonance frequency of the cantilever as it produces a sharper resonance peak. This leads to an increase in the quality factor Q which is the key to the sensitivity. Operating near the mechanical resonance frequency of the cantilever, the output signal is greatly amplified.

The sample is magnetised by a dc field applied along the x direction. It is also subject to a small alternating field gradient along the x axis. The idea is that the alternating gradient exerts an alternating force on the sample, which is proportional to the

magnitude of the field gradient and the magnetic moment of the sample. The deflection of the cantilever rods is measured by the voltage output of the piezoelectric element. The AGFM can do measurements in the range 77-400 K. However, the operation of the temperature stage is quite tedious and hence, for low temperature measurements, the VSM was used. Moreover, the AGFM was only used for screening of samples due to its fast acquisition time.

The piezoelectric element is not sensitive to a changing magnetising field. Therefore, the noise coming from the piezo is independent of the value of the magnetising field and its sweep-rate. The sensitivity of the system is limited by mechanical and acoustic noise.

Prior to measurement the sample is located at the centre of symmetry of the gradient coils and the magnet. Using the commercially supplied control software the resonance frequency is calculated and the loop is measured. If we are interested in doing absolute measurements of magnetisation a calibration procedure has to be followed. This is similar to that described for the VSM.

5.4.3. Magneto Optical Kerr Effect Magnetometer (MOKE)

As its names states, this magnetometer is based on the change of polarisation of incident light after the beam is reflected by the sample. When the magnetisation vector is perpendicular to the reflection surface and parallel to the plane of incidence, the effect is called the *polar Kerr effect* (Figure 45a). Usually, normal incidence is used when doing experiments in polar geometry to simplify the analysis. However, when the magnetisation vector is parallel to both the reflection surface and the plane of incidence the effect is known as the *longitudinal Kerr effect* (Figure 45b). In this work, the measurements were done always in the longitudinal configuration.

The model used in the experiment described in section 6.4 was a NanoMOKE2^{TM}. One of the key features of this magnetometer is that it is very sensitive and stable. Signal changes as small as 10^{-3} % can be detected with a measurement time of a few minutes. In its optimum configuration magnetic moments as low as 10^{-12} emu can be detected. Another important feature is its focused beam which can be focused down to 3 μm. This allows small structures to be selected among an array on patterned nano-elements or to

obtain high sensitivity when measuring single isolated nanostructures. A CCD camera together with a built-in microscope allows the sample to be viewed on the computer monitor.

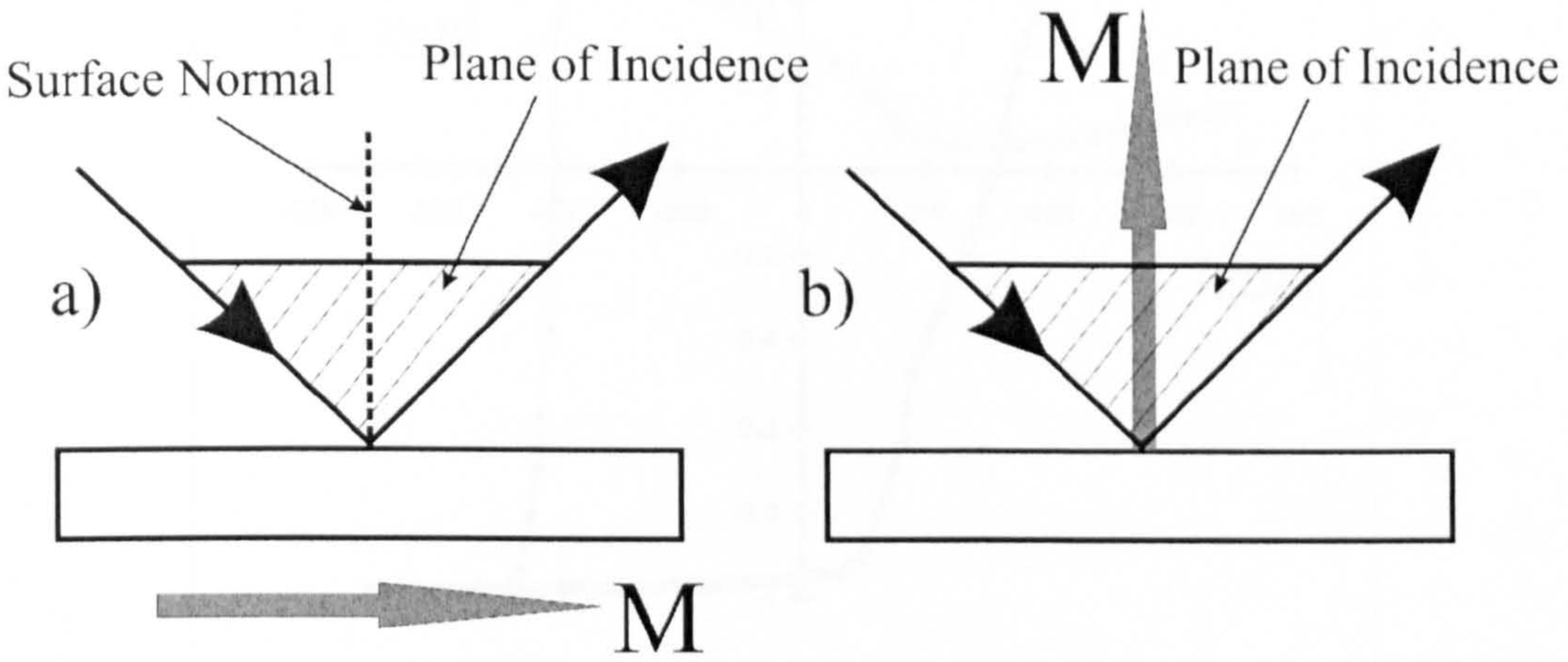

Figure 45. Schematic diagram of a) the polar Kerr effect and b) the longitudinal Kerr effect.

When using the standard quadrupolar magnet the sample is mounted on a X-Y-θ motion stage which is under computer control. Fields as high as 1kOe can be applied with this magnet although highest magneto-optical sensitivity is achieved in the field range ±300 Oe. The sample can travel a maximum of 25 mm along the X and Y directions with a repeatability of 1.0 μm. When doing angular measurements the stage can travel a maximum of 340° with a resolution of 0.001° and repeatability of 0.003°.

The measurements were done using a dipolar electromagnet that replaced the standard quadrupole. Magnetic fields as high as 5kOe can be applied with a minimum focused laser spot of 10 μm for loop sweep-rates of less than 0.2 Hz. A magnetic field as high as 3.5 kOe can be achieved at a sweep-rate of 1 Hz. The electromagnet can be degaussed using the control software with a remanence of less than 1 Oe. Temperature measurements in the range 290-673K were done using a home-made heating stage.

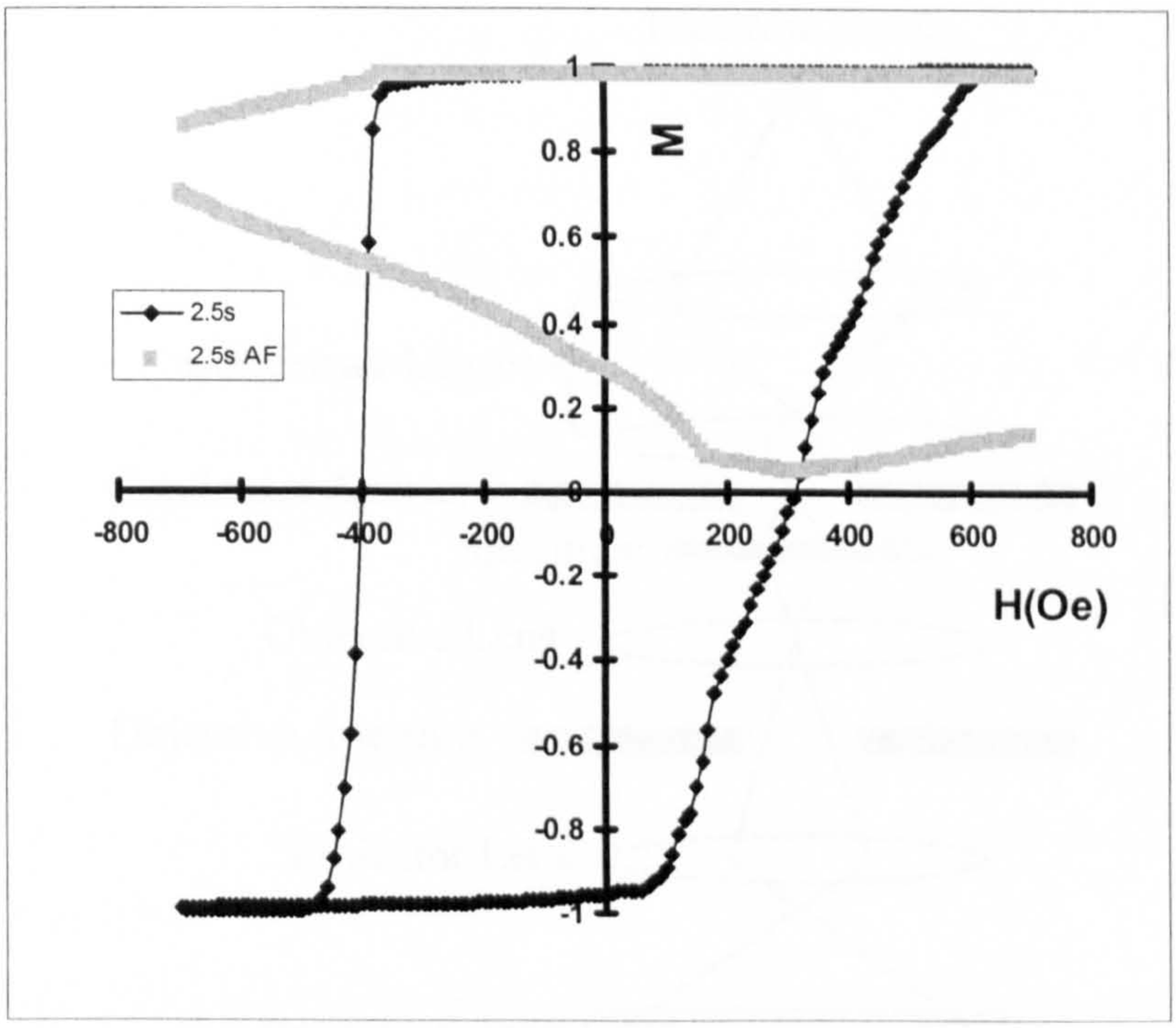

Figure 46. Typical exchange bias loop (black line) and simulated state of order of the antiferromagnet (grey line) (Chantrell, 2004).

In order to reduce the signal to noise ratio averaging over a certain number of loops typically 50 is necessary. This is a serious disadvantage when measuring exchange biased systems as above a certain temperature T_{ACT} EB is dominated by thermal activation and the state of order of the *AF* changes during measurement. The way of determining T_{ACT} has been described in section 5.4.1.1. Figure 46 shows a typical EB loop where the state of order of the *AF* has been simulated (R. W. Chantrell, Private Communication). The sample was held at negative saturation for 2.5 seconds before simulating the ascending branch of the loop. It can be seen that the *AF* changes during the field cycling and that the initial and final states are not the same. This emphasises the fact that in order to obtain reproducible data the *AF* has to be set prior to each measurement and that averaging over a large number of loops is only valid to a first approximation. For the simulation the following parameters were used: K_{AF}=3x10^6 erg/cc, K_F=1x10^6 erg/cc, M_s=1400 emu/cc, $\langle D_{AF}\rangle$=9nm, the exchange between *F* grains and between *F* and *AF* grains was assumed to be equal to 570 Oe.

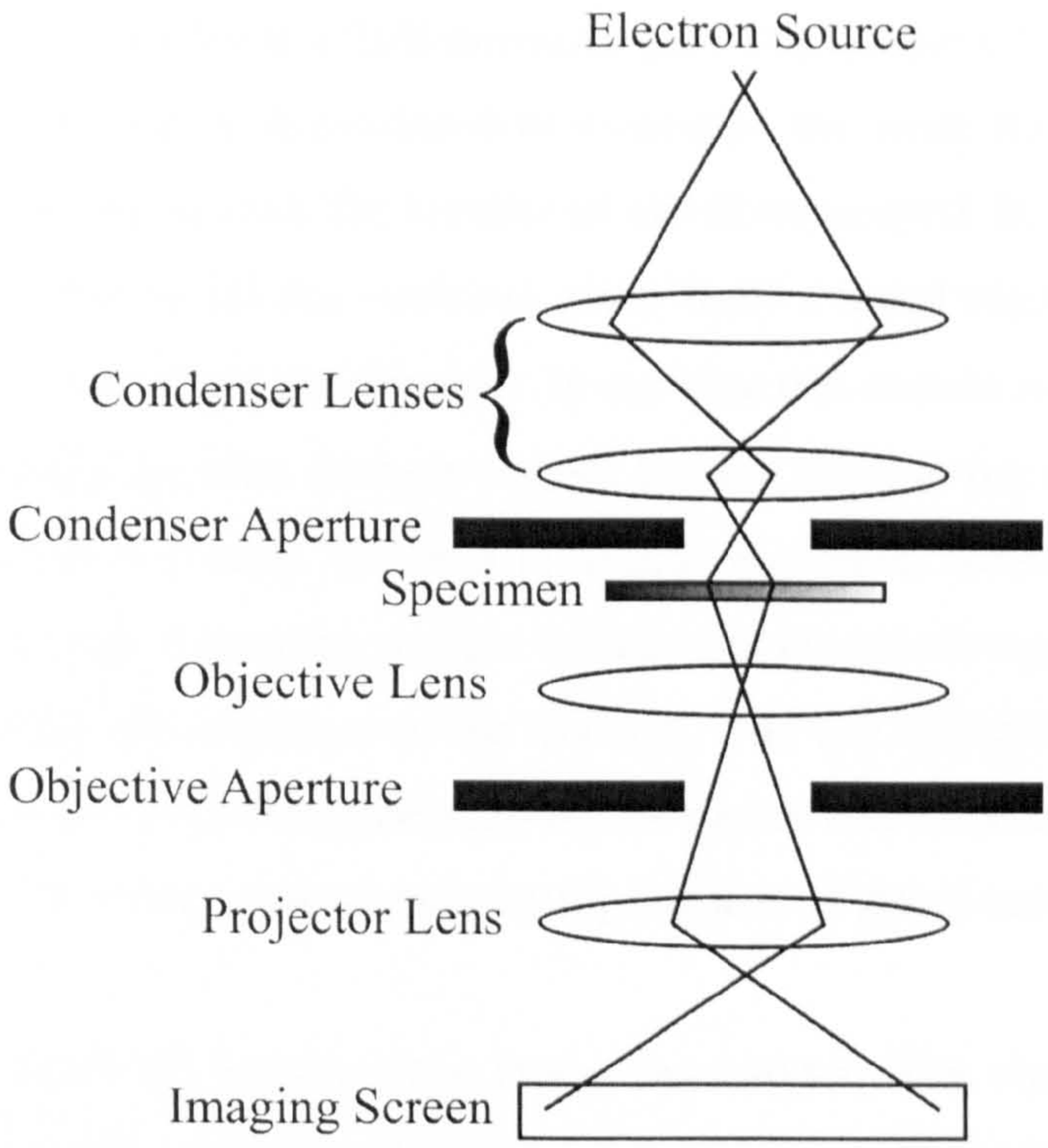

Figure 47. Schematic diagram of a transmission electron microscope.

5.4.4. Transmission Electron Microscope (TEM)

The resolution of an optical microscope is limited by the wavelength (λ) of light. In the case of green light in the middle of the visible spectrum λ is of the order of 550 nm. This limits the resolution of a good light microscope to about 300nm (Williams and Carter, 1996). The concept of an electron microscope was proposed by Knoll and Ruska (1932). The theoretical resolution of a transmission electron microscope (TEM) is below 0.1 nm. The new JEOL FS2200 Cs corrected TEM available in the York-JEOL nanocentre will have a resolution of 0.8 Å. The schematic diagram of a TEM is shown in Figure 47.

A TEM works basically in the same way as an optical microscope. At the top of the column there is a gun or electron emitter that generates the electron beam that travels down the column. This electrons pass through the sample and a series of electron lenses so the image is focused at the imaging screen. Apertures along the column are used to change the contrast and resolution of the image. The column is under vacuum to minimise the interactions between the beam and air molecules. Three parameters control the gun. These are the filament current, the grid bias and the accelerating voltage.

The electron source is a wire or a field emission gun. The former is heated by an electric current until enough energy is produced to overcome the work function of the metal (tungsten). This current controls the number of electrons emitted. In general we want to maximise this number so all the electrons come from a small region of the filament. This is achieved by saturating the filament. In our case this current was 94 μA. The grid bias not only controls the total electron current leaving the gun but also the area of the filament from which it comes. The bias is usually increased/decreased to change the brightness of the image. Normally, a slight variation in the bias is required as a variation in the bias can affect the saturation of the filament. The last variable is the accelerating voltage. The choice of this voltage depends on the nature and thickness of the specimen. Highly energetic electrons are more penetrating but lead to lower contrast.

When the beam heats the sample three things can happen. The electron might not hit any atom of the sample and it would continue travelling in a straight line until it reaches the screen. If however it interacts with the sample the atoms can be scattered either elastically or inelastically i.e. without or with transfer of energy. All the images acquired in this thesis were taken in bright field mode. This means that only the direct beam contributed to the pictures. Scattered atoms were avoided by placing an aperture in the back focal plane. In this type of imaging, mass-thickness contrast and diffraction contrast dominate to the image formation.

It is obvious that the interaction of electrons with heavy atoms will be stronger than with light atoms. This is what is called *mass contrast*. Therefore, if the thickness is homogenous, areas with heavier atoms will appear darker. Another kind of contrast is the *thickness contrast*. This type of contrast is due to the fact that thicker areas will scatter more electrons and therefore will appear darker. However, the same contrast can be obtained for a thick and a thin sample depending on the atomic weight of the atoms. Another important source of contrast is the *diffraction contrast*. If the samples studied are crystalline, like those in this thesis, many electrons are scattered by Bragg diffraction leading to darker areas in the image. Therefore, the presence of light areas is an indication of a poor texture. There are other types of contrast. All of them are variations of diffraction contrast. This can be due to the presence of defects or strains in the sample. However, these are not relevant to the work in this thesis.

5.4.5. Zeiss particle size analyser

A Zeiss particle size analyser has been used to measure the particles' diameter for the grain size studies. Over five hundred particles were measured for each sample. A circular spot of light of varying diameter is projected onto an image and after fully covering the surface of the grain the diameter is automatically registered. The front of the counter has a piece of Plexiglas with a sharp pin at the end of it. There are two knobs (one on each side of the machine) used to vary the size of the light spot. When this spot matches the size of our particle a pedal is depressed and a hole is punched in the photograph. The diameters are correlated to 48 counters, each covering a certain range of diameters. Another counter registers the total number of particles counted. Two size ranges are available via a magnifying lens.

The capability of the HiTUS sputtering system to control the grain size of the deposited films combined with the characterisation techniques described in this chapter have made possible a comprehensive study of the effect of the *AF* grain size on the exchange field in polycrystalline exchange bias samples containing a metallic *AF*.

Chapter 6 Results and Discussion

6.1. Grain size control in sputtered thin films

When the thickness of a sample is reduced towards the nanometre scale, its physical properties are dominated by the microstructure of the film. Two of the most important of these micro-structural properties are grain size and grain size distribution. Several continuous probability densities are commonly used to describe experimental grain growth and grain size distributions in thin films, i.e. Gaussian normal distribution, lognormal distribution, Rayleigh function, gamma function, etc... (Carpenter *et al.*, 1999). Experimental and theoretical studies of grain growth processes in granular systems have shown that the grain size distribution usually follows a lognormal function (Buhrman and Granqvist, 1976). Moreover, the lognormal distribution is the only one that allows only positive variable values while the other distributions permit the occurrence of negative variables, which cannot be the case for grain size/volume distributions. Another important characteristic is that if a number distribution is lognormal, then the area and volume distributions are also lognormal with the same standard deviation (Allen, 1975). This is a really important feature as magnetism is volume science. Hence, a lognormal function has been used to fit the experimental data.

This kind of distribution occurs whenever a random variable's natural logarithm is normally distributed and can therefore be written as:

$$f(D)dD = \frac{1}{\sqrt{2\cdot\pi}\cdot\sigma\cdot D}\cdot\exp\left[-\frac{(\ln(D)-\mu)^2}{2\cdot\sigma^2}\right]dD \qquad \text{Eq. 6.1}$$

where $\ln(D)$ is normally distributed with mean value μ and standard deviation σ. As any other probability density the following normalization condition is satisfied by Eq. 6.1:

$$\int_0^\infty f(D)dD = 1 \qquad \text{Eq. 6.2}$$

The mean value and standard deviation for this distribution are given by Eq. 6.3 and Eq. 6.4 respectively (O'Grady *et al.*, 1983)

$$< D >= e^{\mu+\frac{\sigma^2}{2}} \qquad \text{Eq. 6.3}$$

$$\sigma_D = e^{\mu+\frac{\sigma^2}{2}}\left[e^{\sigma^2} - 1\right]^{1/2} \qquad \text{Eq. 6.4}$$

The easiest way to fit the experimental data is to use directly a standard data analysing software. Alternatively, the standard deviation and mean value of ln(D) can be determined. If N is the total number of grains, the standard deviation of the normal distribution and the mean value are defined as

$$\sigma^2 = \frac{1}{N}\sum_{i=1}^{N}(\ln(D_i))^2 - \left(\frac{1}{N}\sum_{i=1}^{N}\langle\ln(D)\rangle\right)^2 \qquad \text{Eq. 6.5}$$

$$\mu = \frac{1}{N}\sum_{i=1}^{N}\ln(D_i) \qquad \text{Eq. 6.6}$$

The function in Eq. 6.1 can then be easily recomposed by using the calculated values for μ and σ. However, this simple technique is not convenient since a large number of particles need to be measured to obtain a reproducible grain size distribution (Carpenter *et al.*, 1998). Thousands of grains need to be measured implying an enormous amount of time and work, especially when TEM images are used for the particle sizing. Furthermore, the shape of the distribution can be changed just by modifying the number of bins in the histogram.

In this section an efficient way of avoiding these complications is presented by using the cumulative percentage method (CPM) (Allen, 1975). Reasonable lognormal grain size distributions are produced using this statistical method even for a small number of experimental points.

6.1.1. Cumulative Percentage Method (CPM)

A typical CPM frequency curve is shown in Figure 48. The cumulative percentage data is plotted vs. ln(D) and for a particular grain size D_i is obtained by calculating the following percentage undersize sum ($\sum_{n=1}^{i} P_n$), where P_n is the percentage of the total number of particles with a given diameter D_n.

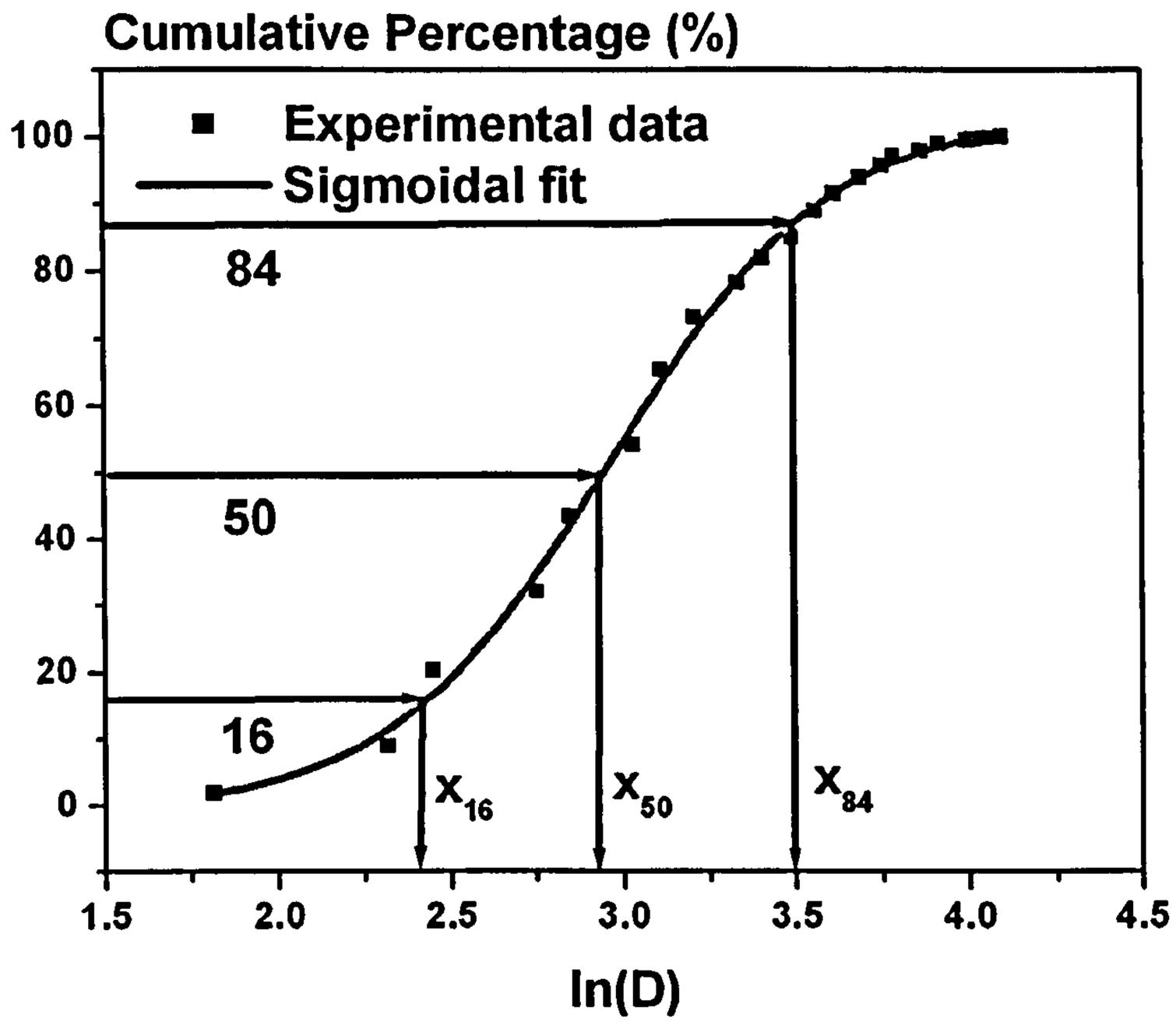

Figure 48. Example of cumulative percentage plot and sigmoidal fit used to calculate the mean and standard deviation of ln(D).

For a symmetrical distribution the mode, mean and median values all coincide. Since ln(D) is normally distributed its mean value μ can be obtained from Figure 48 as it corresponds to the 50% of the cumulative percentage undersize in the plot. The standard deviation σ can be calculated from the same graph and it is given by:

$$\sigma = \frac{x_{84} - x_{16}}{2} \qquad \text{Eq. 6.7}$$

where x_{84} is the 84% size on the cumulative percentage curve and x_{16} is the 16%. Once μ and σ have been calculated the experimental distribution can be fitted. Figure 49 shows an example of a fit to a lognormal function using the CPM. This technique has been used to compute and fit all the experimental particles size data in this thesis.

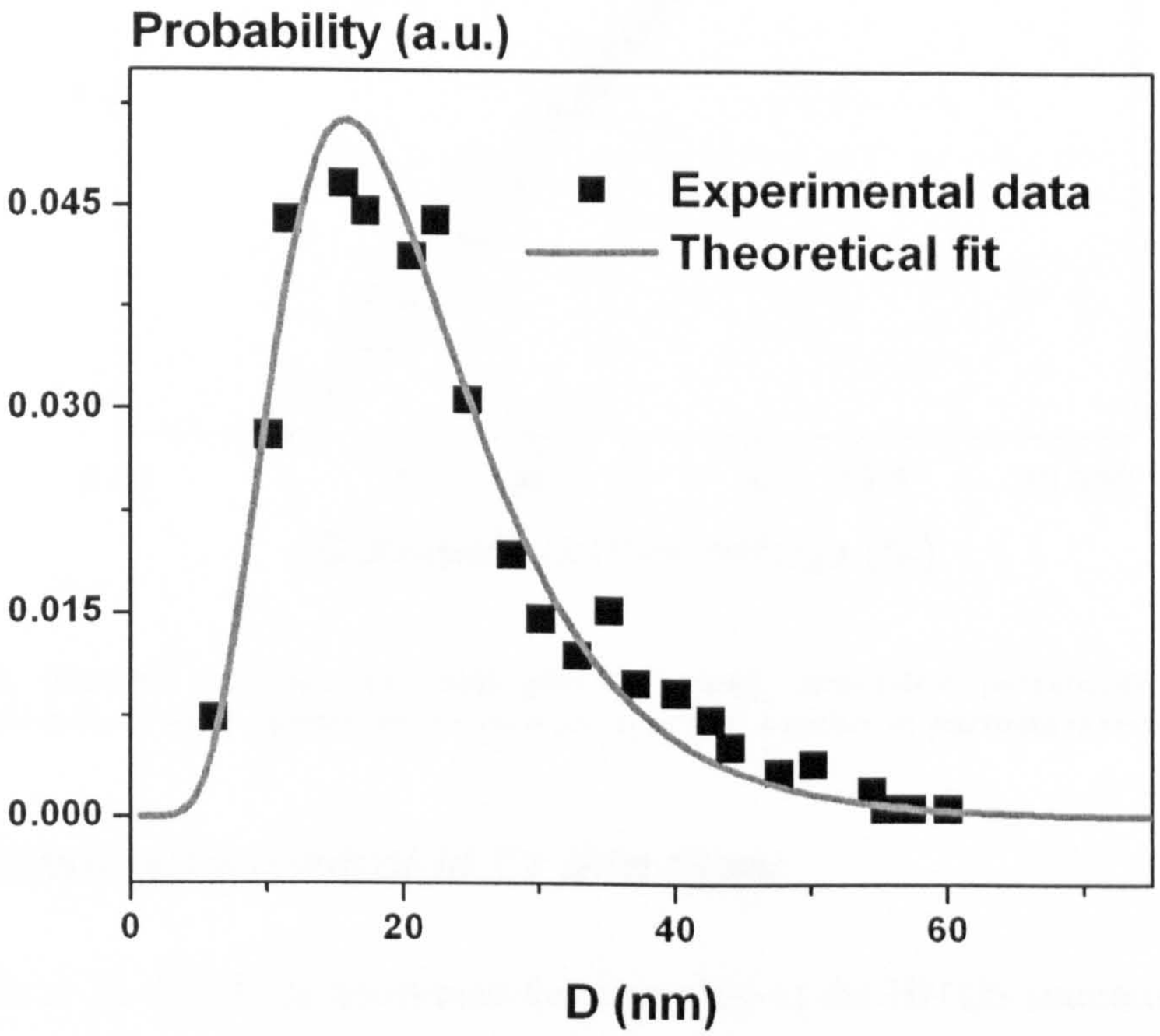

Figure 49. Typical lognormal fit obtained using the cumulative percentage method. 500 particles were measured to generate this fit.

The main advantage of using this method is that it gives good statistics even for a small number of particles (Allen, 1975). The accuracy of the cumulative percentage method is demonstrated in Figure 50, where grain size data is plotted in logarithmic scale as a function of the cumulative percentage frequency for several grain size populations corresponding to a NiFe sample grown using HiTUS. It is clear that for 250 particles counted this technique gives similar results to those corresponding to hundreds of particles. However, over 500 particles were counted to recompose each lognormal function to ensure good statistics.

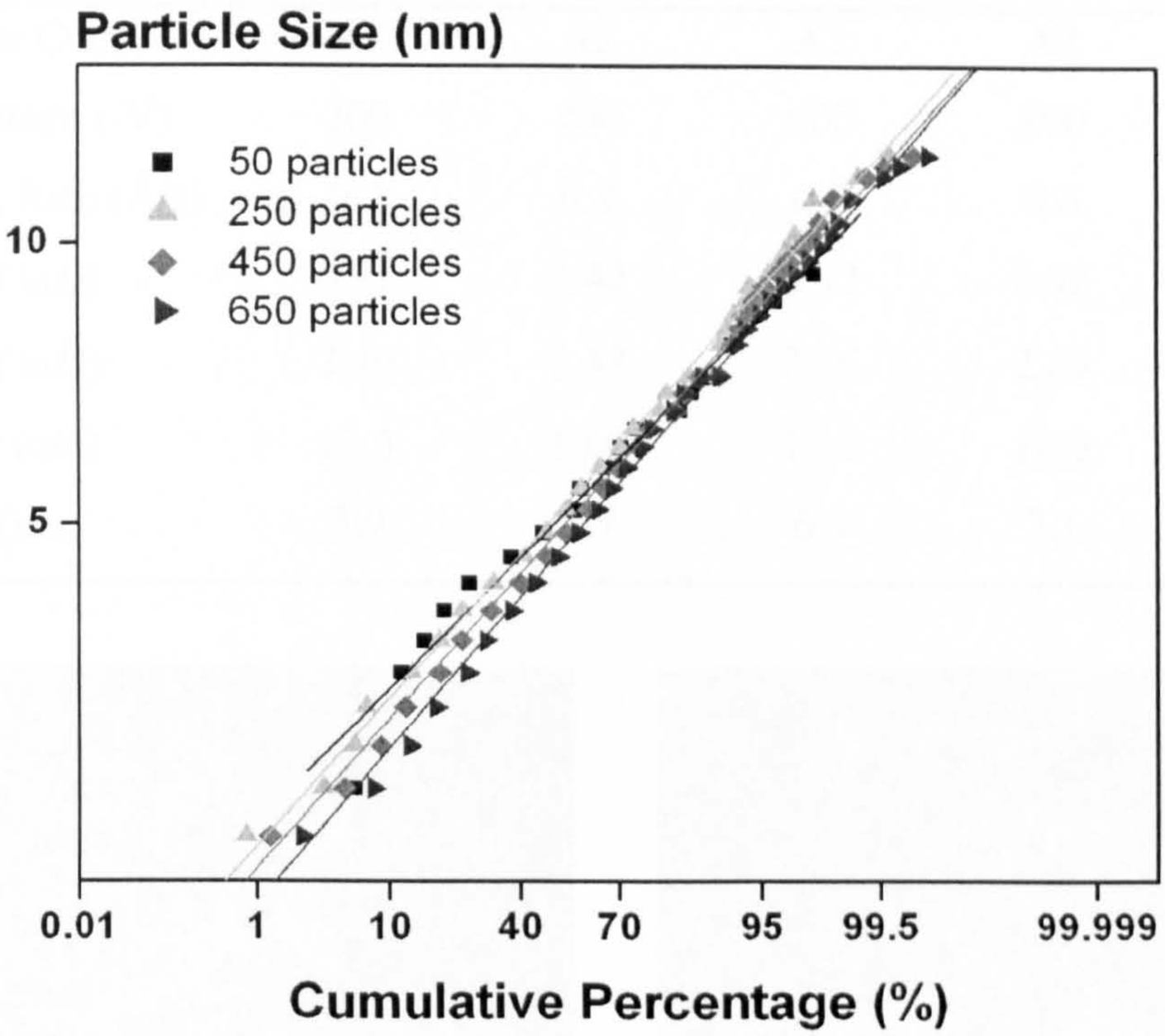

Figure 50. Example of grain size data plotted against cumulative percentage frequency in logarithmic scale. A good agreement between low and high number of particles is shown.

6.1.2. Grain size control in Cr thin films

Vopsaroiu *et al.* (2004) demonstrated the capability of the HiTUS sputtering system to control the grain size in Cr films. However, no information about the width of the distribution or lognormal fits was presented. In this work, both the grain size and grain size distribution have been studied for several materials including Cr. Cr and Cr alloys are widely used in the magnetic recording industry as underlayers for CoCrPt (e.g Oh and Lee, 2001) or CoCrTa (e.g. Jia *et al.*, 2001) where a small and narrow grain size distribution is required to obtain a high recording density. A set of five Cr samples were sputtered on Carbon coated TEM grids. The bias voltage was changed between –200 and –1000 V. All the films were prepared under the same conditions after pumping down to a pressure of about 5.0×10^{-7} mbar. The process pressure was 2.7×10^{-3} mbar and the RF power was fixed at 1.5 kW. The preparation conditions and sample specifications are summarised in Table 2. Figure 51 shows examples of TEM images and histograms for the samples with the smallest (A1) and the biggest (A4) grains. The data was fitted using the cumulative percentage method described in 6.1.1.

Table 2. Grain size results for Cr. The errors in *D* are estimated to be ±3%.

Sample Code	A1	A2	A3	A4	A5
Bias Voltage (-V)	200	400	600	800	1000
Sputtering Rate (Å/s)	0.2	0.3	0.5	0.6	0.7
σ (of ln$D$)	0.31	0.42	0.42	0.42	0.42
μ (of ln$D$)	2.46	2.48	2.66	2.69	2.83
$<D>$ (nm)	12.3	13.0	15.7	16.2	18.5
σ_D (nm)	3.9	5.7	6.9	7.1	8.2

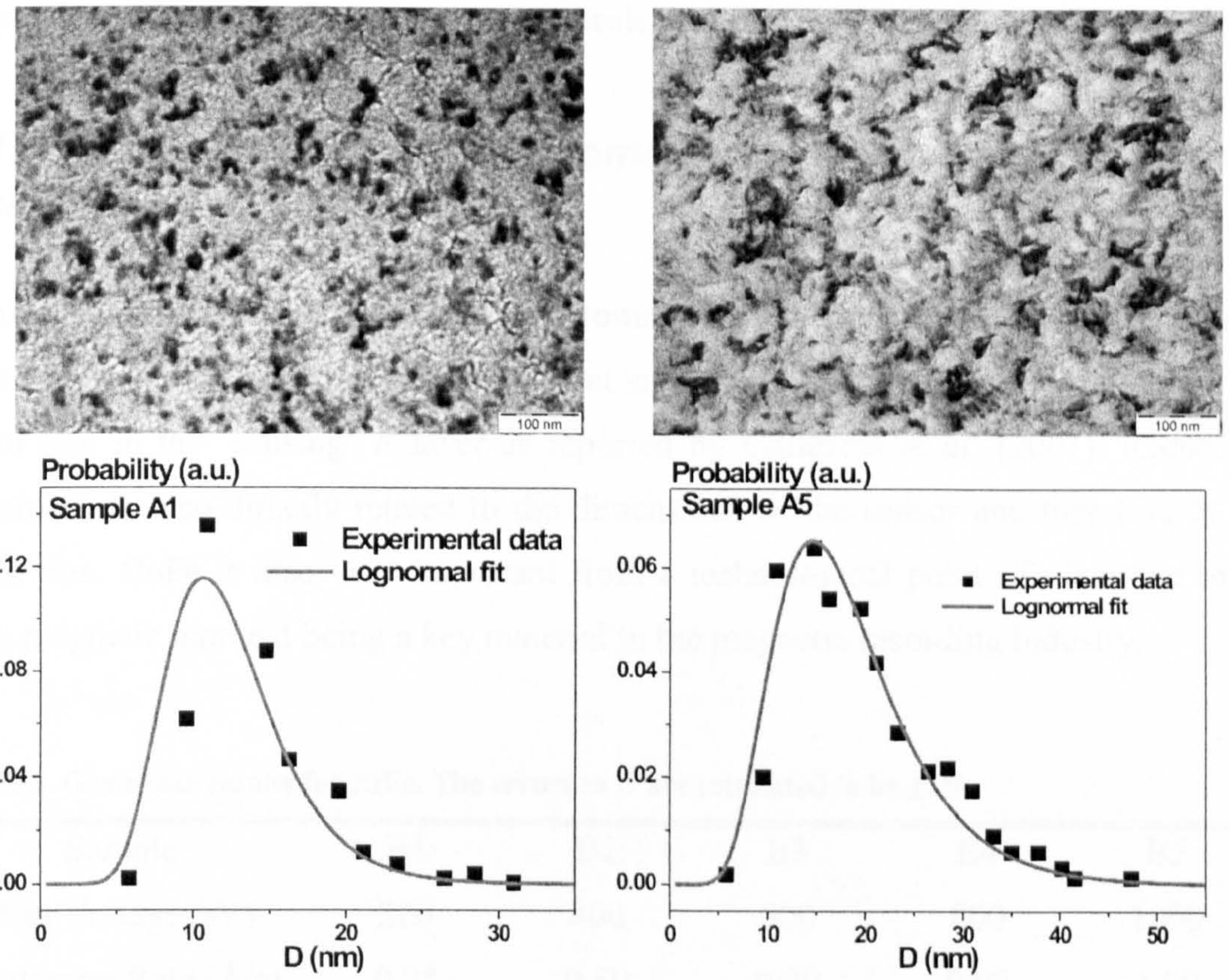

Figure 51. Grain Size distribution and TEM image for samples A1 (left) and A5 (right) respectively.

Only the black contrast in the TEM images was considered as a grain when measuring the grain size. To check the validity of this assumption, the grain size from dark field imaging was compared to that measured from bright field images. This was the basis of an MPhys project in the lab and the results suggested that the grain size was well determined from bight field images. It is clear from Table 2 that the mean grain size increases with increasing sputtering rate. The values obtained for $<D_{Cr}>$ using HiTUS are comparable to those obtained using conventional magnetron sputtering. For

example, an average grain size of about 13nm was reported when using dc magnetron sputtering at –200V and a substrate temperature of about 100°C (Park *et al.*, 2003).

Not only the mean grain size has been observed to increase with the sputtering rate but also its standard deviation. This is very important in the magnetic recording industry as a narrow distribution of grain sizes is required to achieve a high recording density (O'Grady *et al.*, 1998). If the grains are too big the anisotropy energy is big and the grains can hardly be switched. If however the grains are too small, they can switch due to thermal activation leading to loss of data. In particular, the grain size in the Cr layer plays a key role in thin film discs as it controls the grain size in the magnetic layer.

6.1.3. Grain size control in ferromagnetic materials: NiFe and CoFe

Similar results have been obtained for ferromagnetic materials such as NiFe and CoFe. One way to obtain an increase in the output signal from a read sensor is to increase the grain size in the 'sensing' *F* layer as reported by Childress *et al.* (2001). Recording densities are also directly related to the dimensions of the sensor and therefore to the grain size. CoFe is also very important from a technological point of view due to its high magnetic moment being a key material in the magnetic recording industry.

Table 3. Grain size results for NiFe. The errors in *D* are estimated to be ±3%.

Sample	B1	B2	B3	B4	B5
Bias Voltage (-V)	200	400	600	800	1000
Sputtering Rate (Å/s)	0.25	0.50	0.70	0.90	1.00
σ (of ln$D$)	0.36	0.38	0.33	0.32	0.35
μ (of ln$D$)	1.17	1.38	1.55	1.61	1.67
$\langle D \rangle$	3.5	4.3	5.0	5.3	5.7
σ_D (nm)	1.3	1.7	1.7	1.8	2.0

A set of five $Ni_{81}Fe_{19}$ samples 20nm thick were sputtered on Carbon coated TEM grids. The bias voltage was varied between –200 and –1000V between the deposition of each sample. The RF power was 1.5kW and the process pressure was kept constant at 2.7x10^{-}

^{3}mbar. All five samples were sputtered after pumping down to a base pressure of $5x10^{-7}$ mbar. A summary of the preparation conditions is presented in Table 3. Figure 52 shows a typical TEM for a sample grown using –600V bias voltage.

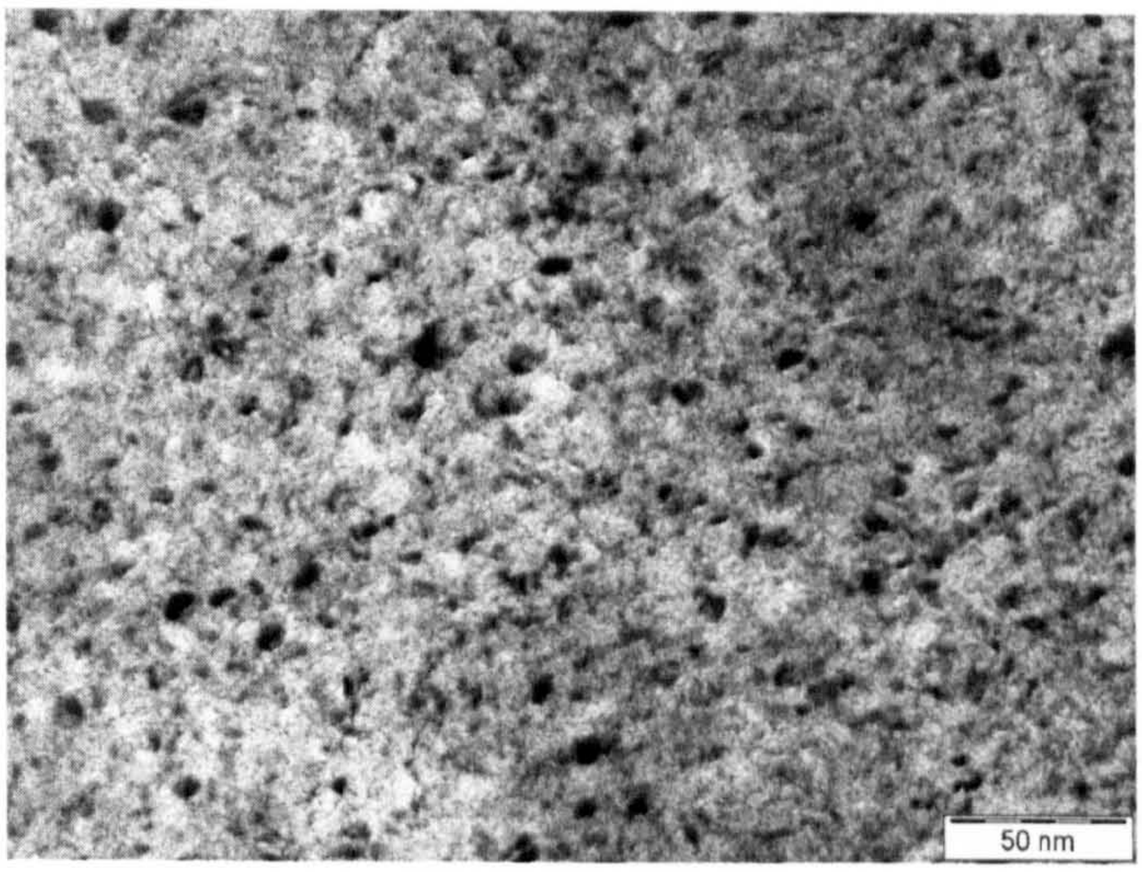

Figure 52. Typical TEM image for NiFe. The image is for a sample grown using -600V bias voltage.

Figure 53 shows typical grain size distribution for samples B1 and B5 respectively. The mean diameter and its standard deviation were determined using the cumulative percentage method.

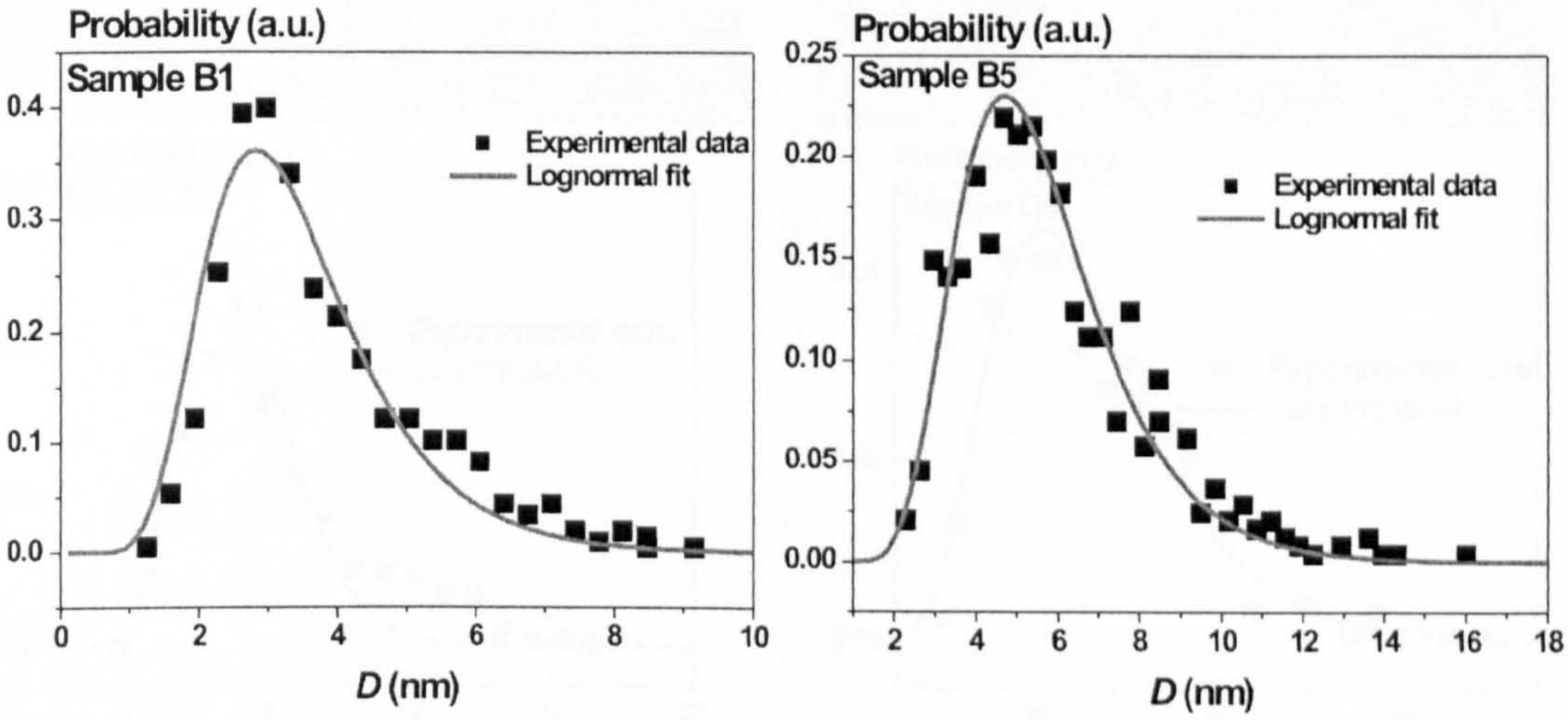

Figure 53. Grain size distributions for samples B1 and B5 respectively.

The same procedure was repeated for a set of 6 CoFe samples each of which was again 20 nm thick. As before, the bias voltage was the variable chosen to control the grain size of the deposited layers. The RF power was fixed at 1.5kW and the process pressure

was kept constant at 2.7×10^{-3}mbar. Before the deposition of each sample the system was pumped to 5.0×10^{-7}mbar. The preparation conditions and the results from the grain size analysis are summarised in Table 4.

Table 4. Grain size results for CoFe. The errors in *D* are estimated to be ±3%.

Sample	C1	C2	C3	C4	C5	C6
Bias Voltage (-V)	120	200	400	600	800	1000
Sputtering Rate (Å/s)	0.10	0.20	0.40	0.55	0.70	0.80
σ	0.22	0.32	0.44	0.38	0.39	0.39
μ (of ln$D$)	1.95	2.59	2.90	2.98	3.10	3.19
$\langle D \rangle$ (nm)	7.2	14.1	20.0	21.2	24.1	26.4
σ_D (nm)	1.6	4.7	9.2	8.3	9.9	10.8

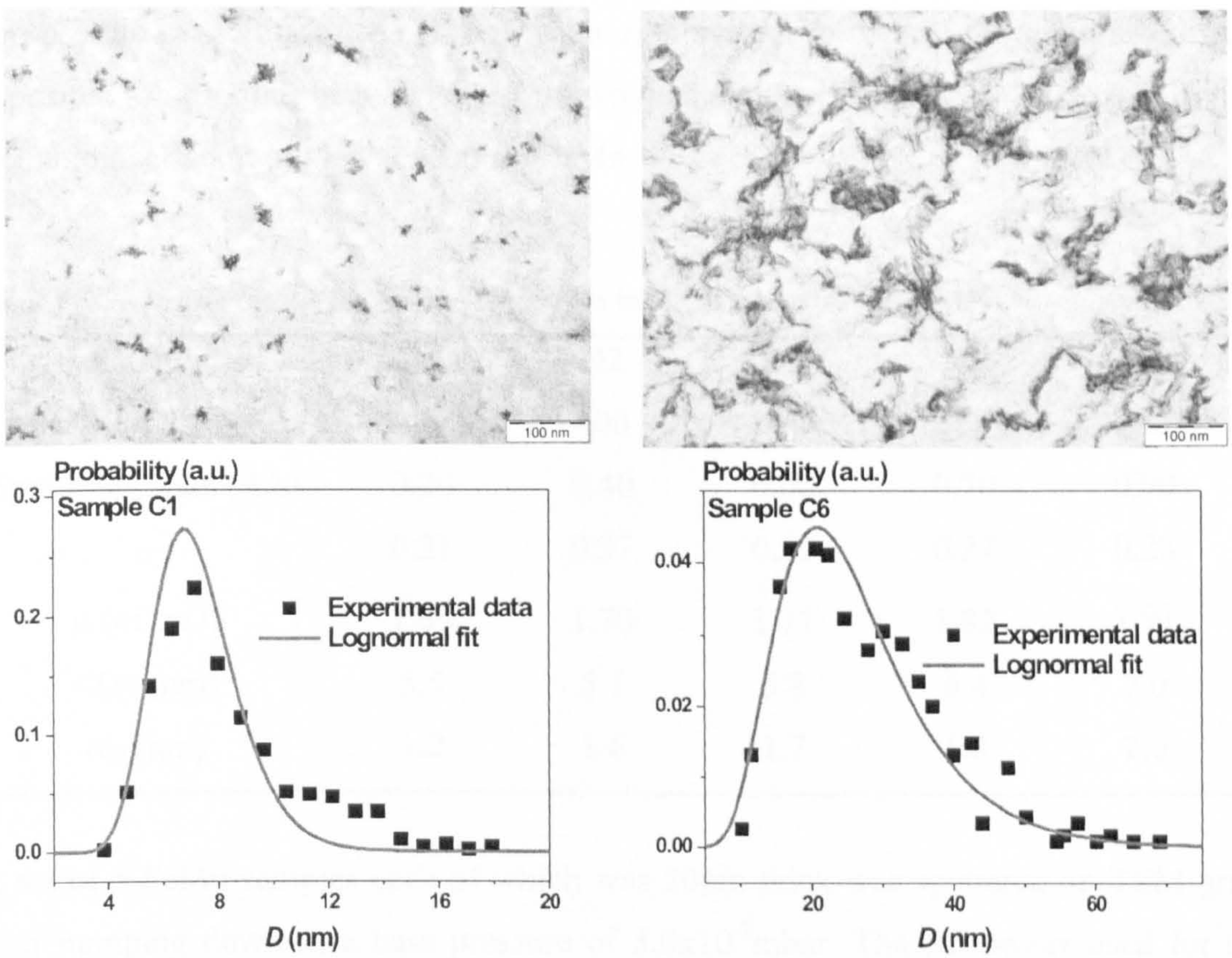

Figure 54. TEM images and grain size distributions for the CoFe samples with the smallest (left) and biggest (right) grains.

Figure 54 shows TEM images and grain size distributions for the samples with the smallest and biggest grains respectively. All the distributions were lognormal. The fact that the grain size can be controlled only through the deposition conditions is really important as the magnetic properties of materials such as CoFe are strongly dependent on the crystallite size (Jung *et al.*, 2003). This will be studied in section 6.2 for $Co_{60}Fe_{40}$ samples prepared using the same conditions as those used for the TEM grids. As for Cr and NiFe not only the mean diameter increases with increasing sputtering rate but also the standard deviation of the distribution increases.

6.1.4. Grain size control in antiferromagnetic materials: FeMn and IrMn

The main objective of this work is to characterise the effect of the grain size of the *AF* layer in polycrystalline exchange biased samples with a metallic *AF* layer. For that purpose the capability of the HiTUS sputtering system to control the grain size of the deposited samples has been extended to two of the most important *AF* materials from a technological point of view: FeMn and IrMn.

Table 5. Grain size results for FeMn. The errors in *D* are estimated to be ±3%.

Sample	D1	D2	D3	D4	D5
Bias Voltage (-V)	200	400	600	800	1000
Sputtering Rate (Å/s)	0.20	0.40	0.60	0.70	0.90
σ	0.21	0.27	0.29	0.27	0.28
μ (of ln$D$)	1.69	1.70	1.71	1.82	1.91
$\langle D \rangle$ (nm)	5.5	5.7	5.8	6.4	7.0
σ_D (nm)	1.2	1.6	1.7	1.8	2.0

A set of 5 FeMn samples each of which was 20nm thick was sputtered on TEM grids after pumping down to a base pressure of 5.0×10^{-7}mbar. The RF power used for the deposition of the samples was 1.5kW while the process pressure was set to 2.7×10^{-3}mbar. The bias voltage was varied between -200 and -1000V in order to change the grain size of the deposited layers. The properties of each sample are summarised in Table 5. As for the other materials all the samples were sputtered in the same run

without breaking the vacuum. Prior to each sputtering process both the substrate and the target were plasma cleaned to eliminate contamination or oxide layers. Again over 500 particles were measured to recompose each lognormal function. Figure 55 shows a TEM image and the grain size distribution for the sample grown using –600V bias voltage.

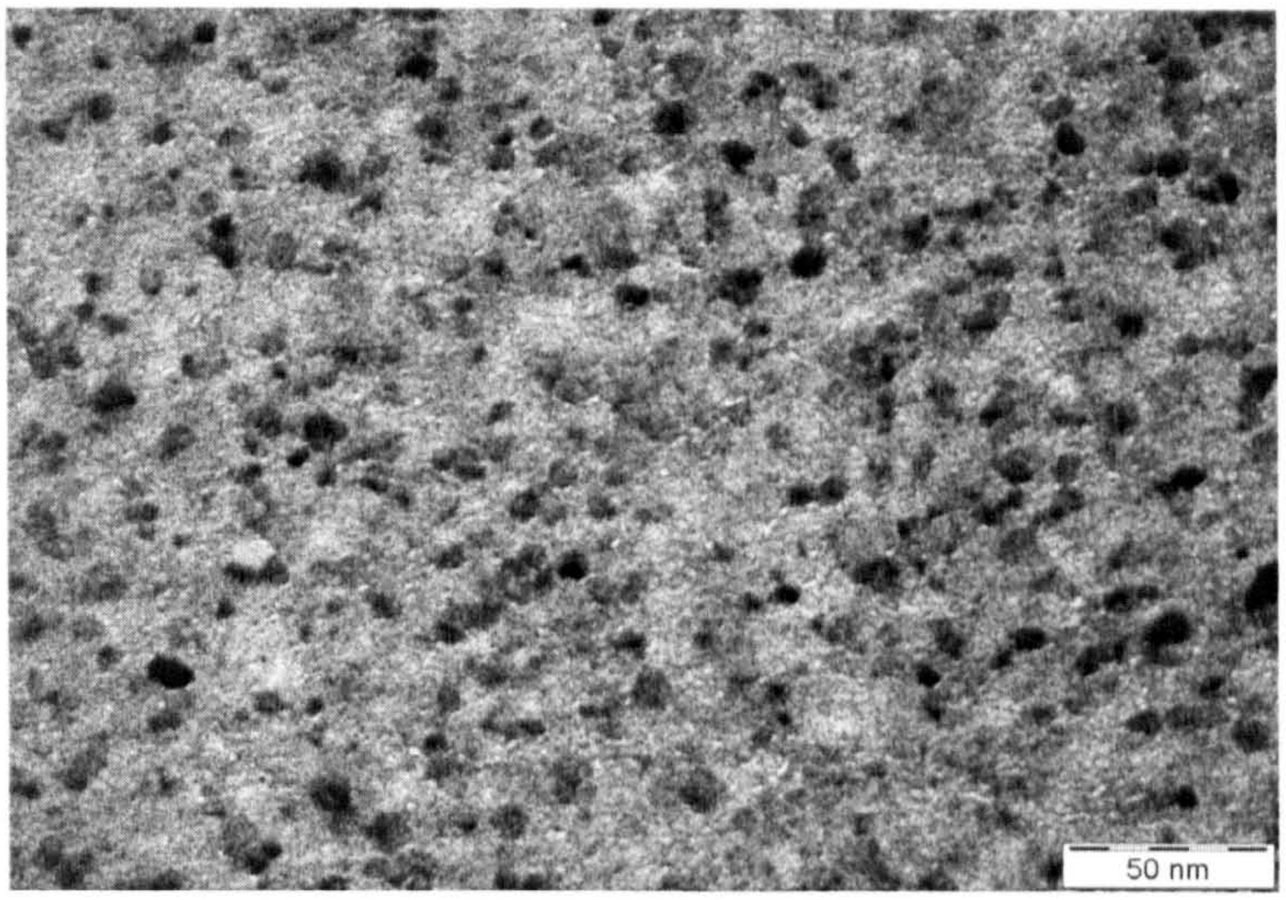

Figure 55. TEM image and lognormal fit for the FeMn sample grown at -600V bias voltage.

Finally the same procedure has been repeated for five IrMn samples. All the samples were 20nm thick. As before, the bias voltage was varied between –200 and –1000V keeping all the other variables constant i.e. RF power and process pressure. Table 6 shows the parameters obtained from the grain size distribution for each sample. Over

500 particles were measured to ensure good statistics. The RF power used during the deposition of the layers was 1.5kW. All the samples were grown after pumping down to $5.0x10^{-7}$mbar and the process pressure was set to $2.7x10^{-3}$mbar. Both the mean grain size and the standard deviation of the distributions increase with increasing sputtering rate/bias voltage.

Table 6. Grain size results for IrMn. The errors in *D* are estimated to be ±3%.

Sample	E1	E2	E3	E4	E5
Bias Voltage (-V)	200	400	600	800	1000
Sputtering Rate (Å/s)	0.20	0.30	0.40	0.50	0.60
σ (of ln$D$)	0.29	0.27	0.32	0.33	0.41
μ (of ln$D$)	1.40	1.75	1.92	2.02	2.20
$\langle D \rangle$ (nm)	4.2	5.9	7.2	8.0	9.8
σ_D (nm)	1.2	1.6	2.4	2.7	4.2

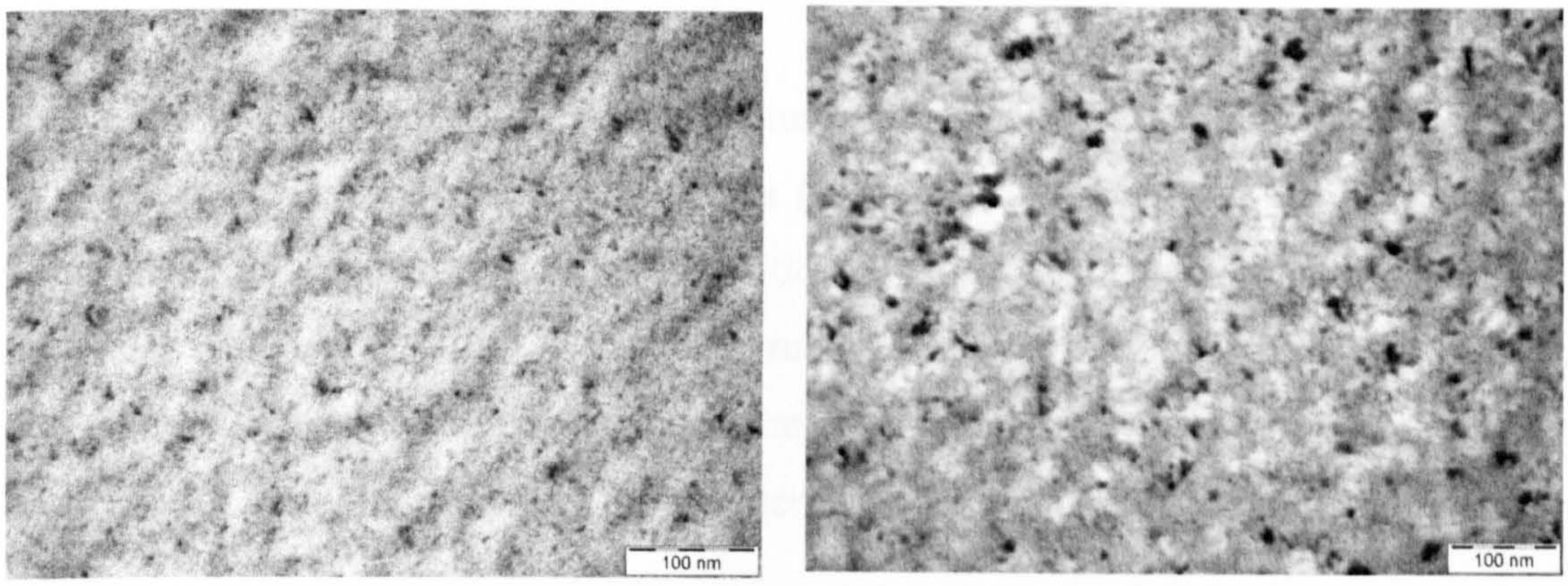

Figure 56. TEM images for the IrMn samples with the smallest (left) and biggest (right) grains.

Figure 56 shows two TEM images corresponding to the samples with the smallest and biggest IrMn grains respectively. The difference in the grain size is evident from the images. Note that the change in grain size achieved for IrMn is much bigger than that for FeMn. Figure 57 shows grain size distributions for the samples grown using –200, -600 and –1000V bias voltage. The increase in the mean grain size and the standard deviation is clear from this plot.

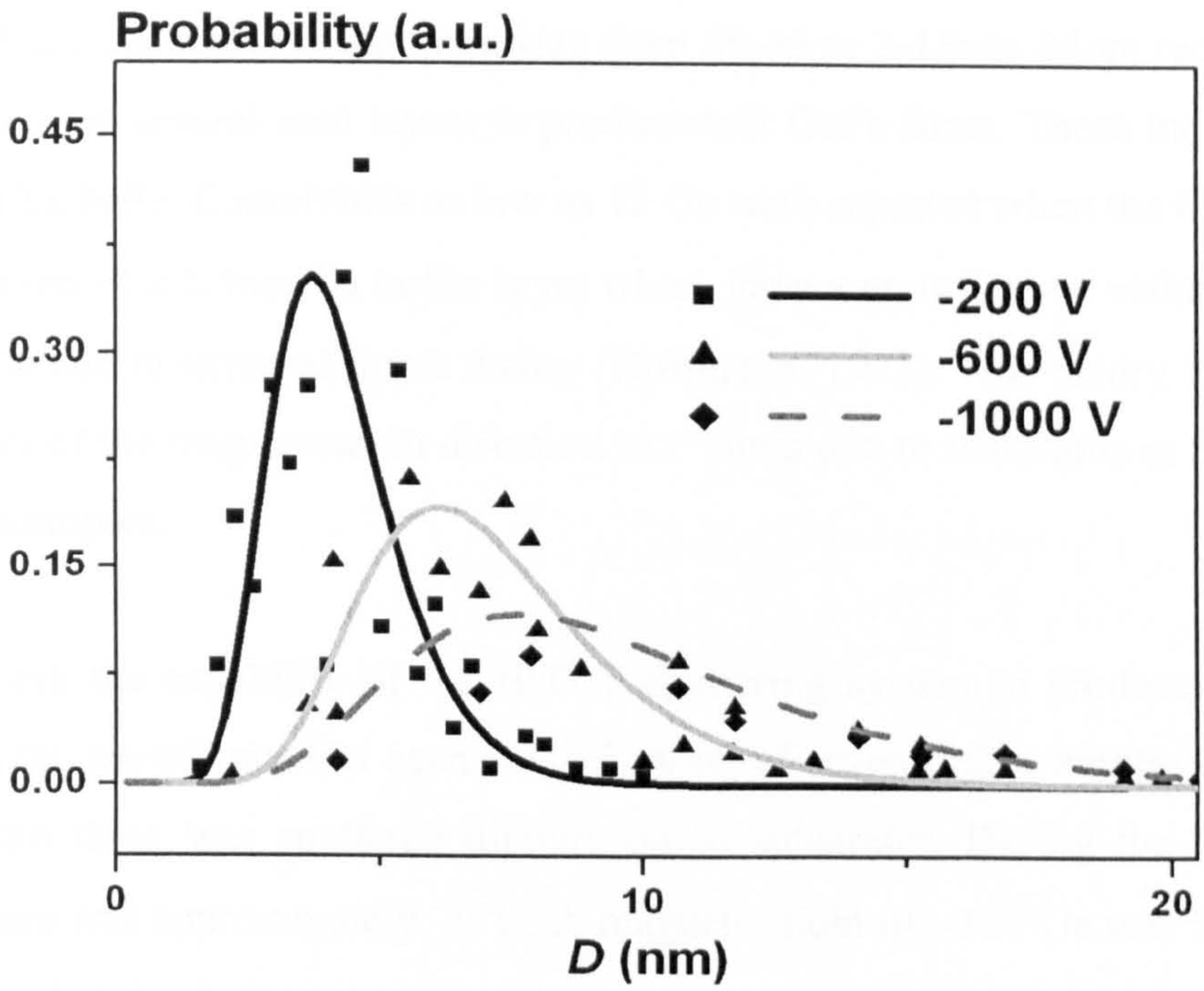

Figure 57. Grain size distributions for the IrMn samples grown using three different bias voltages: -200, -600 and -1000V respectively.

It is interesting to note that the grain structure of the Cr, NiFe, CoFe, IrMn and FeMn is rather different at similar sputtering rates ($\langle D_{CoFe} \rangle > \langle D_{Cr} \rangle > \langle D_{IrMn} \rangle > \langle D_{FeMn} \rangle > \langle D_{NiFe} \rangle$). For identical sputtering conditions the final grain structure for different materials is dependent upon parameters such as binding energy and crystal structure among others. In the following sections the effect of grain size control in the magnetic properties of systems containing these materials will be studied.

6.2. CoFe films with controlled grain size and coercivity

The capability of the HiTUS sputtering system to control the grain size of the samples deposited has been demonstrated. Among all magnetic materials, CoFe alloys are used as soft underlayers in perpendicular media and as the core material of write elements in modern recording heads. However, CoFe does not naturally exhibit soft magnetic properties and usually seed layers or additives are used to reduce the coercive field. Thomson *et al.* (1998) found that polycrystalline CoFe films grown on Au/MgO exhibited soft magnetic properties with a coercivity of 16 Oe. Similar results were

reported by Platt *et al.* (2000) when CoFe was grown on CoO. The reduction in H_c was attributed to a reduction in the grain size from 20-35 to 5-15nm. More recently, Jung *et al.* (2003) used several seed layers to produce soft CoFe films. These included Cu, Ru, NiFe and Ta/NiFe. Coercivities as low as 12 Oe were reported when the CoFe layer was grown on top of a 2.5nm Cu buffer layer which gave a grain size of ≈10nm. The results were explained in terms of ripple theory (Hoffmann, 1973). This theory is based on the fluctuation of the magnetisation direction in *F* films due to variations in the orientation local anisotropies.

In this work the capability of the HiTUS sputtering system to produce soft $Co_{60}Fe_{40}$ films via the growth rate has been studied. A set of seven CoFe samples each of which was 20 nm thick was sputtered directly on Si substrates. During the deposition the temperature was approximately 70°C. A magnetic field of ~300 Oe was applied during the deposition to induce a uniaxial magnetic anisotropy. The base pressure was $5x10^{-7}$ mbar and the process pressure $2.7x10^{-3}$ mbar. Both the target and the substrates were plasma cleaned prior to deposition. The deposition conditions for all the samples are shown in Table 7. The sputtering conditions are the same as those used in section 6.1.3

Table 7. Grain size results and coercivity for CoFe. The errors in *D* are estimated to be ±3%.

Sample	Bias Voltage (-V)	Growth Rate (Å/s)	Mean Grain Size (nm)	H_c (Oe)
A1	120	0.10	7.2±1.6	12
A2	200	0.20	14.1±4.7	20
A3	300	0.30	17.1±5.7	120
A4	400	0.40	20.0±9.2	126
A5	600	0.55	21.2±8.3	117
A6	800	0.70	24.1±9.9	108
A7	1000	0.80	26.4±10.8	121

In order to measure the grain size of the sputtered films another seven CoFe samples were deposited under the same conditions on TEM grids. The grain structure of the samples sputtered on Si substrates is expected to be the same as that on the TEM grids. This is based on the comparison of the grain size of Cr samples grown on Si substrates

and TEM grids (Milena Georgieva and P. J. Grundy, private communication). Grain size distributions and TEM pictures corresponding to the samples with smallest (A1) and biggest (A7) grains are shown in Figure 54 (section 6.1.3). The samples were measured at room temperature using a VSM. Easy axis loops are shown in Figure 58.

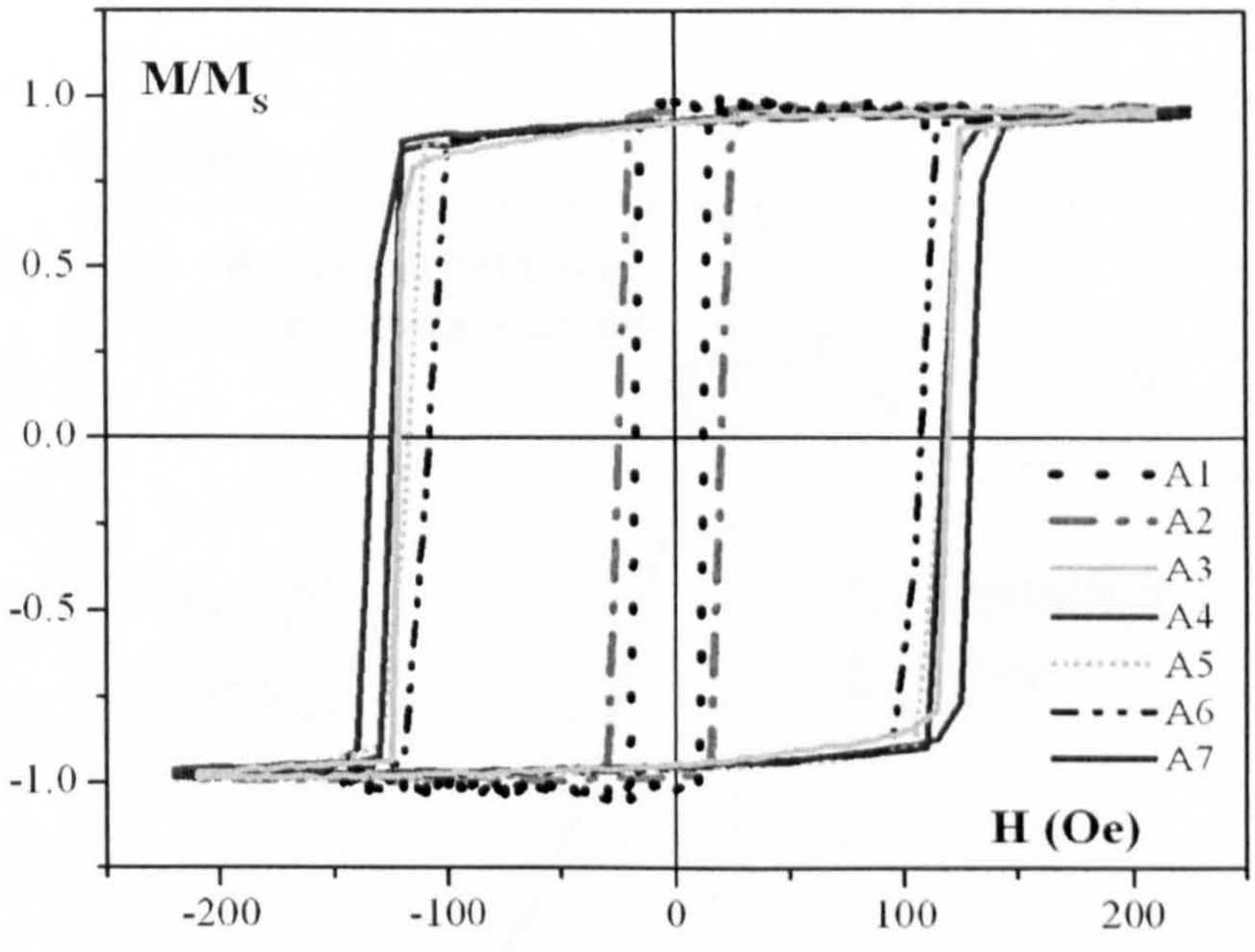

Figure 58. M-H curves for samples A1 to A7.

A clear difference in the coercivity is observed for samples with small and big grains. The variation of the coercivity as a function of the mean grain size is shown in Figure 59. Samples with a mean grain size smaller than 15 nm show soft magnetic properties with coercivities below 25 Oe and a minimum of 12 Oe. A sharp increase of H_c up to 120 Oe is observed for samples with a mean grain size above 15 nm. The coercivity remains almost constant in the range 15-26 nm.

These results can be explained on the basis of the random anisotropy model (Herzer, 1990) originally proposed by Alben *et al.* (1978) for amorphous ferromagnets. In this model the magnetic properties of a polycrystalline sample are strongly dependent on the balance between the local magnetic anisotropy energy and the ferromagnetic exchange energy. For very small grains the exchange energy forces the spins to align parallel and therefore the magnetisation of each grain does not follow the easy direction of each

crystallite. However, for very big grains, the magnetisation can follow the easy direction within each grain and the magnetisation process is determined by the magnetocrystalline anisotropy of the crystallites. The dividing line between these two processes is given by the ferromagnetic exchange length L_{ex} which is the minimum distance over which the magnetisation might change sign without involving exchange energy.

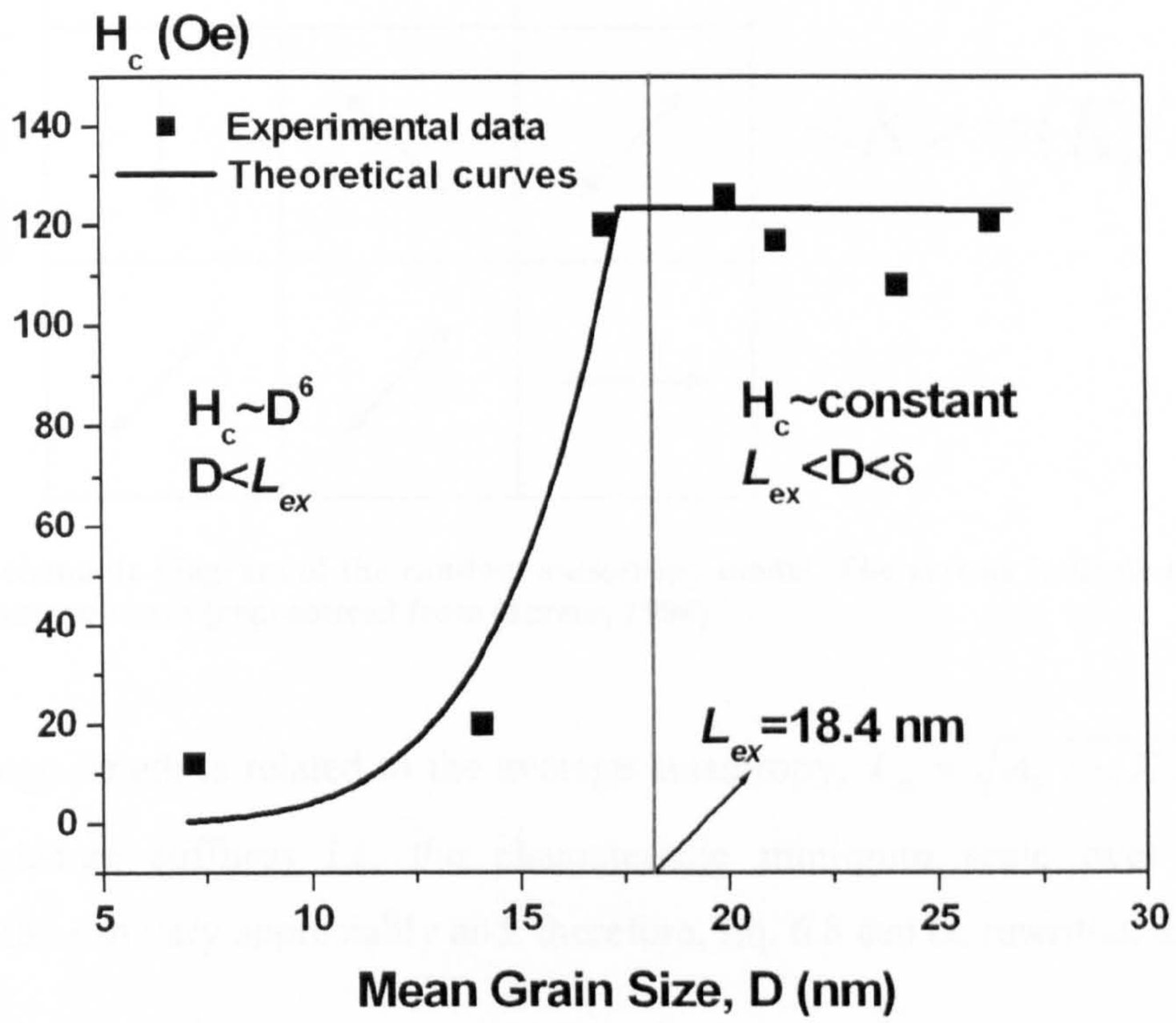

Figure 59. Coercivity as a function of the mean grain size.

The random anisotropy model considers an assembly of ferromagnetically coupled grains of size D with randomly oriented magnetocrystalline anisotropy K_u as shown in Figure 60 (Herzer, 1990). The effective anisotropy affecting the magnetisation process results from averaging over the $N = (L_{ex}/D)^3$ grains contained in a volume L_{ex}^3. The anisotropy density $\langle K \rangle$ will be determined by the mean fluctuation amplitude of the anisotropy energy of the N grains.

$$< K > \approx \frac{K_u}{\sqrt{N}} = K_u \left(\frac{D}{L_{ex}} \right)^{3/2}$$ Eq. 6.8

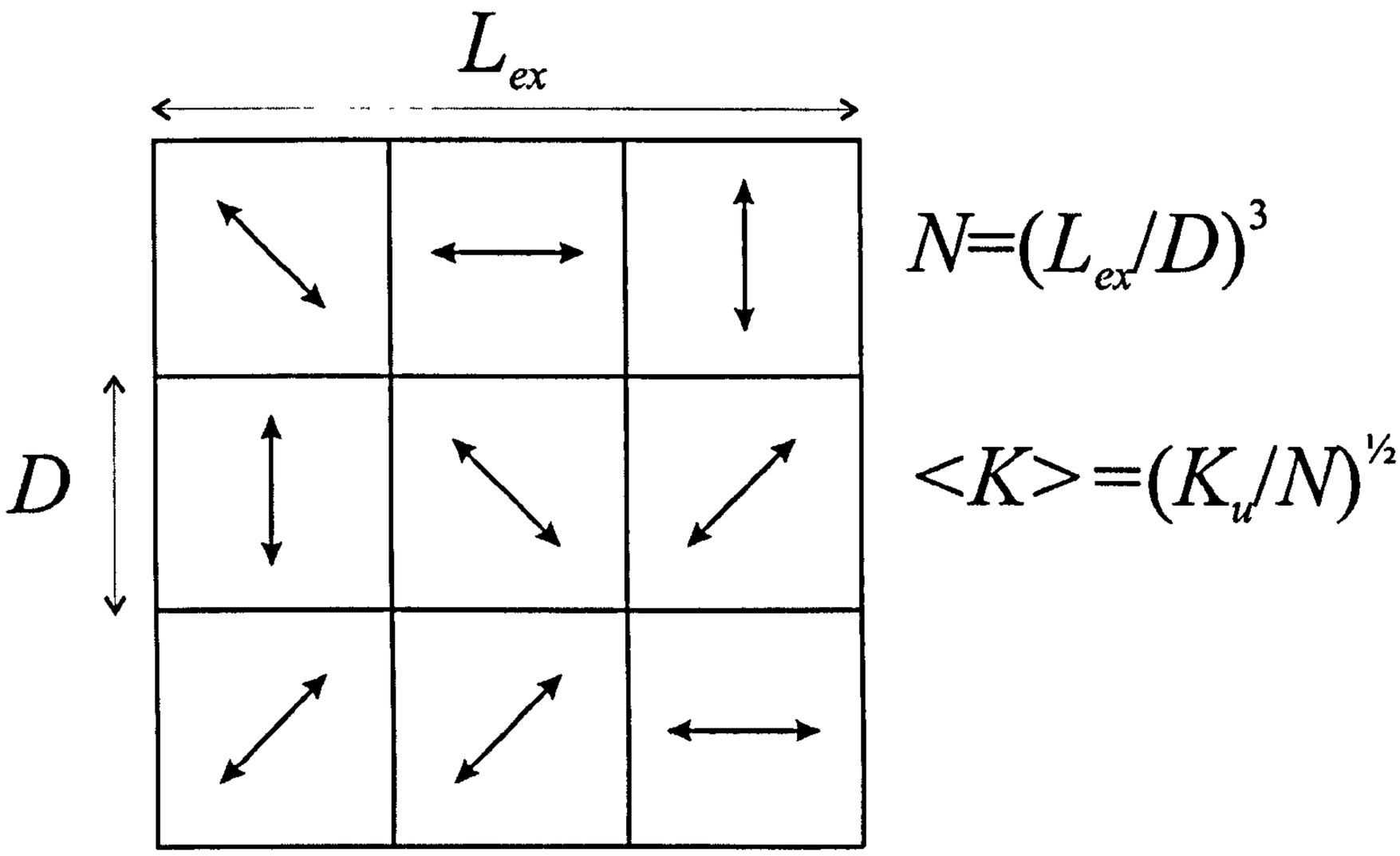

Figure 60. Schematic diagram of the random anisotropy model. The arrows indicate the randomly oriented anisotropy axes (reproduced from Herzer, 1990).

The exchange length is related to the average anisotropy, $L_{ex} = \sqrt{A_F / < K >}$ where A_F is the exchange stiffness i.e. the characteristic minimum scale over which the magnetisation can vary appreciably and, therefore, Eq. 6.8 can be rewritten as:

$$< K > \approx \frac{K_u^4}{A_F^3} D^6$$ Eq. 6.9

This relationship (Eq. 6.9) remains valid as long as the grain size D is smaller than L_{ex}. Using the results from coherent spin rotation (Bozorth, 1951) the coercivity is given by

$$H_c = p_c \frac{< K >}{M_s} = p_c \frac{K_u^4}{A^3 M_s} D^6 ; D < L_{ex}$$ Eq. 6.10

where p_c is a dimensionless factor related to the crystal structure and M_s the saturation magnetisation. When the crystallite size is bigger than the exchange length then the

effective anisotropy is given by the magnetocrystalline anisotropy K_u itself and the coercivity reaches its maximum value (Eq. 6.11).

$$H_c = p_c \frac{K_u}{M_s}; D \cong L_{ex} \qquad \text{Eq. 6.11}$$

Finally, when the grain size exceeds the domain wall width $\delta = \pi L_{ex}$ theory predicts that the magnetisation reversal is driven by domain wall pinning at grain boundaries and the coercivity is given by Eq. 6.12. The grain size of the samples studied in this work is well below the domain wall width in CoFe explaining why this coercivity regime has not been observed in the magnetic measurements.

$$H_c = p_c \frac{\sqrt{AK_u}}{M_s} \frac{1}{D}; D > \delta \qquad \text{Eq. 6.12}$$

In order to explain the transition between the $H_c \propto D^6$ and the $H_c \approx$ constant regimes the exchange length has been calculated. For this purpose the exchange constant A_F has been estimated using the Curie temperature approximation resulting in a value of $A_F = 0.911 \times 10^{-8}$ erg/cm. Using $K_u = 2.7 \times 10^5$ erg/cc the exchange length was calculated to be $L_{ex} = 18.4$ nm. This value is in agreement with the value above which the coercivity is observed to remain constant as shown in Figure 59.

The coercivity of 20 nm thick CoFe films has been controlled by changing the grain size of the deposited films. This unique capability of HiTUS suggests that the role of the *AF* grain size on exchange bias can be studied by varying the deposition conditions without changing other variables (e.g. underlayer thickness Nishioka *et al.*, 1996). This has been the main subject of study of this work and the results from this study will be presented in the next section. Note that this interpretation only applies to polycrystalline *F*/*AF* systems containing a metallic *AF* layer as different mechanisms may apply for different systems.

6.3. Grain Size Effects in Polycrystalline Exchange Biased Bilayers

Two different *AF* systems have been studied in this work, $Fe_{50}Mn_{50}$ and $Ir_{23}Mn_{77}$. Both alloys were chosen due to their importance in technological applications such as spin-valves structures. For room temperature applications the thermal stability of FeMn is sometimes sufficient. However, for higher temperature applications such as read-heads IrMn is much more commonly used due to its higher blocking temperature and exchange bias after deposition at room temperature without any further annealing (van Driel *et al.*, 1999). FeMn was widely used as a pinning material until 1997 when Fuke *et al.* reported spin-valve giant magnetoresistive films with a CoFe/IrMn bilayer. This was of critical importance to bring spin-valve GMR heads that did not require re-setting into practical use.

6.3.1. NiFe/FeMn systems

There have been several attempts to characterise the effect of the *AF* grain size on the exchange field leading to conflictive results. This is due in part to the fact that either the thickness of the seed layer or the morphology of the sample is usually modified in some other way to achieve different grain sizes in the *AF* layer. Another important factor is the nature of the *AF* (i.e. metallic, oxide etc...) as different systems behave differently. It is important to emphasise that in this work only metallic *AF*s have been studied and therefore these results and the conclusions drawn apply only to polycrystalline samples with a metallic *AF* layer.

Samples with composition Si/Cu(10nm)/NiFe(10nm)/FeMn(t_{AF}=7 and 10nm)/Ta(10 nm) were prepared using HiTUS. The grain size was varied only in the *AF* layers which were grown using the same sputtering conditions as those used for the TEM grids. The grain structure in the *AF* layer in the full stack is expected to be the same as that on the TEM grids based on the comparison of the grain size of Cr samples grown on Si substrates and TEM grids (Milena Georgieva and P. J. Grundy, private communication). The Cu and NiFe underlayers may modify the grain structure of the *AF* layer and a slightly different grain structure may occur. However, in the HiTUS sputtering system the substrate is remote from the target and does not have the same role as in

conventional sputtering systems where the distance between the substrate and the target is a few centimetres. Furthermore, even if there is a small change in the grain structure, all the samples will be affected in the same way still giving a grain size effect on the magnetic properties. All the substrates were plasma cleaned prior to deposition and a magnetic field of ≈300 Oe was applied during the deposition to induce unidirectional anisotropy in the NiFe layer. The base pressure was 3.0×10^{-7} mbar and the Ar deposition pressure was 2.7×10^{-3}mbar.

The samples were measured at room temperature using a VSM after resetting the *AF* following the measurement procedure described in Chapter 5. All the hysteresis loops showed an increasing shift towards negative field values for larger sputtering rates. Figure 61 shows the variation of the exchange field and the coercivity with the *AF* grain size. The lines are guides to the eye. Even though the variation in the *AF* grain size was relatively small (30%) it corresponds to a factor 2.2 in volume.

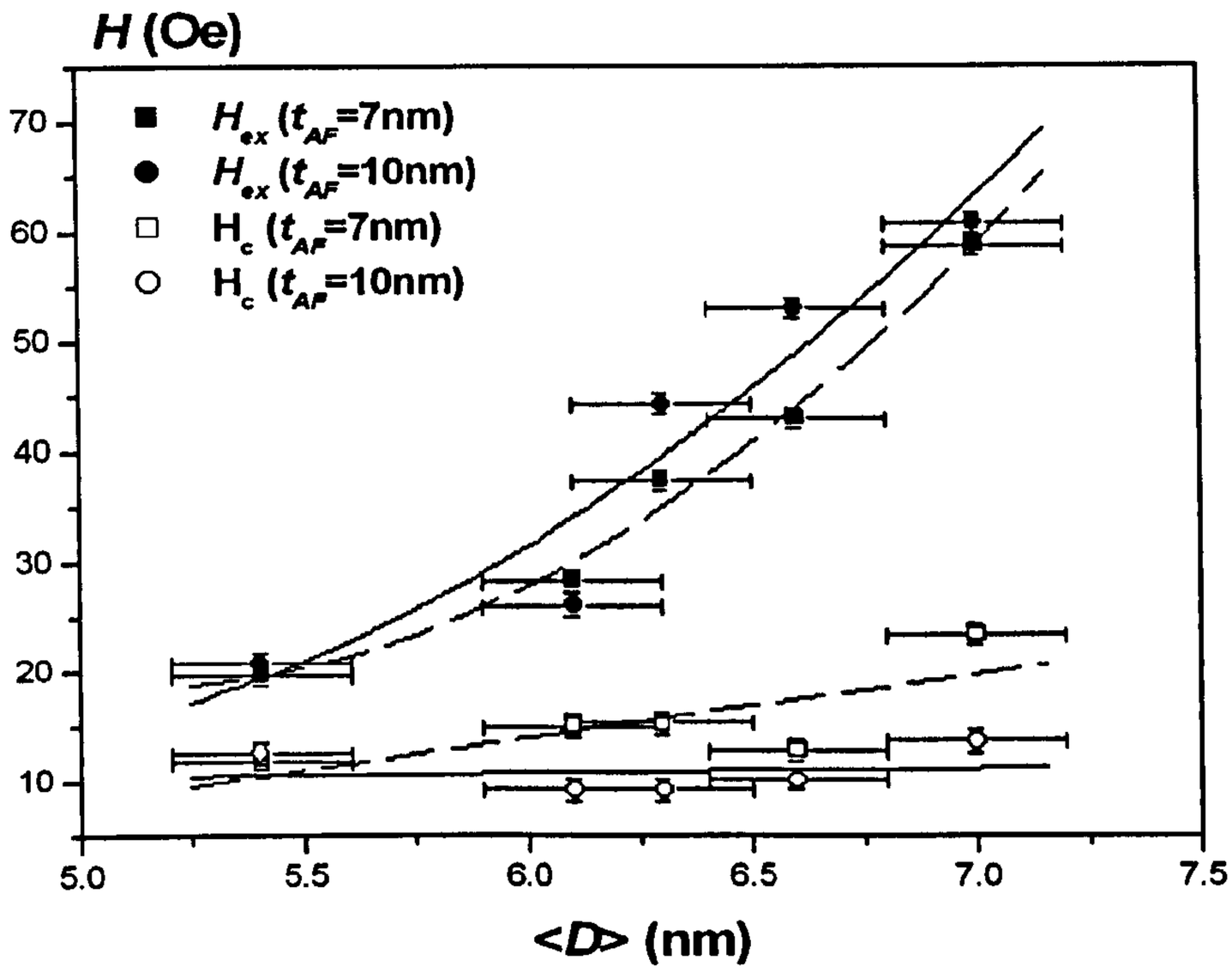

Figure 61. Variation of the exchange field and the coercivity with the *AF* grain size.

Most of the models in the literature are based on the formation of domains in the *AF* layer either parallel (e.g. Mauri *et al.*, 1987a) or perpendicular (e.g. Malozemoff 1987) to the interface. For all applications *AF*s are sputtered polycrystalline films with ≈20nm

grains. It is known that *AF*s are not stable (e.g. Fulcomer and Charap, 1972a) and that limits H_{ex}. This is used to set the *AF* below T_N. A granular model that accounts for thermal activation in the *AF* layer may be able to explain exchange bias containing a metallic polycrystalline *AF* layer. Below a certain volume V_1 the grains are in a 'superparamagnetic' state and they do not contribute to the exchange field (Figure 62). Above that critical diameter the grains are stable and the magnitude of the loop displacement is governed by the state of order in the *AF* layer. However, there is a second critical volume V_2 above which the anisotropy energy of the grains is too big and it is not possible to set those grains (Figure 62). Following this interpretation

$$H_{ex} \propto H_{ex}^{i} \int_{V_1}^{V_2} f(V)dV \qquad \text{Eq. 6.13}$$

where H_{ex}^{i} is an intrinsic exchange field equivalent to the exchange field when the coupling across the interface is perfect.

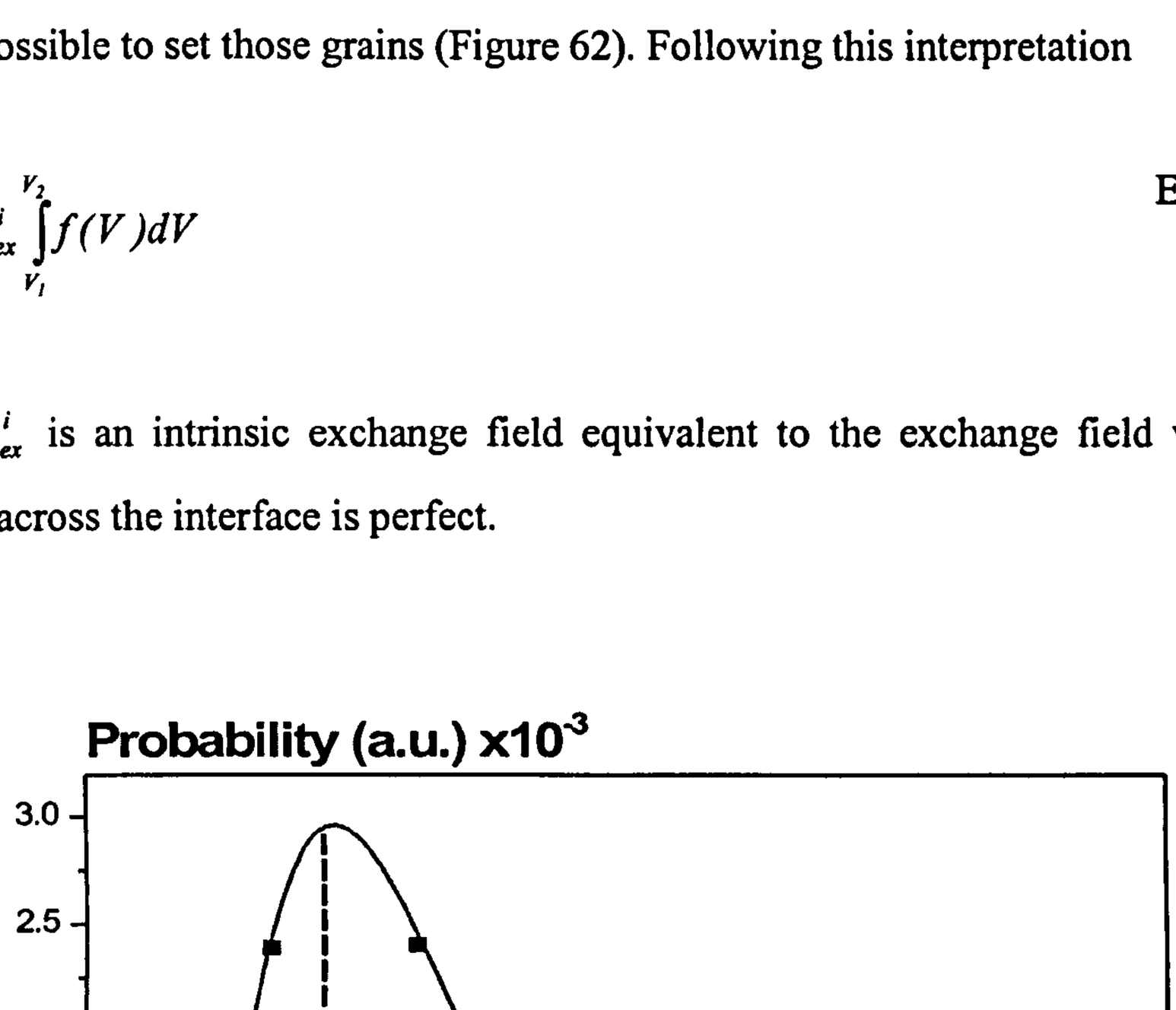

Figure 62. Schematic diagram of the volume distribution within the *AF* layer of an exchange biased system.

6.3.1.1. Determining the anisotropy constant of FeMn

In this work the *AF* is thought of as an assembly of grains distributed in size. Each grain is assumed to be in a single domain state. Single domain particles are subject to thermal activation leading to magnetic transitions over a non-zero energy barrier ΔE. This occurs whenever the thermal energy is large enough to overcome the energy barrier during the time of measurement. The critical volume below which this behaviour is observed depends on several factors such as the anisotropy of the system, the measurement time and the temperature. The relaxation time τ is defined as the time that it takes to the magnetisation to decay $1/e$ (37%) of its original value (Néel, 1949) and it is given by

$$\tau^{-1} = f_0 \exp\left[-\frac{\Delta E}{k_B T}\right] \qquad \text{Eq. 6.14}$$

$$\Delta E = K_{AF} V \left(1 - \frac{H^*}{H_K^*}\right)^2 \qquad \text{Eq. 6.15}$$

where f_0 is the attempt frequency taken to be $10^9 s^{-1}$, V is the volume of the particle, k_B is Boltzmann's constant, K_{AF} is the anisotropy of the grain, T is the temperature, H^* is the exchange field from the F and H_K^* is a pseudo-anisotropy field. In this work the energy barrier was taken to be $K_{AF}V$ to keep the analysis simple as no experimental values for H^* or H_K^* have been found in the literature.

The anisotropy of the *AF* was calculated from the measurement of the median T_B i.e. the temperature at which equal portions of the *AF* are aligned in opposite directions following the measurement procedure described in Chapter 5. This method has the important advantage of removing interfacial effects. As all the measurements were made at 77K the *AF* superparamagnetic fraction was removed. Therefore the median volume is the critical volume at the median blocking temperature. Given the fact that the measurement time is known, i.e. the conditioning time at negative bias, K_{AF} can be determined easily.

$$K_{AF}(T) = \frac{4\ln(t_m f_0) k_B T_B}{V_{AF}} \qquad \text{Eq. 6.16}$$

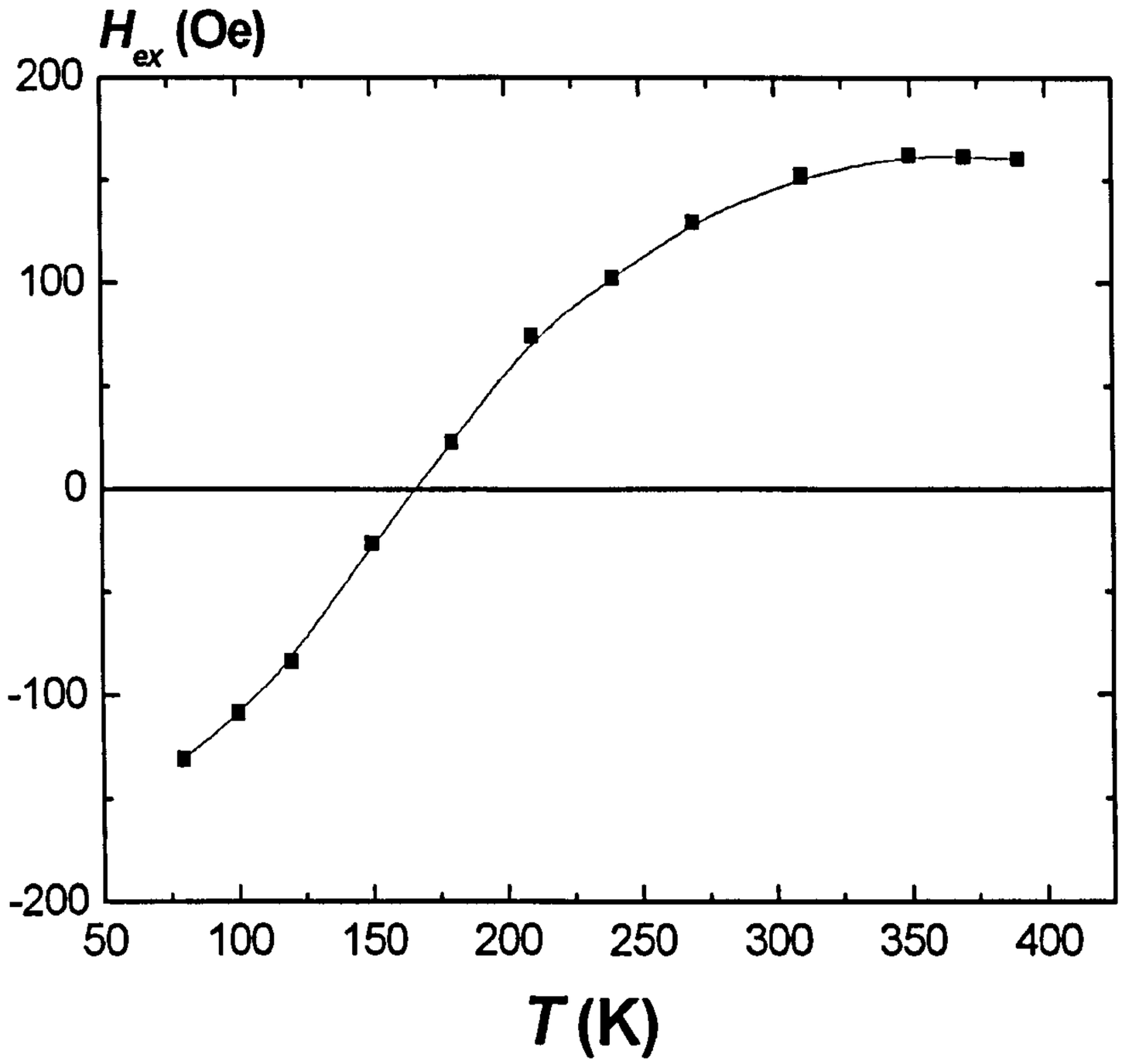

Figure 63. Measurement of the median blocking temperature T_B for a NiFe/FeMn bilayer with D = 3.6nm (S. Manzoor, to be published).

The *AF* was reset by heating the sample to 373K for 90 minutes in the presence of a positive saturating field. The temperature is then quenched to 77K and the field reversed so the A*F* is in negative bias. The temperature is raised to an activation temperature T_{ACT} where the *F* is held at negative saturation for 30 minutes. The system is then cooled to 77K and the loop measured. Figure 63 shows the variation of the exchange field with the activation temperature in the range 77-393K for a Si/Cu(30nm)/NiFe(10nm)/FeMn(10nm)/ Ta(10nm) bilayer (S. Manzoor, private communication). From this graph T_B=165K. A sample with composition Cu(30nm)/NiFe(10nm)/FeMn(10nm) was deposited on a TEM grid in order to determine the median grain size <*D*> in the *AF* layer. Over 500 particles were measured obtaining a value of 3.6nm. The median volume of the distribution is given by

$$< V >= \pi \frac{< D >^2}{4} t_{AF} \qquad \text{Eq. 6.17}$$

The anisotropy constant of FeMn at 165K can now be calculated

$$K_{FeMn}(165K) = \frac{4 ln(1800 \cdot 10^9) k_B \cdot 165}{\pi < D >^2 t_{AF}} = 6.30 x 10^6 \, ergs / cc \qquad \text{Eq. 6.18}$$

In Eq. 6.18 the factor 1800 arises due the measurement time being equal to the conditioning time i.e. 30 minutes. The temperature variation of the anisotropy constant has been assumed to be (R. W. Chantrell, private communication, Khapikov *et al.*, 2000) although different exponents can be found in the literature (e.g. n = 3/2 Xi, 2005)

$$K_{AF}(T) = K_{AF}(0K)\left[1 - \frac{T}{T_N}\right]^3 \qquad \text{Eq. 6.19}$$

In order to calculate the value of K_{FeMn} at different temperatures the bulk value of T_N has been used, i.e. 490K (Nogues and Schuller, 1999), although the real value for thin films might be slightly lower. This way K_{FeMn}(295K)=1.36x10^{6}ergs/cc and K_{FeMn}(373K)=2.95x10^5 erg/cc. These values are much higher than those in the literature e.g. K_{FeMn}(295K)=1.35x10^{5}ergs/cc (Mauri *et al.*, 1987b). This is due to the fact that the anisotropy constant is usually determined from the measurement of the exchange field and, therefore, contributions to the shift of the loop from both the interface and the bulk of the *AF* are present. The exchange coupling constant across the interface J_{INT} will vary between 0 and 1 having an enormous effect when calculating K_{AF}. However, in this work the anisotropy constant has been determined at H_{ex}=0 and therefore these results are independent of the value of J_{INT}. The two critical sizes V_1 and V_2 can now be calculated (see Figure 64). V_1 determines the fraction of the *AF* that is unstable during measurement. The samples were measured at room temperature and the measurement time for each loop was 600s. However, V_2 sets the limit above which the *AF* grains cannot be set and this is calculated from the resetting conditions i.e. 90 minutes at 373K.

$$V_1 = \frac{\ln(600 f_0) k_B 295}{K_{FeMn}(295)} = 810nm^3$$

$$V_2 = \frac{\ln(5400 f_0) k_B 373}{K_{FeMn}(373)} = 5133nm^3$$

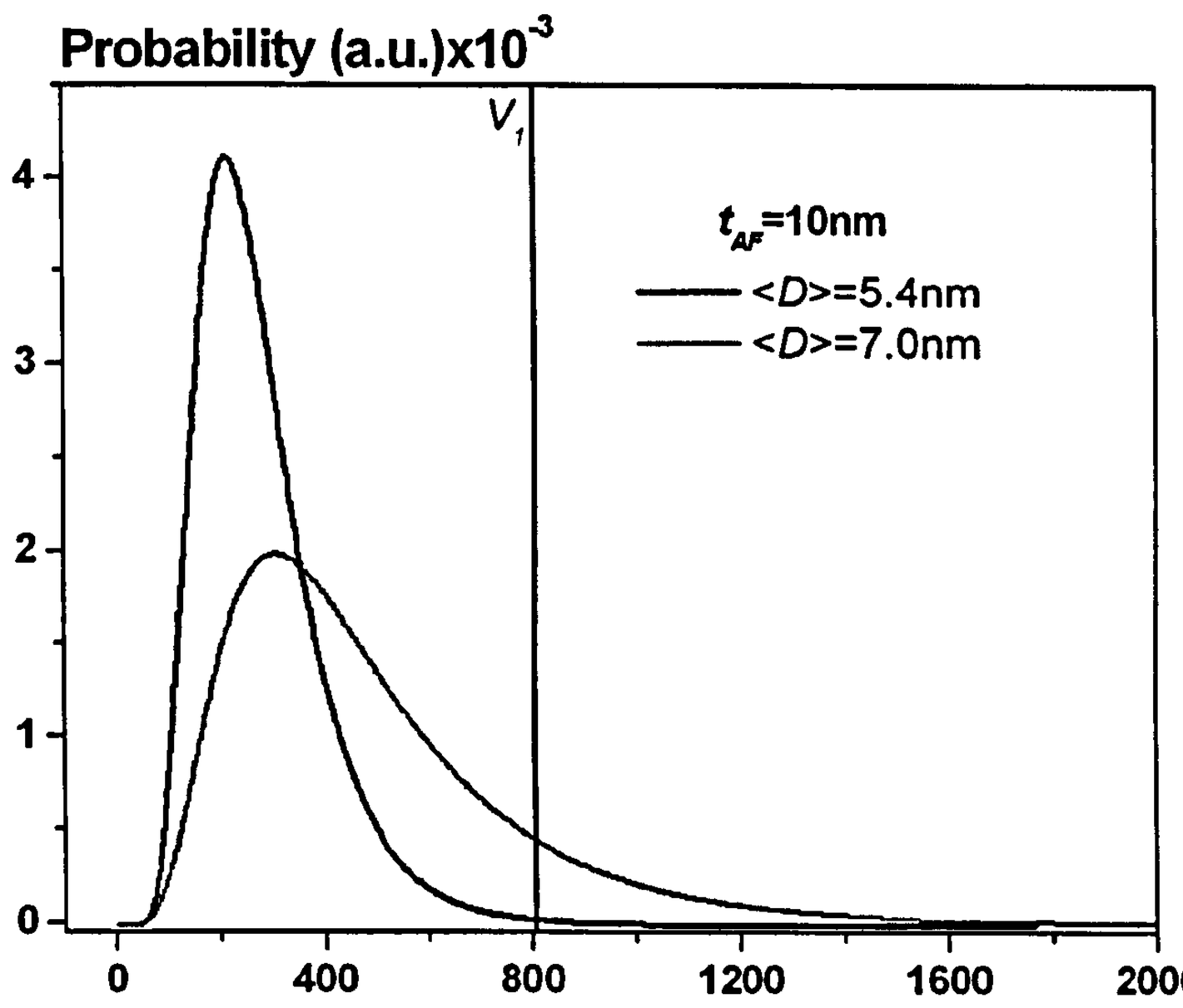

Figure 64. Volume distributions for the samples with biggest and smallest grains respectively. The thickness of the *AF* layer was 10nm.

The volume distributions have been calculated from the measured grain size distributions as indicated by Eq. 6.20. Figure 64 shows the distributions for the samples with the biggest (grey line) and the smallest (black line) grains for the set with t_{AF}=10nm. Even though only a line has been plotted, the lines correspond to real distributions measured from TEM pictures. A similar graph was obtained for the samples with t_{AF}=7nm. Note that only a vertical line corresponding to V_1 is plotted in Figure 64. The value obtained for V_2 would be equivalent to infinity. This suggests that for FeMn there is no fraction of unset grains. It is clear from that graph that the sample with bigger grains has a bigger fraction of the *AF* contributing to the exchange field. It is noteworthy that the sample with the smallest grains is almost 100% thermally

unstable at room temperature while 12% of the *AF* is stable for the sample with bigger grains. This is in agreement with the magnetic measurements shown in Figure 61.

$$f(V) = f(D)\pi\frac{D^2}{4}t_{AF} \qquad \text{Eq. 6.20}$$

Although the exchange field increases by a factor 3 with the grain size, the coercivity was found to remain almost constant. This points to different origins of the uniaxial and the unidirectional anisotropy. From these results the coercivity seems to be controlled by interfacial effects while the exchange field is controlled not only by the spin configuration at the interface but also by the bulk of the *AF*. Khapikov *et al.* (2000) studied the temperature dependence of the exchange field and coercivity in polycrystalline NiO/NiFe bilayers with a thin *AF* layer. A theoretical model was proposed where the *AF* grains were divided into three groups. The smallest grains were assumed to always contribute to the coercivity with a coefficient $\propto K_{AF}(T)$ (Khapikov *et al.*, 2000). These grains governed the low temperature behaviour of H_c. Grains of intermediate size would contribute in a different way depending on the measurement time, temperature and sample history. Finally, the biggest grains would only contribute to the loop displacement. Based on this model a decrease of H_c would be expected with increasing grain size. More measurements need to me made in order to clarify the effect of the *AF* grain size on H_c.

6.3.1.2. Training effects

The phenomenon of training has also been studied in three samples from the set with t_{AF}=7nm. The hysteresis loop for each sample was measured continuously for 6 full cycles at room temperature so the *AF* was thermally unstable. For each sample the maximum negative applied field was $-H_{max}=H_{c1}$-300Oe and the maximum positive field $+H_{max}=H_{c2}$+300Oe, where H_{c1} and H_{c2} are the switching fields on the descending and ascending branch of the hysteresis loop respectively. In addition, the sweep-rate was constant ensuring that the *F* spent equal amounts of time in positive and negative saturation. Hence, the *AF* layer is exposed for equal times to positive and negative exchange fields. The results of these measurements are shown in Figure 65. Based on our understanding of the spin reorientation effect described by Hoffmann (2004), the

changes from the first to the second loop are not due to thermal activation. The data in Figure 65 also shows the training from loops 2 to 6 only normalised to H_{ex} on the first loop. Due to the fact that equal times are spent with the F in either direction, unstable grains reverse to an equal extent so the effects are very small. For the cases shown in the changes for n = 2 to n = 6 are about 1Oe. These effects are believed to be due to either residual spin reorientation or perhaps an element of reversibility in the spin reorientation effect. The grain size effect appears to be a result of this irreversibility since unstable grains are reset by the measurement allowing spin-flop coupling to be formed again.

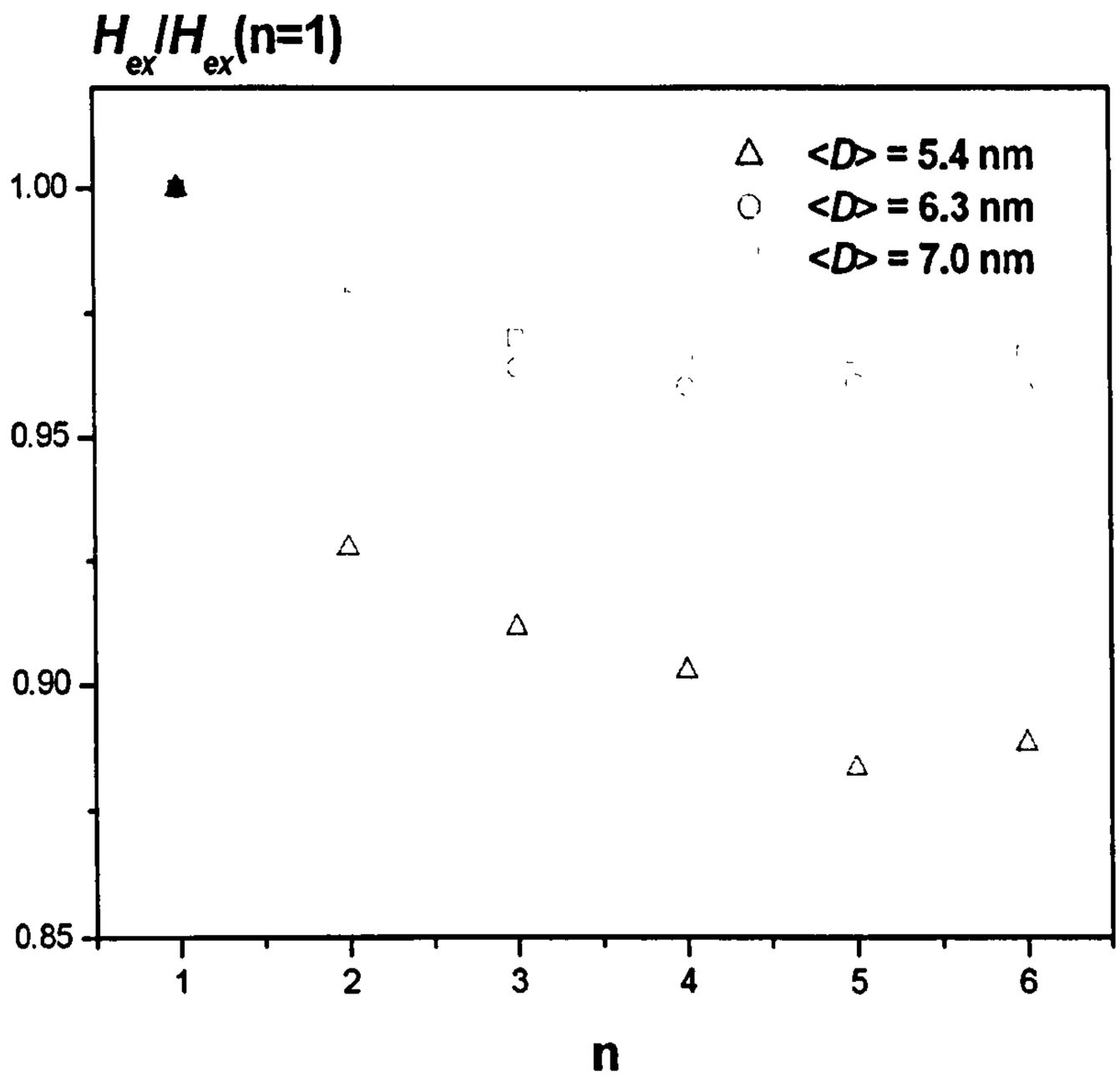

Figure 65. Training effect for different *AF* grain sizes where n is the loop number.

6.3.2. CoFe/IrMn systems

IrMn is a much more important material from the technological point of view compared to FeMn due to its higher thermal stability and blocking temperature. Therefore, a similar study to that described in the previous section has been performed for CoFe/IrMn bilayers. In order to isolate the effect of the *AF* grain size on the exchange field, CoFe/IrMn bilayers were sputtered with the *AF* grown on top of the *F*. Pakala *et al.* (2000a) showed that when the layers are deposited in this order no correlation between the intensity of the IrMn (111) peak and H_{ex} in CoFe/IrMn bilayers was found. Also, the temperature during the deposition of the layers was kept below 100°C and, therefore, disordered fcc IrMn is expected (Tsunoda *et al.*, 2006). The samples were deposited in a magnetic field of approximately 300 Oe which was sufficient to induce a unidirectional anisotropy i.e. no post-deposition magnetic annealing was required avoiding possible changes in the microstructure of the samples.

Table 8. Preparation conditions and grain size data for CoFe/IrMn.

Bias Voltage (-V)	Growth Rate (Å/s)	μ_{lnD}	σ_{lnD}	$\langle D \rangle$ (nm) ±0.2nm
200	0.18	1.49	0.28	4.6
400	0.26	1.79	0.27	6.4
600	0.38	1.97	0.33	7.6
800	0.44	2.13	0.33	8.9

Samples with composition Cu(10nm)/CoFe(2.5nm)/IrMn(t_{AF})/Ta(10nm) (t_{AF}= 2, 3, 4, 6, 8, 10 and 12 nm) were sputtered using HiTUS. For each thickness four samples were grown using different bias voltages (200, 400, 600 and 800V) for the deposition of the *AF* layer i.e. four different grain sizes. The samples were deposited on Si 5mmx5mm precut substrates. The base pressure was 1.5×10^{-7}mbar and the process pressure 2.7×10^{-3}mbar.

In order to measure the grain size of the sputtered films four samples with composition Cu(10nm)/CoFe(2.5nm)/IrMn(6nm) were deposited on TEM grids. These samples were sputtered using the same conditions as for the full stack i.e. the bias voltage was changed between 200 and 800V when depositing the IrMn layer. Pictures in bright field

mode were taken using a TEM and grain size distributions were determined after counting over 500 grains for each sample. All the distributions were lognormal. The results are summarised in Table 8. Figure 66a and Figure 66b show TEM images and grain size distributions for the samples with the biggest and the smallest grain size respectively.

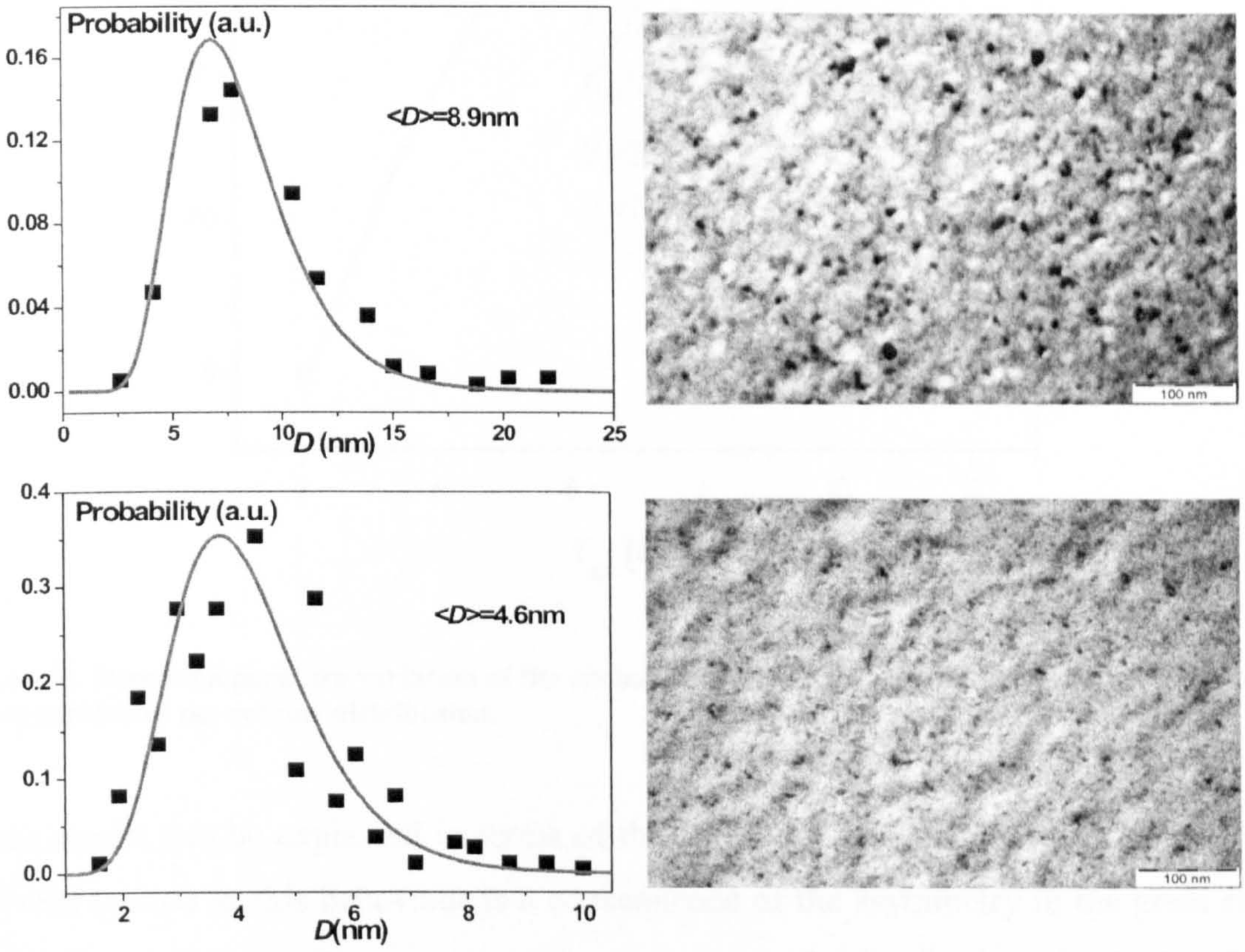

Figure 66. a) TEM image and grain size distribution for the sample with the biggest grains (top) and b) TEM image and grain size distribution for the sample with the smallest grains (bottom).

Figure 67 (grey dots) shows the variation of the exchange field with the thickness of the *AF* layer. The samples were measured at room temperature using a VSM after having reset the *AF* following the resetting procedure described in Chapter 5. Two loops were measured in order to remove the spin reorientation effect described by Hoffmann (2004) for cubic *AF*s. The values of the exchange field correspond to the second hysteresis loop. H_{ex} increases sharply for $t_{AF} \leq 8$nm.

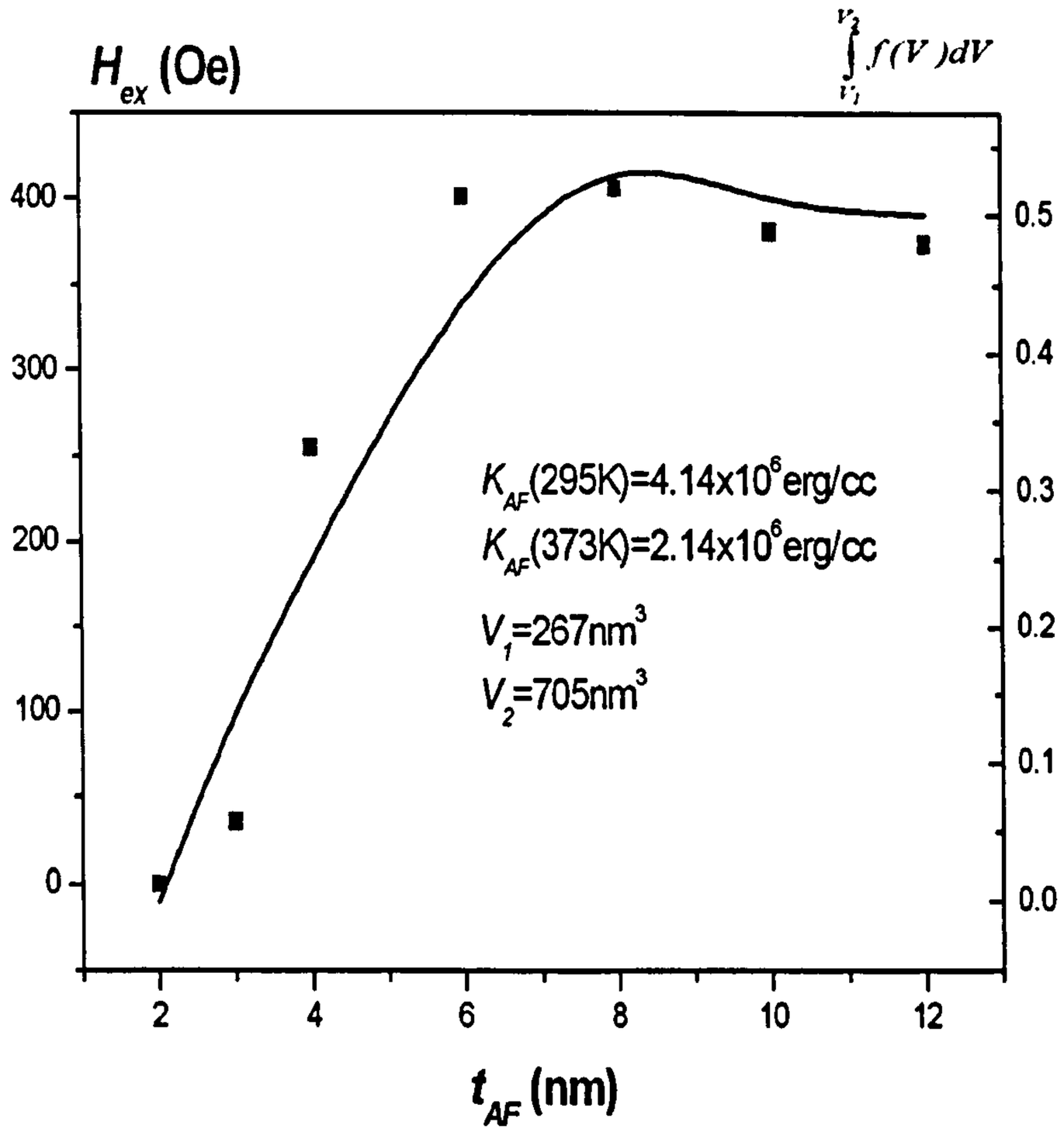

Figure 67. Room temperature variation of the exchange field with the thickness of the *AF* layer and the integral over the volume distribution.

These results can be explained in terms of the granular interpretation suggested in the previous section as this behaviour is a consequence of the asymmetry in the grain size distribution and the resulting pronounced asymmetry in the distribution of volumes. The shape of the curve can be predicted without the use of fitting parameters once it is realised that there are two critical sizes: V_1 below which the *AF* is unstable and V_2 above which the *AF* cannot be set. Even though the grain diameter distribution might be relatively narrow, the distribution of volumes is much broader (Figure 68). This explains why the exchange field increases sharply for low thicknesses and, after reaching a maximum, decreases slowly. In the low thickness range, the fraction of the *AF* grains with a volume bigger than V_1, i.e. the grains that are stable, will increase significantly with t_{AF}, affecting dramatically the magnitude of H_{ex}, while the fraction of grains that cannot be set will be located at the tail of the broad distribution and will represent a minor contribution the loop shift. However, when the thickness of the *AF* layer is increased, the contribution to H_{ex} from the fraction of unset grains, i.e. $V_{AF}>V_2$,

becomes dominant. If thicker samples had been studied the reduction in the H_{ex} with t_{AF} would be much more dramatic.

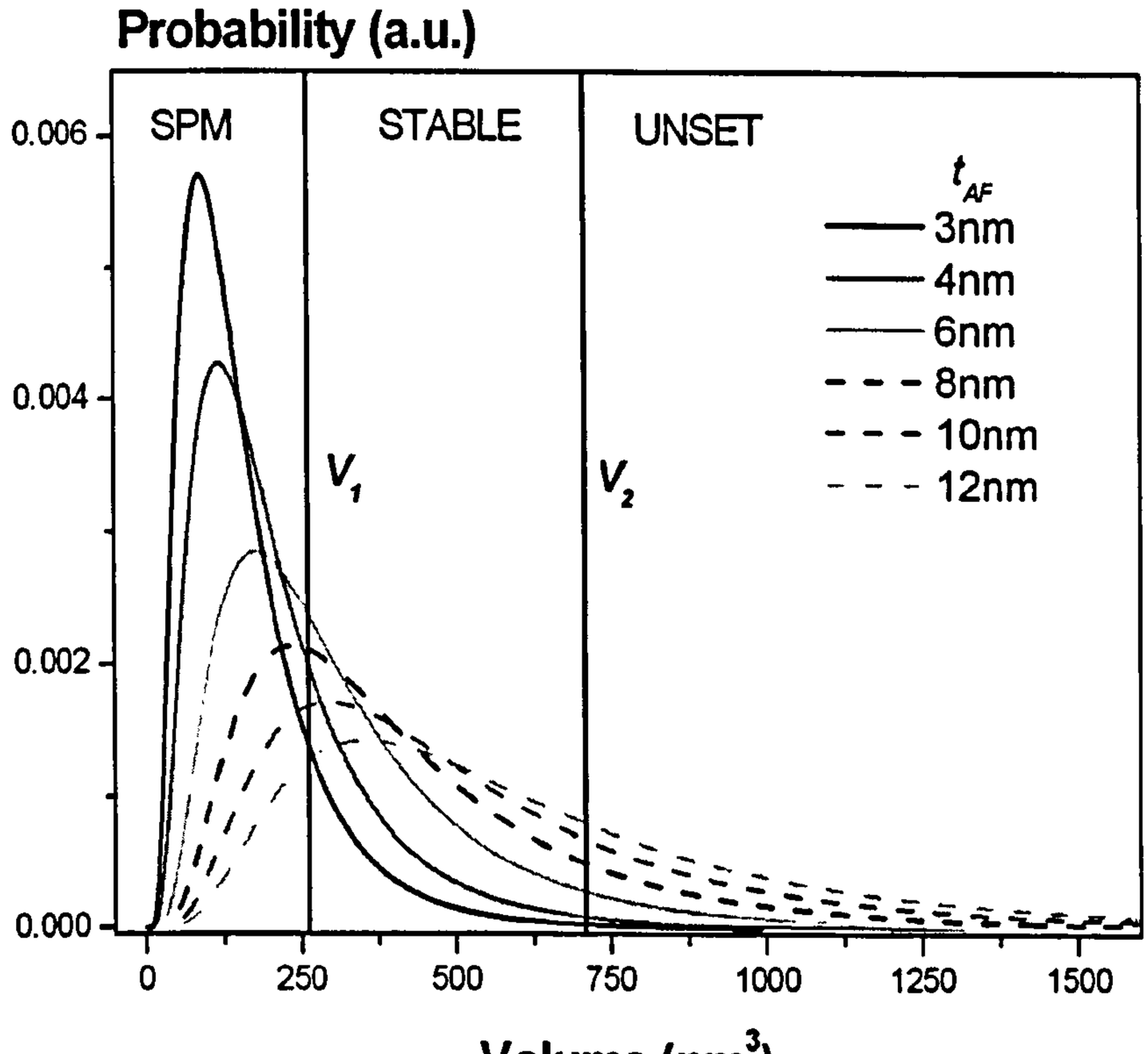

Figure 68. Volume distributions for Si/Cu(10nm)/CoFe(2.5nm)/IrMn(t_{AF})/Ta(10nm) exchange biased bilayers. The bias voltage during the deposition of the layers was kept constant at -600V.

6.3.2.1. Anisotropy of IrMn

In order to examine a quantitative analysis of these results, the integral between V_1 and V_2 of the grain volume distribution has been calculated. In order to calculate the critical volumes the anisotropy constant of the AF has to be determined. This has been done from a measurement of the median blocking temperature as described in section 6.3.1 for FeMn.

$$K_{IrMn}(T_B) = \frac{4\,ln(t_m f_0) k_B \cdot T_B}{\pi < D >^2 t_{AF}} \qquad \text{Eq. 6.21}$$

Figure 69 shows the variation of H_{ex} and H_c with the activation temperature for a CoFe(5nm)/IrMn(4nm) exchange biased bilayer. It is important to note, that even though the peak in the coercivity is quite broad, it does not occur at the median blocking temperature. This is in agreement with previous results in this group (Fernandez-Outon *et al.*, 2004). From that graph $T_B(t_{AF} = 4\text{nm})=236\text{K}$. K_{IrMn} can now be calculated from Eq. 6.18 where t_m was set to 1800 due to the conditioning time being thirty minutes giving a value of

$$K_{IrMn}(236K) = \frac{4\ln(1800 \cdot 10^9)k_B \cdot 236}{\pi < D >^2 t_{AF}} = 6.29x10^6\ ergs / cc$$

The median grain size was measured after growing a sample with the same composition but without the capping layer on a TEM grid resulting in $<D> = 6.8\text{nm}$, $\sigma_{\ln D} = 0.34$.

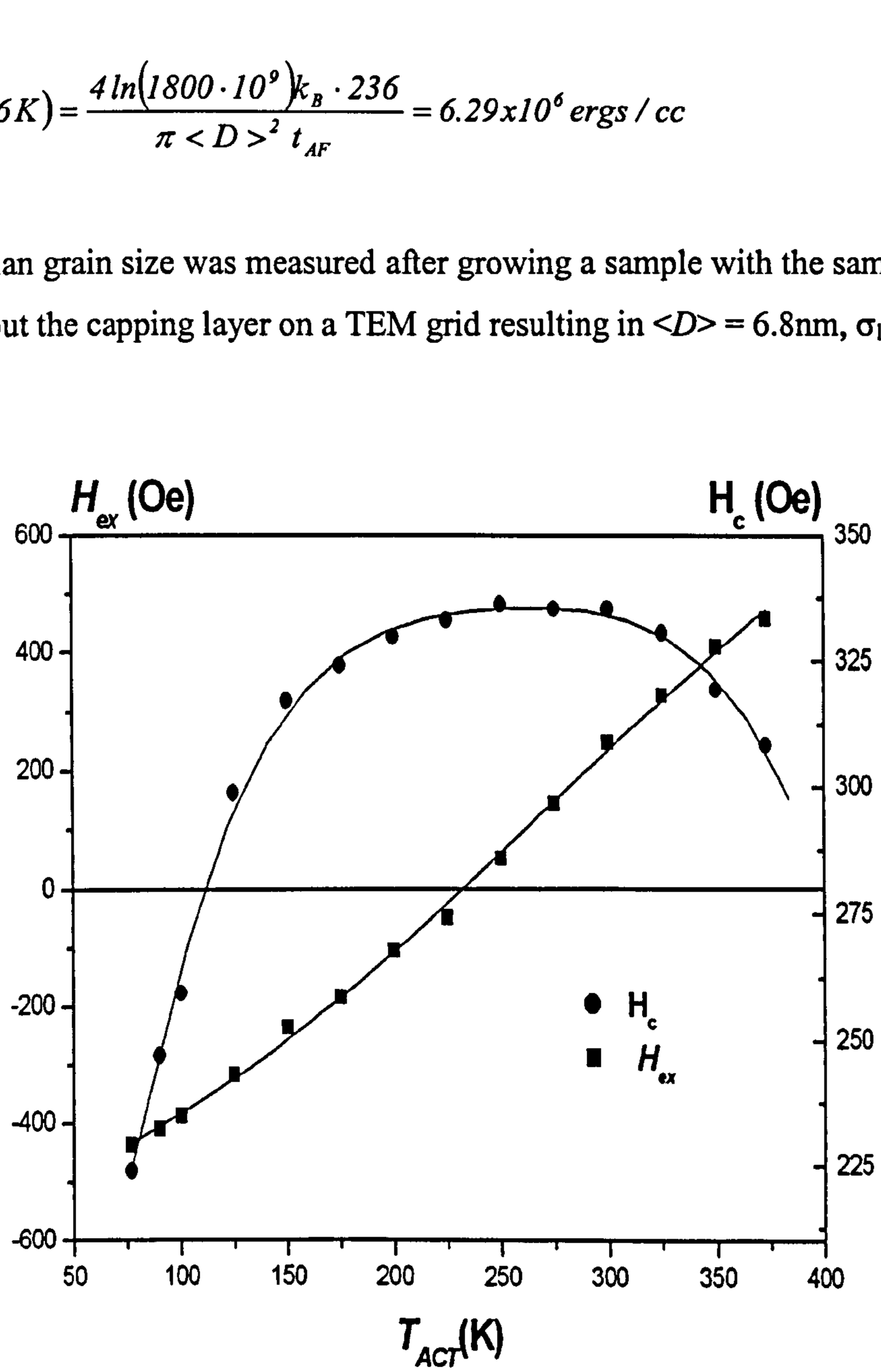

Figure 69. Measurement of T_B for a CoFe(5nm)/IrMn(4nm) bilayer (the lines are guides to the eye).

The anisotropy constant of IrMn at different temperatures can now be calculated using the same temperature dependence as used for FeMn, i.e. $K_{IrMn}(T) \propto (1-T/T_N)^3$: $K_{IrMn}(295K)=4.14\times10^6$erg/cc and $K_{IrMn}(373K)=2.14\times10^6$erg/cc. The critical volumes that set the fraction of the *AF* that contributes to H_{ex} are then given by

$$V_1 = \frac{ln(t_1 f_0)k_B 295}{K_{IrMn}(295)} = 267nm^3$$

$$V_2 = \frac{ln(t_2 f_0)k_B 373}{K_{IrMn}(373)} = 705nm^3$$

where t_1 = 600s as this was the measurement time for each hysteresis loop and t_2 = 5400s as the samples were reset for 90 minutes. The calculated variation of the integral over the volume distribution is shown in Figure 67 (black line). There is a close correlation between the form of the variation of H_{ex} and $\int_{V_1}^{V_2} f(V)dV$ with t_{AF}. This is again consistent with an *AF* grain volume interpretation of exchange bias.

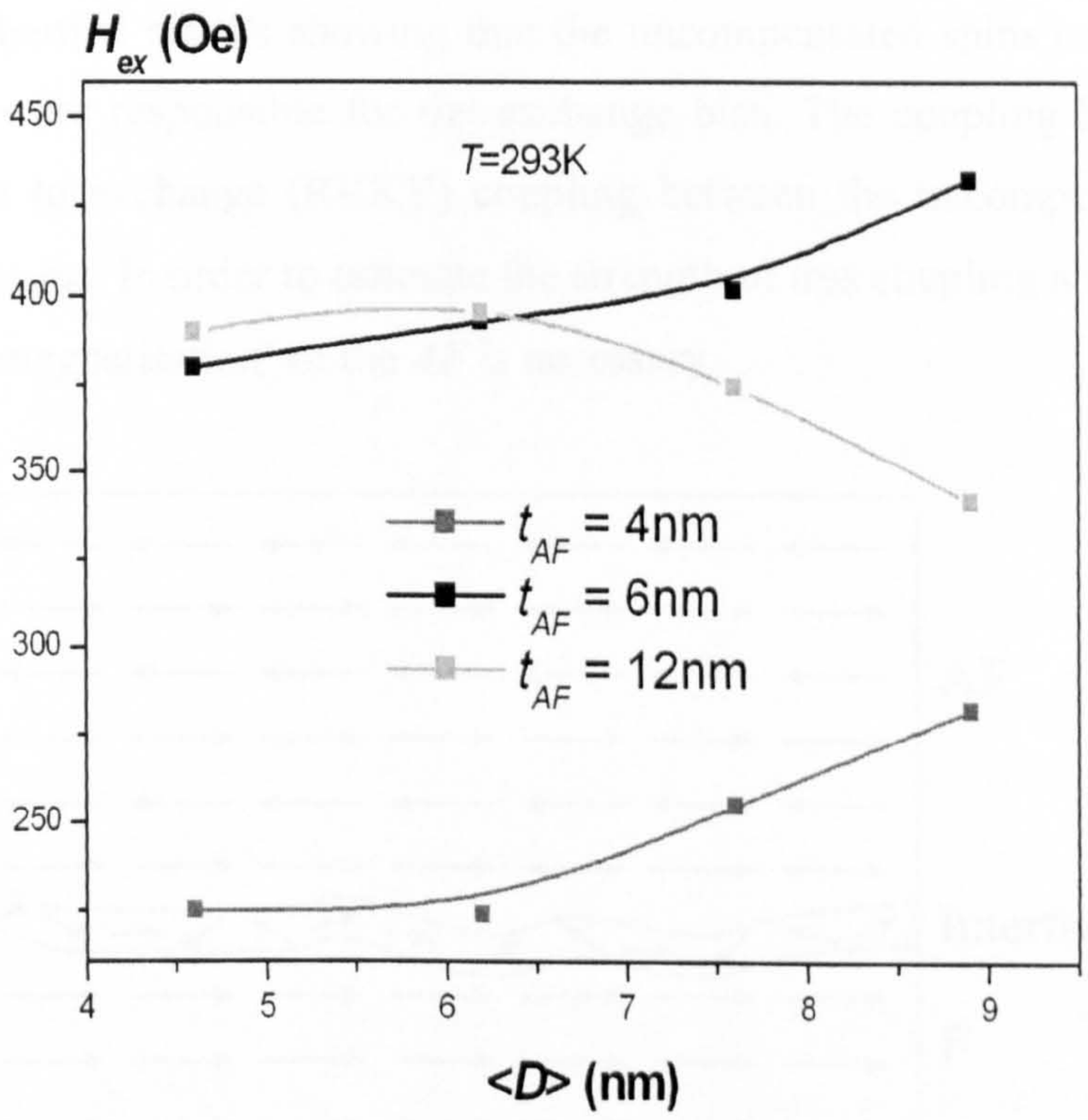

Figure 70. Exchange bias as a function of the *AF* grain size for t_{AF} = 4, 6 and 12nm.

The dependence of H_{ex} on the *AF* grain size has also been studied at room temperature. Figure 70 shows the results for the samples with t_{AF} = 4, 6 and 12nm. The exchange field is observed to increase with the *AF* grain size for the sets with t_{AF} = 4 and 6nm. However for the samples with t_{AF} = 12nm H_{ex} goes through a maximum at $\langle D \rangle \approx$ 6nm decreasing for bigger grain sizes. These results can be explained on the same basis as the thickness dependence of H_{ex} shown in Figure 67.

Even though these results can be explained in terms of the energy barrier to reversal in the *AF* layer, different interpretations can be found in the literature. Usually, models based on the formation of domains in the *AF* layer such as the domain state model are used (Nowak *et al.*, 2002). One of the most important limitations of the initial domain state model was the high value of the anisotropy of the *AF* ($K_{AF} = \infty$) required for the formation of domains in the *AF* layer. However, Misra *et al.* (2004) showed that the anisotropy limit was not a restriction due to the appearance of a peak in the exchange field for intermediate anisotropies (Misra *et al.*, 2004). However, these calculations were made at 0K and thermal activation was not taken into account. Recently, Papusoi *et al.* (2006) have studied the tuning of exchange bias in metallic *AF*s ($Fe_{50}Mn_{50}$) by inserting nonmagnetic Cu defects in the *AF* layer. They applied the domain state model incorporating thermal effects showing that the uncompensated spins on the surface of the *AF* grains were responsible for the exchange bias. The coupling between the *AF* grains was due to exchange (RKKY) coupling between the uncompensated spins of neighbouring grains. In order to estimate the strength of this coupling a measurement of the 'saturation magnetisation' of the *AF* is necessary.

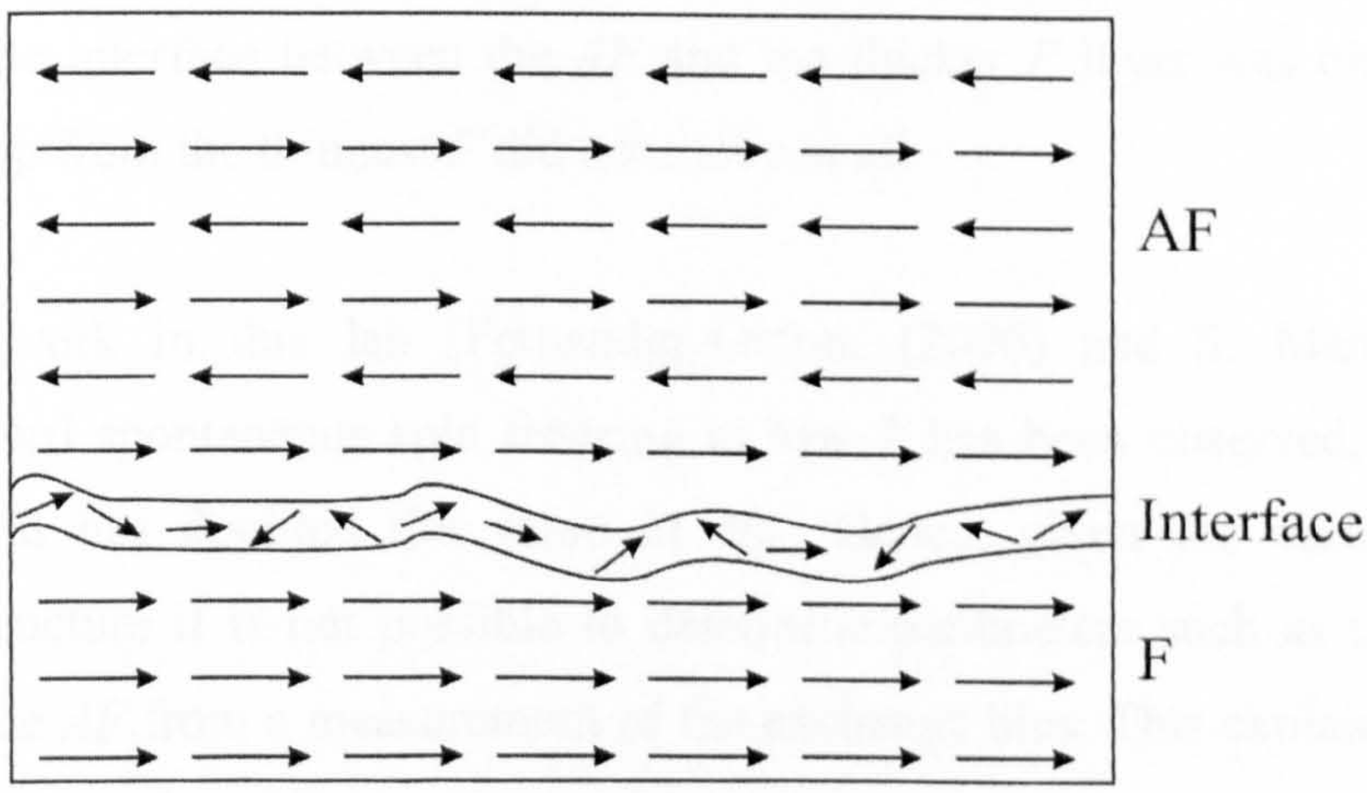

Figure 71. Spin configuration at the interface of an exchange biased bilayer.

6.3.2.2. Granular model of exchange bias

From the data presented in this thesis the key parameter that governs exchange bias is thermal activation of the bulk of the *AF*. Thermal activation limits the fraction of the *AF* that contributes to the loop displacement although the pinning of the *AF* layer is also moderated by the interfacial exchange coupling at the interface. In almost all models of exchange bias it is necessary to introduce a parameter C^* which has been called the interfacial exchange coupling constant to predict the correct value of the loop shift [e.g. Fulcomer and Charap (1972a), Khapikov *et al.* (2000), Nowak *et al.* (2002)]. The correct form of the exchange field is then

$$H_{ex}(T) = C^*(T) H_{ex}^i \int_{V_1(T)}^{V_2(T)} f(V)\,dV$$

where H_{ex}^i is an intrinsic exchange bias. The question then arises as to the exact nature of the interfacial spin contribution. In real systems, especially samples grown by sputtering, the interfaces are rough and the atoms at the interface might be neither ferromagnetic nor antiferromagnetic as shown in Figure 71.

In a recently published work from this lab (Dutson *et al.*, 2006) it has been shown that spin ordering at the interface can be achieved by thermal energy coupled to the exchange field from the *F* without changing the structure of the bulk of the *AF*. Figure 72 shows data from this publication where two *F* layers are pinned by a single *AF* layer. By activating the *AF* at different temperatures in the presence of a negative field, spin ordering at the interface between the *AF* and the thicker *F* layer was observed as the hysteresis loop from the thinnest *F* did not move at all.

In separate work in this lab [Fernandez-Outon, (2006) and S. Manzoor, private communication] spontaneous spin freezing at low *T* has been observed, which in the case of FeMn has doubled the value of H_{ex}. Hence, given the variability of the interfacial structure it is not possible to determine parameters such as the anisotropy constant of the *AF* from a measurement of the exchange bias. This explains why values in the literature are found to be counterintuitive.

From the work in this thesis it is not possible to specify the nature of the spin structure at the interface. There is the possibility that those spins behave like a spin-glass in diluted systems (B. Hillebrands, private communication). At high temperatures the spins at the interface are weakly coupled but when the temperature is reduced below a certain value they can order spontaneously increasing significantly the value of the interfacial exchange coupling. Also, recent data (Fernandez-Outon, private communication) has shown that field ordering is also possible. This latter phenomenon accounts for the need to use large magnetic fields for setting *AF*s in commercial applications (A. B. Johnston, private communication).

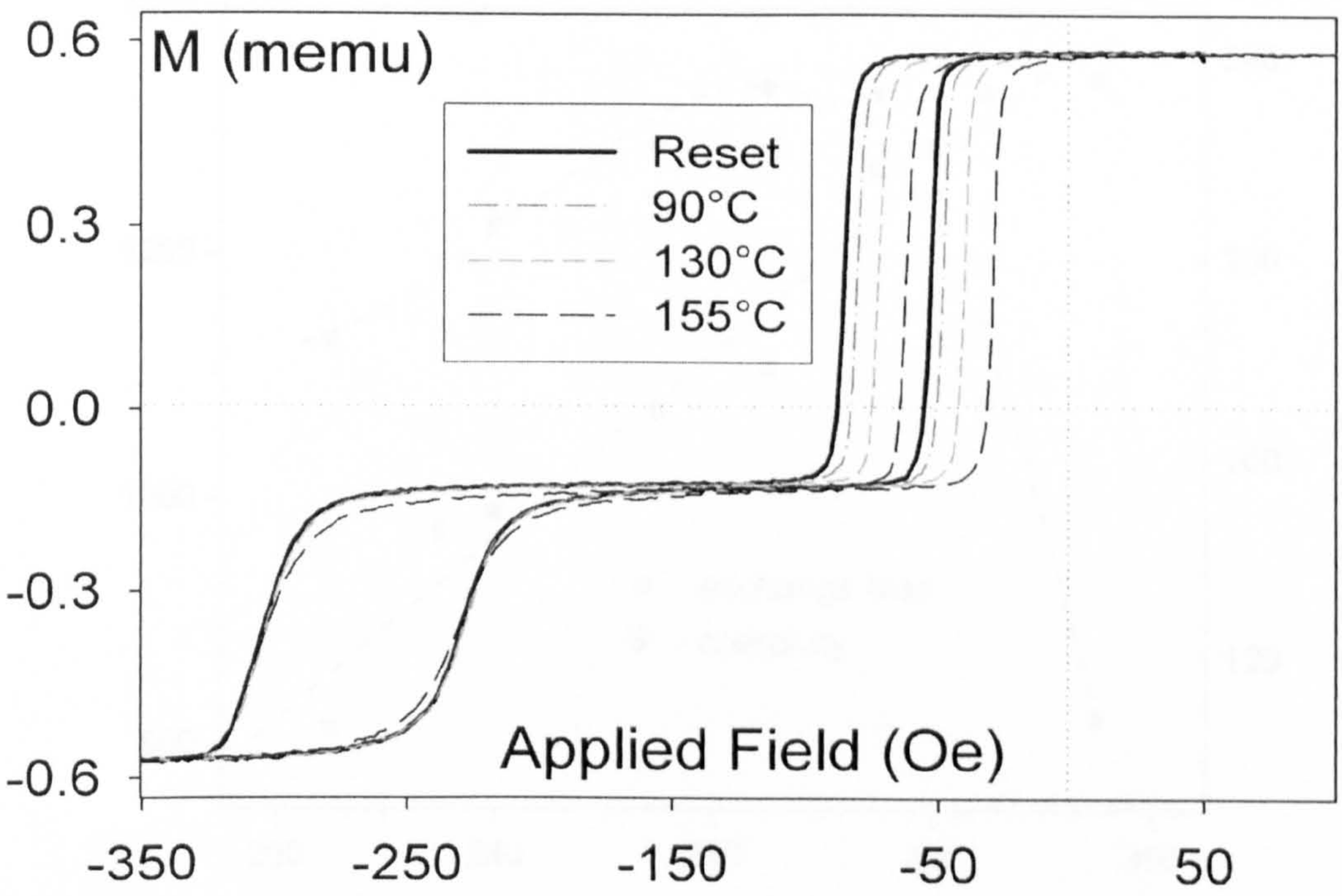

Figure 72. Thermal activation measurements for a CoFe(8nm)/IrMn(5nm)/CoFe(12nm) trilayer at moderate temperatures. Only the interface CoFe(8nm)/IrMn is thermally active (Dutson *et al.*, 2006).

An alternative explanation lies in the domain state model where the interfacial spin ordering contributes to the formation of domains. Such domains would not extend to the bulk of the *AF*. However, from the data presented in this thesis it is not possible to clarify the governing mechanism.

6.4. Annealing Effect on $IrMn/Co_{60}Fe_{20}B_{20}$ Bilayers

In the previous section the effect of the *AF* grain size on the exchange field in polycrystalline CoFe/IrMn bilayers has been reported. The grain size was changed through the deposition conditions. When conventional sputtering techniques are used different parameters such as the thickness of the seed layer are varied to achieve changes in the grain structure of the *AF* layer (e.g. Nishioka *et al.*, 1996). In other cases magnetic annealing has been shown to promote grain growth. For example in-situ deposition annealing at 250°C has been reported to increase the *AF* lateral grain size by 35% in IrMn/CoFe bilayers (Imakita *et al.*, 2005).

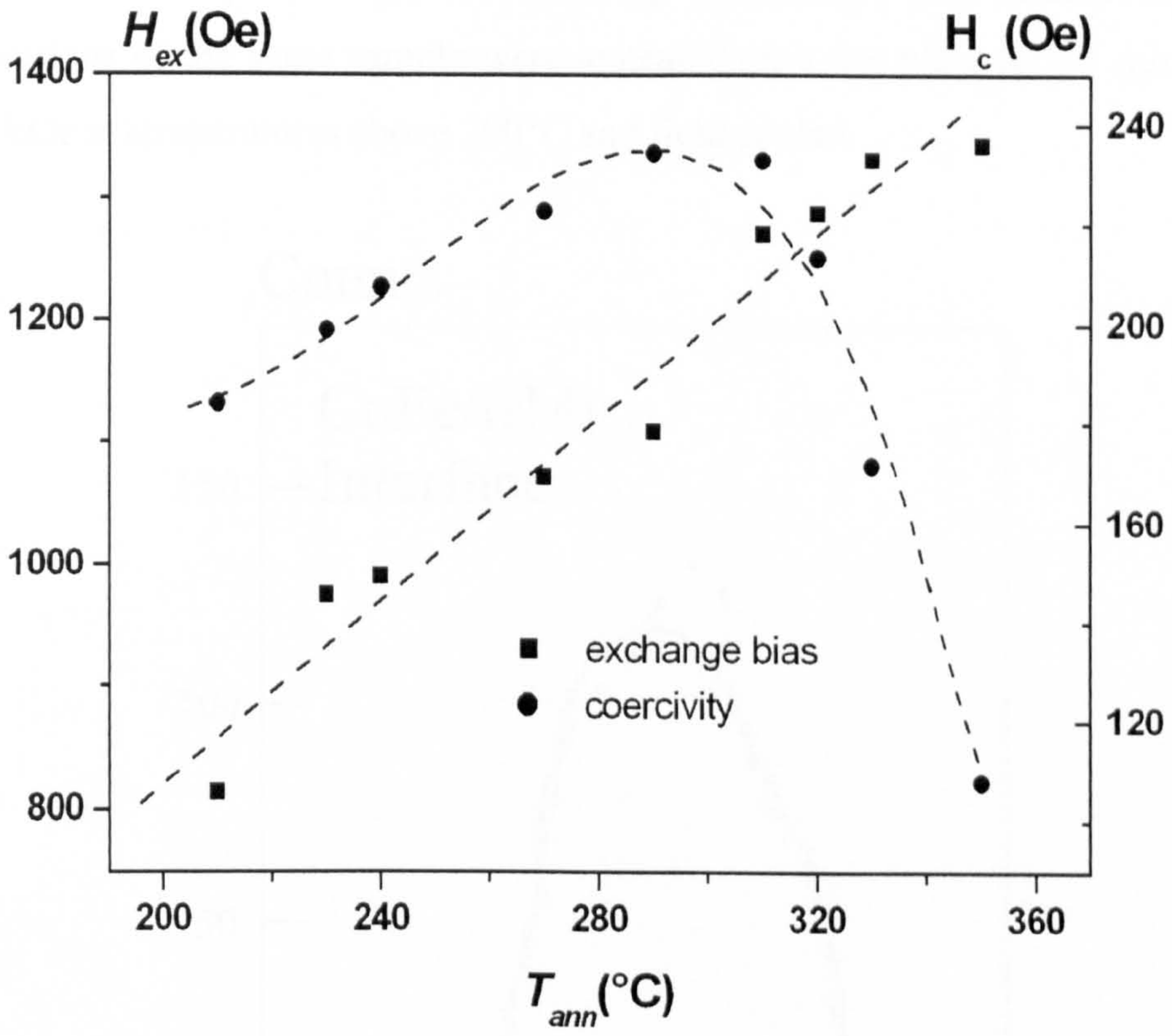

Figure 73. Exchange field and coercivity as a function of the annealing temperature T_{ann}.

In this work IrMn/CoFeB exchange biased bilayers grown using a conventional sputtering system have been subject of thermal treatment and their magnetic properties have been studied. The intention of this systematic study is to promote minor grain growth within the *AF* layer and look at the effect that this might have on the exchange field. This work was done during a three-month industrial placement at SIEMENS Erlangen (Germany) in 2005. The samples were grown by T. Dimopoulos. Is should be

noted that this work was undertaken prior to the full development of the grain size distribution effect in late 2006 and published in the Journal of Magnetism and Magnetic Materials. It is the published analysis the appears here as detailed TEM analysis was not available to reassure the data according to the final model.

A sample with composition Ru(30nm)/IrMn(8nm)/CoFeB(3nm)/Ru(15nm) was deposited by dc and rf magnetron sputtering on a plasma etched, thermally oxidized Si wafer. This is an interesting system as amorphous electrodes increase the TMR effect in comparison with systems using polycrystalline ferromagnets such as CoFe or permalloy. However, this also leads to a large increase of the resistancexarea product (RxA) and this is dependent on the annealing temperature (e.g. Dimopoulos *et al.*, 2005). Sections of the same sample were annealed on a hot plate for 15 minutes in a field of 5kOe at temperatures above 200°C and field cooled.

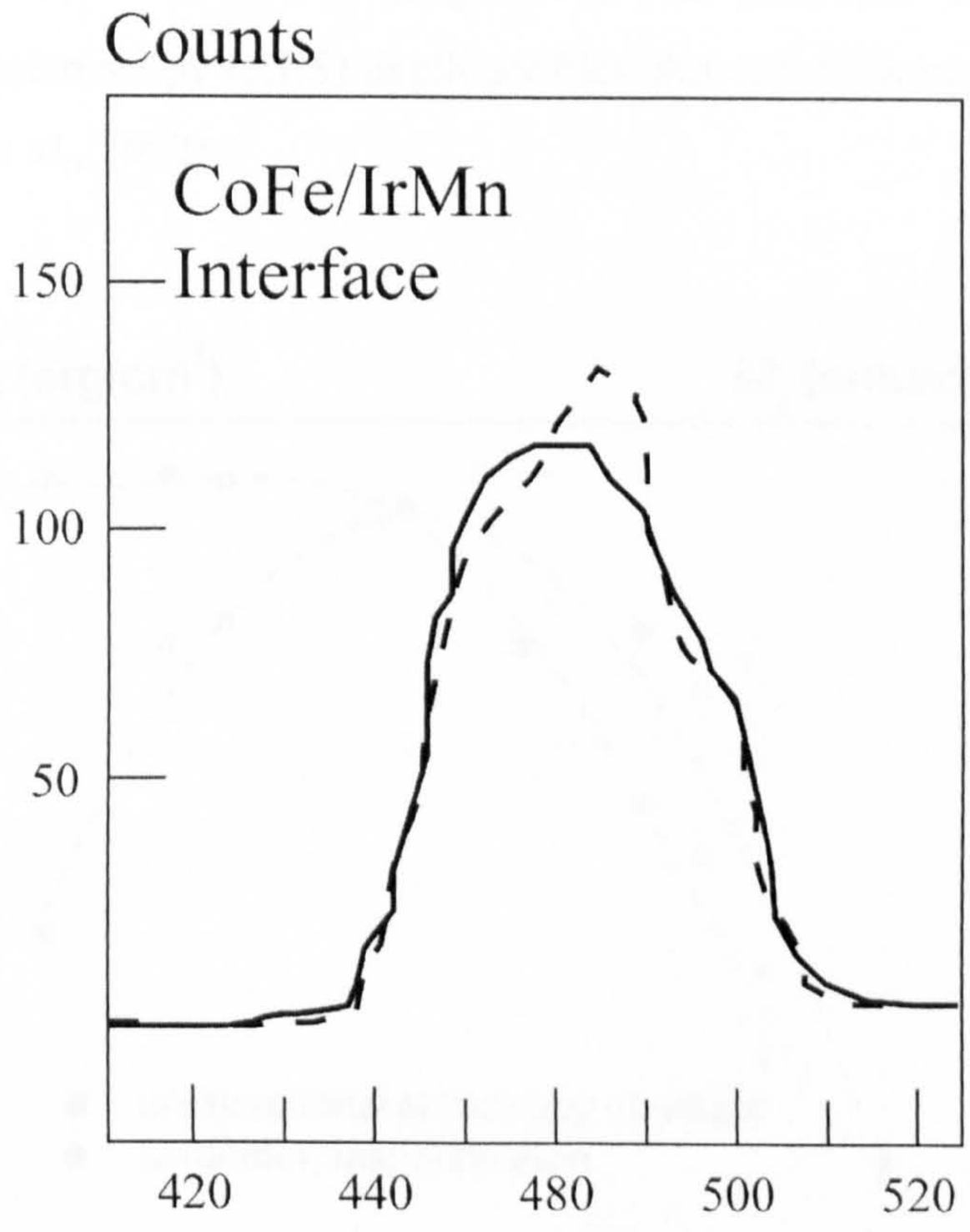

Figure 74. High statistics RBS spectrum for as-deposited junctions (solid line) and annealed at 435°C (dotted line) (reproduced from Cardoso *et al.*, 2000).

Figure 73 shows the variation of the exchange field and the coercivity as a function of the annealing temperature T_{ann}. The exchange field H_{ex} was observed to increase linearly with the annealing temperature whereas the coercivity rises for T_{ann}<300°C and then falls dramatically. This behaviour above 300°C is most probably due to the diffusion of Mn atoms at the *F*/*AF* interface. Cardoso *et al.* (2000) showed that strong interdiffusion starts at the CoFe/IrMn interface above 300°C in CoFe/Al_2O_3/CoFe/IrMn spin tunnel junctions. The junctions were annealed in the range 25-435° and examined by Rutherford backscattering analysis (RBS). Figure 74 shows a high statistics RBS spectrum for as-deposited junctions and annealed at 435°C. Strong interdiffusion at the CoFe/IrMn interface manifested itself in the destruction of the interference peak observed at channel 482 in the as-deposited state (Cardoso *et al.*, 2000). Similar conclusions were reported by Yoo *et al.* (2002) when studying the diffusion characteristics of Mn in exchange biased electrodes IrMn/Ta(0.2nm)/CoFe/AlO_x and IrMn/CoFe/Ta(0.2nm)/AlO_x used in magnetic tunnel junctions annealed at 300°C. Auger Electron Spectroscopy (AES) depth profiles showed diffusion of Mn toward the oxide layer (Yoo *et al.*, 2002).

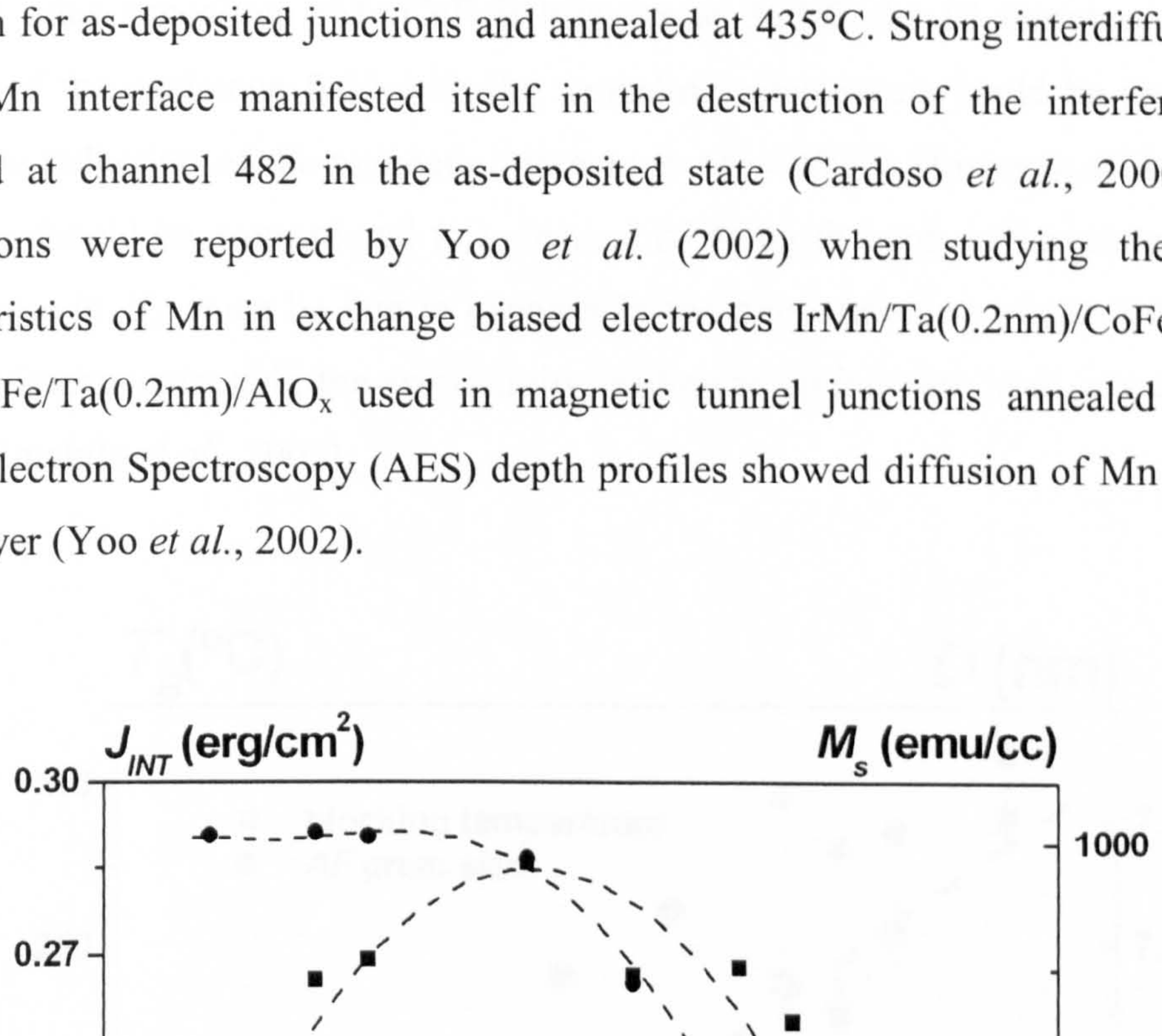

Figure 75. Unidirectional anisotropy constant and saturation magnetisation as a function of the annealing temperature T_{ann}.

The different behaviour of H_{ex} and H_c indicate different origins for the uniaxial and the unidirectional anisotropy. Figure 75 shows the variation of the unidirectional anisotropy constant $J_{INT}=M_s t_F H_{ex}$ and the saturation magnetisation M_s of the *F* layer. The reduction in the magnetic moment above 280°C is again believed to be due to the interdiffusion of Mn across the *F*/*AF* interface and this also results in a reduction of the exchange interaction across the interface. Cardoso *et al.* (2000) reported a reduction of 44% in the magnetic moment of the pinned layer in CoFe/Al_2O_3/CoFe/IrMn spin tunnel junctions after annealing at 435°C for 90 minutes. In this work a reduction of 52% has been observed after annealing IrMn/CoFeB bilayers at 350°C for 15 minutes. The steady increase of the exchange field with the annealing temperature could be thought to be due to the reduction of the magnetic moment in the CoFeB. However, if this were the case, J_{INT} should be proportional to t_F instead of going through a maximum. Therefore the increase in H_{ex} must be due to changes in the microstructure of the samples, most probably improvements in the crystallinity leading to an increase in K_{AF} or minor grain growth (Imakita *el al.*, 2005).

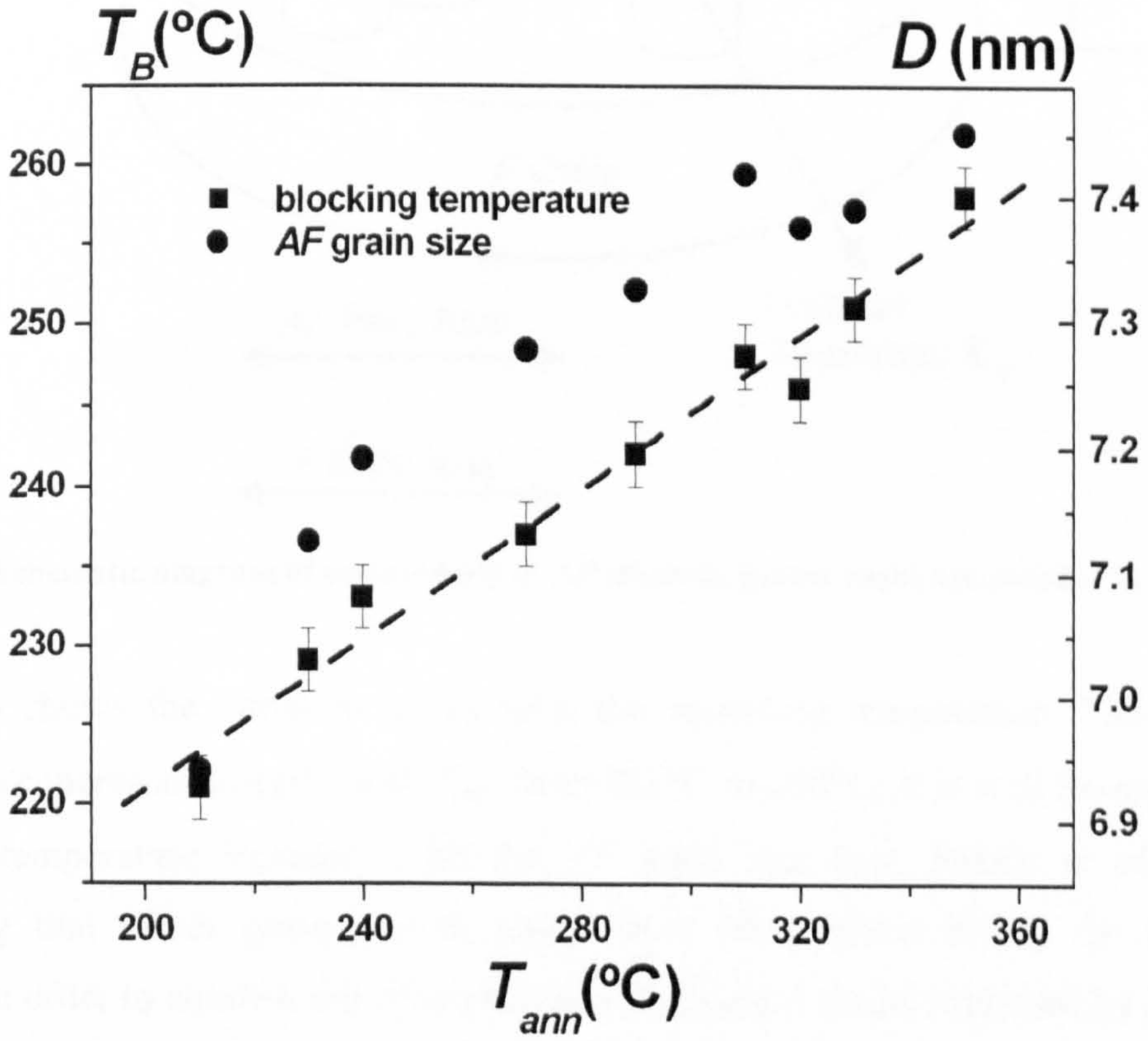

Figure 76. Blocking temperature and calculated *AF* grain size as a function of the annealing temperature T_{ann}.

The dependence of the blocking temperature T_B on the annealing temperature has also been studied. In this study T_B is defined as the temperature at which the exchange bias goes to zero and it was determined following the conventional measurement procedure described in Chapter 4 where hysteresis loops are measured at increasing temperatures until the loop shift vanishes. These measurements were made in SIEMENS using a NanoMOKE2^{TM} system. MOKE measurements were done averaging over 50 loops at a frequency of 1.5 Hz. This measurement procedure had to be used due to the lack of equipment to make low temperature measurements without averaging over a number of loops.

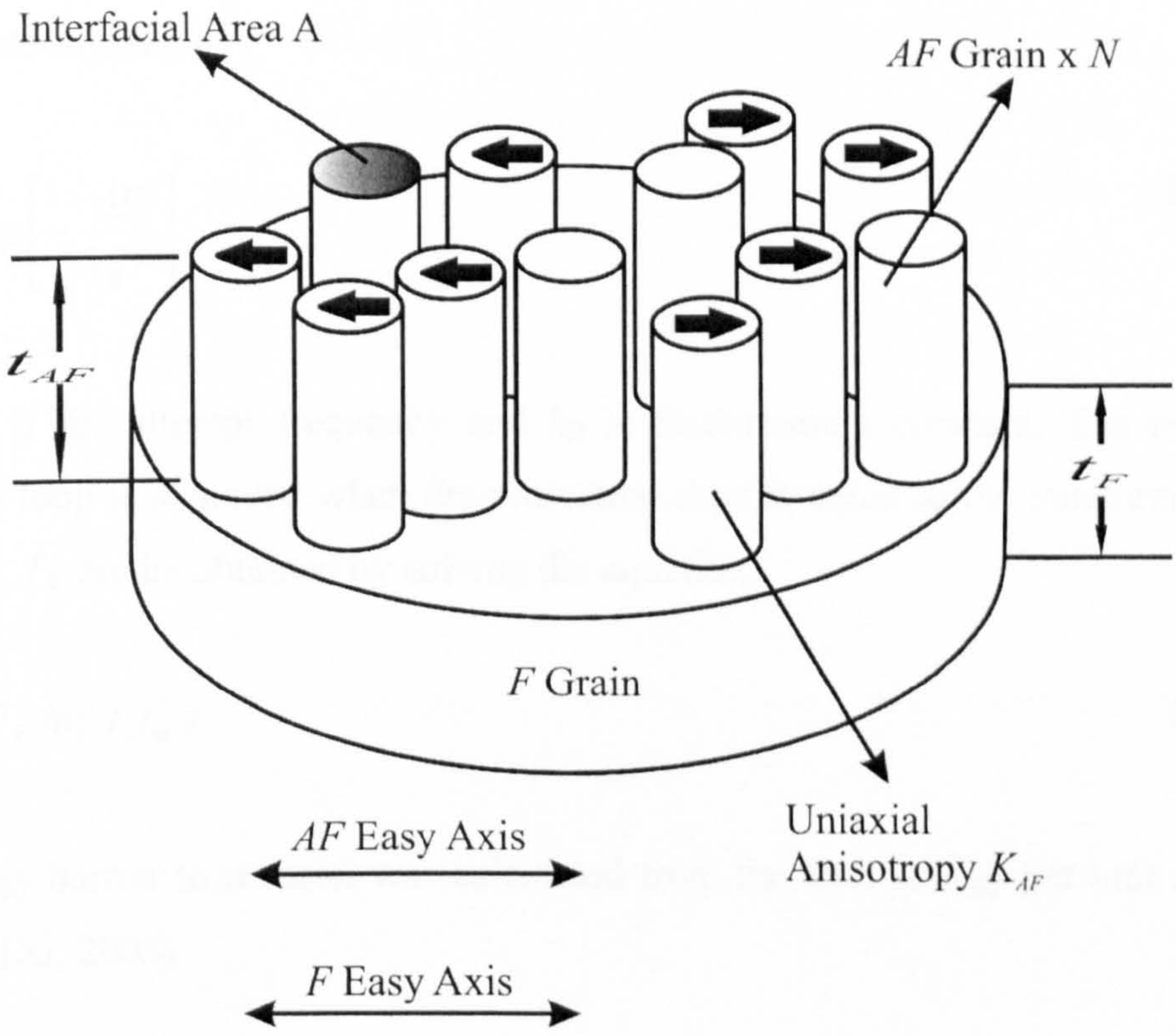

Figure 77. Schematic diagram of an assembly of *AF* identical grains exchange coupled to a *F* layer.

Figure 76 shows the variation of T_B with the annealing temperature. The blocking temperature increases linearly with T_{ann} from 221°C to 258°C. It is well known that the blocking temperature increases with the *AF* grain size (e.g. Pakala *et al.*, 2000b) suggesting that minor grain growth might have taken place during the annealing process. In order to confirm this idea a thermal fluctuation model proposed by Xi (2005) has been used to calculate the *AF* grain size. Xi based his calculations in the conventional measurement procedure so the model can be applied to these results. This

might be sufficient to a first approximation but no major conclusions can be obtained due to the irreproducibility of the data. Note that this irreproducibility affects almost all the data available in the literature as no special care was given to the measurement procedure (Fernandez-Outon *et al.*, 2004). Figure 77 shows a schematic diagram of the model proposed by Xi (2005) where an *F* grain is exchange coupled to an assembly of *AF* grains with an energy/area J_{INT}. In this model T_B was determined from the energy barrier to reversal of the *AF* grains which depended on the grain size *D* among other parameters (Xi, 2005).

The time τ for an *AF* grain to overcome an energy barrier ΔE and switch to another energy state is given by

$$\frac{1}{\tau} = f_0 \exp\left[-\frac{\Delta E}{k_B T}\right] \qquad \text{Eq. 6.22}$$

where f_0 is the attempt frequency and k_B is Boltzmann's constant. The non-shifted hysteresis loop is achieved when the relaxation time is equal to the measurement time t_m. Hence, T_B can be obtained by solving the equation

$$\Delta E = k_B T_B \ln(f_0 t_m) \qquad \text{Eq. 6.23}$$

The energy barrier to reversal was calculated from the total energy per unit area of an *AF* grain (Xi, 2005)

$$\Delta\varepsilon_{\pm} = K_{AF} t_{AF}\left[1 + \left(\frac{J_{INT}}{2K_{AF} t_{AF}}\right)^2\right] \pm J_{INT} \qquad \text{Eq. 6.24}$$

where K_{AF} is the *AF* uniaxial anisotropy constant and t_{AF} the antiferromagnetic layer thickness. The energy barrier of an *AF* grain is given by $\Delta E = \Delta\varepsilon\_D^2$ and, therefore, the *AF* grain size can be calculated. For the calculations K_{AF} was assumed to be 1.8×10^6erg/cc as reported by Carey *et al.* (2001).

$$D^2 = T_B k_B \ln(f_0 t_m)\left\{K_{AF} t_{AF}\left[1+\left(\frac{J_{INT}}{2K_{AF} t_{AF}}\right)^2\right] - J_{INT}\right\}^{-1} \qquad \text{Eq. 6.25}$$

Figure 76 shows the calculated values of the *AF* grain size as a function of the annealing temperature T_{ann}. There is a small increase of the calculated value of D with T_{ann}. However, this corresponds to a 20% increase in volume emphasising the fact that not only the interfacial spins contribute to the magnitude of the exchange field but also the bulk of the *AF*. The correlation between the variation of D and T_B with T_{ann} is good but the possibility that crystallographic changes are not responsible for the increase in T_B cannot be discounted. Furthermore, no temperature dependence of K_{AF} and J_{INT} has been assumed. The structure of the samples has been analysed by grazing incident X-ray diffraction (GID). I have to acknowledge Prof. B. K. Tanner and Dr. A. Lamperti for the X-ray measurements. The superporstion of the Ru (002) and the IrMn (111) peaks made it impossible to associate the peak in the diffraction patterns only to the *AF* layer. In order to extract concluding information either a different material has to be used as a buffer and cap layer or a much thicker *AF* layer has to be grown to increase the contribution from IrMn to the peak. Another possibility is to decrease the total thickness of the Ru layers. The samples studied in this work contained a 30nm thick seed layer and a 15nm capping layer making it too difficult to identify the contribution from the 8nm IrMn layer.

Chapter 7 Conclusions and Future Work

7.1. Conclusions

The capability of the HiTUS sputtering system to produce samples with controlled grain size and grain size distribution without the use of seed layers, additives or annealing has been demonstrated. Control of the grain size is achieved via control of the growth-rate which is most sensitive to the bias voltage. Full grain size analysis of the samples studied was achieved via TEM imaging. All the distributions were found to be lognormal with parameters calculated using a statistical method which ensured good theoretical fitting even for a small number of experimental points. However, over five hundred particles were measured for each sample to ensure good statistics.

Five different materials have been studied: Cr, NiFe, CoFe, FeMn and IrMn. All of them were chosen due to their importance from a technological point of view since all these materials are used in either the fabrication of magnetic hard disks or in read-head. Both the mean grain size and the width of the distribution were found to increase with increasing sputtering rate. A rather different grain structure for different materials at similar sputtering rates was observed. While the grain size in Cr increased from ≈12 to ≈19nm with increasing bias voltage from –200 to –1000V only a rather small increase from ≈4 to ≈6nm was found for NiFe in the same voltage range. Even though this is a small increase in size it corresponds to a 44% increase in volume and this can have a dramatic effect in the thermal stability of magnetic films since it is the volume of the particles that governs the energy barrier to reversal.

One of the most important advantages of HiTUS is the capability to sputter from thick ferromagnetic materials. In particular, soft CoFe alloy films are used as an underlayer for perpendicular media. However, CoFe is naturally hard and different seed layers and/or additives are used to reduce the coercivity. This has the disadvantage of increasing the total thickness of the disk/sensor. Usually, the reduction in the coercivity is attributed to a reduction in the grain size. In this work similar results have been

obtained by changing the bias voltage of the deposited samples sputtered directly on Si substrates. The coercivity was reduced from ≈125Oe to ≈12Oe just by tuning the bias voltage used to deposit the samples.

The principal aim of this work was to clarify the role of the antiferromagnetic grain size on exchange bias. This is an issue that still remains unclear fifty years after the discovery of exchange bias and many conflicting reports can be found in the literature regarding this topic. This, in part, is due to the fact that different systems might behave differently and this is not usually taken into account when interpreting the data. Another key parameter is that most of the studies in the literature are not specific with respect to the measurement conditions. It is known that antiferromagnets are thermally unstable and thermal activation occurs during measurement unless careful measurement procedures are followed.

Two different antiferromagnetic systems have been studied in this work both of which are metallic: FeMn and IrMn. The latter is the most important antiferromagnet from a technological point of view due to its high thermal stability and large exchange anisotropy achievable after heat treatment at moderate temperatures. In this work all the data has been interpreted via a simple granular model incorporating a measured grain volume distribution. It has been found that this model can explain all the data presented in this work when account is taken of the separate contributing effects to H_{ex} such as spin reorientation and interfacial spin disorder. Our ability to produce samples with controlled grain size has allowed a systematic study to be made.

Samples with different antiferromagnetic thicknesses and grain sizes were prepared using HiTUS. In this work it has been shown that a full understanding of the energy barrier to reversal within the *AF* layer is necessary for the explanation of exchange bias in systems containing a polycrystalline metallic *AF*. Also it has been shown that there is no clear relationship between the unidirectional and the uniaxial anisotropy. The granular theory has predicted the right shape for the *AF* thickness and the *AF* grain size dependence of the exchange field. Also it has been shown that not only the grain size is important but also the width of the distribution plays a crucial role in determining the fraction of the *AF* that is set and stable at a given temperature. Therefore, narrowing the

AF volume distribution could significantly increase the pinning properties of the *AF* layer.

A critical development has been the measurement of the anisotropy constant of antiferromagnets K_{AF} from a measurement of the median blocking temperature only, leading to $K_{IrMn}(293K) = 4.14x10^6 erg/cc$ and $K_{FeMn}(293K) = 1.36x10^6 erg/cc$. This method has the key advantage that the anisotropy values obtained are independent of the interfacial structure. Critically this calculation was made exclusively using experimental data with no fitting parameters other than the temperature dependence of K_{AF} used. Since the form of the $H_{ex}(t_{AF})$ is determined by the form of the lognormal distribution function rather than the limits on the integral, the exact form of $K(T)$ is not important.

There is little data in the literature regarding the value of K in *AF*s but usually it is determined from a measurement of H_{ex} where contributions from both the bulk of the *AF* and the interface are present. It is noteworthy that the values obtained in this work are significantly higher than those in the literature, especially for FeMn. We believe that the understanding of the correct form of the distribution of blocking temperatures and the role of interfacial spins accounts for those discrepancies and implies that our results are more reliable. The fact that our data can be used to obtain the correct form of the $H_{ex}(t_{AF})$ curve would seem to confirm this assertion.

The fact that exchange bias has not been fully explained after 50 years is an indication of the complexity of this subject. All the results obtained in this work are consistent with a granular model similar to that of Fulcomer and Charap (1972). This in contrast with the vast majority of models in the literature, which may apply to systems containing an oxide or single crystal antiferromagnet. The granular approach coupled with an understanding of interfacial ordering, and where thermal activation of the *AF* grains is taken into account, is able to give a full explanation of the data presented in this work.

7.2. Future Work

The work in this thesis has shown that the majority of the experimental features observed in metallic polycrystalline exchange biased systems can be explained by a grain volume model of exchange bias. There are still several features that remain open such as the control of K_{AF}, the role of crystallinity and the role of orientation. A project is being prepared to study these effects as part of a EU collaborative grant.

The energy barrier to reversal is given by $K_{AF}V_{AF}$. Using HiTUS the volume of the grains can be controlled. However, the anisotropy also needs to be tuned in order to achieve thermally stable grains that can be set. Tsunoda and co-workers (e.g. Tsunoda *et al.*, 2006) have published a series of papers during the last few years where $L1_2$-phase Mn_3Ir was reported in the compositional range 22-32% Ir. This is an ordered alloy with a Néel temperature ≈900K, 200K higher than that of disordered IrMn. Different seed layers and deposition procedures were used indicating that a Ru underlayer as thin as 5nm is enough to achieve a highly anisotropic *AF* layer. Ru was chosen due to its high melting point to avoid interdiffusion between the *AF* and the underlayer. The intention is to look at the role of crystallinity in the energy barrier *KV* using the technologies described herein.

Other work ongoing in the lab has shown that the inability to set the *AF* is significant (Fernandez-Outon, private communication). Interestingly, the growth of exchange bias with setting time at a given temperature has shown the lnt dependence predicted in this work. However, due to the nature of the log function, increasing the resetting time cannot be used to set highly anisotropic grains. In order set the whole distribution it is necessary to combine control of K_{AF} with control of the grain size. Due to the difficulty in setting the bigger grains a narrower distribution of grain sizes will be necessary. Anisotropy is an intrinsic property of a material. However, when the grain size is reduced to the nanometre scale, grain boundaries become an important fraction of the total volume of the grain. At the grain boundaries the order is broken as each atom does not have the right number of neighbours and, therefore, a dependence of K_{AF} on the grain size may occur. The same behaviour might be expected when the thickness of the *AF* layer is reduced to a few atomic layers as reported by Stenbeck *et al.* (2004). A

study of the finite size effect on K_{AF} is now possible using the techniques described in section 6.3.1.

The data presented in this work refer to the contribution to H_{ex} from the bulk of the *AF*. Other contributions such as that due to the interface have also been studied in an ongoing project in the laboratory although those measurements are not included in this thesis. There is clearly a requirement to study the interfacial spin structure of exchange bias systems and the parameters that govern it. Some of the measurement techniques employed in this work can be used for this study. Resetting the *AF* at different fields has shown to increase H_{ex} only in the first loop. However, when the detailed measurement procedure to determine $H_{ex}(T_{ACT})$, described in Chapter 5, is followed the results are independent of the resetting field as long so the *F* is saturated. This suggests that the order established by resetting at high fields is broken after the field is reversed. Since it is the bulk of the *AF* that is thermally activated when holding the sample at negative bias, this implies that the spin ordering is only established at the interface. Also, as the order is easily broken, it is possible that those interfacial spins are free spins coming from the *F* and/or the *AF*. This can be a consequence of the lack of crystallization at the grain boundaries. Therefore, it seems possible to control the degree of order at the interface although new measurement protocols might be necessary due to the apparent weakness of this ordering.

The work in this thesis has been very successful in predicting several features of exchange bias and a significant contribution to this has been the use of good measurement protocols. Having used measurement protocols that have been shown to work for polycrystalline exchange biased systems it is now obvious to apply the same protocols to other systems such as single crystals or oxide films where domain walls within the *AF* are possible.

Chapter 8 Appendices

List of Symbols

δ	Domain wall width
τ	Relaxation time
χ	Magnetic susceptibility
ρ	Density
γ	Molecular field constant
β	Angle between the magnetisation and the *F* anisotropy axis
α	Angle between the *AF* sublattice magnetisation and the *AF* anisotropy axis
θ	Angle between the applied field and *F* anisotropy axis
Θ	Angle between the applied and the cooling field direction
ξ	Interface thickness between the ferromagnet and the antiferromagnet in an exchange biased bilayer in the model of Mauri *et al.* (1987a)
ψ	Fitting parameter in the model of Mauri *et al.* (1987)
ζ	Anisotropy term in the model of Mauri *et al.* (1987)
κ	Fitting parameter in the model of Mauri *et al.* (1987)
ϕ	Angle between adjacent spins
γ	Molecular field constant
Φ	Ordering temperature
σ	Standard deviation
μ	Mean value
$\Delta\sigma$	Effective pressure from the interfacial energy difference in the model of Malozemoff (1987)
δ^*	Magnetic energy at the interface in the model of Mauri *et al.* (1987a)
σ_0	Domain wall energy at 0K
σ_{0A-B}	Specific magnetisation of an antiferromagnetic sublattice at 0K

$\alpha_1\ \alpha_2\ \alpha_3$	Cosines of the angles that the magnetization vector makes with the crystal axis in a cubic crystal
$\sigma_{A\text{-}B}$	Specific magnetisation of an antiferromagnetic sublattice
α_{crit}	Critical angel in the model of Stiles and McMichael (1999a)
σ_{DW}	Energy per unit area in a domain wall
ΔE	Energy barrier
ΔE_c	Critical value of the energy barrier
$\Delta\varepsilon_{\pm}$	Energy per unit area of an antiferromagnetic grain in the model of Xi (2005)
$<D>$	Mean grain size
$<V>$	Median volume
a	Lattice parameter
A	Cross sectional area
A_{AF}	Exchange stiffness of the antiferromagnet
AC	Alternate current
AES	Auger Electron Spectroscopy
A_F	Exchange stiffness of a ferromagnet
AF	Antiferromagnet
AF-AF	Exchange stiffness at the interface between a ferromagnet and an antiferromagnet
AGFM	Alternating Gradient Force Magnetometer
Bcc	Base centred cubic
C	Curie constant
C^*	Interfacial exchange coupling constant
c/a	Axial ratio of an elongated particle
CPM	Cumulative percentage method
DC	Direct current
DW	Domain wall
E_a	Magnetocrystalline anisotropy energy
EB	Exchange Bias
E_{ex}	Exchange energy
E_{exc}	Intergranular exchange coupling
EMF	Electromagnetic force

F	Ferromagnet
$f(V)$	Distribution of volumes
f_0	Attempt frequency
Fcc	Face centred cubic
FMR	Ferromagnetic resonance
GID	Grazing incident diffraction
GMR	Giant magnetoresistance
H	Magnetic field
H_c	Coercivity
H_{c1}	First coercive point. Value of the coercive field for the first branch of the loop
H_{c2}	Second coercive point. Value of the coercive field for the second branch of the loop
H_D	Demagnetising field
HDD	Hard Disk Drive
H_{ex}	Exchange field
H_{ex}^{i}	Intrinsic exchange bias
HiTUS	High Target Utilisation Sputtering
H_K	Anisotropy field
H_K^*	Pseudo anisotropy field
H^*	Exchange field in an antiferromagnet produced by a ferromagnet
H_m	Molecular field
J_F	Exchange coupling constant between ferromagnetic spins
J_{AF}	Exchange coupling constant between antiferromagnetic spins
J_{ij}	Exchange integral
J_{INT}	Interface exchange constant between the F and a AF grain
K	Magnetocrystalline anisotropy constant
K_{AF}	Antiferromagnet uniaxial anisotropy constant
k_B	Boltzmann's constant
K_s	Shape anisotropy constant
K_u	Uniaxial anisotropy constant of a ferromagnet
L	Domain length

L_{ex}	Exchange length
m_{AF}	Magnetic moment of the antiferromagnet
MBE	Molecular beam epitaxy
MFM	Magnetic Force Microscope
$\underline{M}_i$	Magnetisation vector of an individual grain
MOIF	Magneto-Optic Indicator Film technique
MOKE	Magneto Optical Kerr Effect
MRAM	Magneto Random Access Memory
M_S	Saturation magnetisation
N	Number of atoms
N	Number of grains
$N_a\, N_c$	Demagnetising factors along the semi axes of an elongated particle
N_D	Demagnetising factor
$P_{+/-}$	Probability of an AF grain of being aligned parallel/antiparallel to the applied field
p_c	Dimensionless factor related to the crystal structure of a given material
q	Centre-to-centre distance between adjacent grains
Q	Quality factor
r_{3d}	3d shell radius
r_a	Atomic radius
RBS	Rutherford Backscattering analysis
RF	Radiofrequency
r_{ij}	Interatomic distance
RKKY	Indirect exchange interaction
RxA	Resistance area product in a magnetic tunnel junction
$S_{i,j}$	Atomic spin
T	Temperature
t	Time
t	Thickness
T_{ACT}	Temperature of thermal activation
T_{ann}	Annealing temperature

T_B	Blocking temperature
T_C	Curie temperature of a ferromagnet
t_{crit}	Antiferromagnetic thickness below the exchange field vanishes
TEM	Transmission Electron Microscopy
t_m	Measurement time
TMR	Tunnelling Magneto Resistance
T_N	Néel temperature of an antiferromagnet
T_{NA}	Thermal-activation-free temperature
TRM	Thermo Remanent Magnetisation
T_s, T_q	Cooling temperatures in the experiment of Gökemeijer and Chien (1999a,b)
UHV	Ultra high vacuum
V	Volume of a particle/grain
V_1	Critical volume below which the antiferromagnetic grains are thermally unstable
V_2	Critical volume above which the antiferromagnetic grains cannot be set
VSM	Vibrating Sample Magnetometer
z	Parameter of the order of 1 introduced as a consequence of interface irregularities (Imry and Ma, 1975)

References

A

Ajan, A., and Akamoto, I., *J. Appl. Phys.* **92** p.6099 (2002)

Alben, R., Becker, J. J., and Chi, M. C., *J. Appl. Phys.*, **49** p.1653 (1978)

Ali, M., Marrows, C. H., and Hickey, B. J., *Phys. Rev. B.*, **67** p.172405 (2003)

Allen, T., 'Particle size measurement', *2nd Ed, London Chapman & Hall* (1975)

Ambrose, T., and Chien, C. L., *J. Appl. Phys.*, **83** p.6822 (1998)

Andra, W., Danan, H., and Ropke, U., *IEEE Trans. Magn.*, **20** p.102 (1984)

B

Baibich, M., Broto, J., Fert, F., Nguyen Van Dau, Petroff, F., Etienne, P., Creuzet, G., Friederich, A., Chazelas, J., *Phys. Rev. Lett.*, **61** p.2472 (1988)

Bean, C. P., Livingston, J. D., *J. Appl. Phys. Suppl.*, **30** p.1205 (1959)

Berkowitz, A. E., Kodama, R. H., 'Exchange anisotropy in Nanomagnetism: Multilayers, Ultrathin films and textured media', *Bland, J. A. C., Mills, D. L., Editors* To be published (2005)

Binek, Ch., Borisov, P., Chen, X., Hochstrat, A., Sahoo, S., and Kleemann, W., *Eur. Phys. J. B*, **45** p.147 (2005)

Blamire, M., and Hickey, B., *Nat. Mat.*, **5** p.87 (2006)

Bozorth, R. M., 'Ferromagnetism', D. Van Nostrand Company, Canada (1951)

Bozorth, R. M., Ferromagnetism, *IEEE New York* (1993)

Brown, W. F., J. Appl. Phys. Suppl., **30** p.130 (1959)

Burham, R.A., and Granqvist, C.G., *J. Appl. Phys.*, **47** p.2220 (1976)

C

Cardoso, S., Freitas, P. P., de Jesus, C., Wei, P., and Soares, J. C., *Appl. Phys. Lett.*, **76** p.610 (2000)

Carey, M. J., Smith, N., Gurney, B. A., Childress, J. R., and Lin, T., *J. Appl. Phys.*, **89**

p.6579 (2001)

Carling, S. G., Visser, D., Hautot, D., Watts, I. D., Day, P., Ensling, J., Gütlich, P., Long, G. J., and Grandjean, F., *Phys. Rev. B.*, **66** p.104407 (2002)

Carpenter, D. T., Codner, J. R., Barmak, K., and Rickman, J. M., *Mater. Lett.*, **41** p.296 (1999)

Chantrell, R. W., "*Thermally activated reversal in exchange coupled bilayers*" ULTRABIAS summer school (2004)

Chen, Y. J., Lottis, D. K., Dahlberg, E. D., Kuznia, J. N., Wowchak, A. M., and Cohen, P. I., *J. Appl. Phys.*, **69** p.4523 (1991)

Childress, J. R., Carey, M. J., Wilson, R. J., Smith, N., Tsang, C., Ho, M. K., Carey, K., MacDonald, S. A., Ingall, L. M., and Gurney, B. A., *IEEE Trans. Magn.*, **37** p.1745 (2001)

Choi, Young-suk, Petford-Long, Amanda K., and Ward, Roger C. C., *Thin Solid Fims*, **489** p.186 (2005)

Choukh, A. M., *IEEE Trans. Magn.*, **33** p.3676 (1997)

Craig, B. R., McVitie, S., Chapman, J. N., Johnston, A. B., and O'Donnell, D. O., *J. Appl. Phys.*, **100** p.053915 (2006)

Cullity, B. D., Introduction to magnetic materials, *Addison-Wesley Publishing Company* (1972)

D

de Witte, A. M., El-Hilo, M., O'Grady, K., and Chantrell, R. W., *J. Magn. Magn. Mat.*, **120** p.184 (1993)

Devasahayam, A. J., Sides, P. J., Kryder, M. H., *J. Appl. Phys.*, **83** p.7216 (1998)

Dimopoulos, T., Gieres, G., Wecker, J., Wiese, N., Luo, Y., and Samwer, K., *J. Appl. Phys.*, **98** p.073705 (2005)

Dutson. J. D., Huerrich, C., Vallejo-Fernandez, G. V., Fernandez-Outon, L. E., Mao, S., Chantrell, R. W., and O'Grady, K., *In Press, J. Phys. D. Appl. Phys.*

E

$\mathcal{F}$

Fernandez-Outon, L. E., K. O'Grady, and Carey, M. J., *J. Appl. Phys.*, **95** p.6852 (2004)

Fernandez-Outon, L. E., *Measurement protocols for exchange biased systems*, PhD Thesis, University of York, (2006)

Flanders, P. J., *J. Appl. Phys.*, **63** p.3940 (1988)

Folks L., Street R., Woodward R., and McCormick P.G., *J. Appl. Phys.*, **75** p.6634 (1994)

Foner, S., *Rev. Sci. Inst.*, **30** p.548 (1959)

Fraune, M., Rüdiger, U., Güntherodt, G., Cardoso, S., and Freitas, P., *Appl. Phys. Lett.*, **77** p.3815 (2000)

Fuke, H. N., Saito, K., Kamiguchi, Y., Iwasaki, H., and Sahashi, M., *J. Appl. Phys.*, **81** p.4004 (1997)

Fuke, H. N., Saito, K., Yoshikawa, M., Iwasaki, H., and Sahashi, M., *Appl. Phys. Lett.*, **75** p.3680 (1999)

Fulcomer, E., Charap, S. H., *J. Appl. Phys.*, **43** p.4184 (1972a)

Fulcomer, E., Charap, S. H., *J. Appl. Phys.*, **43** p.4190 (1972b)

$\mathcal{G}$

Gökemeijer, N. J., and Chien, C. L., *J. Appl. Phys.*, **85** p.5516 (1999)

Gökemeijer, N. J., Cai, J. W., and Chien, C. L., *Phys. Rev. B*, **60** p.3033 (1999)

Goodman, A. M., O'Grady, K., Laidler, H., Owen, N. W, Portier, X., Petford-Long, A. K., and Cebollada, F., *IEEE Trans. Magn.*, **37** p.565 (2001)

$\mathcal{H}$

Herzer, G., *IEEE Trans. Magn.*, **26** p.1397 (1990)

Hesinberg, W., *Z. Physic* **49** p.619 (1928)

Hoffmann, A., *Phys. Rev. Lett.*, **93** p.097203 (2004)

Hoffmann, H., *IEEE Trans. Magn.*, **9** p.17 (1973)

I

Imakita, K., Tsunoda, M, and Takahashi, M., *J Appl. Phys.*, **85** p.3812 (2004)

Imakita, K., Tsunoda, M, and Takahashi, M., *J Magn. Magn. Mat.*, **286** p.248 (2005)

Imry, Y., and Ma, S.K., *Phys. Rev. Lett.*, **35** p.1399 (1975)

J

Jia, H., Veldeman, J., and Burgelman, M., *J. Magn. Magn. Mat.*, **223** p.73 (2001)

Jiles, D., 'Introduction to Magnetism and Magnetic Materials', *Chapman & Hall* 2nd Ed. (1998)

Jimbo, M., Komiyama, K., Shirota, Y., Fujiwara, Y., Tsunashima, S., and Matsuura, M., *J. Magn. Magn. Mat.*, **165** p.308 (1997)

Joffe, I., and Heuberger, R., *Phil. Magn.*, **314** p.1051 (1974)

Jung, H. S., and Doyle, W. D., *IEEE Trans. Magn.*, **39** p.2291 (2003)

Jung, H. S., Doyle, W. D., and Matsunuma, S., *J. Appl. Phys.*, **93** p.6462 (2003)

Jungblut, R., Coehoorn, R., Johnson, M., aan de Stegge, J., and Reinders, A., *J. Appl. Phys.*, **75** p.6659 (1994)

Juraszek, J., Fassbender, J., Poppe, S., Mewes, T., Hillebrands, B., Engel, D., Kronenberger, A., Ehresmann, A., and Schmoranzer, H., *J. Appl. Phys.*, **91** p.6896 (2002)

K

Kale, R. B., and Lokhande, C. D., *Appl. Surf. Sci.*, **223** p.343 (2004)

Keller, J., Miltényi, P., Beschoten, B., Güntherodt, G., Nowak, U., and Usadel, K. D., *Phys. Rev. B*, **66** p.014431 (2002)

Kerr, E., van Dijken, S., and Coey, J. M. D., *J. Appl. Phys.*, **97** p.093910 (2005)

Khapikov, A. F., Harrell, J. W., Fujiwara, H., and Chou, C., *J. Appl. Phys.*, **87** p.4954 (2000)

Kim, J. C., Heo, N. H., Chai, K. H., Na, J. G., Woo, J. S., and Kim, G. M., *Scripta Mater.*, **38** p.1405 (1998)

Kim, M. J., Kim, H. J., Kim, K. Y., Jang, S. H., and Kang, T., *J. Magn. Magn. Mat.*, **239** p.195 (2002)

Kittel, C., 'Introduction to solid state physics', 7th Ed., *Wiley New York* (1996)

Kiwi, M., J. *Magn. Magn. Mat.*, **234** p.584 (2001)

Knoll, M., and Ruska, E., *Z. Physic*, **78** p.318 (1932)

Koon, N.C., *Phys. Rev. Lett.*, **78** p.4865 (1997)

$\mathcal{L}$

Larson, B. E., Hass, K. C., Ehrenreich, H., and Carlsson, A. E., *Phys. Rev. B.*, **37** p.4137 (1988)

Lee, L. L., Laughlin, D. E., and Lambert, D. N., IEEE Trans. Magn., 30 p.3951 (1994)

Li, H., Freitas, P. P., Wang, Z., Sousa, J. B., Gogol, P., and Chapman, J., *J. Appl. Phys.*, **89** p.6904 (2001)

Li, Z., Zhang,S., *J. Appl. Phys.*, **89** p.7272 (2001)

Lin, T., Mauri, D., Staud, N., Hwang, C., Howard, J. K., and Gorman, G. L., *Appl. Phys. Lett.*, **65** p.1183 (1994)

Liu, C., Yu, C., Jiang, H., Shen, L., Alexander, C., and Mankey, G. J., *J. Appl. Phys.*, **87** p.6644 (2000)

$\mathcal{M}$

Maat, S., Takano, K., Parkin, S. S. P., and Fullerton, E. E., *Phys. Rev. Lett.*, **87** p.087202 (2001)

Malkinski, L., O'Keevan, T., Camley, R. E., Celinski, C., Wee, L., Stamps, R. L., and Skrzypek, D., *J. Appl. Phys.*, **93** p.6835 (2003)

Malozemoff, A.P., *J. Appl. Phys.*, **63** p.3874 (1988a)

Malozemoff, A.P., *Phys. Rev. B*, **35** p.3679 (1987)

Malozemoff, A.P., *Phys. Rev. B.*, **37** p.7673 (1988b)

Manzoor, S., Vopsaroiu, M., Vallejo-Fernandez, G., and O'Grady, K., *J. Appl. Phys.*, **97** p.10K118 (2005)

Matsumoto, M., Morisako, A., Takei, S., and Taijima, J., *J. Magn. Soc. Japan*, **21**

p.509 (1997)

Mauri, D., Kay, E., Scholl, D., and Howard, J. K., *J. Appl. Phys.*, **62** p.2929 (1987a)

Mauri, D., Siegmann, H.C., Bagus, P.S., and Kay, E., *J. Appl. Phys.*, **62** p.3047 (1987b)

McCord, J., Schäfer, R., Mattheis, R., and Barholz, K. U., *J. Appl. Phys.*, **93** p.5491 (2003)

Meiklejohn, W. H., and Bean, C. P., *Phys. Rev.*, **102** p.1413 (1956)

Meiklejohn, W. H., *J. Appl. Phys.*, **33** p.1328 (1962)

Miltényi, P., Gierlings, M., Keller, J., Beschoten, B., Güntherodt, G., Nowak, U., and Usadel, K. D., *Phys. Rev. Lett.*, **84** p.4224 (2000)

Misra, A., Nowak, U., and Usadel, K. D., *J. Appl. Phys.*, **95** p.1357 (2004)

Moodera, J. S., and Mathon, G., *J. Magn. Magn. Mat.*, **200** p.248 (1999)

Moodera, J. S., Kinder, L. R., Wong, T. M., and Meservey, R., Phys. Rev. Lett., **74** p.3273 (1995)

$\mathcal{N}$

Néel, L., *Ann. Phys.*, (Paris) **2** p.61 (1967)

Néel, L., *Comp. Rend. Acad. Sci.*, **228** p.664 (1949)

Néel, L., *Comp. Ann. Phys.*, (Paris) **5** p.99 (1949)

Ng, V., Chen, F. H., and Adeyeye, A. O., *J. Magn. Magn. Mat.*, **260** p.53 (2003)

Nishioka, K., Hou, C., Fujiwara, H., and Metzger, R. D., *J. Appl. Phys.*, **80** p.4528 (1996)

Nishioka, K., *J. Appl. Phys.*, **86** p.6305 (1999)

Nishioka, K., Shigematsu, S., Imagawa, T., and Narishige, S., *J. Appl. Phys.*, **83** p.3233 (1998)

Nogues, J., Lederman, D., Schuller, I.K., and Rao, K.V., *Appl. Phys. Lett.*, **68** p.3186 (1996)

Nogues, J., Schuller, I. K., *J. Magn. Magn. Mat.*, **192** p.203 (1999)

Nowak, U., Usadel, K. D., Keller, J., Miltényi, P., Beschoten, B., and Guntherodt, G., *Phys. Rev. B*, **66** p.014430 (2002)

O

O'Grady, K., Dova, P., and Laidler, H., *Mater. Res. Soc. Symp. Proc.*, **517** p.231 (1998)

O'Grady, K., Holloway, L., and Antel Jr., W. J., *IEEE Trans. Magn.*, **38** p.2741 (2002)

O'Handley, R. C., Modern Magnetic Materials: Principles and Applications, *John Wiley & Sons* (2000)

Oh, S. C., and Lee, T. D., *IEEE Trans. Magn.*, **37** p.1504 (2001)

Ostanin, S., Razee, S. S. A., Staunton, J. B., Ginatempo, B., and Bruno, E., *J. Appl. Phys.*, **93** p.453 (2003)

P

Paccard, D., Schlenker, C., Massenet, O., Montmory, R., and Yelon, A., *Phys. Status Solidi*, **16** p.301 (1966)

Pakala, M., Huai, Y., and Anderson, G., IEEE Trans. Magn., 36 p.2620 (2000b)

Pakala, M., Huai, Y., and Miloslavsky, L., *J. Appl. Phys.*, **87** p.6653 (2000a)

Papusoi, C., Hauch, J., Fecioru-Morariu, M., Güntherodt, G., *J. Appl. Phys.*, **99** p.123902 (2006)

Park, J. K., Kim, J. H., Park, S. I., Lee, H. M., and Oh, D. Y., *Script. Mater.*, **48** p.1161 (2003)

Parkin, S. S. P., and Speriosu, V. S., Magnetic Properties of Low Dimensional Systems II, *Ed. Springer (Berlin)* p.110 (1990)

Parkin, S. S. P., More, N., and Roche, K. P., *Phys. Rev. Lett.*, **64** p.2304 (1990)

Platt, C. L., Berkowitz, A. E., Smith, D. J., and McCartney, M. R., *J. Appl. Phys.*, **88** p.2058 (2000)

Pohkil., T., Linville, E., and Mao, S., *J. Appl. Phys.*, **89** p.6588 (2001)

Q

$\mathcal{R}$

Rickart, M., Guedes, A., Franco, N., Barradas, N. P., Diaz, P., MacKenzie, M., Chapman, J. N., and Freitas, P. P., *J. Phys. D: Appl. Phys.*, **38** p.2151 (2005)

Rose J., Chapman J.N., Phillips G.N., Laidler H., and O'Grady K., J. Magn. Magn. Mat. **177** p.223 (1998)

$\mathcal{S}$

Saito, M., Kakaihara, Y., Watanabe, T., and Hasegawa, N., *J. Magn., Soc. Japan*, **21** p.505 (1997)

Sang, H., Du, Y. W., and Chien, C. L., *J. Appl. Phys.*, **85** p.4931 (1999)

Sato, T., Tsunoda, M., and Takahashi, M., *J. Magn. Magn. Mat.*, **240** p.277 (2002)

Seu, K. A., Huang, H., Lesoine, J. F., Showman, H. D., Egelhoff, W. F., Gan, L., and Reilly, A. C., *J. Appl. Phys.*, **93** p.6611 (2003)

Schulthess, T.C., and Butler, W.H., *J.* Appl. Phys., **85** p.5510 (1999)

Schulthess, T.C., and Butler, W.H., *Phys. Rev. Lett.*, **81** p.4516 (1998)

Shull, C. G., and Smart, J. S., *Phys. Rev.*, **76** p.1256 (1949)

Shull, R. D., Shapiro, A. J., Gornakov, V. S., Nikitenko, V. I., and Zhao, H.-W., *J. Appl. Phys.*, **93** p.8603 (2003)

Slater, J. C., *Phys. Rev.*, **35** p.509 (1930a)

Slater, J. C., *Phys. Rev.*, **36** p.57 (1930b)

Slater, J. C., *Phys. Rev.*, **49** p.537 (1936)

Stamps, R. L., *J. Phys. D: Appl. Phys.*, **33** p.R247 (2000)

Staunton, J. B., Ostanin, S., Razee, S. S. A., Gyorffi, B. L., Szunyogh, L., Ginatempo, B., and Bruno, E., Phys. Rev. Lett., **93** p.257204 (2004)

Steenbeck, K., Mattheis, R., and Diegel, M., *J. Magn. Magn. Mat.*, **279** p.317 (2004)

Stiles, M. D., McMichael, R. D., *Phys. Rev. B*, **59** p.3722 (1999a)

Stiles, M. D., McMichael, R. D., *Phys. Rev. B*, **60** p.12950 (1999b)

Stiles, M. D., McMichael, R. D., *Phys. Rev. B*, **63** p.064405 (2001)

Stuart, R. V., 'Vacuum technology, thin films, and sputtering. An introduction', *Academic Press New York* (1983)

Suess, D., Kirschner, M., Schrefl, T., Scholz, W., Dittrich, R., Forster, H., and Fidler, J., *J. Appl. Phys.*, **93** p.8618 (2003)

T

Takahashi, M., and Tsunoda, M., *J. Phys. D: Appl. Phys.*, **35** p.2365 (2002)

Takano, K., Kodama, R. H., Berkowitz, A. E., Cao, W., Thomas, G., *Phys. Rev. Lett.*, **79** p.1130 (1997)

Thomson, T., Riedi, P. C., Platt, C. L., Berkowitz, A. E., *IEEE Trans. Magn.*, **34** p.1045 (1998)

Thwaites, M. J., "High Density Plasmas", U.S. Patent No. 6,463,873 (15 October 2002)

Tomeno, I., Fuke, H. N., Iwasaki, H., Sahashi, M., *J. Appl. Phys.*, **86** p.3853 (1999)

Tondra, M., Daughton, J. M., Wang, D., Beech, R. S., Fink, A., and Taylor, J. A., *J. Appl. Phys.*, **83** p.6688 (1998)

Tsunoda, M., Imakita, K., Naka, M., and Takahashi, M., *J. Magn. Magn. Mat.*, **304** p.59 (2006)

Tsunoda, M., Konoto, M., and Takahashi, K., *IEEE Trans. Magn.*, **33** p.7896 (1997)

Twardowski, A., Swagten, H. J. M., de Jonge, W. J. M., and Demianiuk, M., *Phys. Rev. B.*, **36** p.7013 (1987)

U

Umebayashi, H., Ishikawa, Y., *J. Phys. Soc. Japan*, **21** p.1281 (1966)

Uyama, H., Otani, Y., Fukamichi, K., Kitakami, O., Shimada, Y., and Echigoya, J., *Appl. Phys. Lett.*, **71** p.1258 (1997)

V

Van der Heijden, P. A. A., Maas, T. F. M. M., de Wonge, W. J. M., Kools, J. C. S., Roozeboom, F., van der zaag, P., *Appl. Phys. Lett.*, **72** p.492 (1998)

Van der Zaag, P. J., Ijiri, Y., Borchers, J. A., Feiner, L. F., Wolf, R. M., Gaines, J. M., Erwin, R. W., and Verheijen, M. A., *Phys. Rev. Lett.*, **84** p.6102 (2000)

Van der Zaag, P. J., Wolf, R. M., Ball, A. R., Bordel, C., Feiner, L. F., and Jungblut, R., *J. Magn. Magn. Mat.*, **148** p.346 (1995)

Van Driel, J., Coehoorn, R., Lenssen, K.-M., Kuiper, A. E. T., and Boer, F. R. de, *J. Appl. Phys.*, **85** p.5522 (1999)

Van Driel, J., de Boer, F. R., Lenssen, K.-M. H., and Coehoorn, R., *J. Appl. Phys.*, **88** p.975 (2000)

Vopsaroiu, M., Georgieva, M., Grundy, P. J., Vallejo-Fernandez, G., Manzoor, S., Thwaites, M. J., and O'Grady, K., J. Appl. Phys., **97** p.10N303 (2005a).

Vopsaroiu, M., Thwaites, M. J., Rand, S., Grundy, P. J., and O'Grady, K., *IEEE Trans. Magn.*, **40** p.2443 (2004)

Vopsaroiu, M., Thwaites, M. J., Vallejo-Fernandez, G., Lepadatu, S., and O'Grady, K., *J.Opt. and Adv. Mat.*, **7** p.2713 (2005b)

W

Wang, G., Yeh, T., Lin, C-L., Siversten, J. M., and Judy, J. H., *IEEE Trans. Magn.*, **32** p.4660 (1996)

Wang, S. X., Sun, N. X., Yamaguchi, M., and Yabukami, S., *Nautre (London)*, **407** p.150 (2000)

Wang, Y. G., and Petford-Long, A. K., *J. Appl. Phys.*, **92** p.6699 (2002)

Webb, B., and Schultz, S., *IEEE Trans. Magn.*, **24** p.3006 (1988)

Wee, L., Stamps, R. L., Malkinski, L., Celinski, Z., and Skrzypek, D., *Phys. Rev. B*, **69** p.134425 (2004)

Williams, D. B., and Carter, C. B., 'Transmission electron microscopy. A book for materials science', *Kluwer Academic/Plenum Publishers* (1996)

Wuory, E. R., and Judy, J. H., *IEEE Trans. Magn.*, **20** p.1867 (1984)

X

Xi, H., Bian, B., Mountfield, K. R., Zhuang, Z., Laughlin, D. E., and White, R. M., *J. Magn. Magn. Mat.*, **260** p.273 (2003)

Xi, H., Bian, B., Zhuang, Z., Laughlin, D. E., and White, R. M., *IEEE Trans. Magn.*, **36** p.2644 (2000)

Xi, H., *J. Magn. Magn. Mat.*, **288** p.66 (2005)

Y

Yagami, K., Tsunoda, M., and Takahashi, M., *J. Appl. Phys.*, **89** p.6609 (2001)

Yamaoka, T., *J. Phys. Soc. Japan*, **36** p.445 (1974)

Yamaoka, T., Mekata, M., and Takaki, H., *J. Phys. Soc. Japan*, **36** p.438 (1974)

Yang, F. Y., Chien, C. L., Ferrari, E. F., Li, X. W., Xiao, G., and Grupta, A., *Appl. Phys. Lett.*, **77** p.286 (2000)

Yoo, C-s, Jeong, H. D., Lee, J. H., Yoon, C. S., Kim, C. K., Yuh, J. H., Ando, Y., Kubota, H., and Miyazaki, T., *IEEE Trans. Magn.*, **38** p.2715 (2002)

Yoon, S. Y., Lee, D. H., Jeon, D. M., Yoon, D. H., and Suh, S. J., *Surface & Coatings Technology*, **193** p.272 (2005)

Yuasa, S., Katayama, T., Fukushima, A., Kubota, H., Suzuki, Y., and Ando, K., "*Giant TMR Effect over 400% at room temperature in fully epitaxial Co/MgO/Co Magnetic Tunnel Junctions with bcc Co(001) electrodes*" ICMFS (2006)

Z

Zhang, K., Zhao, T., and Fujiwara, H., *J. Appl. Phys.*, **91** p.6902 (2002)

Zhao, T., Zhang, K., and Fujiwara, H., *J. Appl. Phys.*, **91** p.6890 (2002).

Zhou., S. M., Liu, K., and Chien, C. L., *Phys. Rev. B.*, **58** p.R14717 (1998)

Zhu, J., "*Thermal and current driven noise in magnetoresistive sensors*", APDSC (2006)

Zhu, J.-G., and Bertram, H. N., *J. Appl. Phys.*, **66** p.1291 (1989)

Ziljstra, H., *IEEE Trans. Magn.*, **MAG-15**, 1246 (1979)

Ziljstra, H., *Rev. Sci. Instrum.*, **41** p.1241 (1970)

Publications

1. "Annealing effect on thermal stability and microstructure in IrMn/$Co_{60}Fe_{20}B_{20}$ bilayers", G. Vallejo-Fernandez, T. Dimopoulos, M. Ruehrig, and K. O'Grady, In Press, *Journal of Magnetism and Magnetic Materials*
2. "Bulk and interfacial effects in exchange biased systems", J. D. Dutson, C. Huerrich, G. Vallejo-Fernandez, L. E. Fernandez-Outon, G. Yi, S. Mao, R. W. Chantrell, and K. O'Grady, *Journal of Physics D: Applied Physics,* **40** p.1293 (2007)
3. "The role of interfaces in CoFe/IrMn exchange biased systems", G. Vallejo-Fernandez, M. Vopsaroiu, L. E. Fernandez-Outon, and K. O'Grady, *IEEE Transactions on Magnetics*, **42** p.3008 (2006)
4. "Thermal instabilities in exchange biased materials", L. E. Fernandez-Outon, G. Vallejo-Fernandez, S. Manzoor, and K. O'Grady, *Journal of Magnetism and Magnetic Materials*, **303** p.296 (2006)
5. "Grain size effects in metallic thin films prepared using a new sputtering technology", M. Vopsaroiu, M. J. Thwaites, G. Vallejo-Fernandez, S. Lepadatu, and K. O'Grady, *Journal of Optoelectronics and Advanced Materials*, **7** p.2713 (2005)
6. "Grain size effects in exchange biased NiFe/FeMn bilayers", S. Manzoor, M. Vopsaroiu, G. Vallejo-Fernandez, and K. O'Grady, *Journal of Applied Physics*, **97** p.10K118 (2005)
7. "Preparation of high moment CoFe films with controlled grain size and coercivity", M. Vopsaroiu, M. Georgieva, P. J. Grundy, G. Vallejo-Fernandez, S. Manzoor, and K. O'Grady, *Journal of Applied Physics*, **97** p.10N303 (2005)
8. "Deposition of polycrystalline thin film with controlled grain size", M. Vopsaroiu, G. Vallejo-Fernandez, M. J. Thwaites, J. Anguita, P. J. Grundy, and K. O'Grady, *Journal of Physics D: Applied Physics*, **38** p.490 (2005)